Site GT2: foliated to layered gabbro transition[1]

Kelemen, P.B., Matter, J.M., Teagle, D.A.H., Coggon, J.A., and the Oman Drilling Project Science Team[2]

Keywords: Oman Drilling Project, OmanDP, Samail ophiolite, gabbro traverse, layered gabbros, foliated gabbros, Wadi Gideah, Site GT2, Hole GT2A, lower crust

Chapter contents

Introduction

Site GT2 is located in Wadi Gideah ~4 km south of Hole GT1A in a small subsidiary valley west of the main wadi-course (Fig. F1). The scientific targets of Site GT2 are to document the transition from foliated gabbros that make up the mid- to upper parts of the plutonic sequence of the Samail ophiolite down to modally layered gabbros that crop out in the lower crust of the ophiolite similar to those sampled in Hole GT1A (Fig. F2). Although regions of foliated gabbros and layered gabbros can be recognized in the field and the transition between these rock types is an important zone where the mode of magmatic differentiation and the ratio between melt and cumulate changes significantly, it is commonly difficult to recognize the transition in the field. The proposed hole should intersect both foliated and layered gabbros and document the transitions between them (Fig. F2). In addition, by drilling an inclined drill hole trending to the northeast, Hole GT2A may intersect one of the north-northwest–trending, steeply dipping greenschist facies altered and mineralized fault zones that occur in the region and further test the role of these features in the hydrothermal cooling of the mid- to lower oceanic crust.

Geological setting

Site GT2 sits in an area of relatively flat wadi gravels east of more rubbly terrain that marks the flooding channels in this small tributary valley. The ridge immediately to the east comprises foliated gabbros that transition into a mixed assemblage of foliated and layered gabbros toward the ridgeline. The diffuse layering in the foliated gabbros strikes to the north-northwest and shows moderate dips to the southwest (s/d 227 ± 13/50° ± 12°SW; Koepke et al., pers. comm.). The better defined magmatic layering in the layered gabbros is approximately parallel to the diffuse fabric of the foliated gabbros (Fig. F2). The rocks are predominantly olivine gabbros to gabbros with rare hornblende-gabbro veinlets. In the main tributary, a large (tens of meters) zone of greenschist facies hydrothermal alteration and mineralization crops out on the eastern slopes of Wadi Gideah associated with a steep westerly dipping (~79°) fault zone (s/d 340/79°W).

Operations

An overview of all holes drilled is given in Table T2 in the **Methods** chapter. Drilling operations and core curation information are reported in Table T1.

All times are reported as local time in Oman (UTC + 4 h).

[1]Kelemen, P.B., Matter, J.M., Teagle, D.A.H., Coggon, J.A., and the Oman Drilling Project Science Team, 2020. Site GT2: foliated to layered gabbro transition. *In* Kelemen, P.B., Matter, J.M., Teagle, D.A.H., Coggon, J.A., and the Oman Drilling Project Science Team, *Proceedings of the Oman Drilling Project*: College Station, TX (International Ocean Discovery Program). https://doi.org/10.14379/OmanDP.proc.107.2020
[2]**OmanDP Science Team affiliations.**

MS OmanDP-107
Published 21 August 2020

Hole GT2A drilling summary

- Spud-in: 25 Dec 2016, 12:45 h
- First core on deck: 25 Dec 2016, 14:00 h
- Surface casing (HW) installed: 26 Dec 2016, 6 m
- Surface casing extended: not applicable
- NW casing installed: 05 Jan 2017, 152.15 m
- Final core on deck: 17 Jan 2017, 16:33 h
- Total depth (TD) of borehole: 406.55 m

Geology summary

- Bedrock was reached at 12 m (not vertical depth because hole is inclined).
- Recovered a mixture of foliated and layered gabbros and olivine gabbros, sometimes strongly altered in the vicinity of fault zones (up to 1 m thick) or hydrothermal veins.
- No clear boundary or transition between foliated and layered gabbros; instead, both were sampled throughout.

Technical issues

Experienced general “teething” issues with brand new drill rig, as well as loss of circulating fluid into formation. The latter was exacerbated by insufficient supply of groundwater delivered by the Lalbuksh water truck. This was eventually resolved by increasing the number of deliveries per day.

Operations summary

- 24 Dec 2016: after weeks of delays, rig arrived at Site GT2 on Christmas Eve. Science team set up core logging tent, tarp, core tables, and DMT core scanner. A yellow drill rig (not used to drill any OmanDP cores) and drilling equipment, water tanks, and site office were delivered by truck.
- 25 Dec 2016: a brand new orange custom-made GSC-03 rig arrived in the early morning, and drilling started at ~12:00 h with spud-in of Hole GT2A. First core on deck: 12:45 h.
- 26 Dec 2016: overnight, 100% water loss at 0–7 m. Surface casing was installed in early morning to 6 m to reduce loss of circulating fluid. A leak in a rig hydraulic hose resulted in further downtime and required repair offsite. Coring restarted shortly before 15:00 h.
- 27 Dec 2016: drill bit changed before drilling started for the day; 7 cores were drilled; excellent recovery. Drilling fell into a smooth rhythm from ~08:30 h, each 3.05 m core taking ~1 h to drill.
- 28 Dec 2016: smooth operations until 15:00 h when drillers’ water supply was exhausted (water tanker driver will not work after 3 pm), at which point drilling stopped for the day. Lead Scientist on site D. Teagle instigated sampling protocol of 5 cm half-round “background” material every ~20 m to produce thin sections and powders prior to core delivery to D/V *Chikyu*.
- 29 Dec 2016: loss of circulating fluid continued, requiring at least 3 water deliveries. Drilling advance: 27 m; core recovered: 28.1 m (recovery ~ 104%). Very few intervals were missing, but areas of faulting resulted in crumbly friable cores. Most surprising is the very high fracture porosity of the core. Oxidation of fractures and fault gouges is present but much less than higher in hole. Late in the day we learned that the drillers (subcontractor) had not been instructed to drill 7 days a week. Following communications with Zaher al Sulaimani and J. Matter, subcontractors agreed to work half-days on Fridays (until ~11:00 h). TD = 81.7 m.
- 30 Dec 2016: rig start: 07:22 h; rotation start: 08:00 h; first core: 08:37 h; 4 full cores drilled before the drillers left for Friday Prayer. Rig maintenance: 10:20–10:45 h. Science team stayed on site until ~14:30 h catching up on curation and scanning and hosted visitors from Ibra Ministry of Regional Municipalities and Water Resources Ibra office. TD = 93.9 m.
- 31 Dec 2016: encouraged drillers to start rig earlier to receive first core on deck at ~07:30 h rather than after 08:00 h. Zaher al Sulaimani visited the site at ~13:00 h and discussed that he may return in a week to survey Sites GT1, GT2, and GT3 by drone. 8 cores drilled; we celebrated the borehole passing 100 m depth, ending the day (and year!). TD = 117.25 m.
- 01 Jan 2017: the New Year was welcomed with good core.
- 02 Jan 2017: major downtime due to rig issues; a problem with the thermal cutout on the main rig engine (Cumins) required extended maintenance. Replacement of a dirty fuel filter seemed to fix the problem (after a lot of blue smoke on morning startup). Borehole continued to lose water with no drilling fluid return, resulting in rising torque (system pressure) on the top drive (should be ~100 kg/m^2 and steady). For most of the day torque was >150 kg/m^2 and at times >200 kg/m^2. Wali (Chief Driller) stressed the importance of restoring circulation. A plan was agreed upon to pull out (POOH) HQ rods and bit, reenter (RIH) with casing shoe and old HQ rods as a temporary liner to full depth (~149.7 m), and then drill ahead with NQ assembly to clear cuttings and conserve water and filling fluid. Water supply remained an issue; no deliveries in the afternoon.
- 03 Jan 2017: 1 core pulled: ~30 cm drilled to balance rods. Recovered short piece of altered gabbro. TD = 149.7 m. Day principally spent POOH HQ rods and bit, inserting a liner of old HQ rods (NW

casing) with casing shoe, and RIH with new NQ bit and NQ rods. Science team caught up with curation, scanning, and descriptions.

- 04 Jan 2017: no cores drilled, no advance. NQ drill string was in the well but HQ spindle couldn't be released from the top drive so that it could be replaced with NQ spindle. Much of the day was spent trying have an HQ–NQ adapter made. This was not complete by 17:45 h but assured that it would be put right by the morning. A Cummins diesel engineer was also on site for much of the day servicing the rig engine. It was not clear that they established reasons for the overheating a couple of days before.
- 05 Jan 2017: an HQ–NQ adapter was constructed overnight. Rig start: 07:45 h; rotation start: 07:50 h. Drilling team pulled Cores 59Z (20 cm advance) and 60Z (10 cm advance), but the core barrel was empty—high fluid pressures and no core. Return of drilling fluid was good. Issue was with core entering the core catcher. Wali tripped out NQ pipe and bit to check bottom-hole assembly and found that the bit and core catcher were mis-fit. Still waiting for correct equipment at end of day.
- 06 Jan 2017: finally back to coring. Rig stopped at various stages for maintenance. Wali estimated the water table in the hole to be at 67 m.
- 07 Jan 2017: minor rig stoppages; 9 cores pulled.
- 08 Jan 2017: minor rig delays; 10 cores pulled.
- 09 Jan 2017: some time spent adding a few centimeters of HW casing (2.6–3 m) to the top of the hole to reduce vibration. Lack of drill water a constant issue throughout the day; the hole was only returning ~20%–30% of drill water, so 3–4 tanker loads were required. System pressure was 150–160 kg/m^2 but stable.
- 10 Jan 2017: good day of drilling. Rig service after last core was pulled at 16:35 h.
- 11–12 Jan 2017: drilling continued smoothly.
- 13 Jan 2017: no drilling – rest day for drillers.
- 14 Jan 2017: 11:17 h, first attempt at recovering Core 122Z failed; core catcher was broken—a small piece of core was caught in the core catcher. The core barrel was run a second time to retrieve the core, and the piece that was stuck in the core catcher was broken on deck. Wali told us that when this hole is finished (400 m), before pulling the casing (150 m) he will ream the hole to install HW casing for another 6 m (12 m total), as he knows from Juerg that cameras and logging equipment need to be deployed in the well later.
- 15 Jan 2017: further issues with core catcher and fragmented cores.
- 16 Jan 2017: more stoppages due to lack of water supply, despite use of larger capacity tanker.
- 17 Jan 2017: Hole GT2A is complete.
- 18 Jan 2017: Wali informed us that after trying to deepen the surface casing by another 6 m, he stopped after 80 cm because the pressure was rising and not safe. He then POOH the NW casing, leaving 6.8 m of surface casing of HW size.
- 19 Jan 2017: science team and Nehal spent the day sorting boxes and lids. The rig was moved to Site GT1, along with rods and other accessories. Mud pits were filled in. The science team wrapped up boxes in tarps to protect from possible rain, took tarp down, and closed up tent.

Igneous petrology

Major rock types

The downhole variations of lithology and rock types in Hole GT2A are shown in Figures F3 and F4 and Table T2, as well as supplementary Tables ST1 and ST2. The main lithology is dominated by olivine gabbro (65.4%), followed in abundance by olivine-bearing gabbro (15.8%) and olivine melagabbro (7.9%). Minor rock types are gabbro (3.1%), gabbronorite (2.5%), varitextured gabbro (0.7%), troctolite (0.5%), anorthositic gabbro (0.4%), and troctolitic gabbro (0.4%).

Lithologic units

Unit I

Igneous Intervals 2–7
Sections 10Z-2, 29 cm, through 39Z-4, 92 cm
Depth: 12.56–103.26 m
Lithology: medium- and fine-grained granular olivine gabbro, olivine-bearing gabbro, and olivine melagabbro; coarse-grained varitextured gabbro

The main rock type in Unit I is fine- to medium-grained olivine gabbro with intercalations of olivine-bearing gabbro, olivine melagabbro, and some domains of coarse-grained varitextured gabbro. Except for the varitextured gabbro, all rock types display granular to nearly equigranular textures. This unit is also generally characterized by decreasing modal abundance of olivine downhole (from ~15% to 2% olivine).

Unit II

Igneous Intervals 7–11
Sections 40Z-1, 0 cm, through 77Z-4, 72 cm
Depth: 103.26–203.70 m
Lithology: medium grained granular olivine gabbro, olivine-bearing gabbro, and olivine melagabbro

The transition from Unit I to Unit II is identified by a slight increase in olivine content and fewer sections with fine-grained layers. The main rock type of Unit

II is medium-grained olivine gabbro with intercalations of olivine-bearing gabbro and olivine melagabbro. The modal abundance of olivine increases toward the bottom of the unit, and olivine melagabbro (with some troctolite layers) becomes the dominant rock type. In general, the unit is characterized by several domains with highly deformed and sheared foliations (e.g., Sections 44Z-3 through 45Z-2).

Unit III

Igneous Interval 11
Sections 87Z-1, 0 cm, through 105Z-3, 4 cm
Depth: 203.70–284.65 m
Lithology: medium-grained olivine gabbro, olivine-bearing gabbro, olivine melagabbro, and gabbro

The transition from Unit II to III is identified by a distinct decrease in the modal abundance of olivine and gabbro layers at the top of the unit. However, the main rock type in Unit III is medium-grained olivine gabbro and olivine-bearing gabbro with intercalation of gabbro and olivine melagabbro. Deformed and sheared foliations are less abundant (and if present, less distinct) than in Unit II.

Unit IV

Igneous Interval 12
Sections 105Z-3, 4 cm, through 109Z-3, 36 cm
Depth: 284.65–293.92 m
Lithology: fine-grained granular gabbronorite

The transition from Unit II to Unit IV is marked by a decrease in grain size and the appearance of orthopyroxene. The major rock type in Unit IV is fine-grained gabbronorite (and depending on the modal abundance of olivine, olivine gabbronorite and olivine-bearing gabbronorite) with 1–20 cm wide layers of medium- and coarse-grained olivine-rich gabbros.

Unit V

Igneous Intervals 13–18
Sections 109Z-3, 36 cm, through 151Z-3, 72 cm
Depth: 293.92–406.77 m
Lithology: medium- and fine-grained granular olivine gabbro, olivine-bearing gabbro, and olivine melagabbro

The transition from Unit IV to Unit V is identified by the absence of orthopyroxene and an increase in grain size. The major rock type in Unit V is medium-grained olivine gabbro with minor olivine-bearing gabbros and olivine melagabbros, all of which exhibit granular textures and equigranular grain size distribution. The modal abundance of olivine generally increases toward the bottom of the unit (from ~8% to 30%), and the igneous layering is characterized by the appearance of multiple fine (0.5 cm wide) olivine-rich bands (informally termed "tiger" layers in the visual core description [VCD] comments).

Core descriptions

Modal variations

Modal abundances of the primary magmatic phases were estimated visually on the most representative part of the core section. Compositions are as follows (see supplementary Table ST1).

- Olivine-bearing gabbros:
  - Olivine: 1–10 vol% (average: 3 vol%)
  - Plagioclase: 20–76 vol% (average: 54 vol%)
  - Clinopyroxene: 22–78 vol% (average: 43 vol%)
- Olivine gabbros:
  - Olivine: 5–67 vol% (average: 14 vol%)
  - Plagioclase: 7–80 vol% (average: 48 vol%)
  - Clinopyroxene: 10–72 vol% (average: 38 vol%)
- Olivine and olivine-bearing gabbronorites:
  - Olivine: 1–9 vol% (average: 7 vol%)
  - Plagioclase: 37–60 vol% (average: 49 vol%)
  - Clinopyroxene: 15–40 vol% (average: 26 vol%)
- Gabbros:
  - Plagioclase: 26–78 vol% (average: 61 vol%)
  - Clinopyroxene: 22–74 vol% (average: 39 vol%)
- Varitextured gabbros:
  - Plagioclase: 51–86 vol% (average: 75 vol%)
  - Clinopyroxene: 3–8 vol% (average: 6 vol%)
- Troctolite and troctolitic gabbros:
  - Olivine: 24–77 vol% (average: 47 vol%)
  - Plagioclase: 13–71 vol% (average: 48 vol%)
  - Clinopyroxene: 2–13 vol% (average: 6 vol%)
- Olivine gabbronorites and olivine-bearing gabbronorites:
  - Olivine: 1–9 vol% (average: 7 vol%)
  - Plagioclase: 37–60 vol% (average: 49 vol%)
  - Clinopyroxene: 15–40 vol% (average: 26 vol%)
  - Orthopyroxene: 2–13 vol% (average: 6 vol%)
- Gabbronorites:
  - Plagioclase: 57–60 vol% (average: 59 vol%)
  - Clinopyroxene: 20–37 vol% (average: 27 vol%)
  - Orthopyroxene: 6–20 vol% (average: 14 vol%)

Olivine mode gradually decreases in the upper 100 m *Chikyu* adjusted depth (CAD) (lithologic Unit I) and then is consistently low but variable at 100–210 m (lithologic Unit II) (Fig. F5). At the top of lithologic Unit III, olivine mode is at its lowest but gradually increases until ~250 m then decreases irregularly to 280 m, where gabbronorites occur (lithologic Unit IV). Olivine mode increases irregularly downhole in lithologic Unit V to 375 m, where it plateaus at 15–20 modal%. Coincidently with the decrease in olivine mode, plagioclase and clinopyroxene mode increase and decrease, respectively, down to 100 m. The plagioclase and clinopyroxene modes fluctuate around 50 and 40 vol%, respectively, down to 400 m at the bottom of the hole and do not show a steady increase or a decrease in the lowermost 100 m.

Grain size variations

The average grain size of rock samples ranges from fine (<1 mm) to medium (1–5 mm) grained except for a varitextured (>3 mm) interval at 71.5–81.1 m (igneous Interval 6) (Fig. F6). Excluding a pegmatitic interval and olivine gabbro (>2 mm) intervals at 41.9–46.9 m (igneous Intervals 3–5), the maximum and modal lengths of olivine, clinopyroxene, and plagioclase in the upper 100 m (lithologic Unit I) are smaller than those at 100–211 m (lithologic Unit II). After a sharp increase in grain size at 227–230 m near the top of lithologic Unit III, grain size regularly decreases down to 270–280 m toward the top of Unit IV. Through lithologic Unit V, the maximum lengths of clinopyroxene and plagioclase remain around 3 mm, whereas olivine grain size shows a spike at 330–350 m.

As in Hole GT1A, macroscopically identified coarse-grained olivine crystals are elongate to tabular in shape and consist of olivine subgrains aligned subparallel to foliation defined by surrounding plagioclase and clinopyroxene under the microscope (Fig. F7A; see Thin section descriptions).

Textures

Similar to Hole GT1A, most rock samples have undergone metamorphic (hydrothermal) alteration along veins and shear zones that partly obscures the original igneous (and/or structural) textures. Also cataclastic shearing, crystal-plastic deformation, and partial recrystallization, some of which occurred at high temperatures, overprint some original magmatic features (see Structural geology). However, primary igneous textures are still well preserved in most of the least deformed and least altered samples. All rock samples have a granular texture (see supplementary Table ST1). Although rocks with ophitic or poikilitic texture are not present, within the granular matrix ophitic or poikilitic clinopyroxene oikocrysts commonly occur in most core samples (Fig. F7B; see Thin section descriptions).

Olivine occurs mostly as anhedral tabular to elongate crystals, although subhedral equant to subequant crystals are also present. Plagioclase forms anhedral to subhedral tabular to subequant crystals partly or totally enclosed by large clinopyroxenes. Subrounded to rounded clinopyroxene is included in some plagioclase (Fig. F7C). Clinopyroxene is commonly anhedral to subhedral with subequant to tabular habit and generally encloses rounded or tabular plagioclase (totally or partially) and, less commonly, olivine. Fragmentary oikocrystic clinopyroxene crystals are common (Fig. F7B). Discrete orthopyroxene crystals characterize the gabbronorites in lithologic Unit IV. Here, orthopyroxenes form prismatic subhedral to anhedral crystals. Unit IV is also characterized by Fe-Ti oxide filling interstices between pyroxenes and plagioclase. Tiny oxide crystals are also present in most rocks as inclusions in olivine and clinopyroxene.

Contacts

A total of 32 lithologic contacts and changes in lithology were recognized in Hole GT2A in addition to numerous contacts within magmatic intrusions with the same lithology and igneous interval numbers. Because of recovery gaps (38% of the total), many contacts were not observed directly other than as a change in rock type across a gap in recovery. The contacts recovered were classified as either lithologic or structural. Lithologic contacts were further classified based on variations in either modal mineralogy (25%) or grain size (34%), whereas structural contacts are related to faulting (Fig. F8). Lithologic and structural contacts constitute 19 of 20 recovered contacts; only 1 contact is tectonic.

The nature of lithologic contacts may be either sharp (Fig. F8A, F8C, F8D) or gradational (Fig. F8B). Gradational lithologic contacts are a gradual change in either grain size or modal abundance of constituent minerals, or both. Figure F8B shows an example of a gradational contact between igneous Intervals 16 and 17, where modal abundance of olivine gradually increases upsection. Sharp contacts were observed at the boundary between Units III and IV delineated by major changes in both the mode and grain size of constituent minerals (Fig. F8D).

Three types of contact geometry were observed: planar, curved, and irregular. Planar and curved contacts are either concordant or discordant to the structures of the adjacent two lithologies. Figure F8A shows examples of planar and curved contacts where foliation is discordant against the contacts. The discordant contact may be due to precipitation of primary minerals from magma on erosional surfaces of fine-grained crystal mush. Discordant crosscutting relationships of the host foliation and layering and engulfment of the host rocks within the invaded rock can result in contacts that follow the outlines of grain boundaries and grains in the invaded rock that are not broken to make room for the invading magma (Fig. F8D). One interpretation is that a melt intruded a partly consolidated crystal mush so that grains of the invaded country rock were easily separated from one another during intrusion. Sheared contacts commonly display weak foliation adjacent to the contact in one or both bordering lithologies. In many cases, cataclastic deformation and brittle fragmentation developed along the contact (Fig. F8E).

Igneous layering

Grain size layering and modal layering are present in rocks from all the lithologic units of Hole GT2A; however, layering is most intense in Units II and III and least strongly developed in Unit I (Fig. F9). The general layer thickness ranges 0.5–130 cm (Figs. F9, F10), and layers with thickness of 0.5–30 cm are by far the most abundant (Fig. F10). Layers with thickness of ~80–90 cm appear to be absent, but as this is the average length scale of a single section, layering on this scale might not be picked up easily.

Layering in Unit I is dominated by shorter length scales at the top (~0.5–30 cm thick layers), and the nature of the layering results from sharp changes in grain size. Towards the bottom of the unit, layering is dominated by changes in the modal abundance of olivine, and the thickness of the layers increases (and in some cases exceeds the length of one individual section). In Unit II, layering is mostly modal with average layer thickness of ~20 cm. Where layering results from changes in grain size, the average layer thickness is larger (25–100 cm). The boundaries between different layers are mostly sharp, but in some cases (e.g., Sections 40Z-4, 42Z-3, 43Z-1, and 43Z-2), the modal abundance of olivine changes gradationally. Layering in Unit III is mainly characterized by modal layering, and layer thicknesses are ~30 cm. Some thicker (~60 cm) layers are present at the center of the unit. Layering in Unit IV is characterized by thin, mostly centimeter-scale bands of coarser grained material intercalating the generally fine-grained gabbronorites in this unit.

In Unit IV, layers are most commonly defined by different alignments of olivine crystals (Fig. F11). In some cases, olivines are aligned in thin bands (informally termed "tiger" layers in the VCD comments) or clustered together (named "spotty" layers in the VCD comments).

Thin section descriptions

Principal lithologies

From Hole GT2A of the Oman Drilling Project, 75 thin sections were described by the igneous petrology team in the shipboard laboratory onboard *Chikyu*. We briefly summarize the results of thin section descriptions in Table T3. Detailed descriptions of each thin section are available in **Supplementary material** > **B_Thin section descriptions**. The variety of rock types present in Hole GT2A is much richer than in Hole GT1A. The main rock types in Hole GT2A are olivine gabbro and olivine-bearing gabbro with minor amounts of gabbro, olivine melagabbro, anorthosite, troctolitic olivine gabbro, troctolite, disseminated oxide olivine gabbro, oxide olivine gabbro, disseminated oxide gabbronorite, and olivine-bearing gabbronorite. Both fine- and medium-grained gabbroic rocks are common throughout Units I–III, but fine-grained rocks are dominant in Units IV and V (Fig. F12A). Most samples display weak to strong foliation defined by alignment of plagioclase.

Olivine mostly occurs as anhedral grains but displays a rich variety of habits and morphology (Fig. F13). Modal olivine has larger variety in Units I–III but it is poorer in variety in Units IV and V (Fig. F12B). The relationship is similar to that of the variation in grain size and Mg# of whole rock (see **Geochemistry**). Olivine has completely altered to talc, serpentine, chlorite, and tremolite in more than 50% of occurrences.

Plagioclase has mainly subhedral shapes but is anhedral in more recrystallized samples. The habit of plagioclase is commonly subequant to tabular, but elongated plagioclase occurs in some of the more foliated samples. Weak to strong plagioclase shape-preferred orientation defines planar magmatic foliations (Fig. F13). Plagioclase zoning is rare and weakly developed in many samples from Hole GT2A (Fig. F14A). Foliated plagioclase crystals uncommonly display zoned structures in some fine- to medium-grained gabbroic rocks (e.g., interval 75Z-2, 12.5–16.5 cm). Olivine and clinopyroxene crystals are contained outside of a euhedral core in such zoned plagioclase (Fig. F14B). We can also find large "phenocrystic" plagioclase with distinct zoning in some fine-grained samples, as described later (Fig. F14C).

Clinopyroxene commonly displays anhedral shape and subequant habit and commonly includes a few small inclusions of plagioclase. Brown amphibole blebs ubiquitously occur in clinopyroxene grains and have a same extinction angle in a clinopyroxene grain.

Orthopyroxene is basically found only in fine- to medium-grained gabbronorite samples from Unit IV (e.g., interval 105Z-4, 40–45 cm) except in troctolite adjacent to gabbronorite. It mostly occurs as discrete crystals with subhedral to anhedral shape. Discrete orthopyroxene crystals commonly have clinopyroxene exsolution lamellae. Rare rounded olivine grains are included in some orthopyroxene (e.g., interval 105Z-4, 40–45 cm).

Opaque minerals commonly occur in gabbronorite from Unit IV and oxide to disseminated oxide olivine gabbros from Unit V. In Unit IV, magnetite commonly occurs around orthopyroxene grains (e.g., interval 108Z-1, 39–42 cm). In oxide olivine gabbro, some sulfide grains (up to several hundred micrometers) occur adjacent to large anhedral magnetite grains (e.g., interval 110Z-1, 15–18 cm). Interestingly, whole-rock FeO^t and SO_3 contents of Unit V gabbros are generally higher than in other units (see **Geochemistry**).

Detailed observations and special features

Olivine melagabbro

Olivine melagabbros comprise the base of modally and some size-graded layers (e.g., Sections 75Z-1 through 75Z-4, 83Z-2 through 83Z-3, 84Z through 85Z, and 141Z-2; Fig. **F15A**). Within a single layered sequence, the olivine mode gradually increases from olivine-bearing gabbro at the top to olivine melagabbro at the bottom. The boundary between olivine melagabbro and olivine-bearing gabbro is macroscopically sharp and planar (Fig. **F15B**) but microscopically sutured (Fig. **F15C**). The modal amount of olivine in olivine melagabbro is ~40–65 vol% (Fig. **F12B**). The aspect ratio (long/short axis length) of plagioclase in the olivine melagabbros is relatively higher (up to 4.5).

Fine-grained rocks

Several types of fine-grained rocks are present in Hole GT2A (Table **T3**). Some of fine-grained olivine or olivine-bearing gabbros include much larger plagioclase crystals than other surrounding crystals (e.g., intervals 18Z-1, 52–52 cm; 54Z-3, 18–20 cm; 105Z-4, 40–45 cm; 138Z-1, 84–89 cm; Fig. **F16A, F16B**). Therefore, we can call grain size distributions of some rocks almost porphyritic. These large plagioclases commonly display zoned structures. The core commonly shows rounded or irregular shapes, and some mineral inclusions are present at the edge of the core (Fig. **F16C**). These textures are similar to the dusty zoning observed in plagioclase from volcanic rocks (Tsuchiyama, 1985). The presence of compositionally zoned large plagioclase may suggest that the fine-grained rocks cooled more rapidly than the surrounding medium-grained gabbroic rocks. In fine-grained gabbroic rocks of the same section (54Z-3), we also find a medium-grained gabbroic block (Fig. **F17A**). The shape of the block is irregular but slightly rounded macroscopically (Fig. **F17B**). Microscopically, crystals from the fine-grained rocks are partly included in those in the medium-grained gabbroic block (Fig. **F17C**).

In Unit IV, fine-grained gabbronorite occurs over ~9 m (interval 105Z-3, 4 cm, to 109Z-3, 36 cm). The upper contact of fine-grained gabbronorite shows a macroscopically sharp and irregular boundary (Fig. **F18A**). At the contact between medium-grained troctolite and fine-grained gabbronorite, a film of anhedral orthopyroxene formed rimming olivine crystals in medium-grained troctolite (Fig. **F18B**; 105Z-3, 3.5–7.5 cm). The orthopyroxene films occur only along the side of the olivine rim close to gabbronorite. Fine-grained plagioclase crystals in the gabbronorite have distinct zoning and contain many tiny crystal inclusions in the core (Fig. **F18C**).

Alteration

Hydrothermal alteration is ubiquitous throughout Hole GT2A, and all rocks have undergone water-rock reactions under a range of temperature conditions and fluid compositions and over the lifespan of the Oman ophiolite from the Tethyan ocean ridge crest and ocean floor through obduction to exposure today in the deserts of Oman. Hydrothermal alteration in Hole GT2A manifests as alteration of the host rock (background, patches, halos, and deformation-related types) and through precipitation of secondary minerals in veins. Alteration is highly variable in type and intensity. On the scale of a single ~1 m section, all four of the above categories plus multiple types of hydrothermal veins are present, reflecting the complex history of these rocks.

Alteration types

During macroscopic core description, the alteration team identified and logged 670 intervals of alteration (see the Alteration tab in **Supplementary material** > **E_Tabulated VCD data**). Each alteration interval was defined as an interval within a core section where the alteration assemblage, style, and intensity were similar. Overviews of the alteration and veins downhole are shown in Figures **F19**, **F20**, and **F21**. Alteration intensity is highly variable downhole; total alteration ranges 6%–100% (mean = 44%) (Fig. **F19**). Within this broad range are several depth intervals where the alteration intensity is observed to increase downhole (e.g., 0–80, 120–180, and 200–250 m).

Background alteration

Background alteration is ubiquitous throughout Hole GT2A (Fig. **F20**), occurring in 95% of the 670 defined alteration intervals (Fig. **F20**), and the average proportion of an interval represented by background alteration is 69%. Of all described intervals, 36 (5%) show 100% background alteration. Background alteration intensity ranges 5%–95% (mean = 31%). Background alteration texture is predominantly classified as pervasive or patchy, with banded background alteration the least common type. Background alteration colors are variable; the most common are medium gray, dark gray, and gray-green (Fig. **F22**). Background alteration color is related to the background alteration intensity and secondary mineral assemblage. Background intensity of 0%–25% is generally associated with dark to medium gray, 25%–40% with medium to light gray through greenish and/or partially brownish, 40%–80% with gray-green, partially brown, or orange, and colors of background intensity >80% vary widely. The secondary mineral assemblage of background alteration is dominated by albite + chlorite throughout Hole GT2A (Fig. **F21**); different background alteration colors generally reflect a change from albite dominated to higher chlorite abundances. Amphibole is only identified macroscopically in 3% of all described intervals present in the background alteration assemblage, none between 170 and 300 m. Albite is associated with partial to complete replacement of plagioclase. Chlorite is associated with replacement of olivine, clinopyroxene, and plagioclase. Epidote is observed in only three depth regions (50–60, 130–210, and ~400 m). Pyrite is abundant throughout Hole GT2A, although there is a gap in occurrence at ~250 m. Iron oxyhdroxides are present in the background in three depth intervals: 0–110, 170–270, and 370–400 m.

Patch alteration

Alteration patches are present in 20% of the 670 defined alteration intervals and on average represent 14% of an interval. Patch alteration intensity ranges 15%–100% (mean = 63%). Downhole variation in patch intensity shows cycles of patch intensity increasing with depth (250–300 and 365–400 m). Alteration patches are found throughout Hole GT2A, although their abundance is lower in the uppermost 100 m (Fig. F20) and at 200–300 m. In the intervals 100–200 and 300–400 m, patches have similar abundances. Alteration patches are mostly irregular in shape and are >6 cm in size in the most cases (Fig. F22). The most common colors of alteration patches are different shades of gray, often combined with a green component. The secondary mineral assemblage of alteration patches commonly contains 3–4 different minerals. The most abundant minerals are (most to least abundant) albite, chlorite, and amphibole. Epidote, clinozoisite, and quartz are also found in patches, but almost only in the upper 200 m. Below 200 m, the abundance of the latter 3 minerals significantly decreases, whereas pyrite starts to form at this depth. Alteration patches commonly appear to be related to primary differences in the igneous modal abundances and grain size (e.g., intervals 48Z-1, 0–17 cm, or 99Z-3, 55–67 cm). Rare examples of extensive secondary mineral precipitation consume the width of the core and could be interpreted as either large patches or large veins. Examples of this texture include large intervals of clinozoisite at 62Z-1, 13–22 cm (Fig. F22).

Halo alteration

Alteration halos are the second most prevalent alteration feature after background alteration and are present in 87% of the 670 defined alteration intervals, representing on average 28% of an interval. Halo alteration intensity ranges 35%–100% (mean = 90%). Individual alteration halos associated with specific veins were not recorded as rigorously because of time constraints. The Vein log in **Supplementary material** > **E_Tabulated VCD data** contains 147 vein halos with a mean width of 13 mm, found throughout Hole GT2A (Fig. F20). Alteration halo width was more systematically recorded in the comments; these indicate that halo width is highly variable and that a large proportion of halos are 1–2 mm in width. The largest halos recorded are >10 cm. Most of the halos are irregular in shape, and only single examples show a symmetric shape around veins (e.g., interval 70Z-1, 8–42 cm). Alteration halo color is highly variable; examples include white, light gray, dark gray, green, dark green, yellow-green, light brown, yellow, and pink (Fig. F22). The most abundant halo color is white, followed closely by halos in different shades of gray. Most of the halo-bearing alteration intervals contain halos of several colors, and individual halos are also frequently multilayered. The color variability is a reflection of secondary mineral assemblages and alteration intensity present within the alteration halos. Secondary minerals present in halos include albite, amphibole, chlorite, clinozoisite, epidote, iron oxyhydroxides, laumontite, prehnite, pyrite, quartz, and zeolites. Albite and chlorite are generally ubiquitous in alteration halos, and amphibole is the third most common mineral phase. Epidote and clinozoisite are present to a lesser extent; clinozoisite disappears below 350 m. The other minerals listed previously are present irregularly: iron oxyhydroxides are present mostly in the upper 200 m and then return at 350 m. Quartz is very common below 70 m, increasing abundance downhole to 180 m, and then decreasing down to 400 m.

The most abundant halo type, white halos, are found throughout the hole. Their size ranges 1–10 cm and up to 40 cm in single cases. These halos are associated with a range of vein compositions; the most common is chlorite + prehnite. The next most abundant halo type is gray/dark gray. These halos are predominantly <5 mm wide, with rare examples up to 40 mm, and are associated with <0.5 mm amphibole veins. Dark green and light green halos are found throughout the hole, also of very variable sizes between 1 and >25 mm with rare examples up to >100 mm. These halos are predominantly associated with chlorite + prehnite veins.

Deformation-related alteration

Deformation-related alteration is present in 17% of the 670 defined alteration intervals and on average represents 27% of an interval. These intervals are highly variable and include localized incipient brecciation to shear zones to extensive intervals of full brecciation (up to 85 cm). Deformation-related alteration intensity ranges 35%–100% (mean = 90%). This alteration type is the most variable in terms of scale, composition, and complexity (Fig. F22). Deformation-related alteration ranges from 2–3 cm bands to 50 cm and is generally associated with brecciation and fault zones. Many deformation zones contain clasts (centimeter scale) of mostly highly altered host rock. Deformation-related alteration is present throughout Hole GT2A (Fig. F20), although the highest proportions of deformation-related alteration (80%–100% of an alteration interval) are found at discrete depths that correlate with major fault zones identified in Hole GT2A. The dominant secondary mineralogy is similar to the other alteration types with chlorite + amphibole + epidote + albite found in most examples of deformation-related alteration. In contrast to background, halo, and patch alteration, quartz is one of the more abundant secondary minerals and is present in 55% of all deformation-related alteration occurrences of Hole GT2A. Deformation-related alteration also contains secondary minerals that are not observed elsewhere in Hole GT2A, such as prehnite, laumontite, and clay.

Veins

Hydrothermal veins are ubiquitous throughout Hole GT2A and form an important record of hydrothermal alteration in the lower crust. A total of 3745 veins (width > 1 mm) were logged individually following the method used for Hole GT1A. Veins <1 mm width were counted in each core section, and their volume and composition were captured following the "Vein net" method. Each assemblage in a core section was recorded in the comments to preserve as much information as possible. Veins represent ~5% of the total split core surface area; the area represented within each section is shown in Figure F23. Downhole, vein density is highly variable and ranges 3–162 veins per meter (mean = 62 veins/m) (Fig. F24). The overall vein density is dominated by veins <1 mm wide and the average density for the >1 mm veins is 9 veins/m (range = 0–30 veins/m). The vein density in Hole GT2A shows several pronounced changes with depth when all vein widths are included. Vein density is higher and most variable in the uppermost 100 m of Hole GT1A (average vein density = 78 veins/m, range = 13–162 veins/m). At 100–120 m, overall vein density decreases, followed by a progressive increase toward 200 m. This trend is not present when only veins >1 mm are considered. Vein density shows the least variation in the lowermost 200 m of Hole GT2A (range = 4–83 veins/m) with less pronounced increase in vein density discernible at 320–360 m. Preliminary analysis suggests no correlation between these trends of increasing vein density and proximity to fault zones (Fig. F24). Vein assemblages (>1 mm) are dominated by the following (in decreasing abundance): quartz; chlorite + prehnite; laumontite; chlorite + quartz; chlorite + laumontite; prehnite; and epidote. All of these assemblages, with the exception of epidote, are found throughout Hole GT2A (Fig. F25). Epidote and zoisite veins are more prevalent shallower than 250 m; below this depth zoisite veins are mostly absent and epidote veins are uncommon. Anhydrite is also found in veins within Hole GT2A; it first appears at ~100 m depth and occurs irregularly to the bottom of Hole GT2A. Anhydrite veins are typically associated with intervals containing deformation (e.g., Sections 64Z-2 and 113Z-1; Fig. F26). Veins containing Fe oxyhydroxides are present down to 200 m; this phase is only found in veins with other minerals (in particular chlorite ± prehnite ± calcite ± laumontite). Calcite-bearing veins are present to 35 m as either pure calcite or calcite ± Fe oxide ± laumontite. Amphibole rarely occurs in veins >1 mm, but amphibole-bearing veins <1 mm are present in 10% of all logged sections and reflects the greater abundance and frequency of amphibole within the alteration assemblages in Hole GT2A.

A total of 114 crosscutting relationships were recorded throughout Hole GT2A, predominantly consisting of 2 veins crosscutting each other (V1 = earliest), but examples including 3–4 veins are also present. Most but not all of the secondary minerals observed in Hole GT2A have crosscutting relationships that record a complex history; particular assemblages are cut by and cut the same minerals. Amphibole-bearing veins are exclusively recorded as V1. Epidote- or zoisite-bearing veins are mostly but not always associated with V1 relative ages. The secondary minerals quartz, chlorite, and prehnite occur in vein assemblages that are associated equally with V1 and V2 relative ages. Laumontite-bearing veins are predominantly associated with V2 relative ages. In contrast to Hole GT1A, anhydrite observed in Hole GT2A preserves a crosscutting relationship (interval 112Z-1, 18–20 cm) where anhydrite crosscuts an epidote + quartz vein (Fig. F26).

XRD results

To aid mineral identification, XRD analysis was completed on 87 samples from Hole GT2A (Table T4). XRD results for zeolites predominantly confirm thomsonite as the zeolite phase (Na-Ca-bearing zeolite). These results were integrated into the downhole secondary mineral plots and recorded in the alteration and vein logs where appropriate.

Thin section descriptions

Thin section observations of the alteration assemblages present in Hole GT2A are broadly consistent with macroscopic core descriptions; these are dominated by greenschist facies assemblages of amphibole ± chlorite ± albite ± epidote ± clinozoisite. Overall alteration intensity as determined from thin sections is highly variable both within and between thin sections and exhibits a range of 10%–100%, consistent with estimates of overall alteration intensity from core logging (6%–100%). Groundtruthing estimates of alteration intensity from core logging scale to thin section is complicated: overall alteration intensity at core scale is a weighted calculation based on alteration type (background, halo, patch, or deformation related) and intensity. Thin sections typically only sample one alteration type and therefore the overall alteration intensity for that interval is not necessarily a useful comparison. Alteration intensity was both under- and overestimated when observations of thin sections are compared to the intensity of the relevant alteration type, with no systematic offsets discernible at this stage. Thin section estimates of alteration intensity are generally (not always) within 10% of the intensity estimated for the alteration type in that interval, and the estimates of alteration intensity from the core-based observations are considered to be an acceptable estimate.

Olivine is variably altered in terms of intensity and assemblage. In some samples olivine is completely replaced by chlorite. Examples include replacement of olivine by serpentine ± magnetite, chlorite, Fe oxyhydroxides, or assemblages of chlorite ± talc ± magnetite (Fig. **F27**). Replacement textures include serpentine mesh textures, prominent talc + serpentine rims, and complete pseudomorphic replacement. Core-scale observations of olivine replacement likely underestimate the presence of serpentine, and talc was not logged. Olivine readily undergoes alteration, and even when overall alteration intensity is low in a thin section, olivine always exhibits partial alteration.

Clinopyroxene demonstrates more uniformity in terms of the alteration assemblage, but the intensity of replacement is highly variable. At the lowest alteration intensities, small (tens of micrometers) patches of pleochroic brown and pleochroic green amphiboles are present both within grains and along the grain boundaries of clinopyroxenes (Fig. **F28**). At higher alteration intensities, in addition to brown and green amphiboles, chlorite replaces clinopyroxene.

Plagioclase alteration is variable in terms of intensity, assemblage, and texture. At the lowest alteration intensities, plagioclase exhibits microcracks throughout with rare small spots of chlorite. As plagioclase replacement intensifies, a range of assemblages are observed including secondary plagioclase, epidote, clinozoisite, chlorite, and prehnite, generally exhibiting pseudomorphic texture. Complete replacement of plagioclase is observed in some thin sections and can be associated with a complete loss of primary texture (Fig. **F29**).

Cataclastic bands observed in thin section Sample 21Z-2, 50–52 cm, are associated with extensive grain size reduction but do not appear to have a significantly higher degree of alteration. The larger of these cataclastic bands has a thin irregular halo that is associated with more chlorite, but most show no increased alteration. These structures are highly localized and occur within a host rock of that is extensively altered and hosts chlorite-prehnite alteration patches (Fig. **F30**).

A ubiquitous feature in thin sections exhibiting lower degrees of alteration intensity (<50%) is a network of veins along grain boundaries. These are typically 5–20 µm in width and although more readily observed between plagioclase crystals (Fig. **F31**) also exist around clinopyroxene crystals. These veins are light green in plane-polarized light (PPL) and are likely amphibole or chlorite, and in some examples have thin 50 µm green halos. These veins may be analogous to the high-temperature (HT) alteration facies described in the literature (Bosch et al., 2004). At higher degrees of alteration intensity this microvein network is not observed and is likely overprinted.

Crosscutting vein relationships are observed in thin section and support the overall sequence of secondary mineral formation identified in the cores. Thin section Sample 17Z-3, 15–17 cm, hosts multiple vein types: epidote + clinozoisite with chlorite halos; chlorite; and prehnite + quartz and zeolite + carbonate. Epidote + clinozoisite veins dominate, and some veins have cores of prehnite + quartz. Zeolite + carbonate veins crosscut epidote + clinozoisite veins. Thin section Sample 78Z-1, 32.5–33.5 cm, hosts chlorite veins that are crosscut by prehnite + carbonate veins.

Large centimeter-scale halos are present in Hole GT2A. An example of this is an epidote-clinozoisite vein and multilayered halo with an inner gray halo and outer white halo (Sample 123Z-4, 15–18.5 cm). In thin section the large epidote-clinozoisite vein is polycrystalline, epidote crystals are generally smaller than the clinozoisite, and overall the vein is asymmetric with one side dominated by small (~50 µm) epidote. The opposite side has a thin subparallel prehnite + chlorite vein adjacent to the vein (Fig. **F32**). The gray halo is characterized by replacement of almost all plagioclase by epidote or clinozoisite and limited replacement of clinopyroxene by chlorite and/or prehnite. The white halo is characterized by absence of epidote and chlorite and domination by secondary plagioclase (Fig. **F33**).

Relative timing

From the crosscutting vein relationships and overprinting halos, the relative timing of each of the secondary minerals can be deduced. From earliest to latest, the following sequence is present:

1. Amphibole
2. Epidote + zoisite (+ minor quartz)
3. Chlorite + prehnite + quartz
4. Anhydrite
5. Laumontite; calcite
6. Gypsum

This sequence is similar to the sequence observed in Hole GT1A and reflects a generalized trend from high-temperature alteration to lower temperature alteration and is also consistent with observations in the modern ocean crust (e.g., Alt et al., 2010). Amphibole is definitely the earliest phase, as it is the only mineral present in crosscutting relationships exclusively as V1 (earliest vein); no other minerals are observed to cut amphibole. Quartz is rarely observed to be cut by amphibole, epidote, or zoisite and is therefore inferred to become more abundant at a later stage. The relative timing of anhydrite is constrained by one crosscutting relationship. Laumontite is found to cut all the minerals with the exception of calcite and gypsum. Calcite veins are rarely observed in crosscutting relationships (1 occurrence where a calcite vein cuts an epidote + quartz vein) and is mostly constrained to the uppermost part of the hole. It may be the latest phase and reflect modern reactions, but this is not definitive from the crosscutting records. Gypsum is found in 3 veins of >1 mm width and in all cases completely cuts across the core and is always associated with an interval of intense deformation. It preserves no relative timing and so is placed last in the sequence.

Structural geology

Hole GT2A provides a 400 m long core across the downward projection of the mapped transition zone between the foliated and layered gabbro sections of the Samail ophiolite in Wadi Gideah, Oman. Numerous structures are present and recorded, including well-developed magmatic fabrics and layering, very limited crystal-plastic deformation, heavily veined and fractured intervals, and several fault zones exhibiting both normal and reverse senses of shear. It is worth emphasizing that Hole GT2A is inclined with a plunge of 60° to the horizontal. Consequently, the core reference frame (CRF) is not horizontal relative to the surface of the Earth and dip angles measured on the core need to be considered with caution and care taken to rotate measurements back into the geographic reference frame. Below is a summary of our major findings, beginning with the highest temperature structures and ending with the lowest temperature structures.

Magmatic structures

Foliated–layered gabbro transition

Hole GT2A was drilled with a plunge of 60° from the horizontal to the northeast to intersect at a gentle angle the foliation and layering in the gabbros that dip 46°–69° to the southwest as mapped at the surface. The surface mapping of a boundary between the foliated gabbros and a transition zone with gabbros exhibiting both foliation and layering projects to ~50 m in Hole GT2A and is inferred to correlate with a relatively dramatic change in dip of the foliation from 50° to 30° in the CRF. The location of the boundary between the bottom of the transition zone and the layered gabbros is poorly constrained by surface mapping but is inferred to intersect the hole at ~175 m. This may correlate to a zone of changing foliation dip from ~40° to ~10° at ~140–180 m in the CRF. Throughout the following section, the magmatic structures of each of the three surface-mapped sequences (the foliated gabbro sequence, the transition zone, and the layered gabbro sequence) will be compared.

Magmatic contacts

The majority of the relatively rare intrusive magmatic contacts in the core are subparallel to the magmatic layering, making them hard to distinguish from the boundaries between magmatic layering. Two examples illustrating this difficulty can be found in the layered gabbro sequence at 310.12 and 303.33 m. Here, two thin (21 and 11 cm thick), more coarse grained, possibly intrusive olivine gabbro layers (intervals 114Z-4, 36–57 cm, and 112Z-3, 13–24 cm) have relatively sharp boundaries and exhibit no foliation but are conformable with the surrounding layered olivine and olivine-bearing gabbros. Typically, boundaries between magmatic layering are planar and sharp, defined by modal, phase, and grain size variations (see **Magmatic layering**). More easily recognizable, highly discordant intrusive contacts are even less common in the core. Magmatic veins commonly have discordant contacts but are discussed in **Magmatic veins**. One example of a magmatic contact is shown in Figure **F33D–F33F**. This contact occurs at 284.65 m and is a sharp, irregular contact between olivine-bearing gabbro and gabbro in the layered gabbro sequence (interval 105Z-3, 0.5–10.5 cm).

Other examples of intrusive contacts are found at 115.48 m in the transition zone (Section 44Z-1, 23 cm). This contact is a sharp but subtly irregular contact between olivine gabbro and olivine-bearing gabbro, defined by a change in grain size and mode. An example of a sheared contact, dipping at 49°, can be found in the transition zone at 117.55 m (interval 45Z-1, 25–32 cm). Sharp, planar, faulted contacts are present in the core, but those contacts are low-temperature nonmagmatic faulted contacts and therefore are reported in **Brittle structures**.

Magmatic layering

Magmatic layering is common in the transition zone and layered gabbro sequences, but it is also less commonly present in the foliated gabbro sequence (~0–50 m). The layering is dominantly defined by variations in mineral proportions (ratio layering) and mineral assemblages (phase layering), commonly in combination with variations in grain size (Figs. **F33**, **F34**, **F35**). Pure grain-size layering is less common. Layer boundaries are typically sharp and planar but may also be gradational and less commonly curved (Fig. F34A). Figure F33A–F33C shows an example of a sharp planar contact between olivine gabbro and "spotted" olivine-bearing gabbro showing ratio and grain-size layering at 43.22 m in the foliated gabbro sequence (interval 20Z-2, 24–37 cm). Figure F34 shows spectacular 10–20 cm scale ratio and phase layering exhibited by an anorthosite layer in olivine-bearing gabbro and olivine gabbro layers from 104.75 m in the transition zone (interval 40Z-3, 3.5–47 cm). The photomicrographs in Figure F34B–F34C illustrate the sharp planar contact between olivine-bearing gabbro and anorthosite (interval 40Z-2, 4.5–7.5 cm). Figure F35A–F35B shows examples of 2–15 cm scale ratio, phase, and grain-size layering shown by gabbro and olivine gabbro at 228.92 m in the layered gabbro sequence (interval 86Z-2, 22–62 cm). The boundaries to the layers are most commonly sharp but maybe curved or planar; as an example, the boundary between the olivine gabbro and sheared "tiger" gabbro at Section 86Z-2, 54 cm, is planar. Photomicrographs in Figure F35C–F35D show the microscopic nature of one of the sharp planar boundaries in interval 86Z-2, 22–62 cm, highlighted by the different grain size and composition of the two layers. Another excellent example of 10 cm scale modal magmatic layering in the layered gabbro sequence occurs in interval 141Z-2, 0–62 cm. Clear magmatic, near-solidus-temperature folding of layering was not observed in the core, although rare magmatic folding of the foliation (see Magmatic foliation), which generally parallels the layering, hints that the layering could be folded in a few places in outcrop.

Distinct 1–2 m scale magmatic cycles that begin with sharp-based olivine-rich melagabbros that modally grade upward and fine upward into olivine and olivine-bearing gabbros occur at several depths within the transition and layered sequence gabbros. Good examples of graded layering can be seen over ~30 m in Sections 33Z-1 through 43Z-3 (81.7–115.08 m) in the transition zone and over 9 m in Sections 78Z-4 through 81Z-3 (206.23–215.3 m) in the layered gabbro sequence.

Centimeter-scale magmatic banding, defined as a weaker, more diffuse type of layering with layers on the order of 0.5–1 cm thick, is also present in the core (Fig. F36). Three examples are shown from the layered gabbro sequence. Figure F36A shows distinct ratio and phase banding grading into very diffuse ratio and phase banding formed by anorthositic layers in olivine gabbro at 199.49 m (interval 76Z-3, 16–51 cm). Figure F36B shows irregular subcentimeter-scale phase banding shown by troctolitic layers in gabbro at 220.87 m. This style of banding was termed "tiger" banding during core description (interval 82Z-3, 2–17.5 cm). Finally, Figure F36C–F36E shows an example of thin anorthosite bands, some of which are parallel to the layering/foliation in the gabbros. This anorthositic band is 0.5 cm wide, has sharp, planar boundaries, and occurs in an olivine gabbro at 197.99 m (interval 76Z-1, 35–44 cm).

The dip of layering ranges from 0° to ~50° (mean = 30°) in the CRF. Given that the hole plunges with a dip of 60°, this means the mean dip of the layering is likely ~60° to the southwest in the geographical reference frame, which is consistent with the dip of the magmatic layering mapped at the surface. Layer thickness is variable, ranging from <3 cm to 3 m. However, 4–50 cm scale layers are most common.

Magmatic foliation

Magmatic foliation is ubiquitous throughout the core, present in the foliated gabbro sequence, transition zone, and layered gabbro sequence. Nearly 90% of the core shows foliation (Figs. F37, F38, F39, F40). The magmatic foliation itself is defined by the presence of aligned and elongate plagioclase, pyroxene, and olivine crystals and varies in strength from not present through weak to strong (Figs. F38, F39, F40). Figure F37 shows examples of differing styles and strengths of magmatic foliation defined by olivine in core samples from the layered gabbro sequence. Figure F37A shows moderate olivine foliation defined by elongate olivine crystals in olivine gabbro (interval 114Z-2, 21–46 cm). Elongate plagioclase and pyroxene show consistent foliation. Figure F37B shows strong olivine foliation defined by elongate olivine crystals in olivine gabbro. This style of foliation is typical of the weak "tiger" banding/foliation described during core description (interval 136Z-2, 3–34 cm). Figure F37C shows moderate to weak olivine foliation defined by clumped subgrained olivine crystals. The right-hand side of the core shows the style of foliation typically developed in the "spotted" gabbros described during core description (interval 115Z-2, 9–46 cm).

Figures F38, F39, and F40 show photomicrographs that illustrate examples of the varying strengths and character of foliation from the foliated gabbro sequence, transition zone, and layered gabbro sequence. Strength of foliation can vary from no foliation (Fig. F40D) through very weak (Figs. F38B, F39A) to strong (Figs. F39C, F40C). The strongest foliations have more elongate crystals, with aspect ratios of plagioclase crystals up to 12:1 (Figs. F38D, F39C), subgrained olivine crystals up to 4:1 (Fig. F40C), and pyroxene crystals up to 10:1 (Fig. F39E). Some plagioclase crystals show evidence of annealing and equilibration (Fig. F40D), although plagioclase deformation twins are commonly present (Fig. F38D). All elongated olivine crystals exhibit subgrain development.

Mineral foliations are most commonly parallel and planar; however, rare crosscutting and truncated foliations are present. Figure F41 shows an example from the layered gabbro sequence at 229.26 m, where medium-grained, weakly foliated olivine gabbro exhibiting steeper foliation appears to be truncated at a sharp planar boundary by weakly banded, more gently dipping, finer grained "tiger" olivine gabbro (interval 86Z-2, 44–64 cm). An example of variably dipping olivine foliation within a 50 cm length of core from 283.04 m in the layered gabbro sequence is shown in Figure F42 (interval 105Z-1, 4–57 cm).

Uncommonly, magmatic foliation is folded and/or sheared. Figure F43A shows gently folded and "sheared" olivine foliation in olivine gabbro at 302.20 m in the layered gabbro sequence (interval 112Z-2, 5–30 cm). Figure F43B shows relatively sharply folded olivine foliation in olivine gabbro at 310.74 m in the layered olivine gabbro sequence (interval 116Z-1, 29–54 cm), and the photomicrographs in Figure F43C–F43D show fine-grained foliated olivine gabbro wrapping around a more coarse grained pocket of gabbro from 144.89 m in the transition zone (interval 54Z-3, 54–58 cm). This folding of mineral foliation implies the magmatic layering may be similarly folded, perhaps providing evidence for magmatic flow and shearing within a mostly solidified crystal mush.

The foliation is mostly concordant with the layering and thus exhibits similar dips, which range 0°–50° (except where steepened by drag due to faulting) (mean = 30°) in the CRF (Fig. F44). The dip of the foliation steepens and shallows cyclically with depth (see **Discussion of magmatic structures**, below). However, the dip of the foliation (in the CRF) is generally steeper in the foliated gabbro sequence and transition zone (~40°) but abruptly changes to more gentle dips just above the top of the layered gabbro sequence (~20°; ~160 m).

Magmatic veins

Magmatic veins are extremely rare in the core, with only ~10 dioritic and gabbroic veins recorded. A few were found in the foliated gabbro sequence, but most occur in the transition zone. The dioritic veins are most commonly ~1 cm wide, discordant to foliation, and magmatic layering with sharp irregular or planar margins. Typically, the veins have irregular geometries and extend for at least 10 cm in length, commonly clearly extending beyond the margins of the core. All have moderately coarse grain size (2–4 mm). An example of a dioritic vein with an almost planar margin can be found at 38.45 m in the foliated gabbro sequence (interval 18Z-4, 11–13 cm), and examples of diorite veins with irregular margins can be found at 71.47 and 76.53 m and in the transition zone (intervals 29Z-3, 4–7 cm, and 21Z-2, 0–17 cm).

Discussion of magmatic structures

Hole GT2A plunges with a dip of 60° to the northeast, and so the dips of the foliation and layering measured in the core (Fig. F44) are apparent dips. The dip of the foliation and layering varies from 0° to ~50° (mean = 30°) in the CRF. Given that the dip of the magmatic layering mapped at the surface is 46°–69° to the southwest, this means the mean dip of the layering is likely ~60° to the southwest in the geographic reference frame and thus dipping at an angle of ~30° relative to the regional dip of the paleo-Moho (~26°). Table T5 gives the average dip in the CRF for the foliated gabbro sequence, transition zone, and layered gabbro sequence and the corresponding dips in the geographic reference frame and relative to the paleo-Moho. Broadly, the dip of layering and foliation becomes gentler with depth relative to the paleo-Moho.

In further detail, the variation of the layering and foliation dip with depth exhibits two distinctive features:

1. Rare, localized, and isolated excursions dip as much as 90° (Fig. F44). These excursions are caused by rotation of the layering/foliation due to drag on late brittle faults. Figure F45 shows two examples of local rotation of olivine foliation to steeply dipping (>50°) by brittle faulting (Fig. F45A–F45B) and an example of the olivine foliation exhibiting a kink band due to local shearing (Fig. F45C). Figure F46 highlights excursions to steep dips. However, it is important to recognize that these excursions and other low-temperature faulting and fracturing in the core do not appreciably affect the overall variation in magmatic fabric dip.
2. The overall variation of magmatic layering/foliation dip with depth appears to vary systematically, exhibiting cycles of gradually increasing and decreasing dip over length scales of ~50–75 m (marked in red in Fig. F46). The origin of this cyclic "fanning" of the layering/foliation is unclear, although it appears to be a primary magmatic feature and not a later tectonic feature. One possibility is that it reflects the process of large-scale boudinage as the hot crystal mush flows away from the ridge axis during plate spreading.

Crystal-plastic vs. brittle-plastic deformation

In Hole GT2A, no significant or continuous subsolidus crystal-plastic fabrics were observed at the core scale except for a number of brittle-plastic or semibrittle structures where crystal-plastic deformation is incipient. Crystal-plastic fabrics, where present, are mostly developed in secondary alteration minerals and principally associated with cataclastic zones, sheared veins, or veinlets. During core description, these structures were logged in the brittle deformation worksheet in the column Brittle-plastic fabric or as low-T protomylonite in the fault rocks type (i.e., subgreenschist to low-greenschist facies).

At the core scale, incipient brittle-plastic fabrics are represented by narrow light brown to beige anastomosing layers (2–30 mm wide) or by intervals with protomylonitic textures associated with brittle fabrics (see Fig. **F47**). In thin sections, the light brown layers comprise ultrafine grain-sized anastomosing seams that surround broken submillimetric fragments of the host gabbro or even fragments of plagioclase or epidote. These fabrics display features transitional between foliated cataclasite and low-grade protomylonite. Foliations are defined by microshears, S-C microstructures, and rotation of the incipient foliation.

The primary igneous minerals display undulose extinction, tapered twins, and subgrain development in plagioclase and bent grains and undulose extinction in olivine and less commonly in pyroxene. More commonly, subsolidus crystal-plastic deformation affects secondary minerals such as chlorite, prehnite, amphibole, quartz, serpentine, anhydrite, and zeolites. At the core scale, anhydrite layers and veins are sheared or even syntectonically folded (e.g., Sections 64Z-2 and 103Z-3). In few places, magmatic foliations are rotated in proximity to shear veins and fault zones (e.g., Sections 10Z-3 and 123Z-2).

Brittle structures

Brittle structures are well developed throughout Hole GT2A, and they are present in all sections (see Figs. **F48**, **F49**; Vein log in **Supplementary material** > **E_Tabulated VCD data**). Nearly 1000 shear fractures (including brittle-ductile structures with incipient crystal-plastic deformation) associated with cataclasis or syntectonic mineral fillings or breccia veins were logged. The main features are represented by fault and cataclastic zones, shear veins, and hydrothermal breccia veins. Some whole sections are entirely composed of fault rocks (e.g., Core 25Z; Sections 26Z-3 and 72Z-3).

The deformation intensity of brittle fabric was systematically evaluated and ranked (Fig. **F48B**; see the Brittle deformation sheet in **Supplementary material** > **E_Tabulated VCD data**) downhole; a rank of "minor fracturing" was attributed to most of the shear veins, as they are commonly associated with incipient brecciation of the wall rock and some contain fragments of the wall rock.

During structural core description of Hole GT2A, a semiquantitative scale of the general fracturing intensity in each section (i.e., intensity per ~1 m of core) was developed (see Fig. **F48A**; see the Brittle deformation sheet in **Supplementary material** > **E_Tabulated VCD data**). This scale is based on visual intensity estimates reflecting the spacing, frequency, and volumetric occurrence of brittle structures per section (from slight to complete; see **Structural geology** in the **Methods** chapter). In addition, information was reported about distribution of deformation within the section (e.g., heterogeneous, localized, or widespread/uniformly developed). Figure **F48A** reveals that the fracturing is well developed throughout Hole GT2A with ~58% of the sections characterized by high to complete fracturing. Within these sections, 54% fracturing is localized, 40% heterogeneously distributed, and 31% evenly distributed throughout the section.

In the Hole GT2A cores, at least 254 cataclastic zones and 190 fault zones are present, including hydraulic or hydrothermal breccia veins (e.g., Sections 11Z-3, 17Z-4, 31Z-4, 38Z-3, 57Z-1, 62Z-2, 63Z-2, 73Z-4, 92Z-3, 123Z-3, and 137Z-2; Fig. **F49**). Incipient fracturing associated with shear veins or localized in semibrittle shear fractures is also widely distributed. However, many features are healed microstructures and the host rocks maintain their cohesiveness. Shear veins are commonly accompanied by incipient brecciation or, less commonly, by protomylonitic fabrics defined by alteration minerals (see **Supplementary material** > **E_Tabulated VCD data**). Shear zones are rare, and most are brittle-ductile shear zones.

Fault zones and cataclastic zones occur throughout Hole GT2A, although there are specific intervals of more intense faulting. Figure **F49** illustrates the downhole distribution of fault zones, vertical thicknesses of fault cataclastic zones (thicknesses are not corrected for the features that continue across two sections), and brittle fabric intensity. The combination of the three plots reveals intervals where brittle deformation is concentrated in the most intensively fractured zones and the locations of the major main fault zones. In Hole GT2A, single discrete cataclastic zones and fault zones exhibit variable thicknesses from millimeter to decimeter scale (Fig. **F49**). Fault zones show common multilayered structures (Figs. **F50**, **F51**), heterogeneous grain sizes (mostly submillimeter to centimeter scale), variable degrees of alteration, and different vein densities (see **Alteration**).

Cataclastic zones have textures ranging from narrow millimeter-spaced networks of fractures, centimeter-wide intensely comminuted zones, to variably brecciated rocks at the decimeter scale. The common secondary minerals present in the fault zones are epidote, prehnite, laumontite, chlorite, anhydrite, clay minerals, quartz, amphibole, and serpentine (see also **Alteration**).

Fault rocks show a wide range of grain size and compositions with different degrees of cohesiveness and alteration (see **Alteration**). Cohesiveness of the fault rocks is variable. In general, the fault rocks are less cohesive and even incohesive where gypsum and laumontite are present in the cement or matrix (e.g., interval 15Z-4, 55–90 cm).

Foliated cataclasite and ultracataclasite occur associated with wider multilayered fault zones, quartz, or epidote veins or localized in less fractured host rocks (e.g., Sections 62Z-2, 65Z-2, 67Z-2, 72Z-4, 96Z-2, and 123Z-3). These cataclastic features are commonly gray to green, light green, or creamy in color and of very fine grain size (micrometer scale). At the microscopic scale, transgranural fracturing and intense comminution of the host rock, cataclastic and granular flow, and multiple superposed sharp slip surfaces are present (Fig. **F51**).

Fault breccias with submillimeter to decimeter clast sizes occur in Sections 15Z-4, 25Z-2, 26Z-3, 26Z-4, 64Z-4, 72Z-3, and 92Z-3. Examples of coarse-grained fault breccia include Section 25Z-1, where subrounded clasts are enclosed in a fine-grained matrix with abundant sulfide minerals. In Sections 113Z-1 and 114Z-1, centimeter-sized clasts composed of anhydrite fragments and epidote veins occur (Fig. **F52**).

Intervals of hydrothermal breccia are associated with intense alteration, grain-size reduction, and corrosive wearing of the wall rocks, as well as epidotization and silicification that results in induration and increases in the cohesiveness of the wall rock (e.g., Sections 91Z-3 148Z-1, 148Z-2, and 148Z-3; see Fig. **F53**).

There is a noteworthy coincidence at a number of depths (see supplemental Table **ST1** and the Brittle deformation sheet in **Supplementary material** > **E_Tabulated VCD data**) of centimeter- to decimeter-wide intervals characterized by abundant chlorite, serpentine, secondary amphibole, and sulfide minerals, probably derived from hydrothermal alteration and mineralization of dunitic or troctolitic protoliths. These ultramafic layers commonly display moderate to intense deformation and dark green millimeter-scale shear veins decorated by amphiboles and sulfides. When veining is pervasive, these zones display semicohesive scaly serpentinite fabrics (see Fig. **F54**).

The average dip of the fault zones relative to the CRF is ~45° (range = 30°–60°). Sense of shear observed for 171 faults and cataclastic zones are both normal (58%) and reverse (42%) (Fig. **F55**). Shear fractures with evidence of multiple reactivation phases and superposed senses of shear (mostly reverse over normal sense of movement) are present (e.g., Figs. **F56**, **F57**) as reflected by superposed kinematic indicators and different generations of lineation on slickensides.

General overview of brittle structures

In Hole GT2A brittle deformation is more widespread and evenly distributed downhole compared to Hole GT1A. Incipient fracturing is ubiquitous throughout the hole. Cumulative calculations of damaged intervals reveals that at least 250 m of the recovered rocks are moderately to completely fractured. Fault zones are common and well developed throughout the hole (Fig. **F49**), but nevertheless ~20 main fault zones can be localized. These fault zones display composite multilayered architectures with different types of associated fault rocks. The senses of movement determined for these features are both normal and reverse, although normal movements are more common and mostly predate reverse displacements. Brittle structures show common clues of tectonic reactivation, such as superposed kinematic indications and different generations of slickenlines.

Veins

The orientations and styles of 1655 veins were measured in Hole GT2A. They range in composition from amphibole to epidote to clay and zeolites (see the Alteration sheet in **Supplementary material** > **E_Tabulated VCD data**). Although fewer veins were measured in Hole GT2A compared to Hole GT1A, this does not mean that veins are less abundant but instead reflects changes in the ways that veins were logged in each hole (see **Alteration** in the **Methods** chapter). The majority of fractures are filled with vein material; only ~20 open fractures were identified. All these open fractures occur in the upper 100 m of the hole. Filled fractures only are described below. Note, all angular measurements are with respect to the CRF.

Vein dip distribution

The range in vein dip for all vein types is large, from near-horizontal to near-vertical (Fig. **F58**). The distribution of dips is skewed towards higher dips, with peaks near 50°–60° (Fig. **F33B**) (average = 49°; standard deviation = 19.2°). There appears to be 2 broad trends that divide the hole into 2 domains, with steeper dips trending towards gentler dips at 0–200 and 200–400 m. Veins with subhorizontal dips formed in clusters, for example, near 75–100, 150, 175, 200, 250, and 300 m.

If veins are divided by mineral fill, some patterns emerge (Fig. **F59**). A vein is considered of a particular fill type if it has 50% or more of that mineral. Amphibole veins tend to have steeper dips (average = 74°), although only 10 of the 16 identified were measured. Laumontite veins also have higher dips (average = 50°), and very few veins dip <30°. All other compositions considered, including chlorite, epidote, prehnite, and quartz, seem to have a maximum dip near 45° and taper to both lower and higher dips consistent with a random distribution (see **Structural geology** in the **Methods** chapter).

Slickenfibers

A total of 43 slickenfibers were identified throughout the core (Fig. **F60**). Because of the change in logging practices between the description of Holes GT1A and GT2A, some Hole GT2A slickenfibers were logged in the Brittle worksheet instead of the Vein worksheet. The majority of slickenfibers logged in the Brittle worksheet occur at 300–320 m in black chlorite- and amphibole-rich veins, some in dense networks. The majority of slickenfibers throughout the hole form along veins filled with chlorite and prehnite and to a lesser extent quartz. The plunge of slickenfibers varies from gentle to steep, but most are <30°. When the dip and plunge angles are compared, the majority of slickenfibers indicate oblique- to strike-slip motion; fewer indicate dip-slip motion (Fig. **F60B–F60C**).

Senses of shear

A total of 50 shear sense indicators were identified (Fig. **F61**). Shear sense indicators are typically steps in slickensides and pull-apart veins. Both normal and reverse sense of shear indicators were identified throughout the drilled interval and for the most part overlap in depth. Two intervals at ~225–275 m and below 375 m contain normal shear sense indicators but no reverse shear sense indicators. The intervals where normal and reverse shear sense indicators were identified overlap, but structures with both normal and reverse shear senses are very rare. For the most part, the shear sense indicators formed as discrete structures and did not directly overlap. In one case a clinozoisite vein has both normal and reverse offsets (Fig. **F62D**).

There are some compositional differences between normal and reverse shear sense indicators. The majority of normal shear sense indicators include veins filled with chlorite, prehnite, quartz, epidote, and clinozoisite. The majority of reverse shear sense indicators include veins filled with chlorite, prehnite, quartz, and laumontite. Therefore, epidote and clinozoisite veins almost exclusively form normal shear sense indicators, whereas laumontite veins almost exclusively form reverse shear sense indicators. Chlorite, prehnite, and quartz veins defined both types of shear sense.

Crosscutting relationships

Veins that crosscut and offset other veins may be separated by composition. The majority of first-generation veins are filled with amphibole, epidote, clinozoisite, quartz, prehnite, and chlorite. The majority of second-generation veins include chlorite, prehnite, quartz, and laumontite. Veins filled with amphibole, epidote, and clinozoisite are almost always first generation, and laumontite is almost always a later generation vein. Veins filled with chlorite, prehnite, and quartz are both first and second generation. There are examples of epidote veins crosscut by laumontite veins, quartz veins crosscut by laumontite veins, and quartz crosscutting epidote veins (Fig. **F62**).

Conclusions

Hole GT2A plunges with a dip of 60° to the northeast, and so the dips of the foliation and layering measured in the core (Fig. **F44**) are apparent dips. The dip of the foliation and layering varies from 0° to ~50° (mean = 30°) in the CRF. Given that the dip of the magmatic layering mapped at the surface is 46°–69° to the southwest, this means the mean dip of the layering is likely ~60° to the southwest in the geographic reference frame and thus dipping at an angle of ~30° relative to the regional dip of the paleo-Moho (~26°; see Table **T5**).

About 90% of the core exhibits magmatic foliation. Most of the core, including the foliated gabbro sequence, shows magmatic layering with layer thickness ranging from 3 cm to 3 m and layers dominantly ranging 4–50 cm thick. Overall, the dip of the magmatic fabrics shallow with depth in the core and likely shallow with depth from 40° to 20° relative to the paleo-Moho. The magmatic fabrics also exhibit a 20° cyclic variation of steepening and then shallowing dip, which might reflect boudinage during flow of the hot magma chamber as a consequence of plate separation.

Broadly, the dip of the layering and foliation becomes gentler with depth relative to the paleo-Moho.

In Hole GT2A brittle deformation is more widespread and evenly distributed downhole compared to Hole GT1A. Incipient fracturing is ubiquitous throughout the hole. Cumulative calculations of damaged intervals reveals that at least 250 m of the recovered rocks are moderately to completely fractured. Fault zones are common and well developed throughout the hole (Fig. **F49**), but nevertheless ~20 main fault zones can be localized. These fault zones display composite multilayered architectures with different types of associated fault rocks. The senses of movement determined for these features are both normal and reverse, although normal movements are more common and mostly predate reverse displacements. Brittle structures show common clues of tectonic reactivation, such as superposed kinematic indications and different generations of slickenlines. The Zihlmann-Mueller fault (Zihlmann et al., 2018) identified at the surface with an orientation of 52/251 is most likely the fault encountered at ~190 m.

Brittle structures are well developed throughout Hole GT2A, and they are present in all sections. Nearly 1000 shear fractures (including brittle-ductile structures with incipient crystal-plastic deformation) associated with cataclasis or syntectonic mineral fillings or breccia veins, were logged. The main features are represented by fault and cataclastic zones, shear veins, and hydrothermal breccia veins. Some whole sections are entirely composed of fault rocks (e.g., Core 25Z; Sections 26Z-3 and 72Z-3).

Amphibole veins tend to have steeper dips (average ~ 74°). Laumontite veins also have steep dips (average = 50°), and very few veins dip lower than 30°. All other compositions considered, including chlorite, epidote, prehnite, and quartz, display a most common dip near 45° and taper to both lower and higher dips, consistent with random distributions.

The majority of normal shear sense indicators include veins filled with chlorite, prehnite, quartz, epidote, and clinozoisite. Epidote and clinozoisite veins almost exclusively form normal shear sense indicators, whereas laumontite veins almost exclusively form reverse shear sense indicators. Chlorite, prehnite, and quartz veins defined both types of shear sense.

The majority of first-generation veins are filled with amphibole, epidote, clinozoisite, quartz, prehnite, or chlorite. The majority of second-generation veins include chlorite, prehnite, quartz, and laumontite. Veins filled with amphibole, epidote, and clinozoisite are almost always first generation, and laumontite is almost always a later generation vein. Veins filled with chlorite, prehnite, and quartz are both first and second generation. There are examples of epidote veins being crosscut by laumontite veins and quartz veins being crosscut by laumontite veins and quartz crosscutting epidote veins. This order of vein filling is in agreement with observations made by the alteration team.

Geochemistry

This section summarizes the results of geochemical analyses carried out on Hole GT2A cores on board the *Chikyu* and on samples collected on site and analyzed at the University of St. Andrews prior to visual core description by teams during OmanChikyu Leg 1. Analyses were performed on 63 samples (43 olivine gabbros; 9 olivine-bearing gabbros; 2 troctolites; 2 gabbros; 1 anorthositic gabbro; 1 gabbronorite; and 5 altered olivine gabbros). Selection of samples was based on discussion with representatives from the OmanChiku Leg 1 core logging teams to identify representative areas of plutonic rock and areas where alteration patches and halos were large enough to sample for shipboard geochemistry. An additional 20 samples were cut on site from the core every 20 m during drilling that were analyzed by X-ray fluorescence (XRF) prior to ChikyuOman Leg 1.

X-ray fluorescence was used to quantify major elements on glass beads and trace elements on pressed powder pellets. Inductively coupled plasma–mass spectrometry (ICP-MS) following alkali fusion acid digestion of rock samples was used to characterize trace and rare earth elements (REE) (see **Geochemistry** in the **Methods** chapter). Gas chromatography was used to measure total S, C, N, and H in dried rock powder samples. Data are shown on Figures **F63–F70** and reported in Table **T6** and supplemental Table **ST3**. Major oxide data are reported as measured and volatile-free, and trace elements are reported as recalculated after normalization for loss on ignition (LOI) as a measure for volatile loss (although mass gain through oxidation ferrous iron of Fe^{3+} is likely to be variable between samples). This recalculation was done to allow direct comparison between XRF and ICP-MS trace element data because ICP-MS analysis were carried out on ignited powders.

Inorganic geochemistry

Major, trace, and rare earth elements

Here we use Mg and Ca numbers (Mg# = molar ratios of Mg/[Mg + Fe^{Total}] × 100, and Ca# = molar ratio Ca/[Ca + Na] × 100) and concentrations of trace metals such as compatible (Cr and Ni) and incompatible (Y) elements to investigate chemical differentiation. Compared to olivine gabbros and olivine-bearing gabbros analyzed from Hole GT1A, those from Hole GT2A are more differentiated, having lower Mg#, Ca#, Cr, Ni, V, and Y contents (Fig. **F63**). Olivine gabbros are the most common rock type in Hole GT2A and display the widest range of differentiation: Mg# = 54.8–81.2, Ca# = 90.9–98.3, and the widest range in Cr and Y concentrations (Cr = 19–1576 ppm; Y = 3.6–8.6 ppm) (Fig. **F63**). The second most abundant rock type in Hole GT2A was olivine-bearing gabbro, and these units display a narrower range of differentiation and are less primitive than olivine gabbros: Mg# = 49.0–76.4, Ca# = 88.6–97.5, and narrower ranges in Cr, V, Ni, and Y concentrations (Cr = 3.7–425 ppm; V = 56–238 ppm; Ni = 7.9–142 ppm; Y = 3.77–5.80 ppm). The 2 troctolites analyzed have moderate Mg# and Ca# (71.2–74.6 and 94.1–95.5), among the lowest Cr and Ni concentrations (138–362 ppm and 64–125 ppm, respectively), and are most similar to gabbros (logged as having minimal olivine) that have Mg# and Ca# (73.9–75.2 and 95.3–95.9), low Cr (88–261 ppm) and Ni (36–112 ppm), and the highest Y concentration of Hole GT2A rocks (9.17 ppm). The 1 gabbronorite and 1 anorthositic gabbro sampled have low Mg# (68.6 and 49.0) and

Ca# (90.2 and 90.6). The anorthositic gabbro has the lowest concentrations of compatible elements (Cr = 4 ppm; V = 56 ppm; Ni = 8 ppm), and the gabbronorite has similar compatible element concentrations to troctolites and gabbros (Cr = 139 ppm; V = 156 ppm; Ni = 90 ppm).

In Hole GT2A, across all rock types CaO ranges 8–19.5 wt% and Al_2O_3 spans a wider range of 11.0–31.0 wt%. Similar to the dunite and melaolivine gabbros analyzed from Hole GT1A, some olivine gabbros from GT2A plot toward high MgO and low CaO and Al_2O_3 following a vector characteristic of olivine accumulation when plotted as cross-plots (Fig. **F64**). In contrast, olivine gabbros and olivine-bearing gabbros >19 wt% Al_2O_3 follow a trend indicative of plagioclase accumulation, although this fractionation is not as extreme as that observed in Hole GT1A (Fig. **F64**). Similarly, plagioclase accumulation trends can be discerned for samples with <10 wt% MgO at FeO* < 7.1 wt% and TiO_2 < 0.34 wt%. For samples where there is no evidence for olivine or plagioclase accumulation, the range of CaO and Al_2O_3 contents of olivine gabbro in Hole GT1A is 15–19 wt% and 14–18 wt% for CaO and Al_2O_3, respectively, at MgO contents of 7–10 wt%. Compared with samples from Hole GT1A, there is less evidence for accumulation of plagioclase and olivine in Hole GT2A; the bulk major element chemistry is generally similar in samples from both holes (Fig. **F64**).

Trace elements and REEs are normalized to primitive mantle (Hoffmann, 1988) to assess the systematic behavior of these elements during melting of mantle and further differentiation. Here we show that the concentration of REEs is higher in samples from Hole GT2A than in those from GT1A but not as high as concentrations in Omani lavas (Fig. **F65**). This would be expected if rocks from Hole GT2A are the more differentiated relatives of those analyzed from Hole GT1A. Fractionation of trace elements and REEs between samples from Hole GT1A and Hole GT2A are similar; both suites of rocks are enriched in large-ion lithophile elements (LILEs; Rb, K) and have positive Eu and Sr anomalies indicating plagioclase accumulation, consistent with major element data. Samples from both holes are light REE (LREE) depleted normalized to primitive mantle (unlike Omani lavas that have a flat REE profile; Einaudi et al., 2003; Godard, et al., 2003), negative Nb anomalies, and a negative Zr anomaly, which is also observed in the lavas and may indicate a common magma source (Fig. **F65**). Samples from Hole GT2A generally have lower Eu anomalies than those from Hole GT1A, indicating that less plagioclase accumulation has occurred (Fig. **F66**).

The igneous rocks in Hole GT2A are divided into five igneous units (see **Igneous petrology**). Differences downhole are at a finer scale than the defined igneous units because of sampling ranges of different rock types from each unit; however, the geochemical variability is generally within the same broad ranges in each unit (Fig. **F67**).

In Unit I the upper 9 samples are olivine gabbro, and gabbro was sampled just above the boundary with Unit II. These olivine gabbros show limited variation in concentrations of Al_2O_3 and TiO_2 and have consistent Mg# and Ca#.

Unit II has more variability in rock types sampled: 8 olivine gabbros, 5 olivine-bearing gabbros, 1 anorthositic gabbro, and 1 gabbro. These samples, except the anorthositic gabbro, have narrow ranges of increasing Mg# downhole, variable Ca# and Al_2O_3 concentrations, and lower TiO_2, Cr, and V concentrations than Unit I.

Unit III is composed of olivine-bearing and olivine gabbros and has slightly higher Mg# than Unit II, and Mg# continues to increase through this unit. This unit has the highest Ca#, lowest TiO_2 concentrations, and highest Cr concentrations, coinciding with the highest modal abundances of clinopyroxene in the upper half of the unit and highest modal abundances of olivine in the lower half of the unit observed in thin section.

From Unit IV, the thinnest unit defined at only 9.67 m thick, we analyzed 2 samples: a gabbronorite and an olivine-bearing gabbro. This unit has the lowest Mg# and Ca#, highest TiO_2, lowest Ni concentrations, and Al_2O_3, Cr, and Ni concentrations similar to Units I and II.

Samples from Unit V are mostly olivine gabbros with 1 olivine-bearing gabbro and 1 troctolite. This unit has variable Mg# and Ca# with peaks at 307.8 m of 79.3 and 97.7, respectively, and at 361.3 m of 74.6 and 94.4, respectively. Between these peaks, Mg# and Ca# drop to 61 and <93 and gradually increase (Fig. **F67**). This unit has the highest TiO_2 concentrations, and Al_2O_3 concentrations decrease with depth. Cr, Ni, and V concentrations are variable, with baseline levels slightly more elevated than in Unit II.

General downhole trends that can be extrapolated across lithologic units are increasing Mg# and Ca# between Unit I and Unit III and decreasing TiO_2 between Unit I and Unit III (Fig. **F67**). The most geochemically consistent unit is Unit II, with the narrowest ranges of Mg#, TiO_2, Cr, and Ni, although this unit has the most variable Al_2O_3 concentrations.

Volatile content

The volatile contents of samples were measured using the CHNS elemental analyzer during ChikyuOman Phase 1 (see **Geochemistry** in the **Methods** chapter). Water content measured by CHNS analyzer is on average ~0.3 wt% higher than that measured by loss on ignition (LOI) (Fig. **F68**), indicating that mass gain during ignition due to oxidation of Fe^{3+} to Fe^{2+} occurred. There is no relationship between LOI and CO_2 contents measured by CNHS, with CO_2 contents generally <0.2 wt% in olivine gabbros. Nitrogen was below detection limits in all samples analyzed.

Water, CO_2, nitrogen, and sulfur contents

Samples recovered from Hole GT2A contain 0.5–9.3 wt% H_2O (average = 3.1 wt%; median = 2.8 wt%). Olivine gabbros and olivine-bearing gabbros sampled as "fresh" representative samples of units have higher H_2O contents in identified fault and fault damage zones, where these samples contain higher than median H_2O contents (>2.8 wt%) (Fig. F69), although it is noted that rocks from Hole GT2A are highly fractured and faulted throughout. Samples of visibly altered rocks taken to assess mass change have considerably higher H_2O contents (up to 9.3 wt%), reflecting hydrous alteration to amphibole, epidote, chlorite, and clay minerals.

CO_2 concentrations in samples from Hole GT2A range 0.05–1.2 wt% (average = 0.17 wt%; median = 0.15 wt%), similar to samples from Hole GT1A, but one sample of altered rock that has the highest CO_2 contents recorded in either hole accounts for the higher range (Fig. F69). There is no apparent relationship between CO_2 content and proximity to fault zones in Hole GT2A (Fig. F69). The altered samples analyzed show different alteration styles throughout Hole GT2A. For example; in altered Sample 17Z-4, 56–61 cm (35.75 m), both H_2O and CO_2 are elevated 3 and 8 times background, respectively, indicating both hydration and carbonation are responsible for alteration in this sample. In contrast, Sample 100Z-4, 44–50 cm (295.27 m), has H_2O double that of background and CO_2 within range of background, indicating hydration without carbonation occurred. Unit IV has the lowest H_2O and CO_2 contents in the whole of Hole GT2A, with concentrations below average background values.

The proportion of inorganic carbon (TIC) to organic carbon (TOC) in most samples ranges ~0.5–1 with no definable trend downhole (Fig. F69). This ratio deviates significantly in samples of olivine gabbro that may contain carbonate veins and in some altered olivine gabbros. Sample 12Z-4, 90.5–94.5 cm, collected on site, has a very high TIC/TOC ratio and the lowest TOC content (0.002 wt%). The CO_2 content of this sample is not considerably higher than background values, despite clear carbonate mineralization. In general, there is agreement between the highest CO_2 contents and highest TIC/TOC ratio, indicating that carbonate mineralization is prevalent throughout the drilled interval (Fig. F69).

Altered samples

Five samples of altered gabbro were taken for geochemical analyses to assess mass changes, and in most cases a representative "fresh" sample was also taken for comparison. Samples from Cores 17Z-3 and 17Z-4 are both altered, although Core 17Z-4 is most altered within a cataclastic zone. Generally, most altered samples have higher H_2O and CO_2 than the paired fresh sample, but to assess true mass change without dilution/concentration resulting from relative changes in elemental composition and total mass change, we use Gresen's equation (Grant, 1986),

$$C_i^A = M^O/M^A(C_i^O + \Delta C_i), \quad (1)$$

where

C_i^A = concentration of component i in altered rock,
M^O = mass of original unaltered sample,
M^A = mass in altered sample,
C_i^O = concentration in original, and
ΔC_i = change in concentrations between original and altered samples.

As mass of the original and altered samples is unknown, we use an immobile component such as Zr, ΣREE, TiO_2, or Al_2O_3 to assess overall changes, so M^O/M^A becomes C_x^A/C_x^O, where x is an immobile component. Using these equations and ΣREE as the immobile component for Sample 17Z-4, 56–61 cm, we show mass gains of ~48% Na_2O, >300% H_2O, >500% CO_2, and 84% K_2O. Losses are restricted to CaO (18%) and Sr (23%); TiO_2, Zr, and SiO_2 show no mass change. This is shown graphically using an isocon diagram to compare Samples 17Z-3, 15–20 cm, and 17Z-4, 56–61 cm, in Figure F70.

Core scanning XRF

Sample selection and analysis

A total of 9 cores from Hole GT2A were selected for nondestructive X-ray chemical analysis of the flat surface of the archive half in mapping mode on the XRF core scanner (Table T7). The criterion for selection was cores with as flat a surface as possible without significant secondary alteration. The depth of the selected intervals are listed in Table T7 and shown in Figure F71 along with the unit divisions of Hole GT2A. Samples selected represent 4 intervals from Unit II, 3 intervals from Unit III, 1 from the top of Unit IV, and 1 from Unit V. The conditions of measurement are described in Core scanning XRF in the **Methods** chapter (i.e., high voltage = 30 kV, beam current = 0.04 mA, counting time = 60 s, spot size = 7 mm, spacing between spots = 5 mm; see Table T45 in the **Methods** chapter). The intensity in counts measured at individual spots are tabulated in Tables T8–T16). The average compositions of the intervals are listed in Table T17 with standard deviations.

Analytical results

Downhole compositional variations of major elements, Cr, and Ni for the interval of 9 core sections and color-coded images for variations of major elements, Cr, and Ni in the core sections are shown in Figures F72–F89. In the following section, "X" indicates distance along the core from the top of the section, and "Y" indicates distance across the core.

Core GT2A-52Z-3A, 1–74 cm

Unit II olivine gabbro (138.24–138.97 m) was mapped by CS-XRF (X = 73 cm, Y = 2.0 cm) (Table T8; Fig. F72). The fabric of minerals on the cut surface is inclined at ~45° relative to the Y-axis of the core. Thus the apparent "true" thickness of the interval exposed on the cut surface of the core is ~52 cm. This distance does not take account of the real attitude of the foliation plane. Thus, possible obliqueness of the foliation plane relative to the cut surface of the core may cause some error in estimating "true" thickness of the scanned interval. This interval is characterized by relatively high average compositions of SiO_2 (52.3 wt%) and high Al_2O_3 (16.1 wt%) (Table T17). There is a distinct difference in grain size and modal assemblage between the upper middle (12–36 cm) and the other parts of the section. The upper middle part of the section is fine grained, whereas the other parts are coarse grained (2–5 mm grain size). The boundaries between these three parts occur at 12 and 36 cm from the top of the section. Because of large grain sizes in the uppermost and lowermost parts, the analytical data of individual spots are largely scattered in most elements. In the upper middle part, the concentrations of Al_2O_3 and CaO show waveform patterns. The variations in Al_2O_3 and CaO contents are positively correlated, indicating modal control of these elements by plagioclase. The Fe_2O_3 and MgO contents are negatively correlated with those of Al_2O_3 and CaO, forming a "mirrored" relationship. These results suggest that modal plagioclase is negatively correlated with the olivine mode. The amount of TiO_2 is low, indicating low modal amounts of clinopyroxene. Anorthositic veins occur at 40–48 cm associated with high Al_2O_3 content. In the uppermost (0–12 cm) and lowermost (48–68 cm) parts, the concentration of Al_2O_3 content negatively correlates with TiO_2 and CaO, suggesting that the modal amount of plagioclase is negatively correlated with the clinopyroxene mode and possibly with olivine mode in these intervals. Overall, the upper middle part is more troctolitic compared to the rest of the section, where olivine gabbro is dominant. In the bottom part (68–74 cm) the compositional data seem to be unreliable, as the SiO_2 content is too high and is not consistent with the Si intensity (Table T8).

The color-coded images clearly show the compositional variations along the core (Fig. F73) and are consistent with the observations described above.

Core GT2A-54Z-4A, 4–66 cm

Unit II olivine-bearing gabbro (145.26–145.88 m) was mapped by CS-XRF (X = 62 cm, Y = 3.0 cm) (Table T9; Fig. F74). The fabric of minerals on the cut surface is inclined at ~25° relative to the Y-axis of the core. Thus the apparent true thickness of the interval exposed on the cut surface of the core is ~56 cm. This interval is characterized by moderate average compositions of SiO_2 (51.9 wt%) and Al_2O_3 (12.1 wt%) (Table T17). There is a distinct difference in grain size between the upper and lower parts of the section. The upper part of the section is fine grained, whereas the lower part is coarse grained (2–5 mm grain size). The boundary between these two parts occurs at 26 cm from the top of the section. In the upper part (4–26 cm), the compositional variation of each element is limited to a narrow range relative to the lower part (26–66 cm), where downhole rhythmic patterns are recognized in most elements with a wavelength of ~10–15 cm (equivalent to layer thickness of 9–14 cm after dip correction). The variation patterns of SiO_2, TiO_2, Al_2O_3, and CaO contents are similar to each other, indicating modal control of these elements by plagioclase and clinopyroxene. The variation patterns of Fe_2O_3, MnO, Ni, and MgO contents are the opposite to those of Al_2O_3 and CaO, a mirror relationship. These results suggest that modal amounts of plagioclase and clinopyroxene are negatively correlated with olivine mode.

The color-coded images clearly show the compositional variations along the core (Fig. F75) and are consistent with the observations described above.

Core GT2A-69Z-3A, 2–57 cm

Unit II olivine gabbro (178.175–178.725 m) was mapped by CS-XRF (X = 55 cm, Y = 3.0 cm) (Table T10; Fig. F76). The fabric of minerals on the cut surface is parallel to the Y-axis of the core. Thus, the apparent true thickness of the interval exposed on the cut surface of the core is similar to the length of the X-axis. This interval is characterized by high average compositions of SiO_2 (53.2 wt%) and CaO (18.5 wt%) and low average compositions of Al_2O_3 (14.4 wt%), MgO (6.0 wt%), and Mg# (0.66) (Table T17). Mineral size is uniform throughout the interval. The abundance of all elements is almost constant over the interval, but at 33 cm from the top of the section there is a slight decrease in SiO_2 and CaO content and a slight increase in Fe_2O_3 and MgO. This may indicate that olivine mode locally increases whereas clinopyroxene mode decreases at this position.

The color-coded images of Fe_2O_3, Al_2O_3, and MgO show compositional heterogeneity in the core (Fig. F77), although the contents of all elements are mostly constant over the interval, as described above. The variations of these three elements reflect the slight modal variation of plagioclase relative to that of clinopyroxene through the interval.

Core GT2A-81Z-4A, 1–43 cm

Unit II olivine-bearing gabbro (215.32–215.74 m) was mapped by CS-XRF (X = 42 cm including 6.5 cm of interruption, Y = 3.0 cm) (Table T11; Fig. F78). The fabric of minerals on the cut surface is inclined at ~32° relative to the Y-axis of the core. Thus, the apparent true thickness of the interval exposed on the cut surface of the core is ~35 cm. This interval is characterized by moderate average compositions of SiO_2 (51.3 wt%) and Al_2O_3 (12.5 wt%) (Table T17). The variation patterns of SiO_2, TiO_2, Al_2O_3, and CaO contents are similar to each other, indicating modal control of these elements by plagioclase and clinopyroxene. The variation patterns of Fe_2O_3, MnO, Ni, and MgO contents are negatively correlated with those of Al_2O_3 and CaO. These results suggest that the modal amount of plagioclase and clinopyroxene is negatively correlated with the olivine mode. Overall, the contents of all elements are mostly constant over the interval except in the subinterval between 34 and 43 cm, where the decrease of SiO_2, Al_2O_3, and CaO and the increase of Fe_2O_3, MnO, Ni, and MgO are significant. This may indicate that the modal amount of olivine increases locally, whereas that of plagioclase and clinopyroxene is significantly lower.

The color-coded images clearly show the compositional variations along the core (Fig. F79) and are consistent with the observations described above.

Core GT2A-85Z-1A, 1–59 cm

Unit III olivine-bearing gabbro (225.06–225.64 m) was mapped by CS-XRF (X = 58 cm, Y = 3.0 cm) (Table T12, Fig. F80). The fabric of minerals on the cut surface is parallel to the Y-axis of the core. Thus the apparent true thickness of the interval exposed on the cut surface of the core is similar to the length of X-axis. This interval is characterized by moderate average SiO_2 content (50.0 wt%), relatively low Al_2O_3 content (11.6 wt%), and relatively high CaO content (20.5 wt%) (Table T17). The uppermost part of the interval (1–6 cm) is melanocratic gabbro that is rich in olivine relative to the rest of the interval and is continuous to the normal gabbro with a sharp contact at 6 cm from the top of the section. The core is cracked at 24 cm, but there is a difference in composition above and below the core (i.e., the upper part (6–20 cm) has higher contents of SiO_2, TiO_2, CaO, and Mg# and lower contents of Fe_2O_3, MnO, Ni, and MgO than the lower part (24–40 cm). These differences are caused by the different modal ratios of olivine and clinopyroxene. The upper part has a higher modal ratio of clinopyroxene to olivine than the lower part. The modal content of plagioclase is fairly constant given the uniform Al_2O_3 content of 6–40 cm from the top of the section (except for 20–24 cm, where a crack exists). However, as the modal content of plagioclase gradually increases at 34–40 cm, the Al_2O_3 content increases and then rapidly decreases at 40–42 cm. The relatively low Al_2O_3 content and the low modal content of plagioclase at 42 cm are associated with the high modal content of clinopyroxene, which is diagnosed by a relatively large amount of TiO_2. At 42–52 cm, the Al_2O_3 content and modal content of plagioclase gradually increase and the clinopyroxene mode decreases, as indicated by the decrease in TiO_2 content.

In the color-coded images of Figure F81, the variations of TiO_2, Al_2O_3, and MnO markedly reflect the modal variations of clinopyroxene, plagioclase, and olivine, respectively.

Core GT2A-86Z-2A, 1–52 cm

Unit III gabbro (228.71–229.22 m) was mapped by CS-XRF (X = 51 cm, Y = 3.0 cm) (Table T13; Fig. F82). The fabric of minerals on the cut surface is inclined at ~30° relative to the Y-axis of the core. Thus the apparent true thickness of the interval exposed on the cut surface of the core is ~44 cm. This interval is characterized by moderate average SiO_2 (51.1 wt%) contents and high amounts of Al_2O_3 (16.7 wt%) and CaO (20.6 wt%) (Table T17). Except for the fine-grained subinterval at 32–34 cm, the crystal size is almost uniformly medium over the whole section. The concentrations of all elements measured vary insignificantly at the top (1–24 cm), whereas at the bottom (24–52 cm) the contents of most elements show a wavy pattern. The subintervals (24–31 cm and 34–40 cm) are characterized by decreases in SiO_2, Al_2O_3, and CaO associated with significant increases in Fe_2O_3, MnO, Ni, and MgO. The variation patterns of SiO_2, Al_2O_3, and CaO contents are similar to each other, indicating modal control of these elements by plagioclase. The variation patterns of Fe_2O_3, MnO, Ni, and MgO contents are the exact opposite of the variation patterns of SiO_2, Al_2O_3, and CaO, with a mirror relationship. These results suggest that plagioclase mode is negatively correlated with olivine mode.

The color-coded images clearly show the compositional variations along the core (Fig. F83) and is consistent with the observations described above.

Core GT2A-102Z-2A, 4–71 cm

Unit III olivine gabbro (274.82–275.49 m) was mapped by CS-XRF (X = 68 cm, Y = 3.0 cm) (Table **T14**; Fig. **F84**). The fabric of minerals on the cut surface is inclined at ~20° relative to the Y-axis of the core. Thus the apparent true thickness of the interval exposed on the cut surface of the core is ~64 cm. This interval is characterized by relatively low average compositions of SiO_2 (47.9 wt%), Al_2O_3 (11.7 wt%), and CaO (13.1 wt%) and relatively high contents of Fe_2O_3 (11.1 wt%) and MgO (13.1 wt%) (Table **T17**). Mineral size is almost uniformly medium grained throughout the interval. At the top (4–16 cm), the compositional range of each element is limited to a narrower range than at the bottom (16–72 cm). At the bottom, most elements show a downhole rhythmic pattern with a wavelength of ~10 cm (corresponding to a layer width of 9 cm after dip correction). The contents of most oxides vary irregularly, reflecting significant changes in the mineral modes in this interval. The modal contents of plagioclase and clinopyroxene gradually decrease at 2–20 cm from the top of the section, whereas the olivine mode increases, as shown by decreases of SiO_2, TiO_2, Al_2O_3, and CaO and increases of Fe_2O_3, Ni, and MgO. The compositional peaks of Al_2O_3 and CaO at 24 cm from the top of the section, the peaks of TiO_2 and CaO at 27 cm, and the peaks of Fe_2O_3, NiO, and MgO at 30 cm correspond to the increase of modal content of plagioclase, clinopyroxene, and olivine, respectively. The subinterval 32–37 cm from the top of the section is anorthositic, as indicated by very high Al_2O_3 content associated with sudden decreases of Fe_2O_3, Ni, and MgO. At 37–52 cm from the top of the section, the modal content of plagioclase gradually decreases, whereas that of olivine increases, as indicated by decreases in Al_2O_3 and CaO and increases in Fe_2O_3, Ni, and MgO. There are small peaks in TiO_2 and CaO at 49 cm and 54 cm, indicating thin clinopyroxene-rich veins. The subinterval (52–61 cm from the top of the section) is characterized by high contents of Fe_2O_3, Ni, and MgO and low contents of Al_2O_3 and CaO, indicating an olivine-dominant lithology. The bottom part (61–72 cm) is dunitic to wehrlitic, as shown by increasing TiO_2 and CaO toward the bottom with high Fe_2O_3, Ni, and MgO content.

The color-coded images clearly show the compositional variations along the core (Fig. **F85**) and are consistent with the observations described above.

Core GT2A-105Z-2A, 39–54 cm

Unit III olivine gabbro (284.25–284.40 m) was mapped by CS-XRF (X = 15 cm, Y = 2.0 cm) (Table **T15**; Fig. **F86**). The fabric of minerals on the cut surface is inclined at ~25° relative to the Y-axis of the core. Thus the apparent true thickness of the interval exposed on the cut surface of the core is ~14 cm. Mineral size is uniform throughout the interval. This short interval is characterized by high average compositions of SiO_2 (55.5 wt%) and Al_2O_3 (14.5 wt%) and low average compositions of Fe_2O_3 (7.4 wt%), MgO (4.9 wt%), and CaO (15.9 wt%) (Table **T17**). Overall, the average composition of this interval is consistent with the high modal amount of plagioclase. The contents of all elements are mostly constant over the interval, and a slight increase of Al_2O_3 associated with the decrease of TiO_2 and CaO at the bottom (54 cm from the top of the section) indicates a higher ratio of plagioclase mode to clinopyroxene mode at the bottom relative to the rest of the interval. The Cr content monotonically decreases from 46 cm to the bottom.

The color-coded images clearly show the compositional variations along the core (Fig. **F87**) and are consistent with the observations described above.

Core GT2A-149Z-2A, 1–92 cm

Unit V olivine gabbro (399.8–400.7 m) was mapped by CS-XRF (X = 91 cm, Y = 3.0 cm; Table **T16**; Fig. **F88**). The fabric of minerals on the cut surface is parallel to the Y-axis of the core. Thus the apparent true thickness of the interval exposed on the cut surface of the core is similar to the length of X-axis. This interval is characterized by moderate average compositions of SiO_2 (51.9 wt%) and CaO (16.9 wt%) and low average compositions of Al_2O_3 (11.5 wt%), MgO (6.4 wt%), and Mg# (0.53) (Table **T17**). Mineral size is uniform throughout the interval. The abundances of all elements are mostly constant over the interval, and a sudden decrease in SiO_2 and Al_2O_3 is associated with an increase of TiO_2, Cr, Fe_2O_3, MnO, Ni, and MgO at 46 cm from the top of the section. This may indicate that the modal content of clinopyroxene suddenly increases, whereas the plagioclase mode decreases at this position. Another compositional anomaly is observed at 62 cm from the top of the section, with lower TiO_2 and CaO content compared to the adjacent part, coincident with higher Fe_2O_3, Ni, and MgO content. This anomaly is a result of a lower amount of clinopyroxene and higher amount of olivine. In the lowermost part of the interval, below 70 cm from the top of the section, TiO_2 content is higher and Mg# is lower relative to the upper part. This may indicate an increase in clinopyroxene mode in this interval, probably because of differentiation of crystallizing magma.

The color-coded images of TiO_2, Fe_2O_3, and MgO show compositional heterogeneity in the core (Fig. **F89**) as described above. The variations of these three elements reflect the slight modal variation of clinopyroxene and olivine relative to that of plagioclase through the interval.

Summary

The major element compositional variation of 9 core sections of Hole GT2A was measured using an X-ray fluorescence core scanner. Generally speaking, the cores of Hole GT2A do not show many regular "wavy" or rhythmic compositional patterns, as seen in the cores of Hole GT1A. Instead, thin layers with abnormal compositions and thicknesses of several centimeters to 10 cm tend to abruptly appear in the olivine gabbros of otherwise homogeneous composition. These anomalous compositions are most likely caused by concentration of specific minerals. Perhaps they are related to the penetration of undifferentiated or differentiated melts at a particular depth. Similar to the case of Hole GT1A, core composition mapping by X-ray fluorescence core scanner proved to be very powerful method for identifying the modal composition and layered structure of gabbroic sections. Microprobe analysis of mineral composition will be able to further identify the cause of the tendency of composition variations.

Paleomagnetism

Remanent magnetizations

Measurements of magnetic remanence were made exclusively on discrete 20 mm sided cube samples taken from the working half cores from Hole GT2A because of malfunction of the onboard long-core cryogenic rock magnetometer. A total of 135 discreet samples were measured: approximately 25% were thermally demagnetized, whereas all others were subjected to stepwise alternating field (AF) demagnetization to isolate the characteristic remanent magnetization (ChRM) direction. Additionally, magnetic measurements were made following physical properties measurements on 30 samples located adjacent to thermally demagnetized discrete samples. These additional samples were demagnetized by AF and susceptibility was measured. All magnetic inclinations reported for Hole GT2A are in core coordinates, which differ from the geographic inclinations because of the 60° plunge of the drill hole.

Discrete sample remanence results

Natural remanent magnetization (NRM) intensity values range between 6.56×10^{-3} and 6.92 A/m (geometric mean of all discrete samples = 0.11 A/m) (Table T18; Fig. F90). The NRM orientations vary systematically with depth, changing from shallow negative inclinations down to ~150 m to subhorizontal inclinations at ~150–250 m and to dominantly positive inclinations below 250 m, although the NRM directions in the lower 50 m exhibit significant scatter (Fig. F91). NRM inclinations in the upper part of Hole GT2A are similar to those in Hole GT1A despite the 30° difference in the vertical tilt of the holes. This can likely be accounted for by the finding that the trend of Hole GT2A is nearly perpendicular to the paleomagnetic remanence declination observed in outcrop samples from the Wadi Tayin area (Luyendyk and Day, 1982; Weiler, 2000); therefore, no significant difference in magnetic inclination angles is apparent in the Hole GT2A CRF.

Principal component analysis (PCA) of demagnetization data was used to identify three broad types of remanence components. An A component, which has a low coercivity or low unblocking temperature, was removed by 5–10 mT or 200°C demagnetization in several samples. A stable remanence or C component (ChRM) that trends to the origin at the highest field and temperature steps was identified in all samples. An additional B component with intermediate coercivity or unblocking temperature and a distinct orientation from the ChRM was also distinguished in a number of samples.

As in Hole GT1A, most samples were entirely demagnetized by 600°C with relatively minor changes in remanence occurring up to 475°C (Fig. F92A). Median destructive temperatures range 509°–564°C. Major decreases in remanence intensity generally occurred at 510°–530°C and 550°–580°C. Small decreases in remanence were also observed at ~350°C in some samples (Fig. F92B). The high-unblocking-temperature component was interpreted as the ChRM. Changes in magnetic susceptibility were observed after the later steps of thermal demagnetization, indicating that changes in the magnetic mineralogy occurred as a result of heating over the course of the experiments (Fig. F92C). However, as these changes were only significant at high temperatures (>475°C) and were not associated with abrupt changes in the remanence vector orientations, such alteration is not likely to have affected the directional paleomagnetic results.

AF demagnetization was generally effective at removing the majority of remanence (Fig. F93A); however, many samples exhibited noisy demagnetization behavior at high field steps and some samples retained a measurable remanence even after AF demagnetization at 180 mT (Fig. F93B). The median destructive field (MDF) values vary widely, ranging 4.8–75 mT (mean = 23 mT) (Table T18).

AF demagnetization was also performed on shipboard samples taken next to those used for thermal demagnetization for physical properties measurements (see **Physical properties** in the **Methods** chapter), which included heating samples overnight at 105°C. The NRM direction and intensity of the samples after heating at 105°C are very close to the adjacent thermal demagnetization samples. Thus, low-temperature laboratory heating did not significantly affect the magnetic mineralogy or remanence of the Site GT2 samples. In addition, overall similar demagnetization patterns were observed between the AF and thermal demagnetization results, indicating that the ChRM directions determined by AF and thermal demagnetization results have isolated the same remanence component.

Initial interpretation of remanence results

The distribution of inclinations in discrete samples is illustrated in Figure **F91A**, which shows the downhole inclinations of the lowest, middle, and highest unblocking temperatures and coercivities together with NRM inclinations. The orientations of the A component are highly variable with both positive and negative inclinations, and are therefore not consistent with a modern-field overprint. Rather, this component may represent a minor drilling-induced overprint that is removed shortly after the first demagnetization steps. A total of 67 discrete samples were interpreted to contain possible B components with inclinations that generally mimic the pattern of the NRM directions.

ChRM vectors in the majority of samples have low negative inclinations. A weak trend of decreasing ChRM inclinations downhole can be identified with a significant number of samples with positive inclinations occurring below 200 m. Mean inclinations were calculated using the Arason and Levi (2010) maximum likelihood method (Table **T19**). This results in a mean inclination for the highest unblocking component of –5.62° (k = 36.1, α95 = 2.03°, n = 137). These gentle inclinations are similar to the value reported from the outcrop investigations from previous studies (Weiler, 2000; Morris et al., 2016), and are similar to our results from Hole GT1A (Fig. **F94**; see **Paleomagnetism** in the **Site GT1** chapter).

Magnetic susceptibility

Bulk magnetic susceptibility

Bulk magnetic susceptibilities span a wider range in Site GT2 samples than at Site GT1. Values range between 207.1 and 128,600 × 10^{-6} SI (geometric mean = 2,477 × 10^{-6}) (Fig. **F90**; Table **T20**). The downhole profile of bulk magnetic susceptibility is similar to that of NRM intensity, indicating that as at Site GT1, the variation is controlled by the concentration of magnetic minerals rather than major differences in magnetic grain size or mineralogy. Both NRM intensity and bulk susceptibility have strongly bimodal distributions (Fig. **F90B**) that suggest a strong link to variations in mineralogy or lithology, but detailed petrographic analysis of the samples is required to identify the phases that generate such variations.

The Königsberger ratios, Q, in Hole GT2A range 0.19–7.8 for all samples except one with Q = 16.2. The geometric mean Q value is 1.8, which is notably lower than that of Site GT1. Although the majority of samples have $Q > 1$, a small but significant proportion of the samples are <1, indicating a greater contribution from induced magnetization to the total in situ magnetization of the rocks (Fig. **F90**; Table **T18**). Samples with small Q values are more prevalent in the lowermost 100 m of Hole GT2A, suggesting a shift in the grain size distribution or mineralogy of the Fe oxides in that zone.

Anisotropy of magnetic susceptibility

Anisotropy of magnetic susceptibility (AMS) determinations were performed on all discrete samples prior to stepwise demagnetization to characterize the shape-preferred orientations of magnetic minerals in the core samples. The magnetic fabric strengths indicated by the anisotropy degree, P', range from very weakly anisotropic with minimum values ~1.02 to strong fabrics that exhibit P' values as high as 1.36 (Table **T20**). The poles to magnetic foliation, K_{min}, orientations are scattered about an axis subparallel to the core axis (Fig. **F95**). Magnetic lineations represented by K_{max} exhibit a mean plunge of 22° throughout the hole but vary between plunge angles of 0°–82°. A close correlation is present between the K_{max} inclinations and the variation in dip of the magmatic foliations identified during visual core logging. The dips of both the magnetic and the macroscopic fabrics progressively steepen downhole to a depth of ~150 m, at which point the dip angles abruptly become subhorizontal (Fig. **F96**). This structural threshold coincides with a major fault zone (see Fig. **F35**), below which the fabric dips again, gradually steepening with depth. A similar but less distinct change is K_{max} orientation also occurs at ~350 m depth (Fig. **F96**).

As in Hole GT1A, ChRM directions were used to rotate the AMS fabrics for Site GT2 into a paleomagnetic reference frame. After this rotation, AMS fabrics for Site GT2 display a good clustering of principal susceptibility directions when plotted on a stereoplot relative to a reference ChRM declination of 000. This result indicates that the angle between the K_{max} principal susceptibility axis and the ChRM vector is relatively constant throughout Hole GT2A, as was found in Hole GT1A. K_{min} directions cluster roughly around two distinct axes roughly subparallel to the core axis, whereas K_{max} directions cluster around shallowly dipping directions oriented roughly normal to the reference ChRM vector direction. At ~150 m, where a distinct change in the AMS and magmatic foliation dips occur, the downdip azimuth of K_{min} changes from $+Y$ to $-Y$ downhole (in the paleomagnetic reference frame) and that of K_{max} changes from $-Y$ to $+Y$. It is not clear whether these variations with depth represent changes in the petrofabric orientations or a change in the magnetic remanence directions. Absolute reorientation of each core is required for further interpretation of this preliminary finding. The rotated K_{max} axes in the paleomagnetic reference frame have similar trends in Site GT1 and GT2 samples (Fig. F97) with slightly steeper K_{max} orientations at Site GT2. This similarity may reflect a consistent regional lineation between the two sites.

Magnetic mineralogy

The magnetic unblocking temperatures at 550°–580°C in thermal demagnetization of Site GT2 samples are consistent with fine-grained pure magnetite as the dominant remanence carrier, similar to Site GT1. Small amounts of residual remanence after AF demagnetization at 180 mT may indicate minor quantities of high-coercivity phases such as goethite or hematite. Reflected light microscopy observations were made on a few representative thin sections of Site GT2 gabbro samples. Large bright opaque particles that are interpreted as primary (titano)magnetite phases are more abundant in Site GT2 than in GT1 gabbros. These oxide grains typically exhibit relict oxyexsolution temperatures that appear to have undergone some extent of low-temperature modification or annealing (Fig. F98A). Sulfide minerals were observed in reflected light microscopy of several samples, some of which are interpreted to be pyrrhotite based on their pale yellow appearance (Fig. F98B). Some of this pyrrhotite may occur in the ferromagnetic monoclinic form (Fe_7S_8) and may carry a small proportion of the magnetic remanence. The small decreases in remanence intensity that occur at 300°–350°C in some samples are consistent with the Curie temperature of pyrrhotite at 320°C.

Altered olivines containing secondary opaque mesh textures similar to those seen in Site GT1 olivine gabbros were also observed at Site GT2 (Fig. F98C, F98D). These are typically fine-grained and arranged in elongated aggregations that likely contribute to the well-defined magnetic anisotropy measured for many of the Site GT2 samples.

Physical properties

The physical properties of gabbroic rocks from Hole GT2A were characterized through a series of measurements on whole-round sections, section halves, section-half pieces, and discrete samples (see Physical properties in the **Methods** chapter). All whole-round sections were run through the X-ray computed tomography (X-ray CT) scanner before splitting. We measured magnetic susceptibility and natural gamma ray radiation (NGR) with the Whole-Round Multisensor Core Logger (MSCL-W), point magnetic susceptibility (MSP) and reflectance spectroscopy and colorimetry (RSC) with the Split Half Multisensor Core Logger (MSCL-C), thermal conductivity on section-half pieces, and compressional wave velocity, density, and porosity on discrete samples. The rock names reported in data tables correspond to the primary lithologies assigned by the igneous petrology team (Tables T2, T3).

Whole-round and section-half measurements

A total of 540 core sections from Hole GT2A were measured. Data, except for X-ray CT measurements, are summarized in supplementary Tables ST4 and ST5 and Figure F99. Gamma ray attenuation density was not measured for Site GT2 cores.

X-ray computed tomography

The X-ray CT images were continuously logged for all whole-round core samples obtained from Hole GT2A. Figure F100 shows examples of X-ray CT images from Section 50Z-1. The CT value is a function of the density and chemical composition of the sample in a voxel. Hence, data in plutonic rocks such as gabbro result from a combination of their mineral compositions and porosity structures. For example, modal plagioclase-rich and mafic mineral-rich layering is seen in Section 50Z-1. The layering is also shown in the X-ray CT scan image and the average CT value plot (Fig. F100).

Magnetic susceptibility

Magnetic susceptibility was measured on both the MSCL-W with an 80 mm loop sensor (MS), and the MSCL-C with a contact sensor probe (MSP).

Both linear and logarithm scales of whole-round and point MS values are shown in the downhole plots (Fig. F99). MS and MSP are generally low, $<100 \times 10^{-5}$ SI (Fig. F99; supplementary Tables ST4, ST5), reflecting the absence or low amount of oxides in the recovered rocks. High MS observed in the interval 296.2–304.0 m is consistent with the abundance of oxide gabbronorite in lithologic Unit IV.

Natural gamma radiation

NGR is generally low (average < 1 counts/s) in Hole GT2A cores, except in a few sections where narrow intervals or veins display significantly higher counts (up to ~8 count/s) (Fig. F99). This is similar to other gabbroic cores from Integrated Ocean Drilling Program (IODP) expeditions (e.g., Expedition 360; MacLeod et al., 2017). Compared to Hole GT1A, there are more NGR high peaks in the Hole GT2A cores because magmatic dikes and, more importantly, zones of strong hydrothermal alteration and veins are more abundant (e.g., the bottom of Section 80Z-4; see Fig. F101.

Reflectance spectroscopy and colorimetry

Reflectance spectroscopy and colorimetry data were obtained on the archive halves of some intervals between Sections 29Z-3 and 44Z-3 (71.465–117.66 m depth) and between Sections 84Z-1 and 89Z-4 (222.02–240.325 m) (Fig. **F102**). RSC was measured together with MSP using the MSCL-C. The values of reflectance and chromaticity parameters a*, b*, and L range –4.1–0.84, –5.5–10.26, and 0–81.78, respectively. These color spectrum values suggest that Hole GT2A cores have a wider range of black and white, more greenish, and similar blue-yellow spectra. The specular component included (SCI) setting was used during measurement of Hole GT2A cores, and the data are closer to the actual color than measurements using the specular component excluded setting (SCE; see **Physical Properties** in the **Methods** chapter).

Discrete sample measurements

Density and porosity

Bulk density, grain density, and porosity were calculated from measurements on 137 cubic (2 cm × 2 cm × 2 cm) and 3 irregularly shaped samples taken from the working section halves of Hole GT2A (Table **T22**; Figs. **F103**, **F104**, **F105**). Average bulk and grain densities of cube samples are 2.90 and 2.92 g/cm^3, respectively. The porosity of cube samples is generally very low, ranging 0%–6.3% (mean = 0.9%). These values are biased toward less porous material in Hole GT2A because cube samples were taken from relatively homogeneous intervals with no cracks or veins. Seven irregular shape samples were taken from damaged serpentine-rich intervals to measure density and porosity (Table **T22**; intervals 128Z-1, 8–10 cm; 130Z-1, 9–11 cm; 135Z-4, 30–41 cm; 137Z-3, 50–52 cm; 141Z-2, 41–43 cm; and 142Z-2, 33–35 cm). Highly altered samples (e.g., 26Z-1, 42–44 cm, and 135Z-4, 39–41 cm) show higher porosity, up to 12.5%.

Bulk density of Hole GT2A gabbroic samples roughly correlates with porosity; lower densities correspond to higher porosities (Fig. **F104A**). Grain density is not correlated to olivine mode (Fig. **F104D**).

P-wave velocity

P-wave velocity was measured on 137 cube samples along the 3 principal directions *x*, *y*, and *z* in the CRF. Results are listed in Table **T22** and plotted in Figures **F103**, **F104**, and **F105**. *P*-wave velocity ranges 4.9–7.3 km/s (average = 6.6 km/s). V_P of the Hole GT2A samples is slightly lower on average but essentially similar that of Hole GT1A samples. Some samples (e.g., 26Z-1, 42–44 cm) have slower velocity (mean = 4.86 km/s) because of high background alteration intensity (75%). The more scattered values in Hole GT2A probably represent a sampling bias, as we collected more variably altered samples than from Hole GT1A cores. The apparent anisotropy is generally low and ranges 0–14% (mean = 3.5%). As detailed in **Physical properties** in the **Methods** chapter, the precision of our V_P measurements is on the order of 1.5%. Hence, the lowest measured apparent anisotropies should be treated with caution.

Results for the Hole GT2A samples are plotted in Figure **F105**, together with V_P and density measurements made during IODP Expeditions 304, 305, 345, and 360 on gabbroic (including troctolite) samples from slow-spreading oceanic crust at Atlantis Bank and Atlantis Massif and from fast-spreading crust at Hess Deep, respectively. V_P values from Hole GT2A show similar results to Hole GT1A and are also consistent with previous measurements done on gabbroic rocks at Atlantis Bank and Hess Deep; they show a relatively well defined trend of decreasing densities with decreasing velocity. V_P measurements done on board the *JOIDES Resolution* over time vary notably for Atlantis Bank (Southwest Indian Ridge), Hess Deep (East Pacific Rise), and Atlantis Massif (Mid-Atlantic Ridge). The latter seem to be characterized by significantly lower velocities.

Velocities measured at room pressure show a well-defined inverse correlation with porosity (Fig. **F104A**). There is no obvious correlation between sample V_P and background alteration or olivine mode (Fig. **F104C**). Because the propagation of acoustic waves is primarily controlled by porosity in our samples, the measured velocities and apparent anisotropies cannot be simply related to mineral modes and crystallographic-preferred orientations.

Thermal conductivity

A total of 61 measurements were taken on 59 core pieces from Hole GT2A, mostly from the working half (Table **T23**; Figs. **F106**, **F107**). Thermal conductivity ranges 1.78–2.87 W/m·K (mean = 2.39 W/m·K), and the standard deviation of the average of 6–12 measurements for each piece ranges 0.0–0.25 W/m·K. The thermal conductivities of the Hole GT2A cores are relatively lower than those of Hole GT1A rocks (mean = 2.58 W/m·K). One sample (GT2A-62Z-2, 20–40 cm) of olivine gabbro with 12 vol% olivine and 30% background alteration has the lowest thermal conductivity (1.78 W/m·K). The highest thermal conductivity (2.87 W/m·K) is also shown by an olivine gabbro (GT2A-114Z-3, 41–48 cm). There is no clear correlation between thermal conductivity and lithology or alteration in the Hole GT2A cores (Fig. **F107**). The range of measured values is wider than that of gabbroic cores from IODP Expeditions 304/305, 345, and 360 (Blackman et al., 2006; Gillis et al., 2014; MacLeod et al., 2017).

Imaging spectroscopy

All sections of Hole GT2A were imaged on the *Chikyu* for near-visual infrared (NVIR) and short-wavelength infrared (SWIR) signatures. In all, nearly 600 images were acquired, totaling 3.8 TB. There are some duplicates in this dataset because the lower 250 m of Hole GT2A was imaged while the ship was at sea and not in port. Because frequent vibrations of the ship resulted in poor image quality, some sections of the core had to be redone (see discussion of this issue in the **Methods** chapter). Many images are still affected by vibrations but for a lower percentage of the time.

Eleven images (Table **T24**) were processed to reflectance in consultation with the alteration core description team. The remainder will be analyzed at Caltech. A cursory look at these images identifies the following minerals: epidote, prehnite, chlorite, other phyllosilicates, zeolites (laumontite and thomsonite), amphibole, gypsum, and possible olivine (e.g., Clark et al., 1990, 2007). Other minerals will likely be identified with more detailed analysis of all images of Hole GT2A core sections. One example image of the upper part of Section 91Z-3 is shown in Figure **F108** along with a preliminary mineral map showing several minerals of interest. Veining and heavily altered zones are identified. Most are prehnite bearing, but epidote, chlorite, zeolites (both laumontite and thomsonite), amphibole, and a small area of gypsum are also present. There are also less altered areas with spectral signatures consistent with a calcium-rich pyroxene such as augite. Although many zones of this section are mapped as a single mineral in Figure **F108**, other minerals are also present and will be identified with additional analysis.

Downhole logging and hydrogeological testing

Downhole logging and hydrogeological testing operations and acquisition parameters for Hole GT2A are available in Table **T55** in the **Methods** chapter. Raw and processed data from all downhole logs are available in the **Supplementary material** > **L_Wireline logging** and in the ICDP Oman Drilling Project online data repository (**http://oman.icdp-online.org**).

References

Abers, G.A., and Hacker, B.R., 2016. A MATLAB toolbox and Excel workbook for calculating the densities, seismic wave speeds, and major element composition of minerals and rocks at pressure and temperature. Geochem. Geophys. Geosyst., 17:616–624. https://doi.org/10.1002/2015GC006171

Alabaster, T., Pearce, J.A., and Malpas, J., 1982. The volcanic stratigraphy and petrogenesis of the Oman ophiolite complex. Contributions to Mineralogy and Petrology, 81:168–183. https://doi.org/10.1007/BF00371294

Alt, J.C., Laverne, C., Coggon, R.M., Teagle, D.A.H., Banerjee, N.R., Morgan, S., Smith-Duque, C.E., Harris, M., Arason, P., and Levi, S., 2010. Maximum likelihood solution for inclination-only data in paleomagnetism. Geophysical Journal International, 182:753-771. https://doi.org/10.1111/j.1365-246X.2010.04671.x

Arason, P., and Levi, S., 2010. Maximum likelihood solution for inclination-only data in paleomagnetism. Geophysical Journal International, 182:753–771. https://doi.org/10.1111/j.1365-246X.2010.04671.x

Blackman, D.K., Ildefonse, B., John, B.E., Ohara, Y., Miller, D.J., MacLeod, C.J., and the Expedition 304/305 Scientists, 2006. Proc. IODP, 304/305: College Station TX (Integrated Ocean Drilling Program Management International, Inc.). https://doi.org/10.2204/?odp.proc.304305.2006

Clark, R.N., King, T.V.V., Klejwa, M., Swayze, G.A., and Vergo, N, 1990. High spectral resolution reflectance spectroscopy of minerals. J. Geophys. Res., 95:12653–12680.

Clark, R.N., Swayze, G.A., Wise, R., Livo, E., Hoefen, T., Kokaly, R., and Sutley, S.J., 2007. USGS Digital Spectral Library 06: U.S. Geological Survey, Digital Data Series 231. http://speclab.cr.usgs.gov/spectral.lib06/

Gillis, K.M., Snow, J.E., Klaus, A., and the Expedition 345 Scientists, 2014. Proc. IODP, 345: College Station, TX (Integrated Ocean Drilling Program). https://doi.org/10.2204/?odp.proc.345.2014

Einaudi, F., Godard, M., Pezard, P., Cocheme, J.-J., Brewer, T., Harvey, P., and Coulon, C., 2003. Magmatic cycles and formation of the upper oceanic crust at spreading centers: Geochemical study of a continuous extrusive section in the Oman ophiolite. Geochemistry Geophysics Geosystems, 4(6):8608. https://doi.org/10.1029/2002GC000362

Godard, M., Bosch, D., and Einaudi, F., 2006. A MORB source for low-Ti magmatism in the Semail ophiolite. Chemical Geology, 234:58–78. https://doi.org/10.1016/j.chemgeo.2006.04.005

Godard, M., Dautria, J.M., and Perrin, M., 2003. Geochemical variability of the Oman ophiolite lavas: Relationship with spatial distribution and paleomagnetic directions. Geochemistry, Geophysics, Geosystems, 4(6):8609. https://doi.org/10.1029/2002GC000452

Grant, J.A., 1986. The isocon diagram; a simple solution to Gresens' equation for metasomatic alteration. Economic Geology, 81(8):1976-1982.

Hoffmann, A.W., 1988. Chemical differentiation of the Earth: the relationship between mantle, continental crust, and oceanic crust. Earth and Planetary Science Letters, 90:297-314. https://doi.org/10.1016/0012-821X(88)90132-X

Kusano, Y., Adachi, Y., Miyashita, S. and Umino, S., 2012. Lava accretion system around mid-ocean ridges: volcanic stratigraphy in the Wadi Fizh area, northern Oman ophiolite. Geochemistry, Geophysics Geosystems, 13: Q05012. https://doi.org/10.1029/2011GC004006

Kusano, Y., Umino, S., Shinjo, R., Ikei, A., Adachi, Y., Miyashita, S., and Arai., S., 2017. Contribution of slab-derived fluid and sedimentary melt in the incipient arc magmas with development of the paleoarc in the Oman Ophiolite. Chemical Geology, 449:206–225. https://doi.org/10.1016/j.chemgeo.2016.12.012

Lippard, S.J., Shelton, A.W., and Gass, I.G., 1986. The ophiolite of northern Oman. Geological Society of London Memoir, 11.

Luyendyk, B.P., and Day, R., 1982. Paleomagnetism of the Samail ophiolite, Oman: 2. The Wadi Kadir gabbro section. Journal of Geophysical Research: Solid Earth, 87(B13):10903-10917.

MacLeod, C.J., Dick, H.J.B., Blum, P., and the Expedition 360 Scientists, 2017. Southwest Indian Ridge Lower Crust and Moho. Proceedings of the International Ocean Discovery Program, 360: College Station, TX (International Ocean Discovery Program). https://doi.org//10.14379/iodp.proc.360.2017

MacLeod, C.J., Lissenberg, C.J., and Bibby, L.E, 2013. 'Moist MORB' axial magmatism in the Oman ophiolite: evidence against a mid-ocean ridge origin. Geology, 41:459-462.

Miyashita, S., Adachi, Y., and Umino, S., 2003. Along-axis magmatic system in the northern Oman ophiolite: Implications of compositional variation of the sheeted dike complex. Geochemistry, Geophysics, Geosystems, 4. https://doi.org/10.1029/2001GC000235

Morris, A., Meyer, M., Anderson, M.W., and MacLeod, C.J., 2016. Clockwise rotation of the entire Oman ophiolite occurred in a suprasubduction zone setting. Geology, 44(12):1055-1058.

Pallister, J.S., 1984. Parent magmas of the Semail ophiolite, Oman. In Gass, I.G., et al. (Ed.), Ophiolites and Oceanic Lithosphere: Geological Society Special Publication, 13:63–70.

Pallister, J.S., and Hopson, C.A., 1981. Samail Ophiolite plutonic suite: Field relations, phase variation, cryptic variation and layering, and a model of a spreading ridge magma chamber. Journal of Geophysical Research, 86:2593–2644.

Tsuchiyama, A., 1985. Dissolution kinetics of plagioclase in the melt of the system diopside-albite-anorthite, and origin of dusty plagioclase in andesites. Contributions to Mineralogy and Petrology, 89(1):1-16.

Umino, S., Miyashita, S., Hotta, F., and Adachi, Y., 2003. Along-strike variation of the sheeted dike complex in the Oman Ophiolite: insights into subaxial ridge segment structures and the magma plumbing system. Geochemistry Geophysics Geosystems, 4(3):8618. https://doi.org/10.1029/2001GC000233

Weiler, P.D., 2000. Differential rotations in the Oman ophiolite: paleomagnetic evidence from the southern massifs. Marine Geophysical Researches, 21(3-4):195-210.

Zihlmann, B., Müller, S., Coggon, R.M., Koepke, J., Garbe-Schönberg, D, and Teagle, D.A.H., 2018. Hydrothermal fault zones in the lower oceanic crust: An example from Wadi Gideah, Samail ophiolite, Oman. Lithos, 323:103-124. doi:10.1016/j.lithos.2018.09.008

Figure F1. A. Geological map of the area surrounding Site GT2 in Wadi Gideah, showing the location of Hole GT2A and the trend of the inclined borehole (thick dashed line). **B.** Aerial photograph of the Site GT2 area.

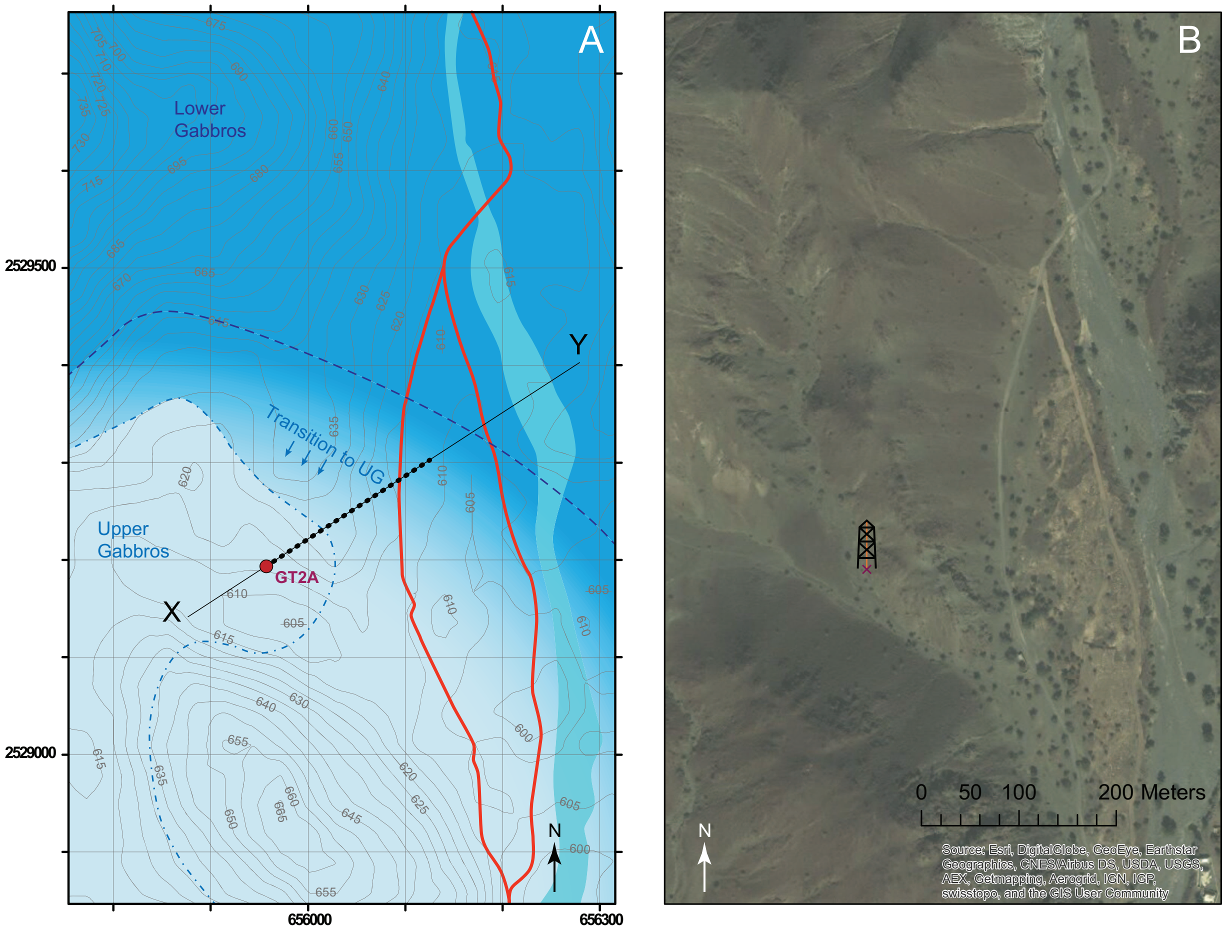

Figure F2. Cross-section along the trend of Hole GT2A. The location of the line of cross-section is shown in Figure **F1**.

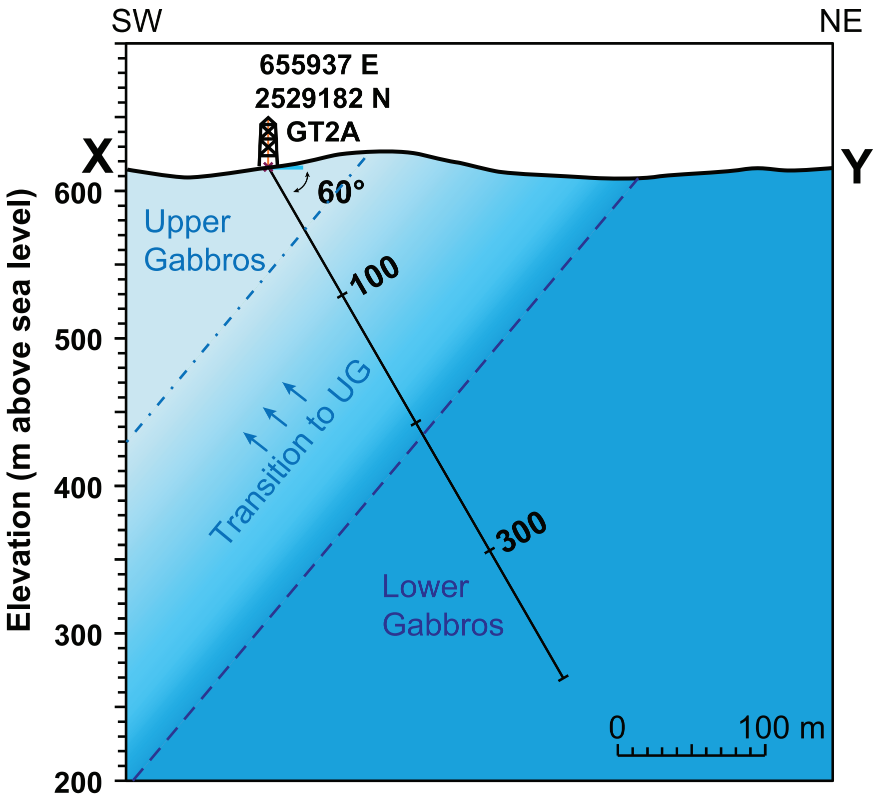

Figure F3. Lithostratigraphic variations and igneous Units I–V in Hole GT2A.

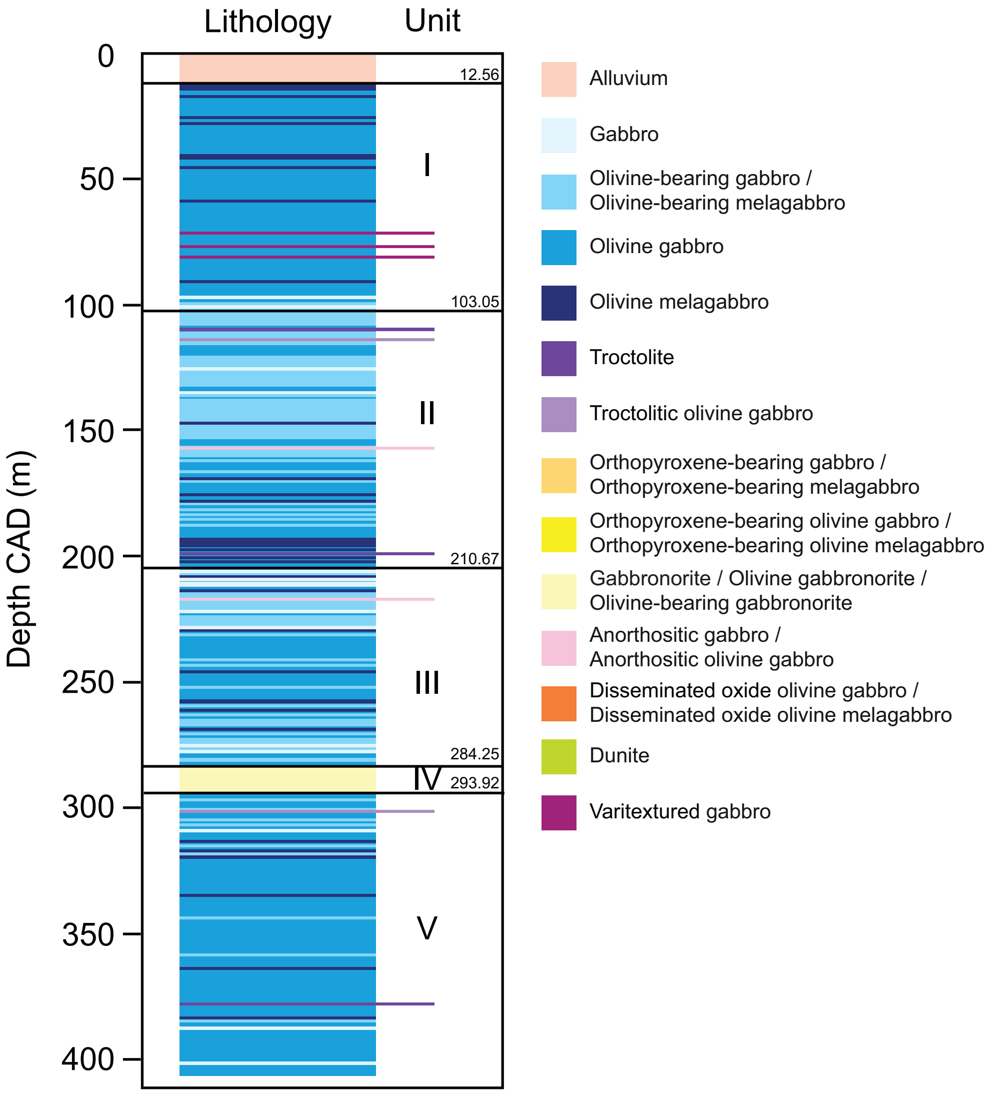

Figure F4. Pie chart of the abundance proportions different rock types in Hole GT2A.

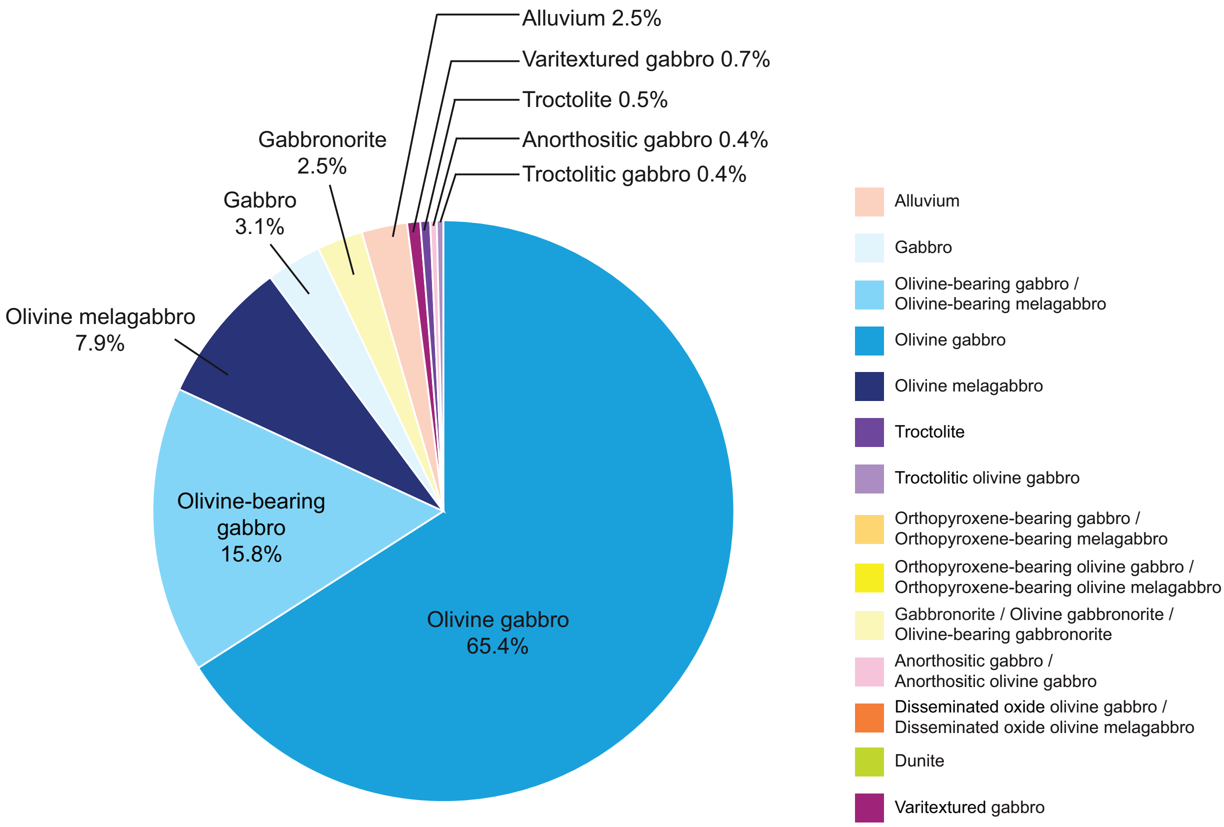

Figure F5. Mineral mode variations with depth in Hole GT2A. Solid and broken lines show the average modal compositions per 10 m interval. Open circles (blue) = olivine, crosses (gold) = plagioclase, diamonds (red) = clinopyroxene.

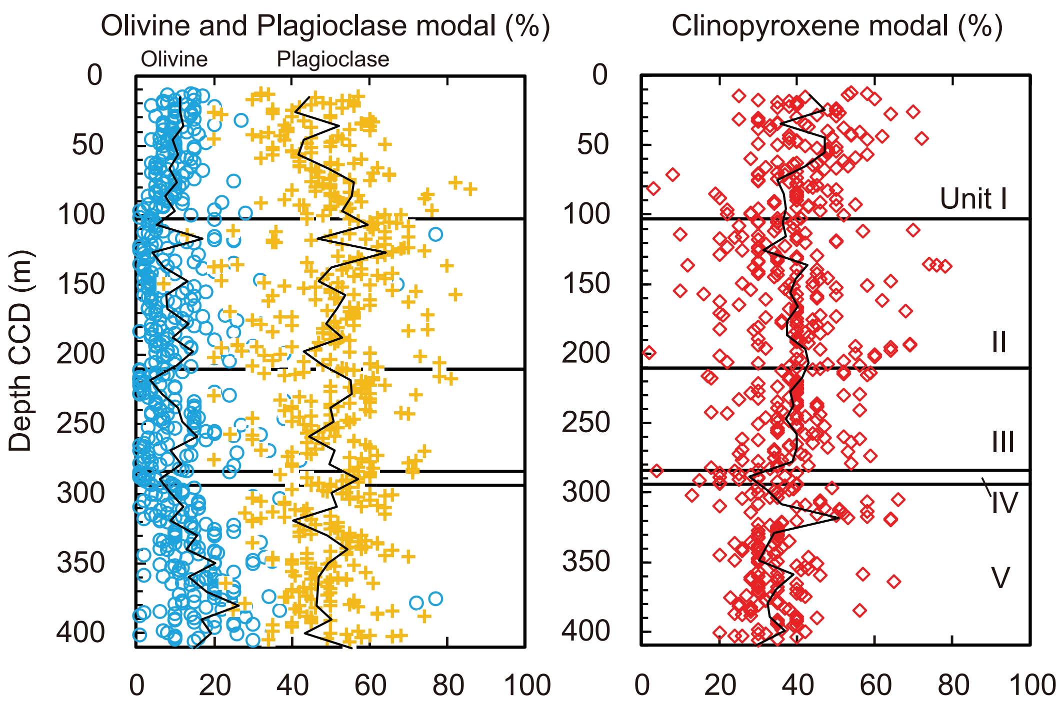

Figure F6. Grain sizes of olivine, plagioclase, and clinopyroxene with depth in Hole GT2A. (**A**, **B**, **C**) Maximum and (**D**, **E**, **F**) modal lengths are shown. Solid lines show the average modal compositions per 10 m interval. Open circles (blue) = olivine, crosses (gold) = plagioclase, diamonds (red) = clinopyroxene.

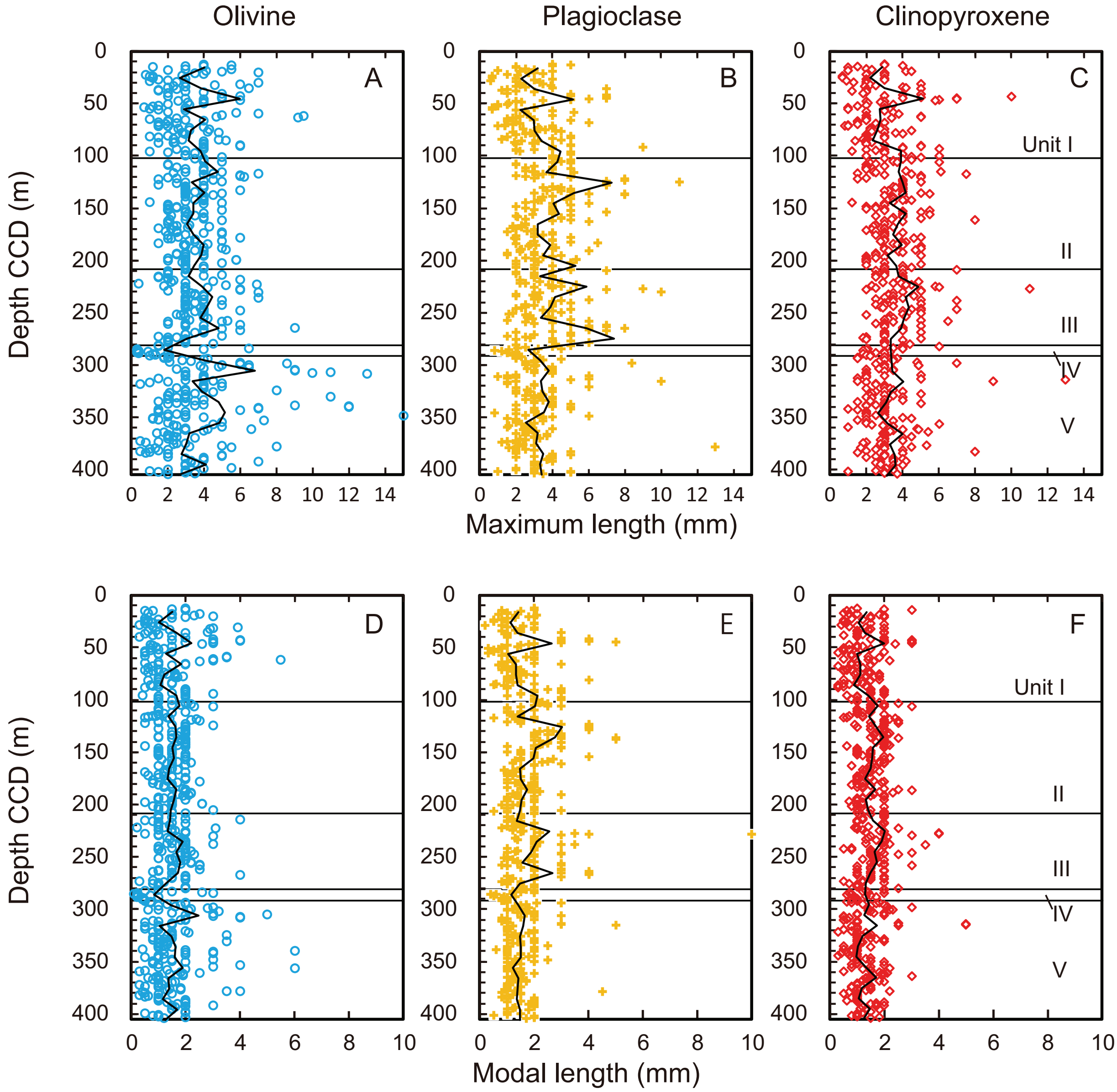

Figure F7. Representative textures of gabbroic rocks from Hole GT2A. (**A**, **C**) Elongate aggregates of olivine (Ol) grains, (**A**, **D**) clinopyroxene (Cpx) oikocrysts, and (**B**, **C**) subrounded crystals of clinopyroxene in plagioclase (Pl).

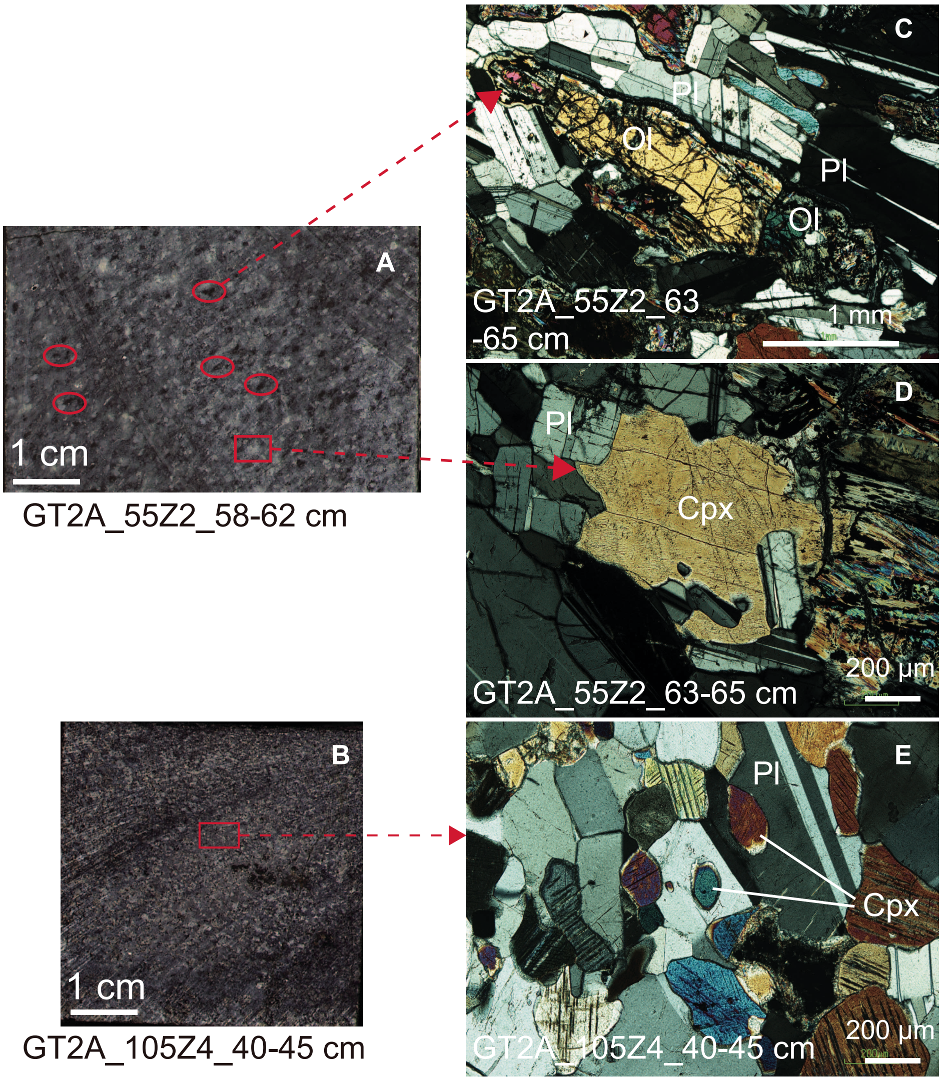

Figure F8. Three types of contacts in Hole GT2A. **A.** Sharp and planar modal contact and sharp curved grain size contact. **B.** Gradual change in both mode and grain size. **C.** Sharp planar contact between Units III and IV varies in both mode and grain size. **D.** Irregular contacts between a coarse-grained varitextured gabbro intrusive vein and the host olivine gabbro. **E.** Sheared contact.

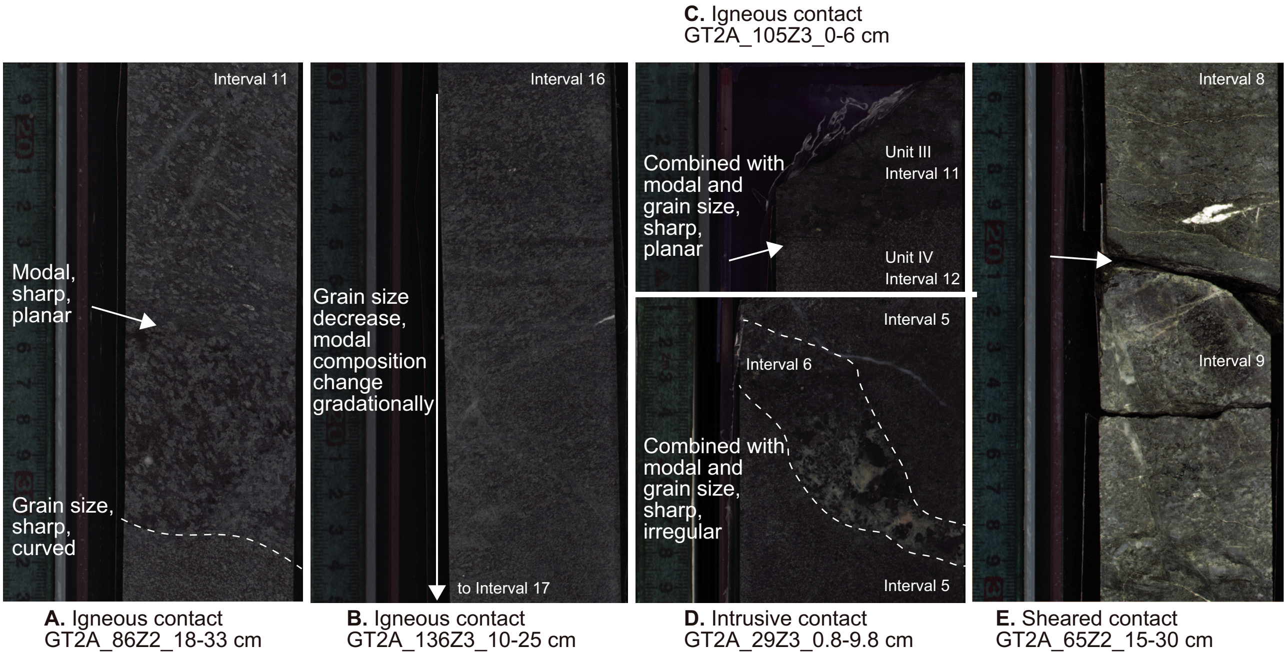

Figure F9. Downhole variations of layer thickness and layer intensity rank, Hole GT2A.

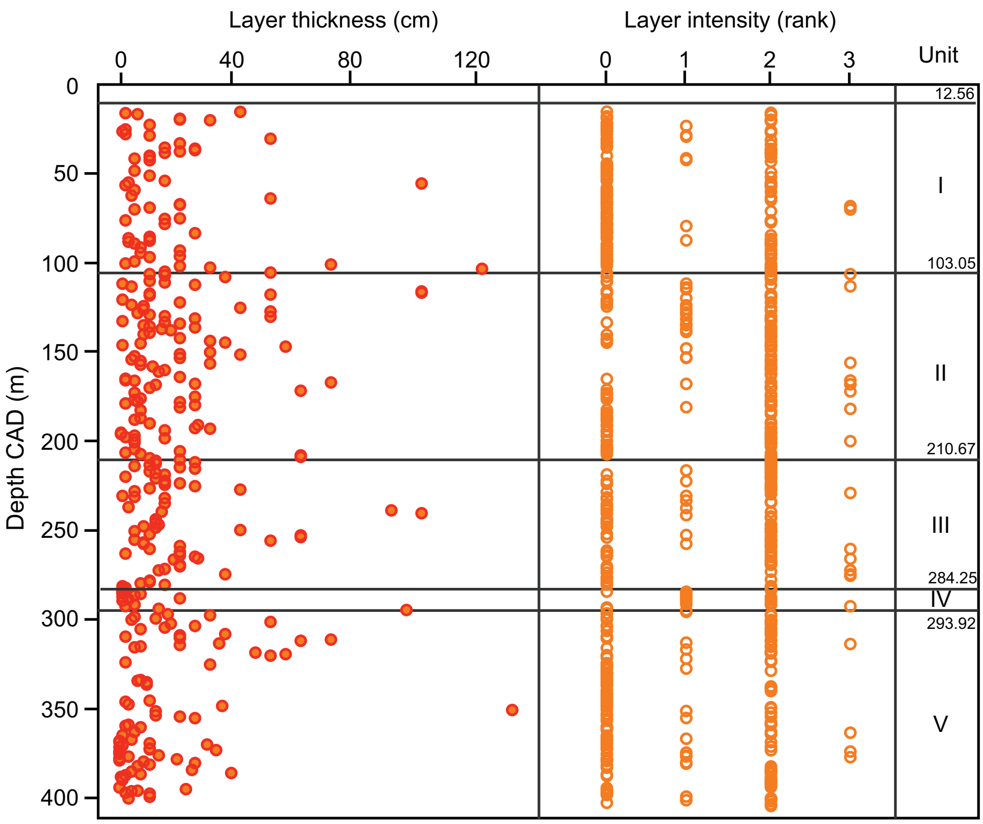

Figure F10. Histogram showing the frequency distribution of binned layer thicknesses.

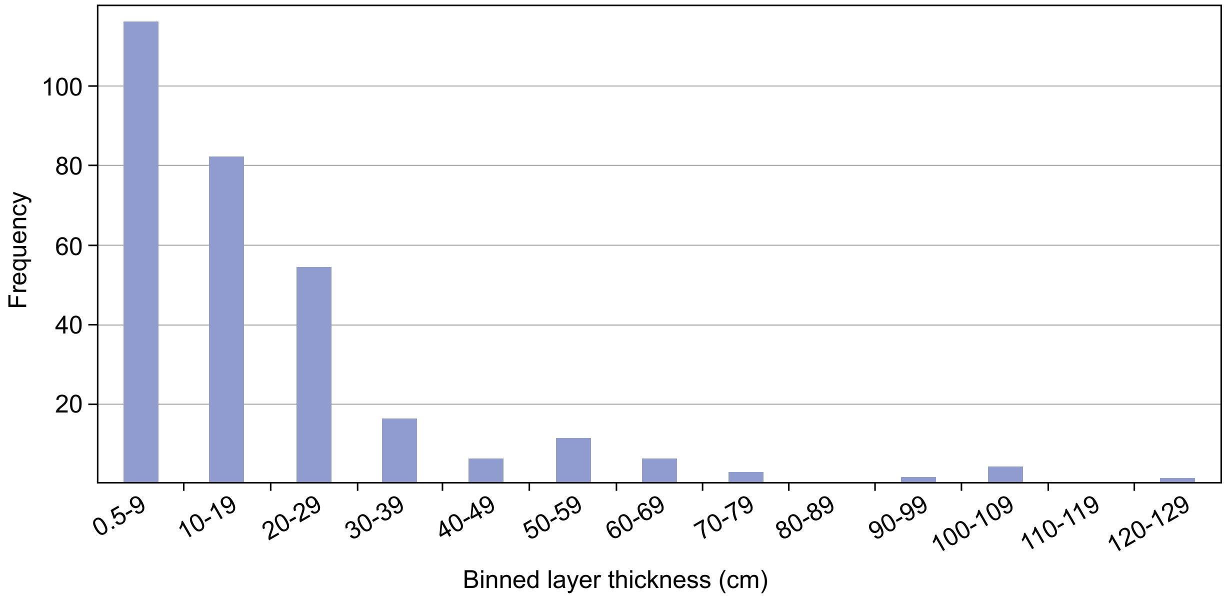

Figure F11. (**A**) Spotty gabbro; (**B**) tiger layer gabbro.

Figure F12. Stratigraphic variations of (**A**) grain size of mineral in millimeters and (**B**) modal% of olivine identified from thin section description. The blue dashed line in A shows 1 mm (the border between fine and medium grained). Ol = olivine, Pl = plagioclase, Cpx = clinopyroxene.

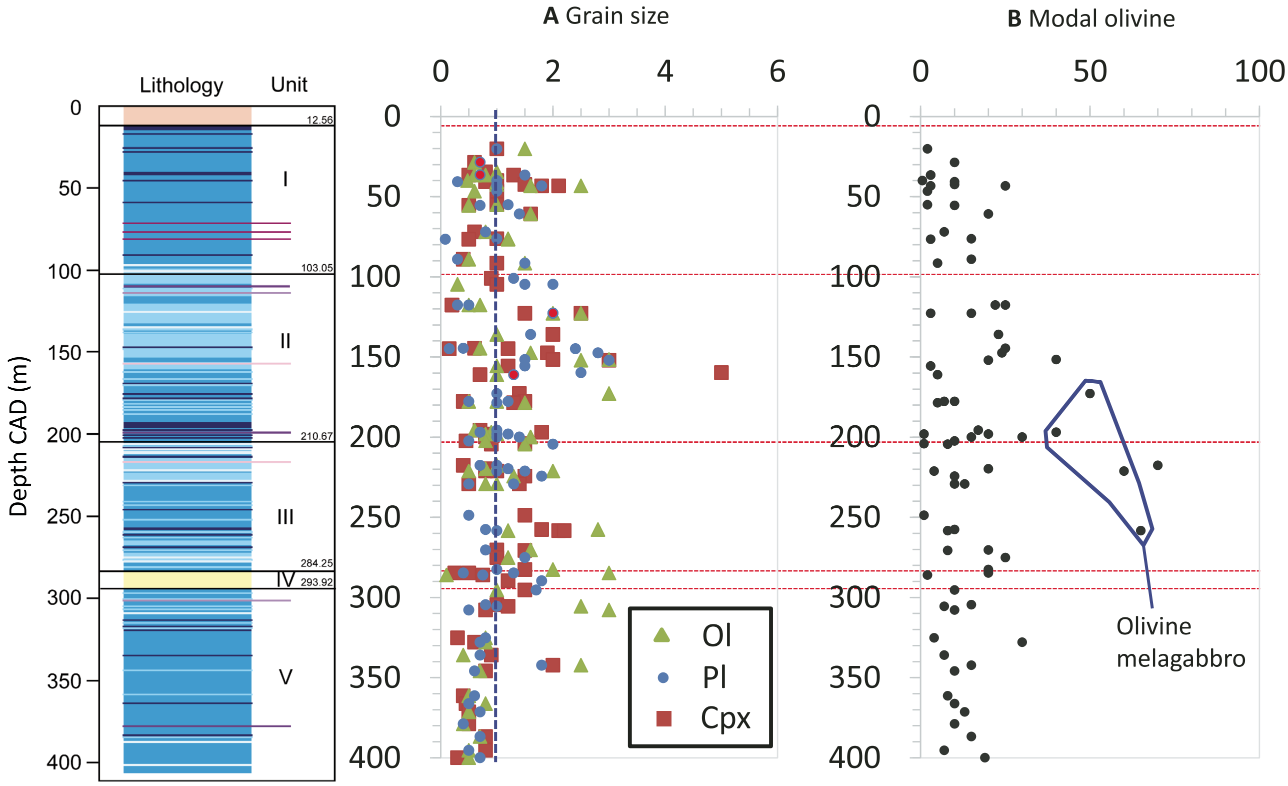

Figure F13. Olivine morphology in different styles of gabbros from Hole GT2A.

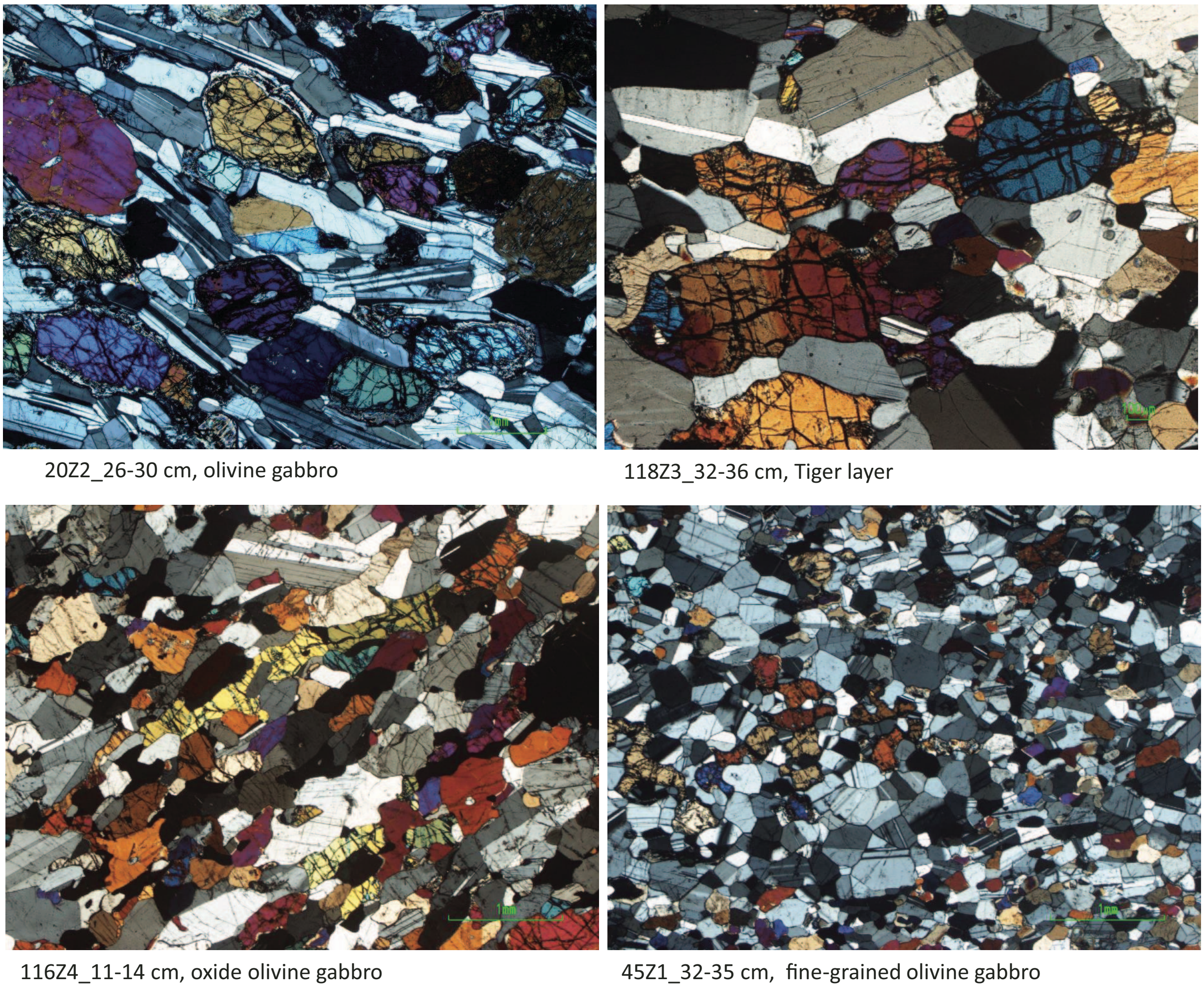

Figure F14. Quality of plagioclase zoning determined by microscopic observation. **A.** Stratigraphic variation of quality of plagioclase zoning (see **Methods** chapter for explanation of grade quality). **B.** Foliated plagioclase crystals display zoned structures in some samples (75Z-2, 12.5–16.5 cm) with olivine and clinopyroxene crystals contained outside of the plagioclase core. **C.** Large "phenocrystic" plagioclase crystals show zoned structures (54Z-3, 18–20 cm). Average grain size of surrounding smaller plagioclase is ~0.4 mm.

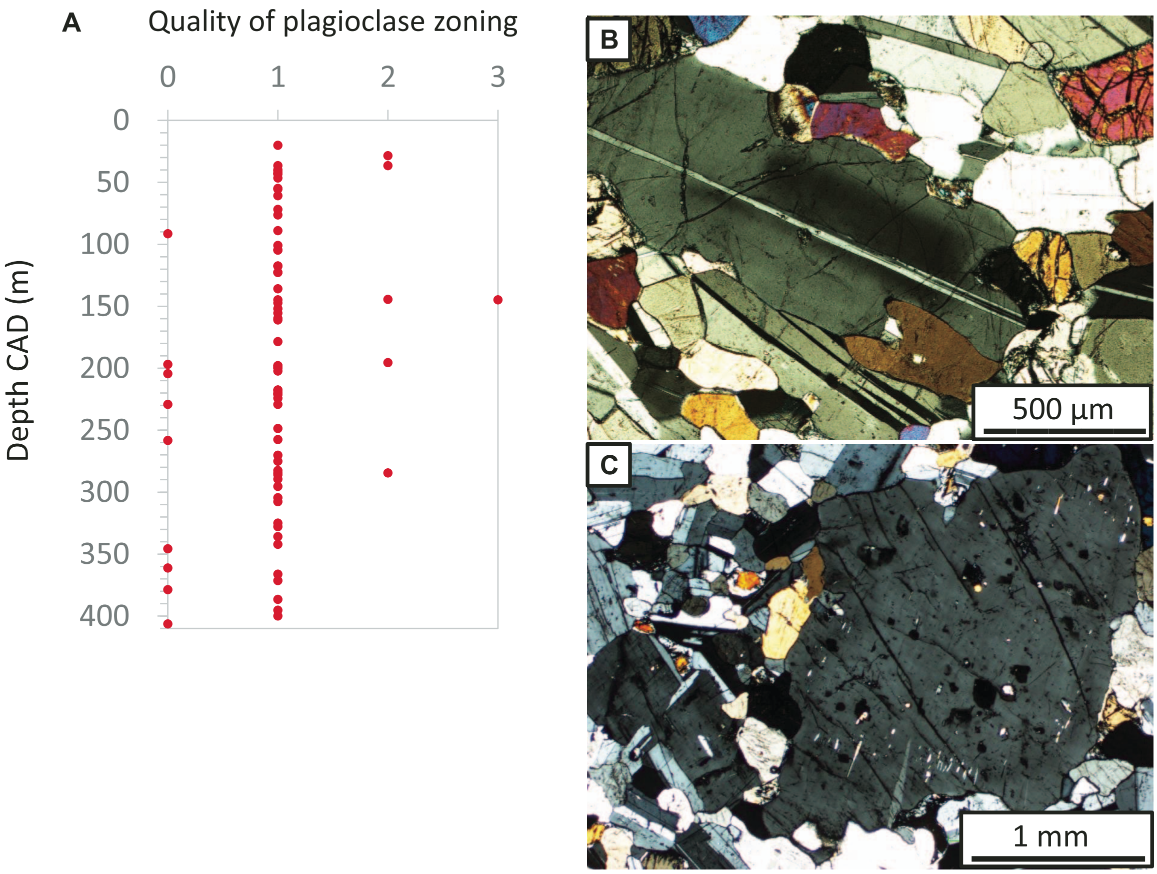

Figure F15. Occurrence of olivine melagabbro. **A.** Modally graded rhythmic layering with olivine melagabbro (arrows). **B**. Closeup of the boundary between olivine melagabbro and olivine-bearing gabbro (83Z-3, 18–27 cm). **C.** Photomicrograph of the boundary between olivine melagabbro and olivine-bearing gabbro (83Z-3, 21–24 cm). Ol = olivine, Pl = plagioclase, Cpx = clinopyroxene.

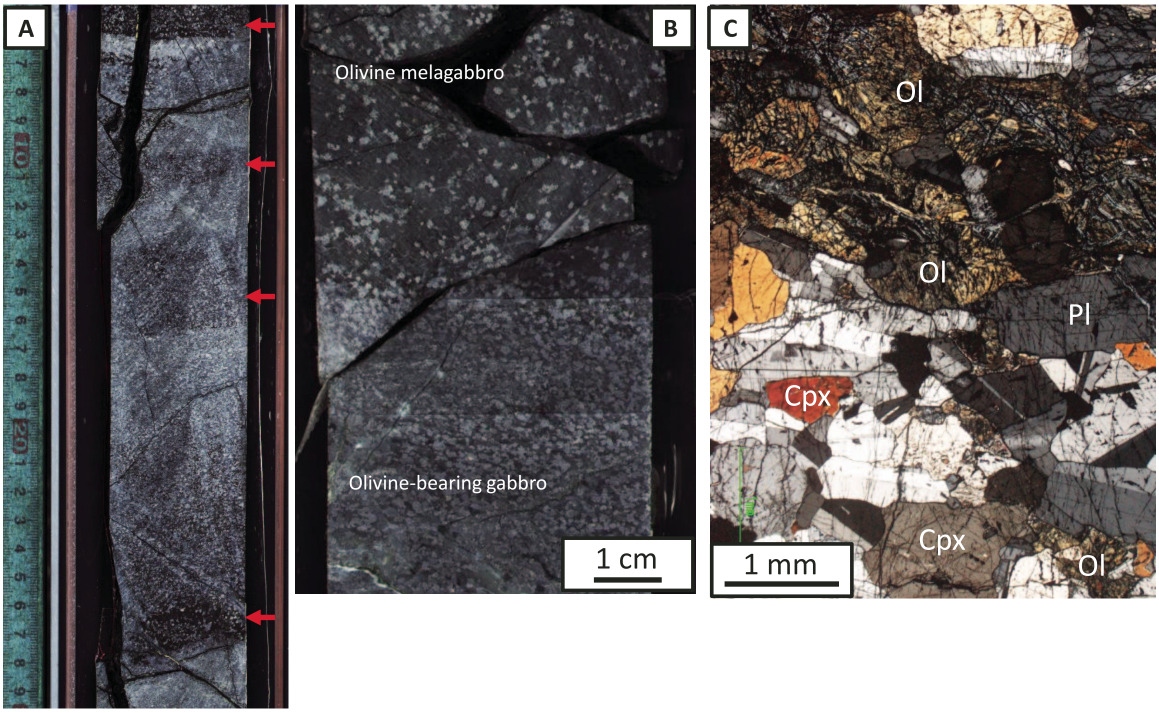

Figure F16. A. Core photo (54Z-3, 14–20 cm; photomicrographs from 54Z-3, 18–20 cm). Photomicrographs of (**B**) fine-grained olivine gabbro showing some large plagioclase crystals are contained, and (**C**) fine-grained olivine gabbro showing elongated crystal inclusions (clinopyroxene?) contained around the rounded core of zoned plagioclase.

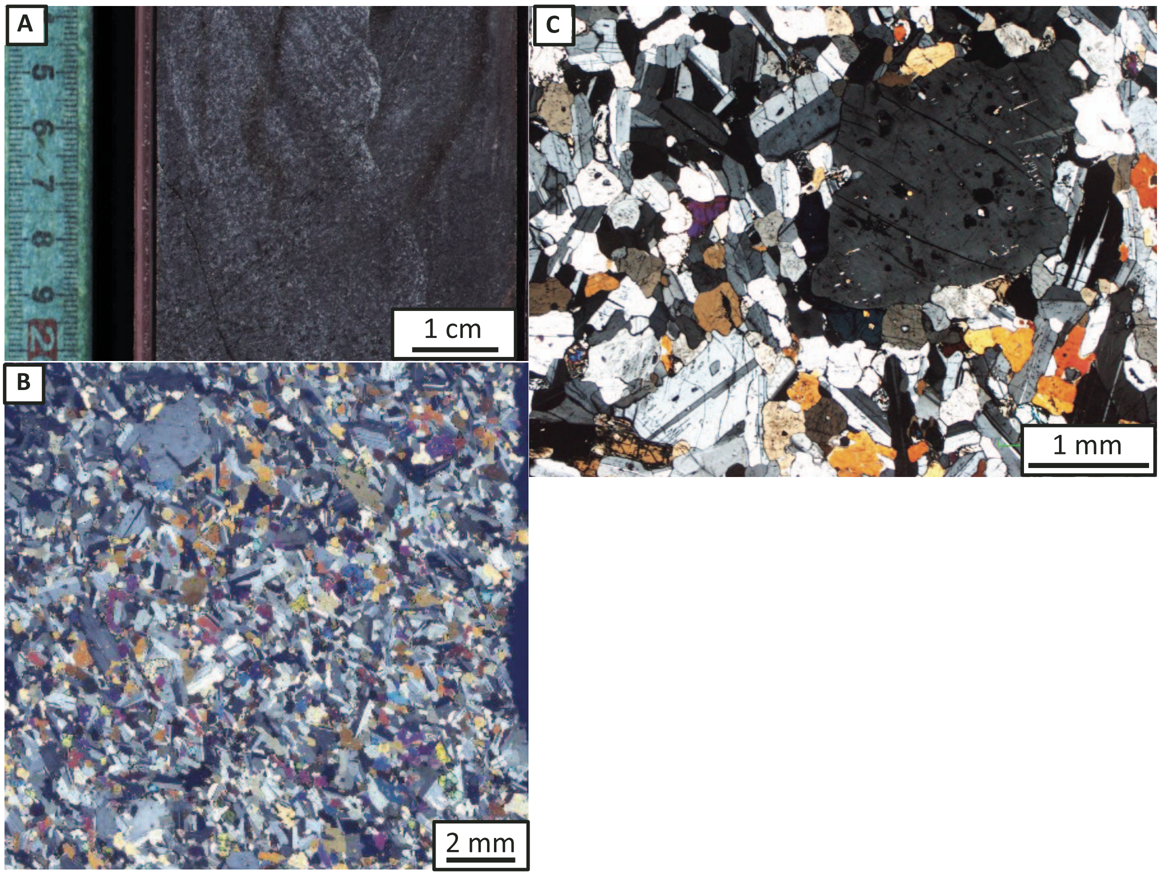

Figure F17. A. Core photo (54Z-3, 52–59 cm). **B.** Closeup of 54Z-3, 54–58 cm; field of view = 3.5 cm. **C.** Photomicrograph of the boundary between fine-grained and medium-grained gabbro.

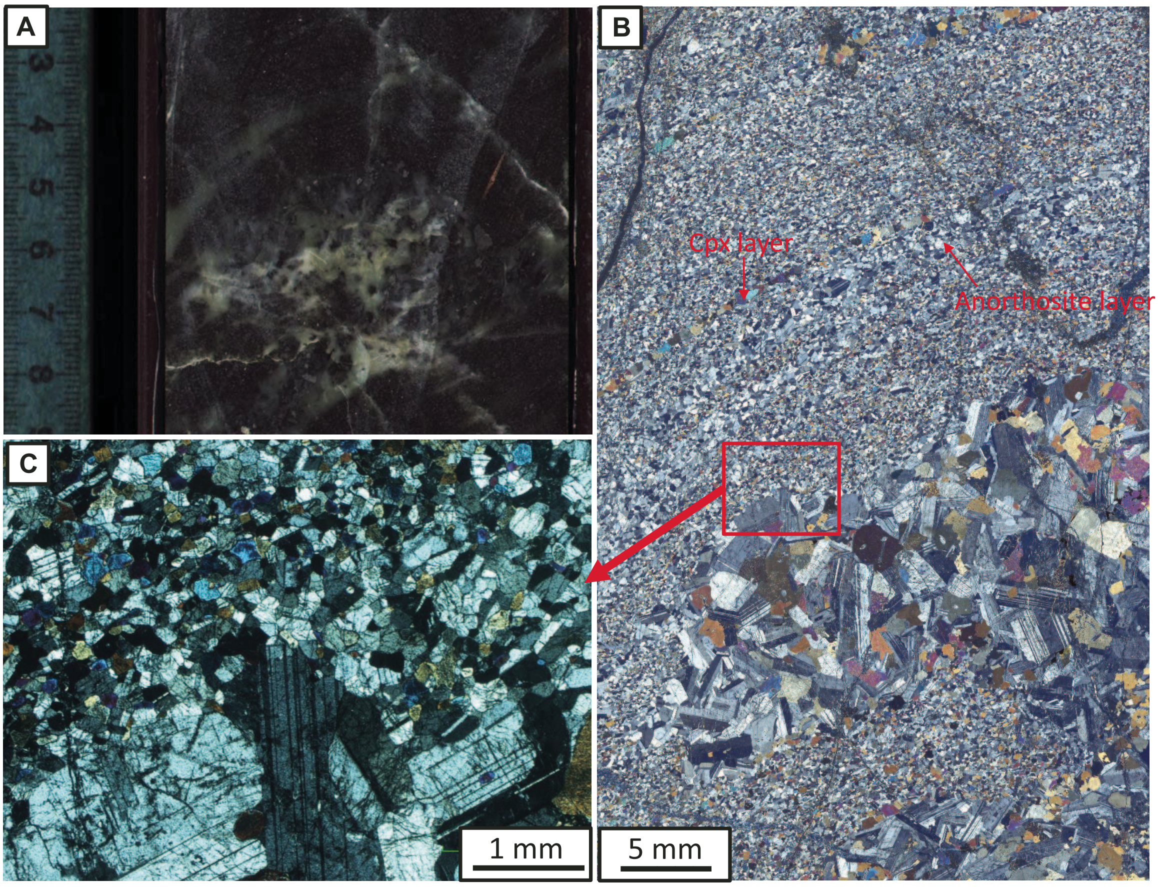

Figure F18. A. Closeup (105Z-3, 3–8 cm; photomicrographs from 105Z-3, 3.5–7.5 cm). Photomicrographs of (**B**) the boundary between medium-grained troctolite (left) and fine-grained gabbronorite (right). The orthopyroxene films occur surrounding a large altered olivine in the medium-grained troctolite. Arrow shows uphole direction, and (**C**) gabbronorite in which plagioclase shows distinct zoning and contains many crystallized melt inclusions in the core (shown by arrows).

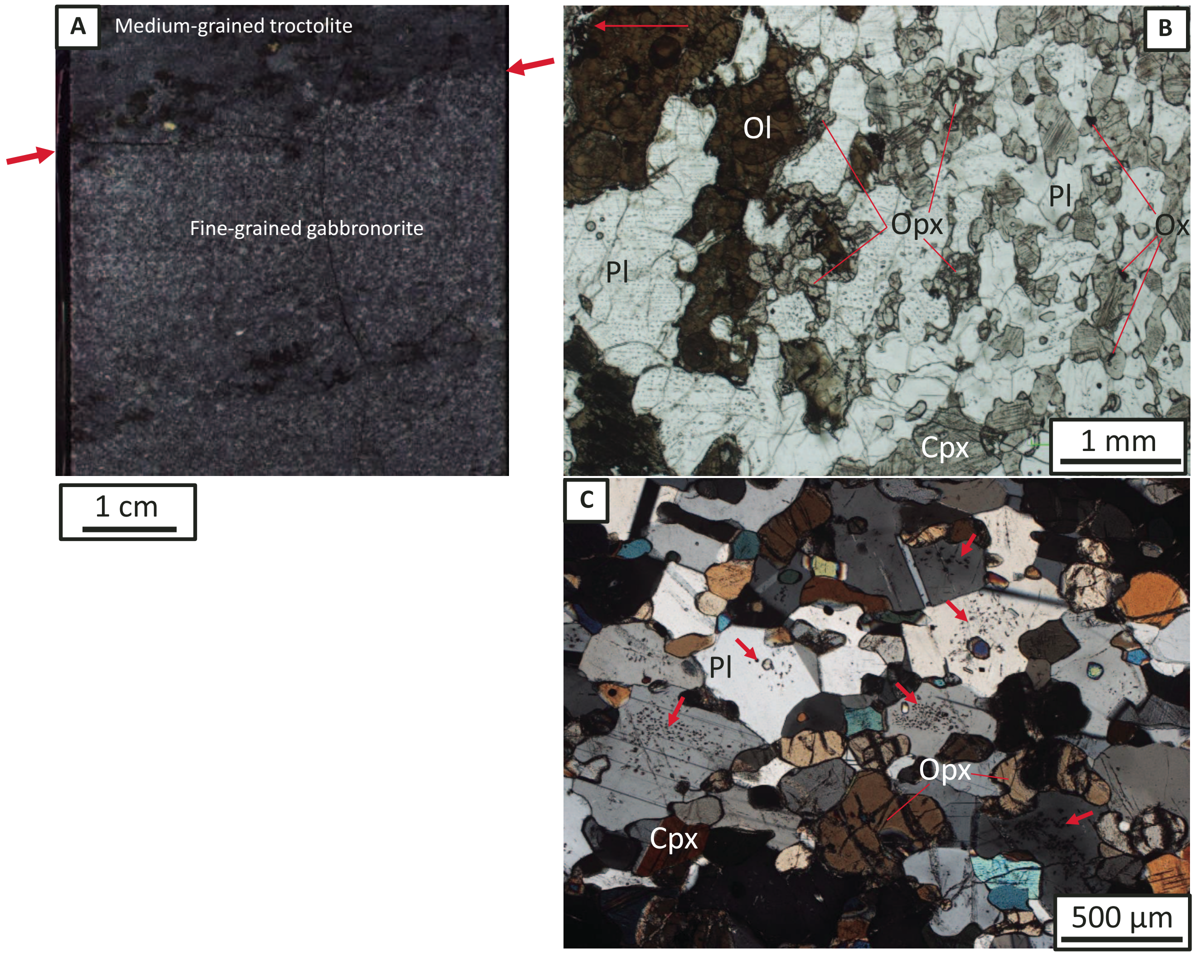

Figure F19. Total alteration intensity downhole in Hole GT2A.

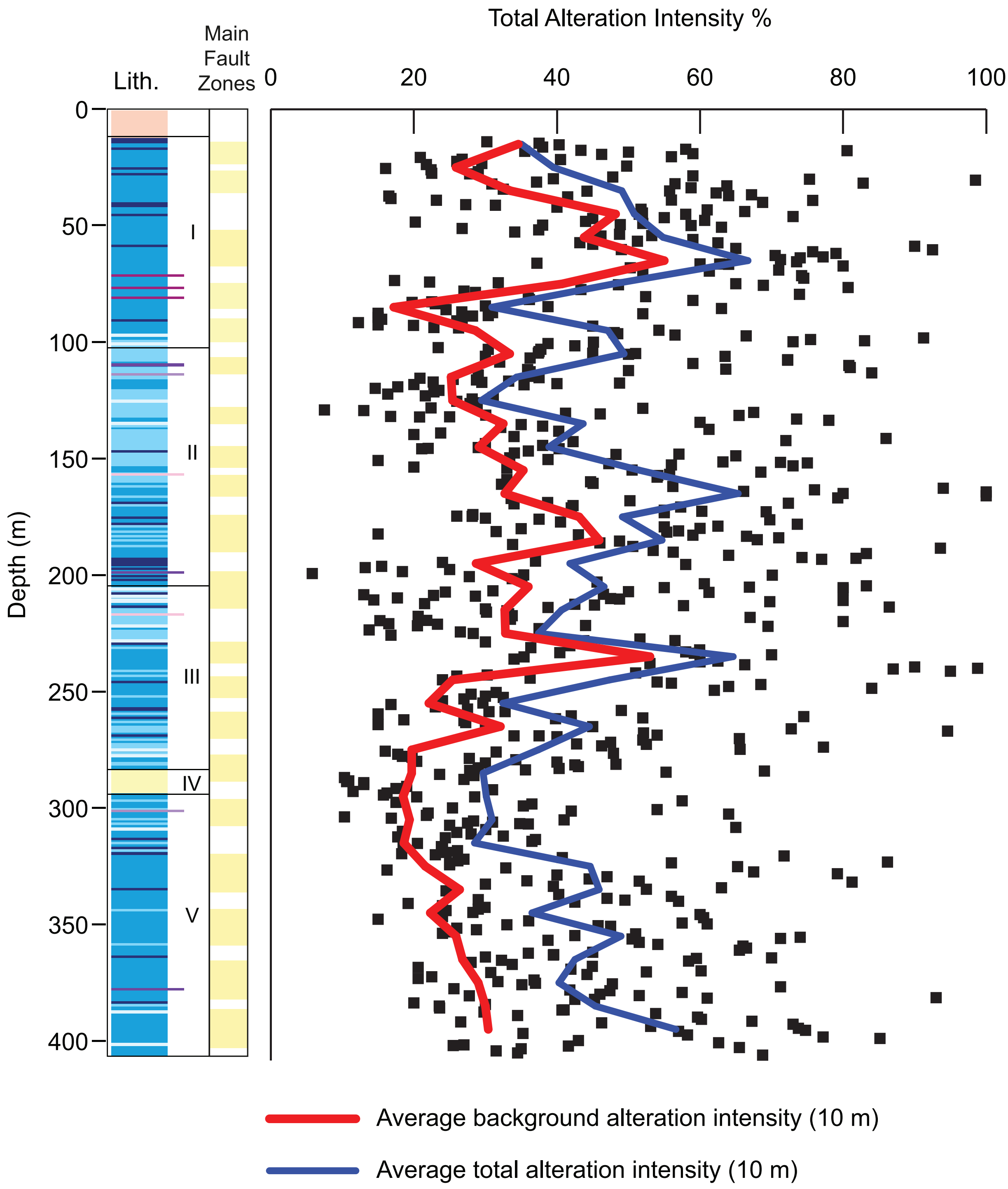

Figure F20. Distribution of the four alteration types with depth in Hole GT2A.

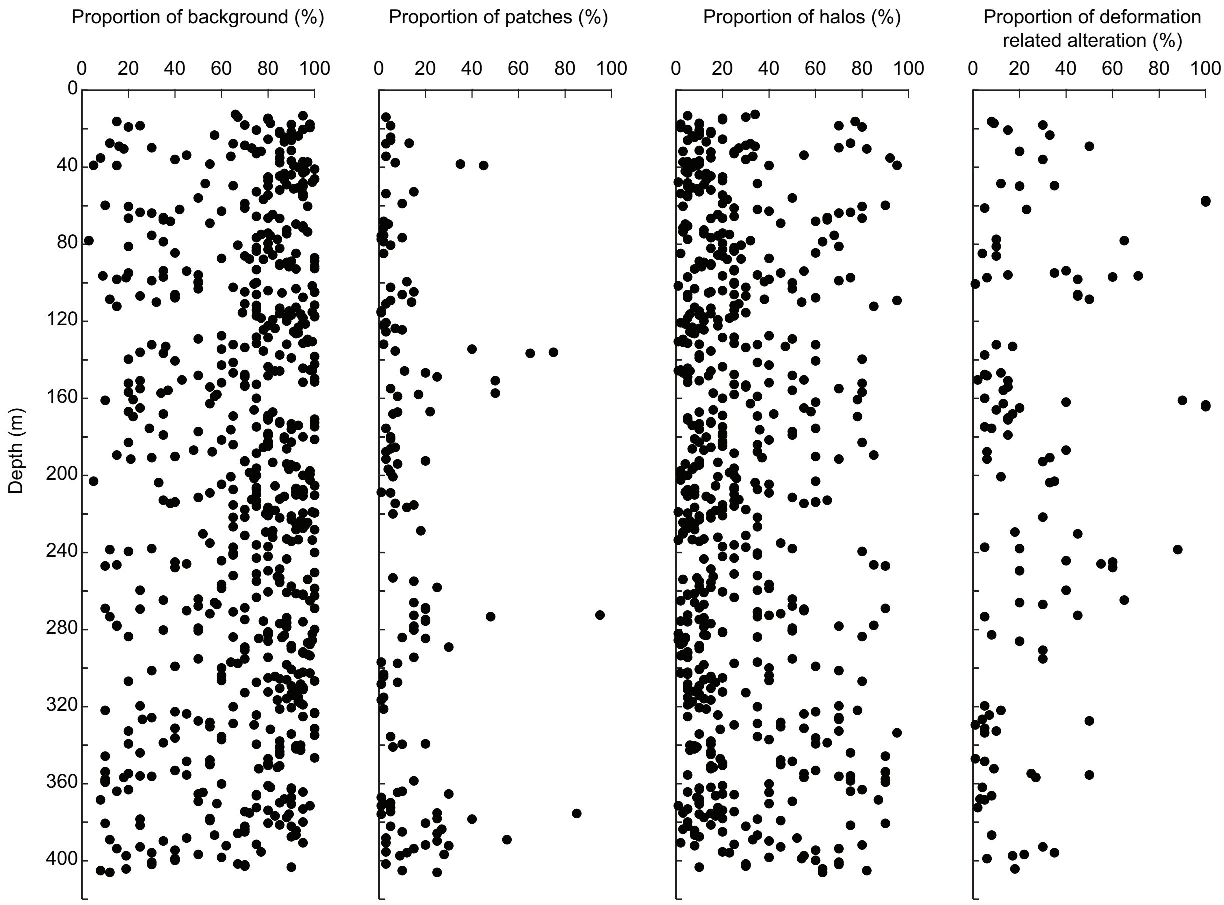

Figure F21. Secondary minerals (in veins and host rock) with depth in Hole GT2A.

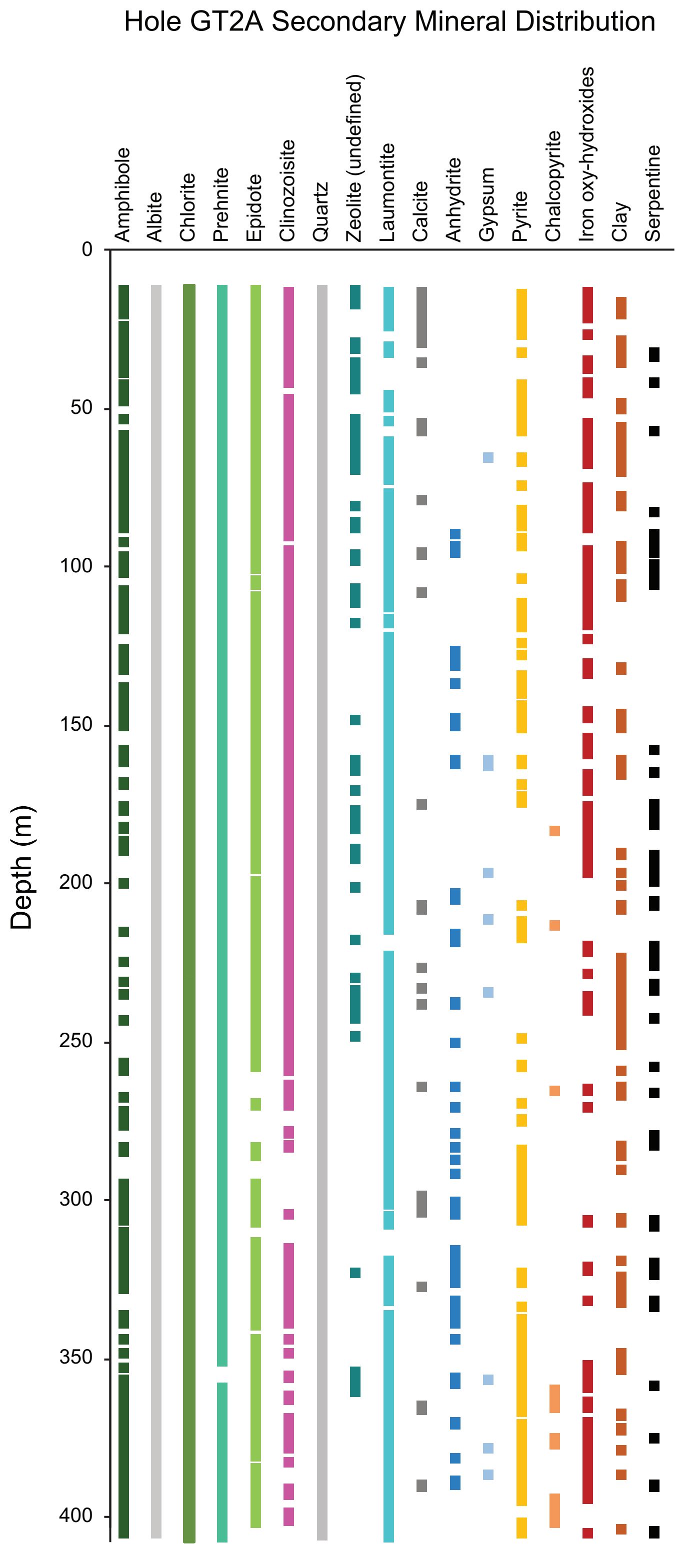

Figure F22. Compilation of the different types of alteration observed in Hole GT2A. Background alteration (from bottom): dark to medium gray; medium gray to green; and medium gray. Alteration patches (from bottom): quartz-rich patch with clinozoisite; clinozoisite-rich patch with minor quartz + chlorite. Halo alteration (from bottom): white secondary plagioclase-rich halo around laumontite vein; layered halo with inner clinozoisite + epidote zone and outer gray halo around an epidote vein. Deformation related (first column from bottom): set of sheared quartz–zeolite-carbonate–bearing veins; brecciated interval with extensive secondary plagioclase alteration of clasts; (second column from bottom): cataclastic zone with complete replacement to chlorite and quartz; zone of brecciated olivine gabbro with partial silicification.

Figure F23. Downhole plot to show the area each secondary minerals occupies within individual veins.

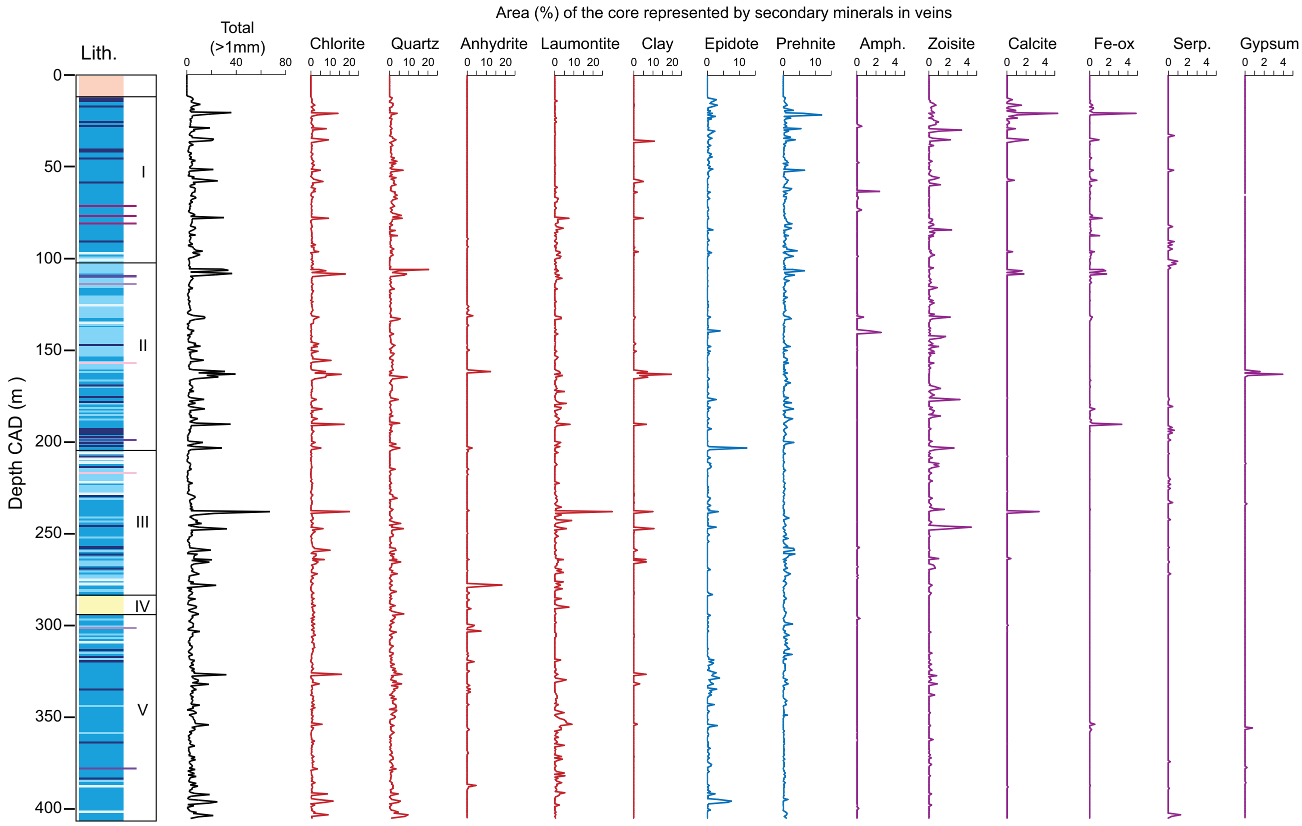

Figure F24. Vein intensity with depth, including veins >1 mm and <1 mm. Vein density calculated as veins/meter on a section-by-section basis.

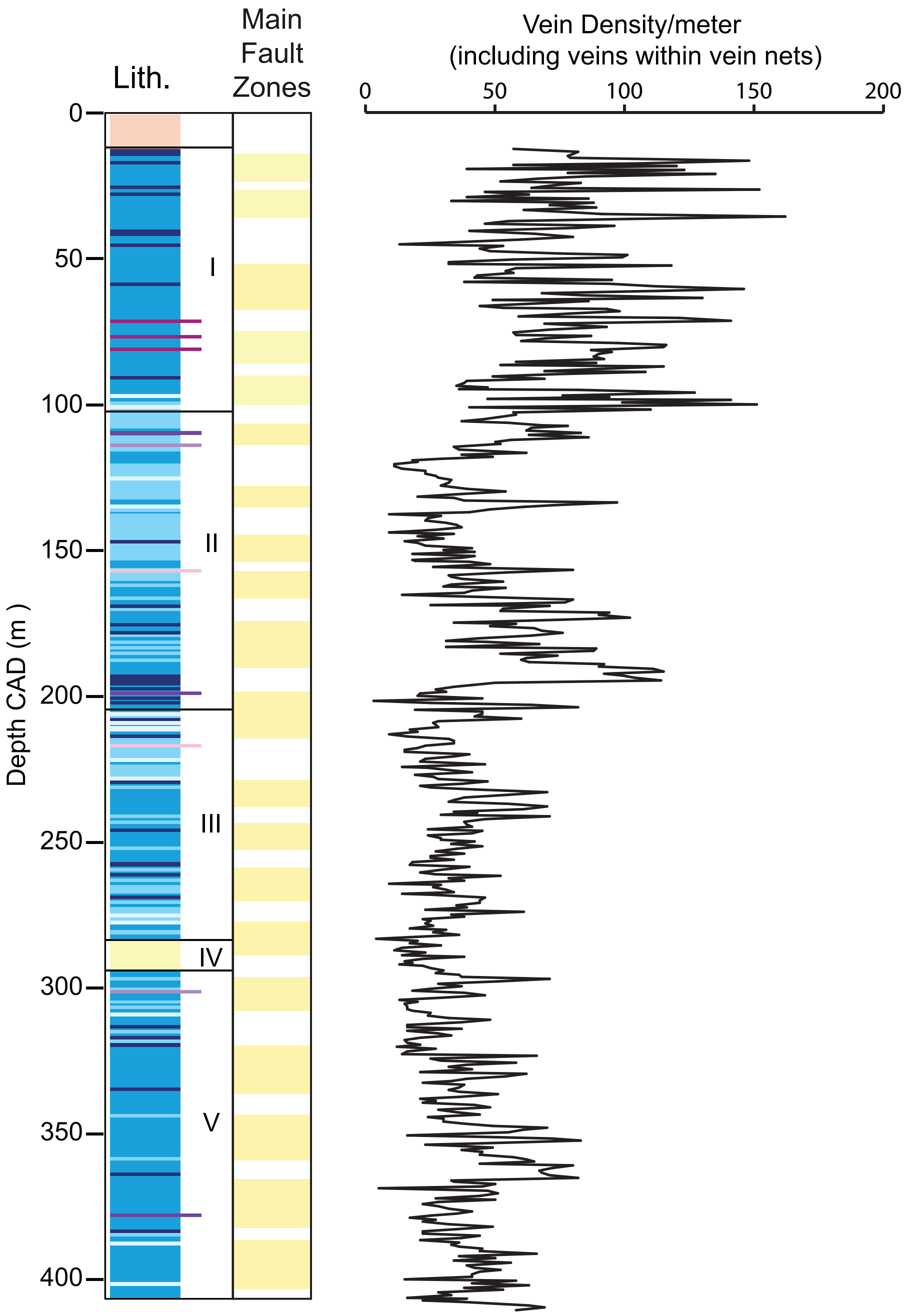

Figure F25. Vein intensity with depth, separated by mineral type. Vein density calculated as veins/meter on a section by section basis.

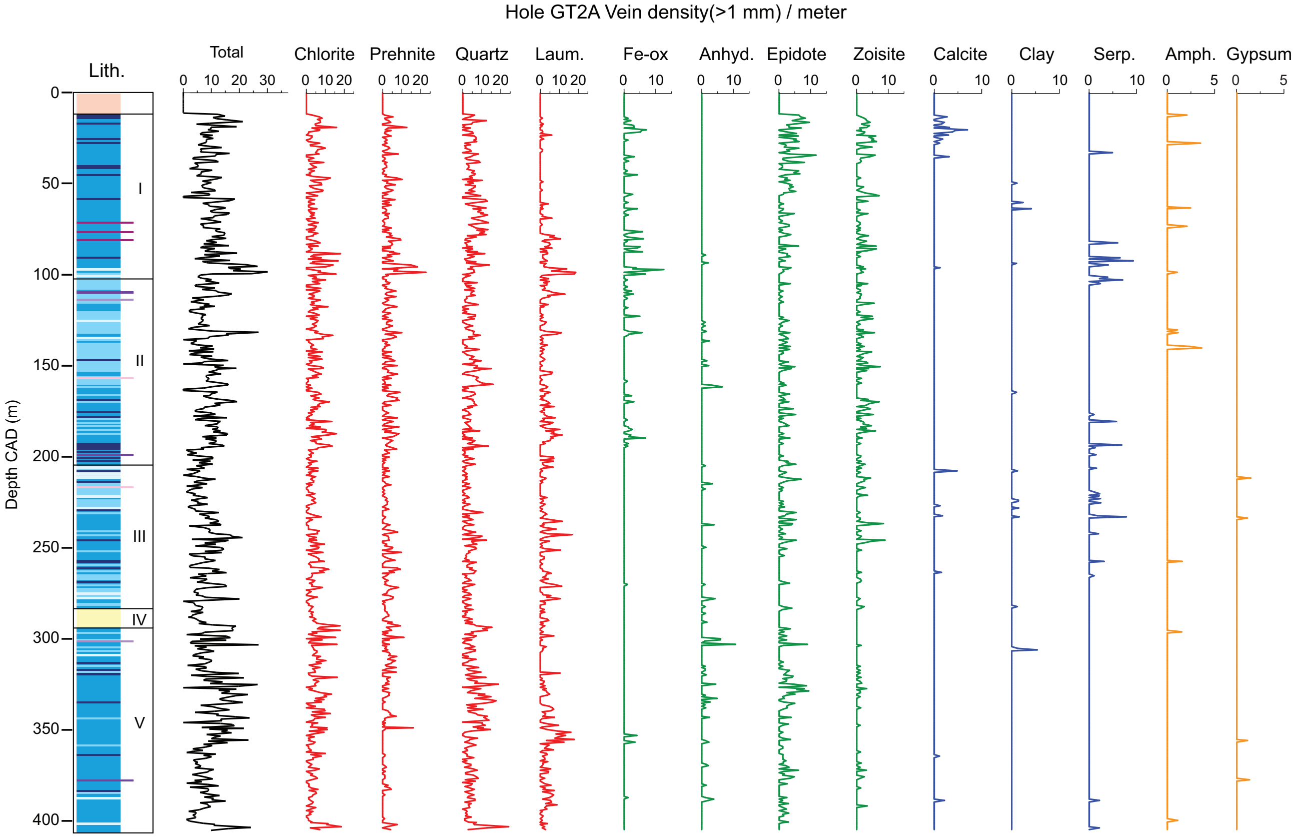

Figure F26. Anhydrite relationships. **A.** Anhydrite is present in large centimeter-sized bands that can cut across the width of the core (64Z, 45–70 cm). **B.** The only observed crosscutting relationship involving anhydrite; the anhydrite vein is crosscutting an epidote + quartz vein (112Z-1, 14–24 cm).

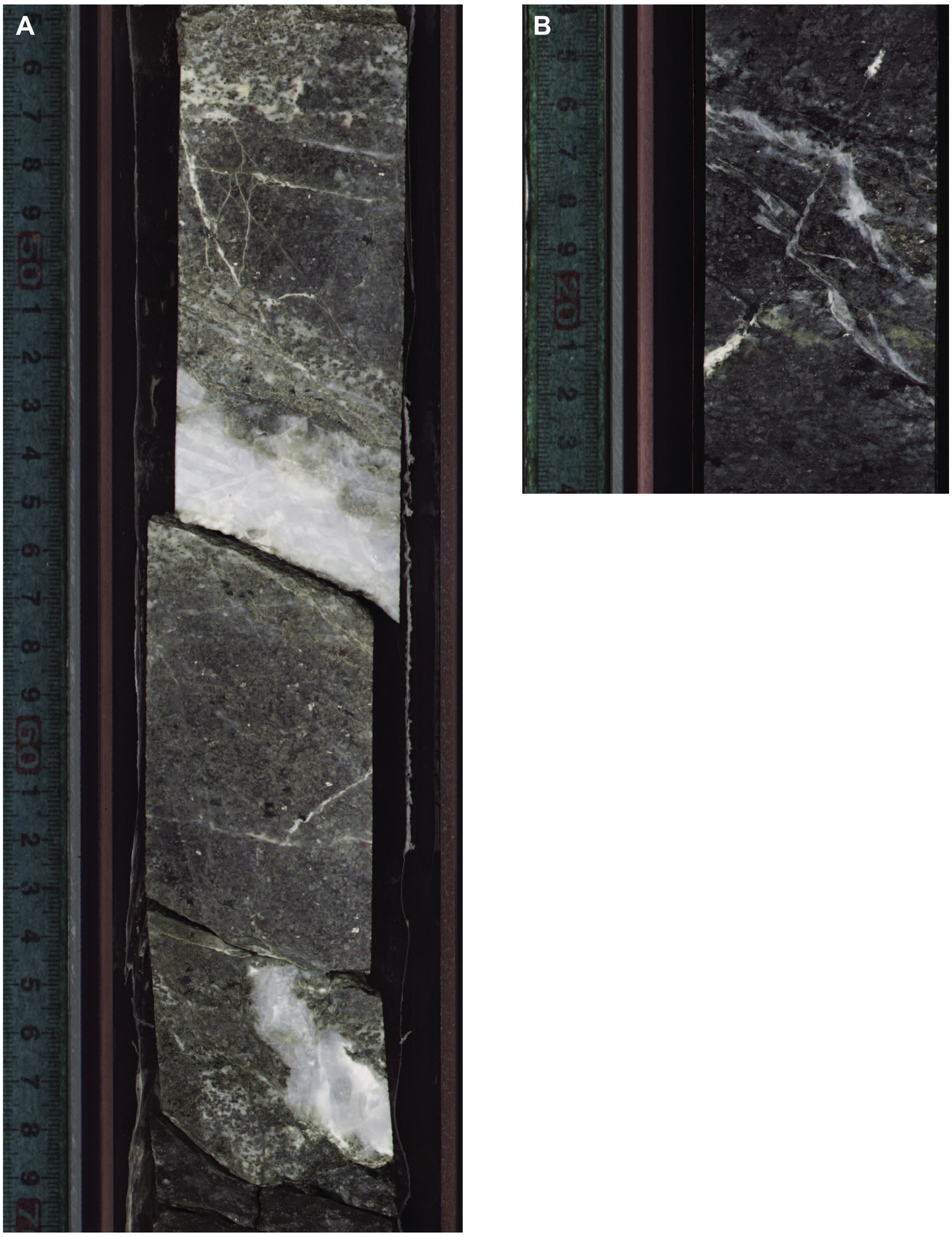

Figure F27. Photomicrographs illustrating alteration of olivine. **A, B.** Olivine crystal showing typical serpentine mesh veining and a strongly brown coloration to Fe oxyhydroxides (100Z-4, 14–cm; A: PPL; B: XPL). **C, D.** Alteration of olivine rim to serpentine + talc (55Z-2, 63–65 cm; C: PPL; D: XPL). **E, F.** Complete replacement of olivine by chlorite + talc + magnetite (55Z-2, 63–65 cm; E: PPL; F: XPL).

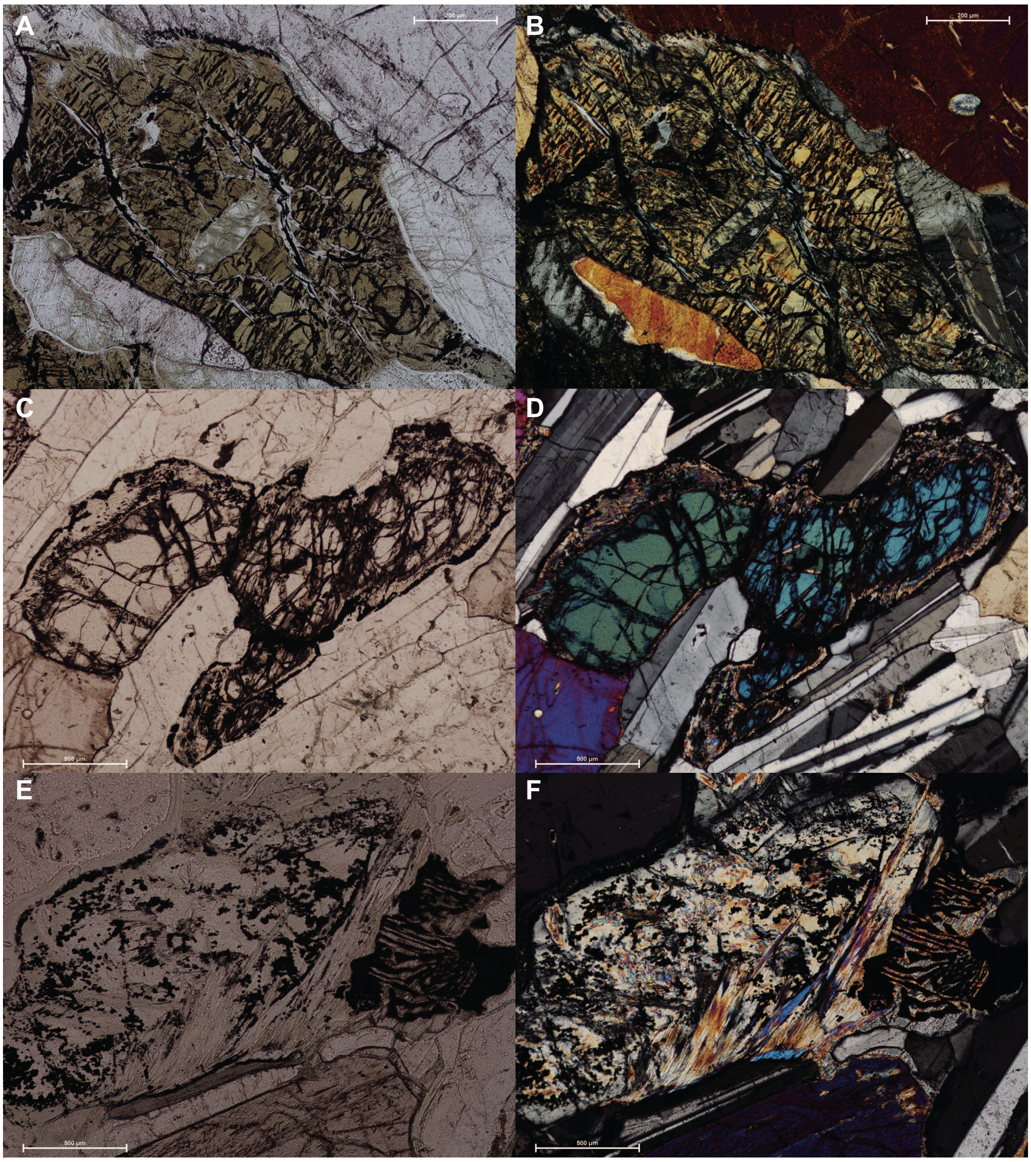

Figure F28. Photomicrographs illustrating clinopyroxene alteration. **A, B.** Typical patches of green and brown amphiboles pseudomorphically replacing clinopyroxene. Plagioclase crystals show complete replacement to chlorite + prehnite (18Z-2, 51–52 cm; A: PPL; B: XPL). **C, D.** Partial replacement of clinopyroxene to chlorite, in this sample the chlorite replacement is forming an interconnected chlorite mesh (142Z-4, 42–45 cm; C: PPL; D: XPL).

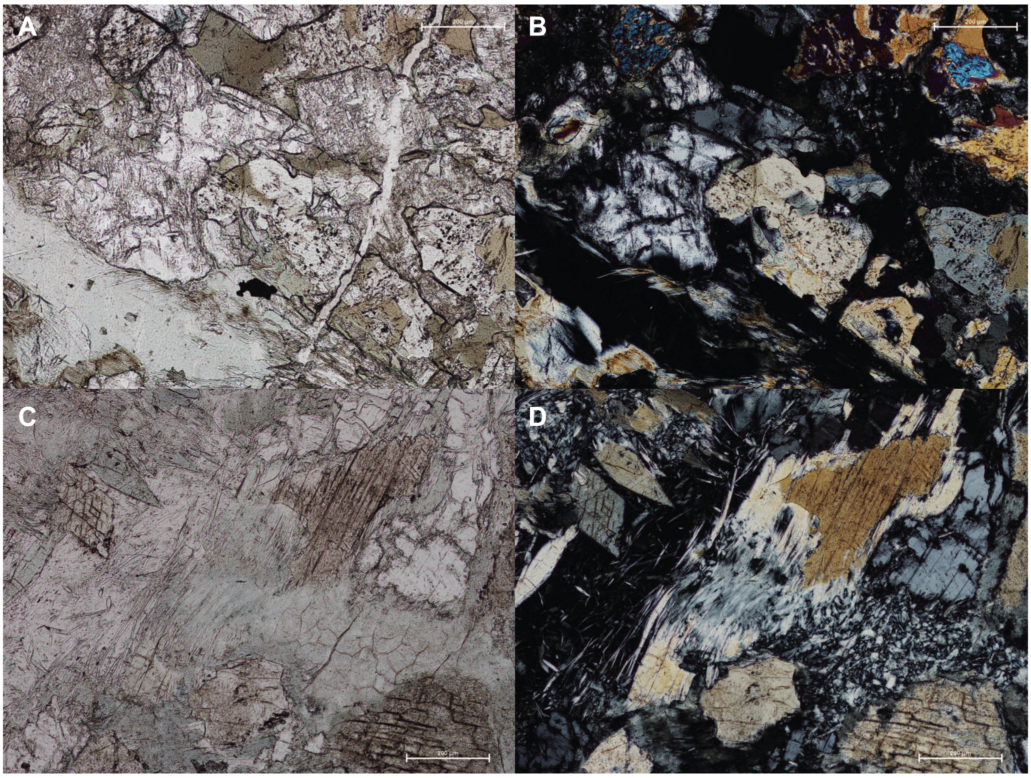

Figure F29. Photomicrographs illustrating alteration of plagioclase. **A, B.** Plagioclase crystals showing limited alteration with microcracks and small (~20 µm) spots of chlorite (19Z-2, 62–65 cm; A: PPL; B: XPL). **C, D.** Complete replacement of plagioclase by clinozoisite with a pseudomorphic texture (17Z-3, 15–17 cm; C: PPL; D: XPL). **E, F.** Complete replacement of plagioclase by fine-grained chlorite and clinozoisite with loss of igneous texture (100Z-4, 44–46 cm; E: PPL; F: XPL).

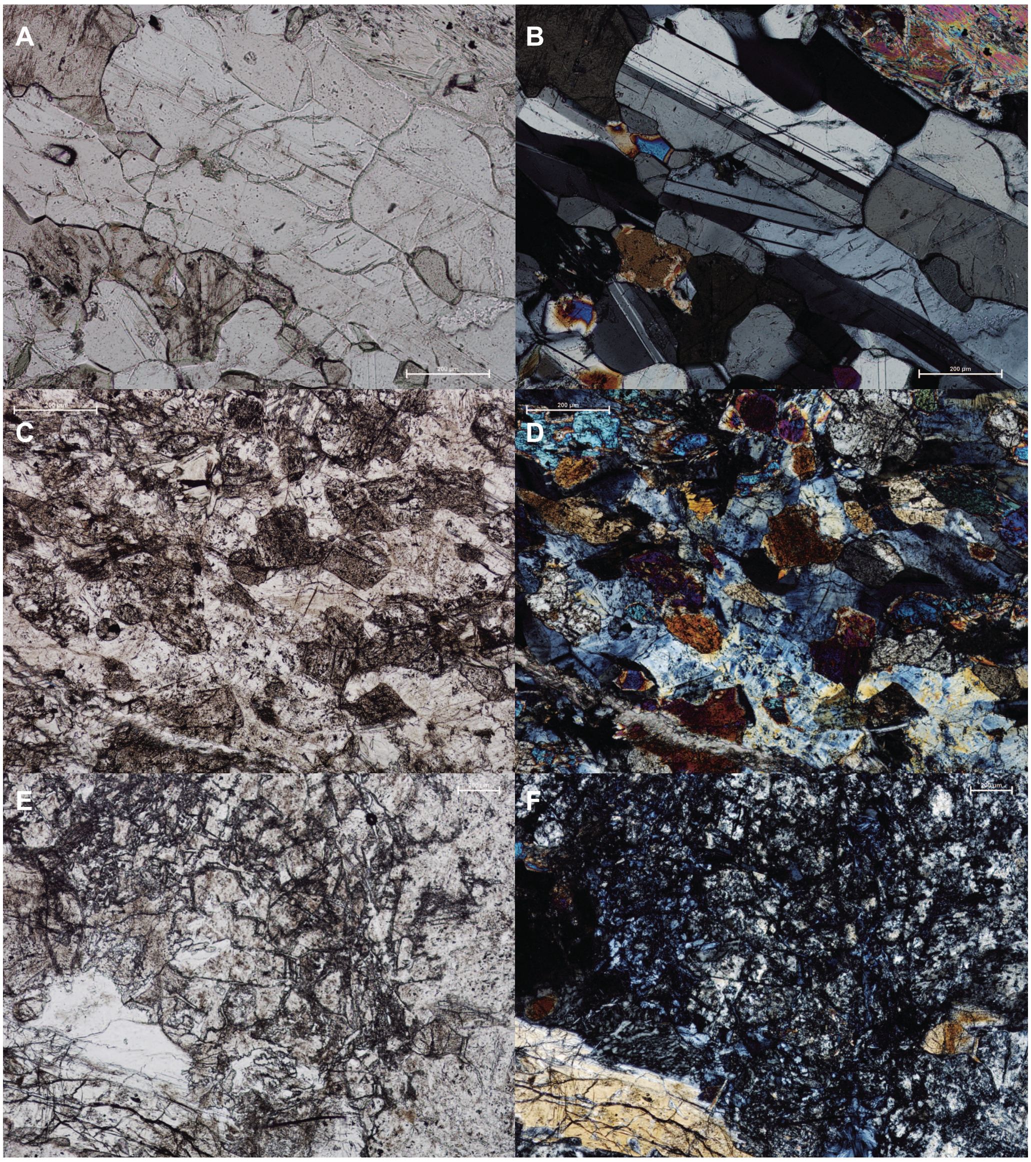

Figure F30. Photomicrographs illustrating alteration around a thin cataclastic band. **A, B.** Chlorite + prehnite alteration zone adjacent to a ~50 µm wide cataclastic band (lower left hand corner of image). Note that close to the cataclastic band some of the igneous phases remain relatively unaltered (21Z-2, 50–52.5 cm; A: PPL; B: XPL).

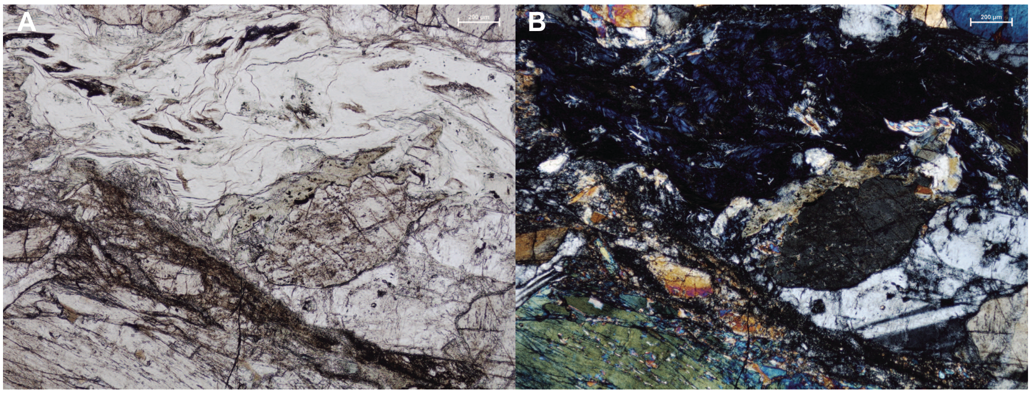

Figure F31. Photomicrographs illustrating veins and crosscutting relationships. **A, B.** Typical grain boundary vein network with veins <20 µm in width and likely composed of either chlorite or amphibole. At higher degrees of alteration, this vein network is not observed (55Z-2, 63–65 cm; A: PPL; B: XPL). **C, D.** Prehnite + quartz + chlorite vein crosscut by a zeolite + carbonate vein (17Z-3, 15–17 cm; C: PPL; D: XPL).

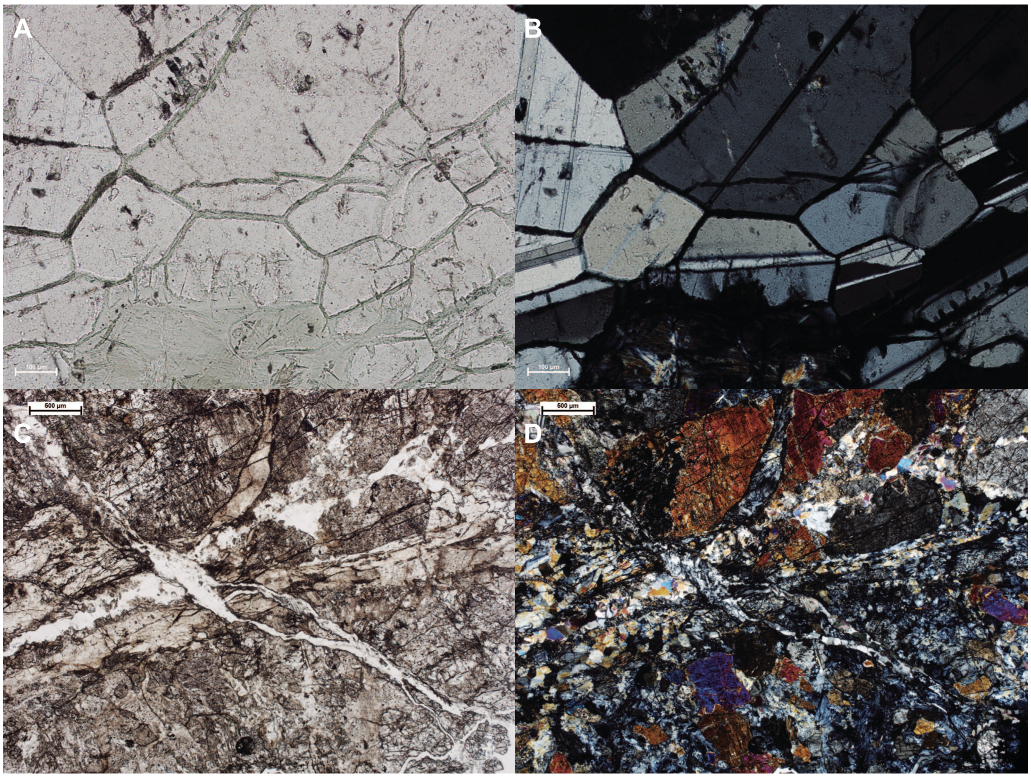

Figure F32. Photomicrographs illustrating vein and halo relationships (123Z-4, 15–18.5 cm). **A, B.** Large epidote + clinozoisite vein, the left margin of the vein is just out of image, note small crystal size. The right margin is visible and is marked by a thin prehnite + chlorite vein (A: PPL; B: XPL). **C, D.** Inner gray halo dominated by pseudomorphic replacement of plagioclase by clinozoisite (C: PPL; D: XPL). **E, F.** Outer white halo dominated by replacement of plagioclase by secondary plagioclase (and absence of epidote/clinozoisite) (E: PPL; F: XPL).

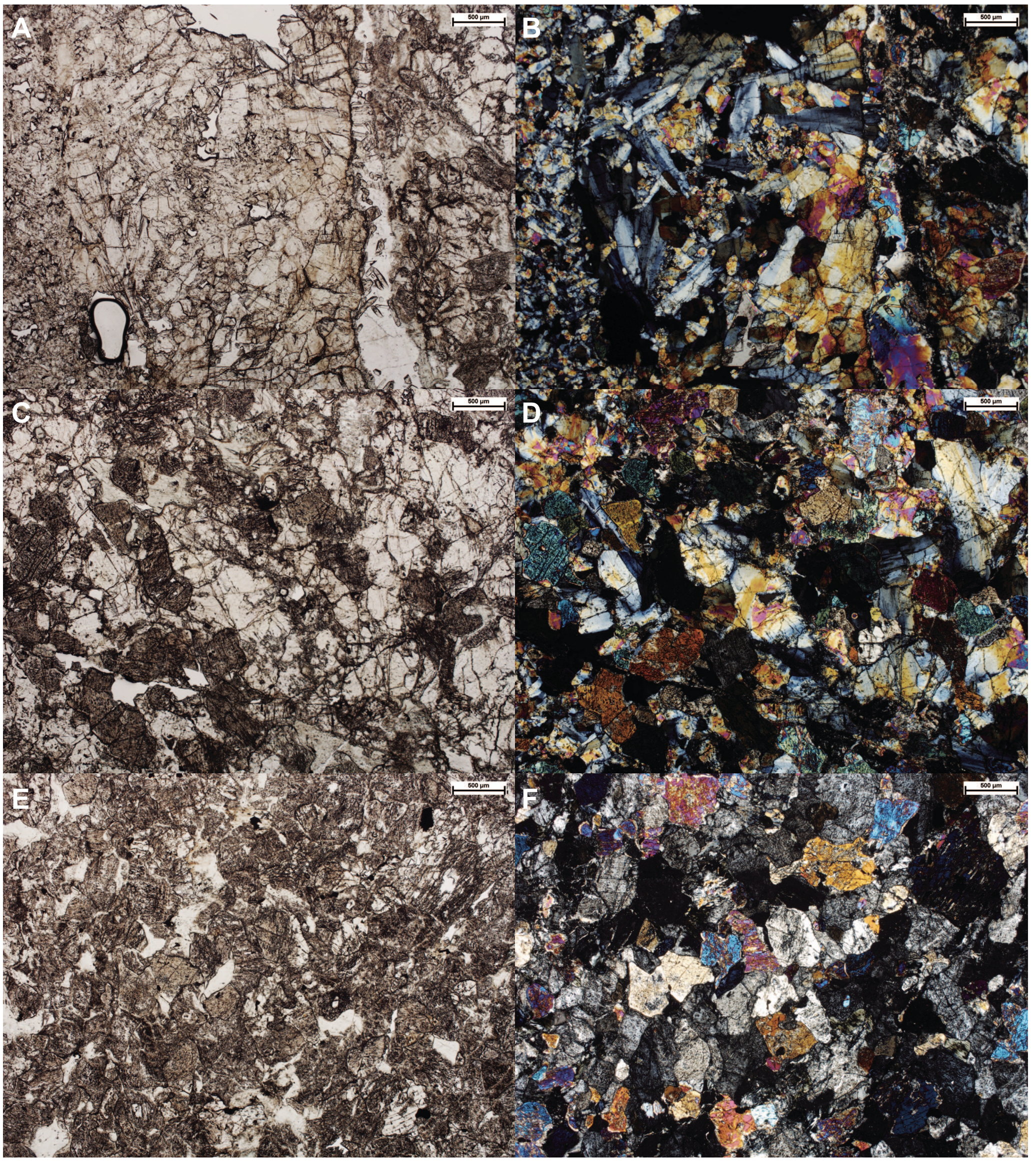

Figure F33. Magmatic contacts in foliated and layered gabbros. **A.** Sharp, planar contact between olivine gabbro and “spotted” olivine-bearing gabbro showing ratio (modal) and grain-size layering within the foliated gabbro sequence. Red box denotes location of photomicrographs. **B, C.** Photomicrograph showing ratio and grain-size layering contact (B: PPL; C: XPL). **D.** Sharp, irregular contact between olivine-bearing gabbro and gabbro in the layered gabbro sequence. Red box denotes location of photomicrographs. **E, F.** Photomicrographs of ratio and grain-size layering contact (E: PPL; F: XPL).

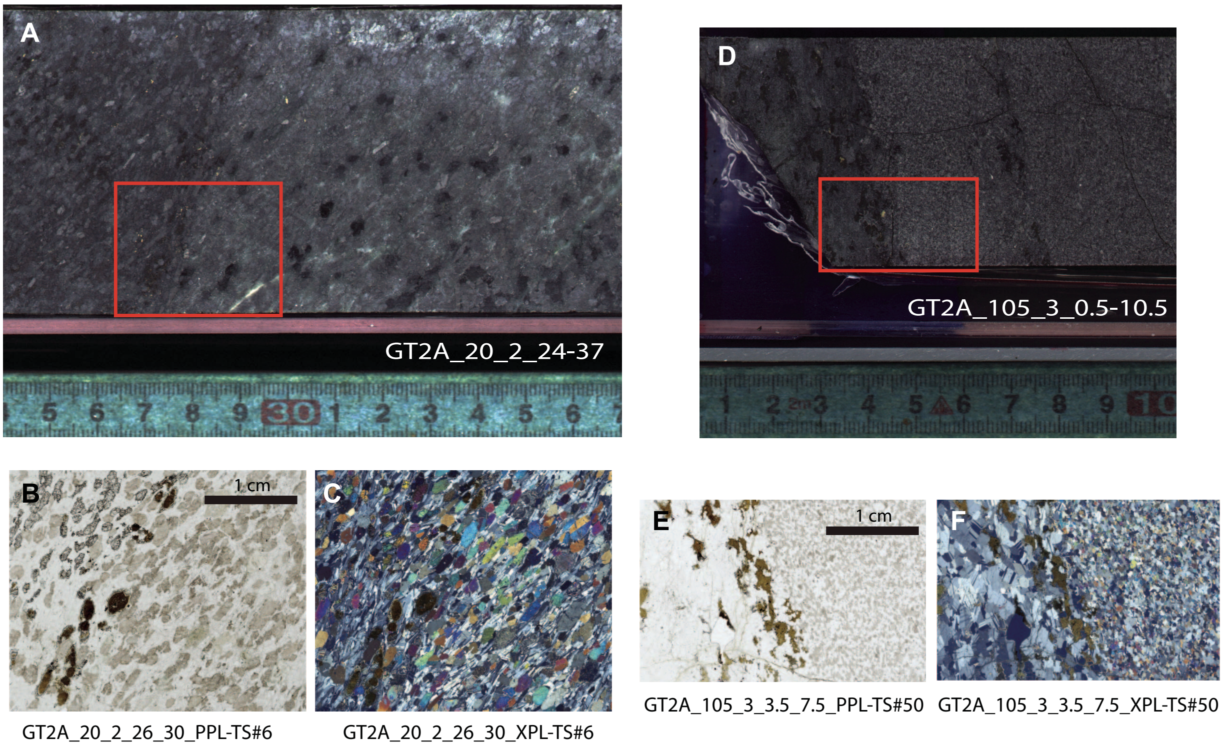

Figure F34. Transition zone showing compositional/modal magmatic layering. **A.** Scale, ratio, and phase layering shown by anorthosite layer within olivine-bearing gabbro and olivine gabbro layers. Red box denotes location of photomicrographs. **B, C.** Photomicrographs of sharp, planar contact between olivine-bearing gabbro and anorthosite (B: PPL; C: XPL).

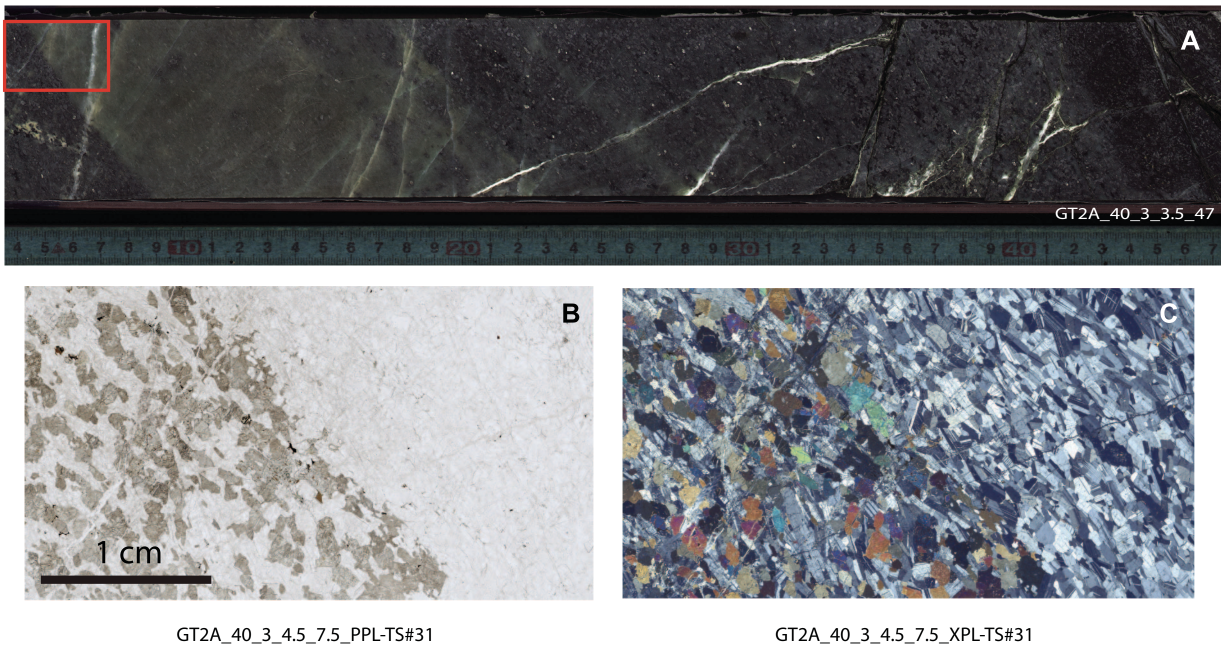

Figure F35. Layered gabbro sequence showing magmatic layering. **A, B.** Scale, ratio, phase, grain-size layering shown by gabbro and olivine gabbro layers. B is marked with dashed red lines to show sharp, planar, and curved contacts. Note planar contact between olivine gabbro and sheared "tiger" gabbro at 54 cm. Red box denotes location of photomicrographs. **C, D.** Photomicrographs of sharp, planar, phase, and grain-size contact between gabbro and olivine gabbro (C: PPL; D: XPL illustrates the difference grain size and composition of the two layers).

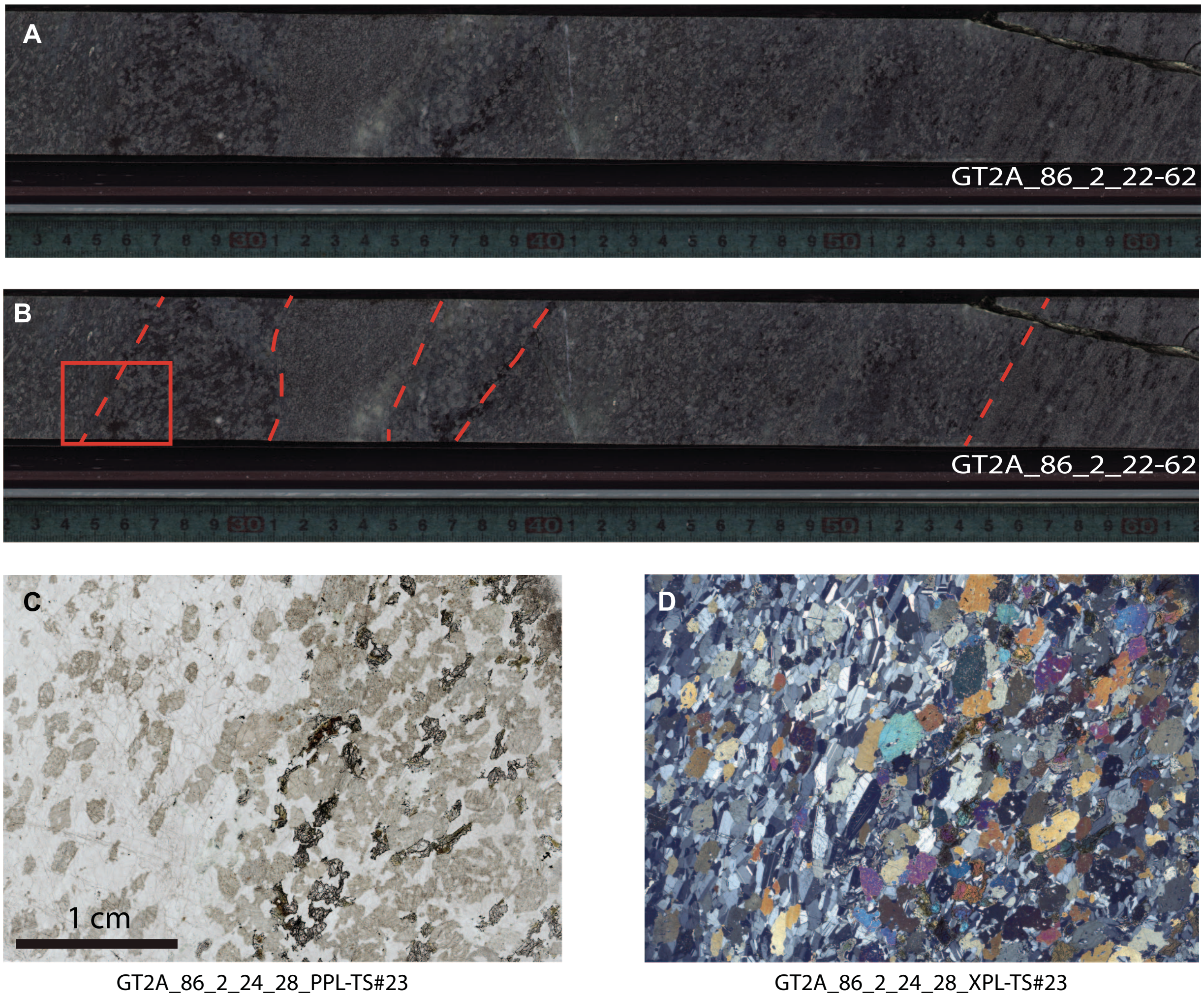

Figure F36. Centimeter-scale magmatic banding. **A.** Distinct ratio and phase banding grading into very diffuse ratio and phase banding shown by anorthositic layers within olivine gabbro. **B.** Irregular, subcentimeter-scale phase banding shown by troctolitic layers within gabbro. This style of banding was termed “tiger” banding during core description. **C.** 0.5 cm wide sharp, planar anorthositic band within olivine gabbro. Red box denotes location of photomicrographs. **D, E.** Photomicrographs of anorthosite band within olivine gabbro (C: PPL; D: XPL).

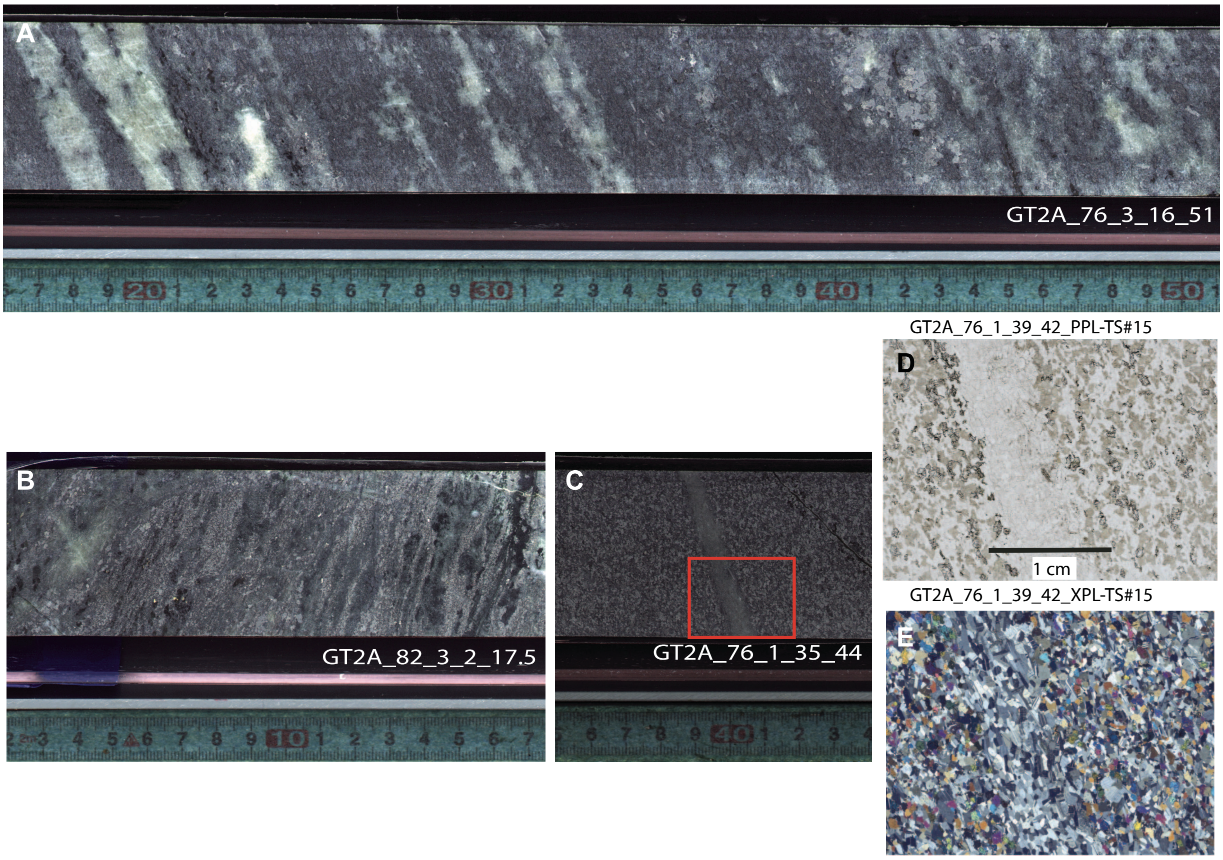

Figure F37. Differing styles and strengths of magmatic foliation defined by olivine. **A.** Moderate olivine foliation defined by elongate olivine crystals in an olivine gabbro. Elongate plagioclase and pyroxene show consistent foliation. **B.** Strong olivine foliation defined by elongate olivine crystals in an olivine gabbro. This style of foliation is typical of the weak "tiger" banding/foliation described during core description. **C.** Moderate to weak olivine foliation defined by clumped subgrained olivine crystals. Right-hand side of the core shows the style of foliation typically developed in the "spotted" gabbros described during core description.

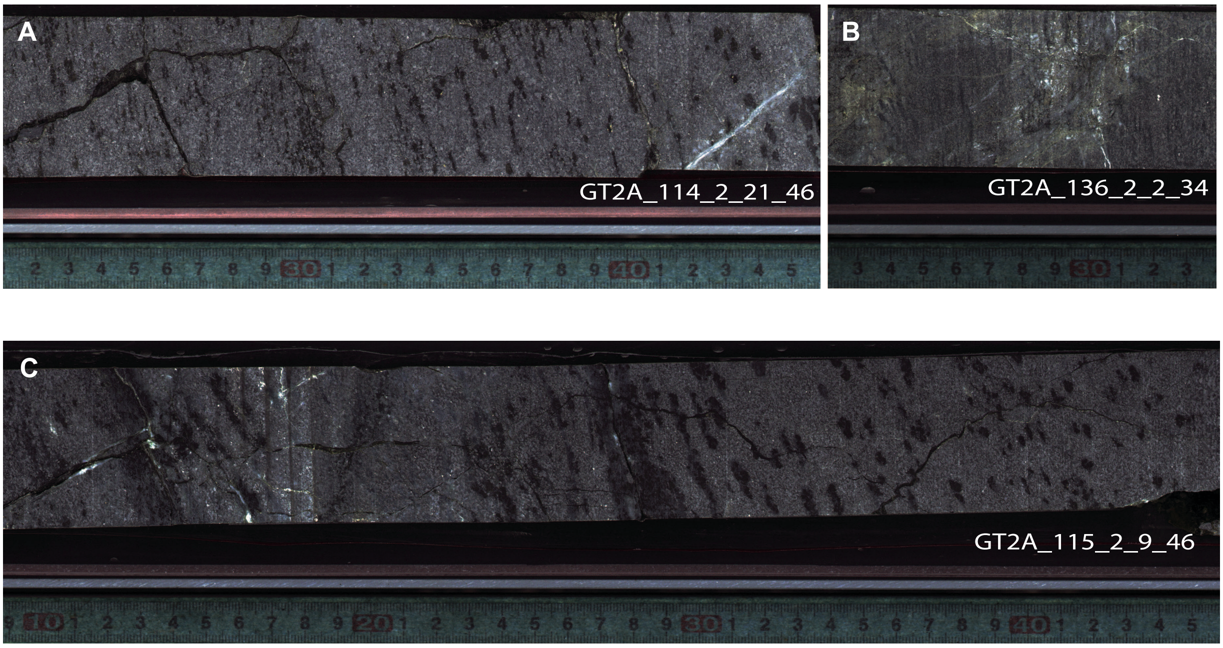

Figure F38. Magmatic foliation within the foliated gabbro sequence. **A.** Moderate foliation within a medium-grained gabbro defined by high–aspect ratio plagioclase and moderate–aspect ratio clinopyroxene crystals. **B.** Very weak foliation within a medium-grained gabbro defined by moderate–aspect ratio plagioclase crystals. **C.** Weak foliation within a fine-grained olivine-bearing gabbro, dominantly defined by high–aspect ratio plagioclase crystals but also by low–aspect ratio clinopyroxene crystals. **D.** Lower half of the photomicrograph shows strong foliation within more coarse grained "spotted" olivine-bearing gabbro defined by high–aspect ratio plagioclase crystals and moderate–aspect ratio clinopyroxene crystals. Upper half of photomicrograph shows strong foliation within a more coarse grained olivine gabbro defined by high–aspect ratio plagioclase crystals, moderate–aspect ratio olivine crystals, and low–aspect ratio clinopyroxene crystals.

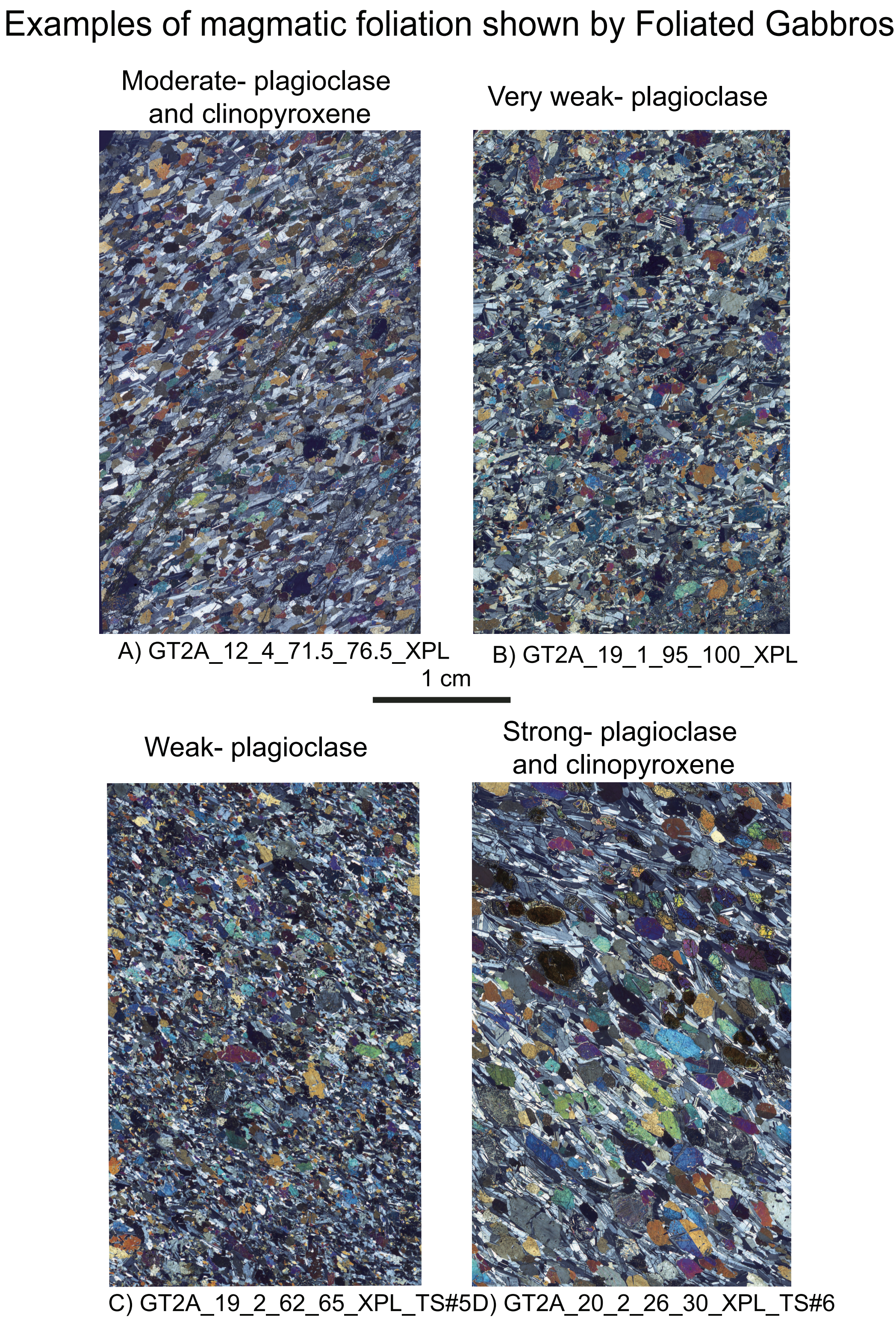

Figure F39. Magmatic foliation within the transition zone gabbro sequence. **A.** Very weak foliation within a fine-grained olivine-bearing gabbro defined by moderate–high aspect ratio plagioclase crystals. **B.** Moderate foliation within a more coarse grained olivine-bearing gabbro defined by moderate–aspect ratio plagioclase and clinopyroxene crystals. **C.** Strong foliation within a medium-grained gabbro dominantly defined by high–aspect ratio plagioclase crystals but also by low–aspect ratio clinopyroxene crystals. **D.** Moderate foliation within a medium-grained olivine gabbro defined by high–aspect ratio plagioclase crystals and low–aspect ratio olivine crystals. **E.** Moderate foliation within a medium-grained gabbro defined by high–aspect ratio clinopyroxene crystals and low–aspect ratio plagioclase crystals.

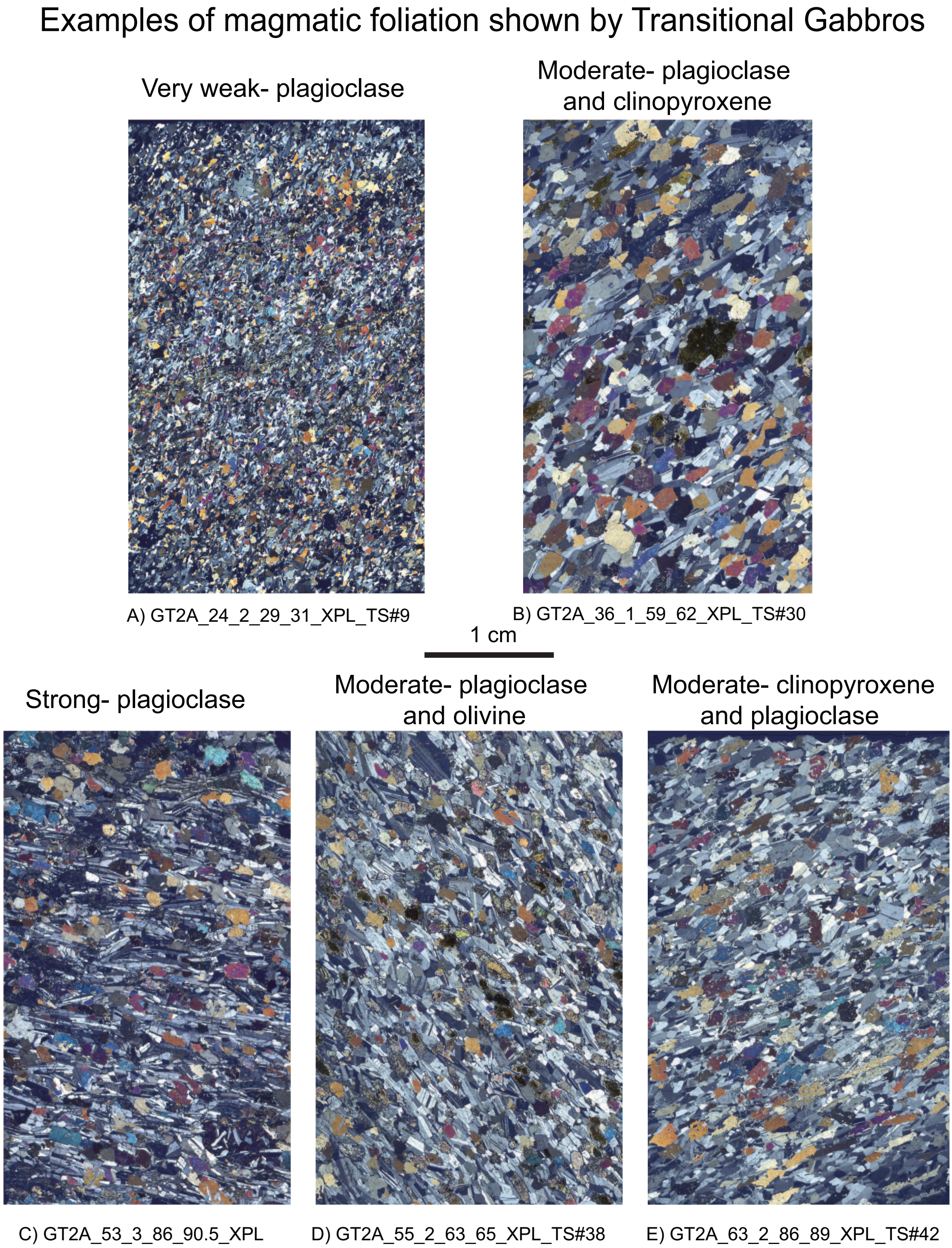

Figure F40. Magmatic foliation within the layered gabbro sequence. **A.** Moderate foliation within a medium-grained gabbro defined by high–aspect ratio plagioclase crystals and low–moderate aspect ratio clinopyroxene crystals. **B.** Strong foliation within fine-grained olivine-bearing gabbro defined by high–aspect ratio plagioclase and low–aspect ratio clinopyroxene crystals. **C.** Strong foliation within a fine- to medium-grained olivine gabbro, dominantly defined by high–aspect ratio plagioclase crystals but also by moderate–aspect ratio olivine and clinopyroxene crystals. **D.** Medium-grained olivine-bearing gabbronorite showing no foliation. **E.** Very weak foliation within a more coarse grained oxide bearing gabbro defined by low–aspect ratio clinopyroxene crystals. **F.** Moderate foliation within medium-grained oxide olivine gabbro defined by low–aspect ratio clinopyroxene crystals, medium–aspect ratio irregular olivine crystals, and medium–aspect ratio plagioclase crystals.

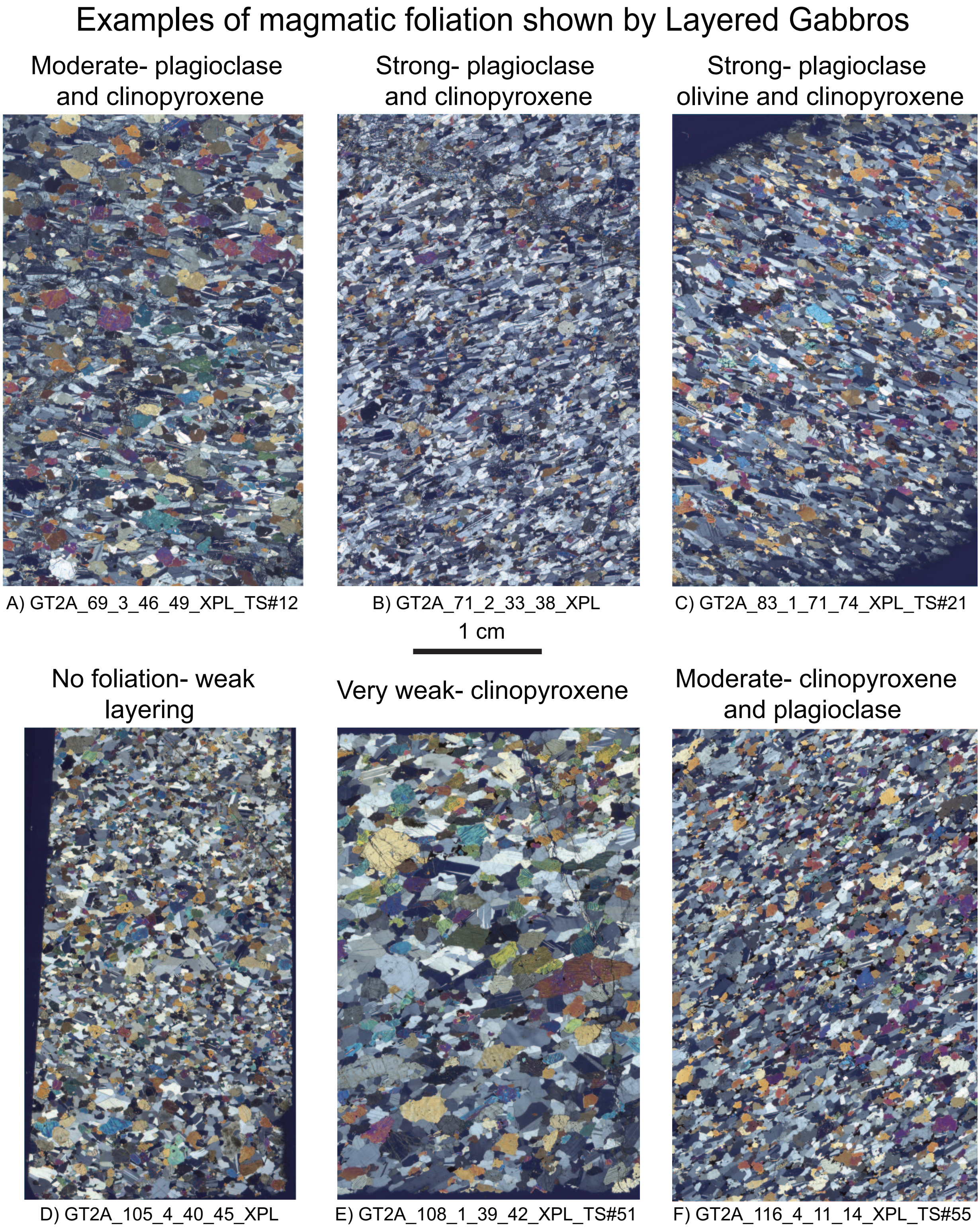

Figure F41. Truncated and crosscutting foliations within the layered gabbro sequence. **A.** Medium-grained weakly foliated olivine gabbro exhibiting steeper foliation (left-hand side) compared to the adjacent weakly banded, finer grained “tiger” olivine gabbro (right-hand side). Red arrows highlight the discordance in foliation. Red box denotes location of photomicrographs. **B, C.** Photomicrographs of the sharp planar contact between the two foliations (B: PPL; C: XPL).

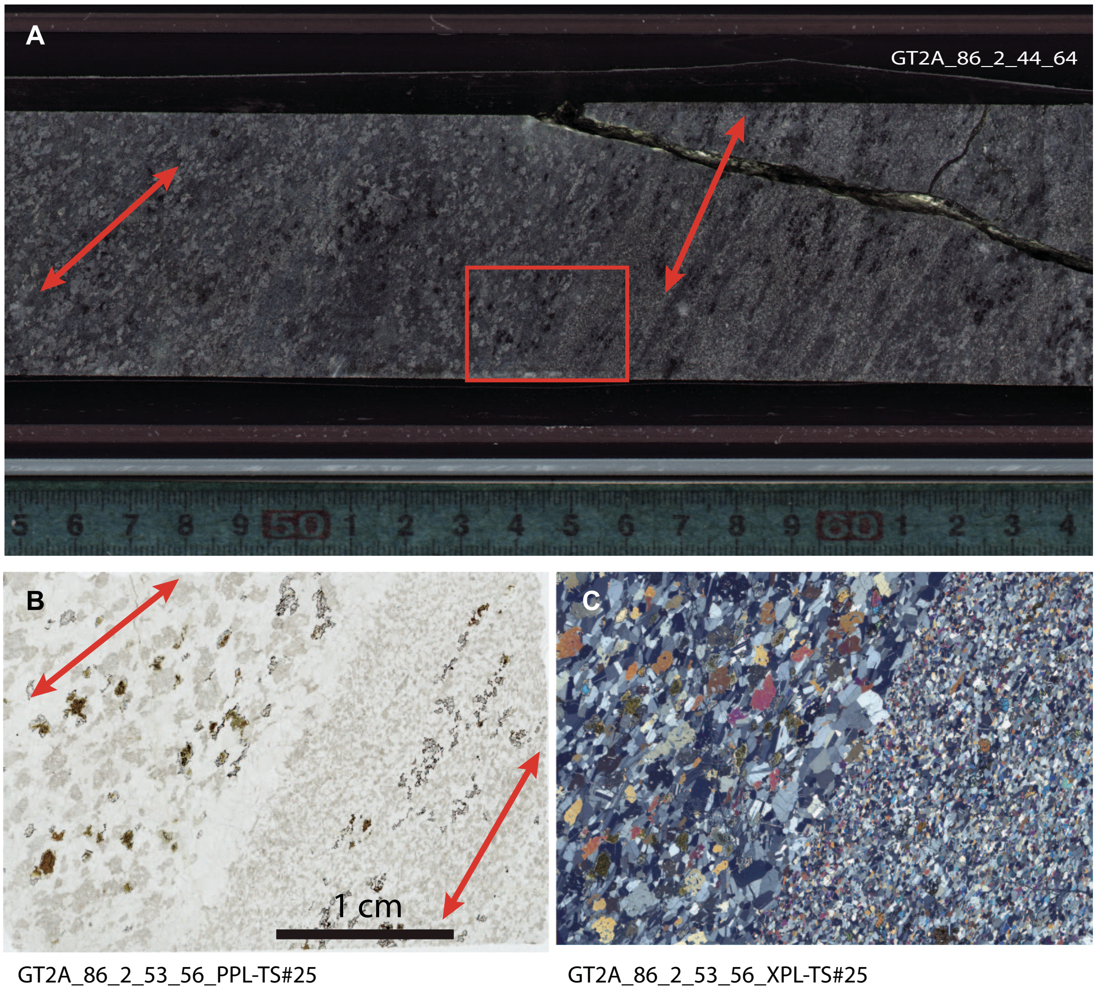

Figure F42. Variably dipping olivine foliations within a 50 cm section of core from the layered gabbro sequence. Red arrows highlight the variably dipping foliation within the various layers of olivine gabbro.

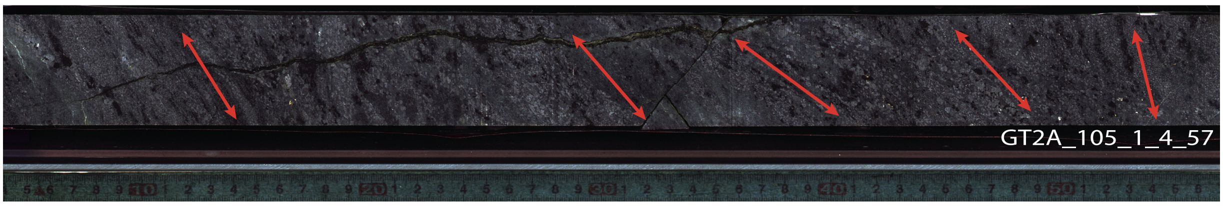

Figure F43. Folding and shearing of olivine foliations within olivine gabbros in the layered and transition sequences. **A.** Gently folded and "sheared" olivine foliation within olivine gabbro from the layered gabbro sequence. **B.** Relatively sharply folded olivine foliation within olivine gabbro in the layered olivine gabbro sequence. **C, D.** Photomicrographs of fine-grained foliated olivine gabbro wrapping around a more coarse grained pocket of more coarse grained gabbro from the transition zone (C: PPL; D: XPL).

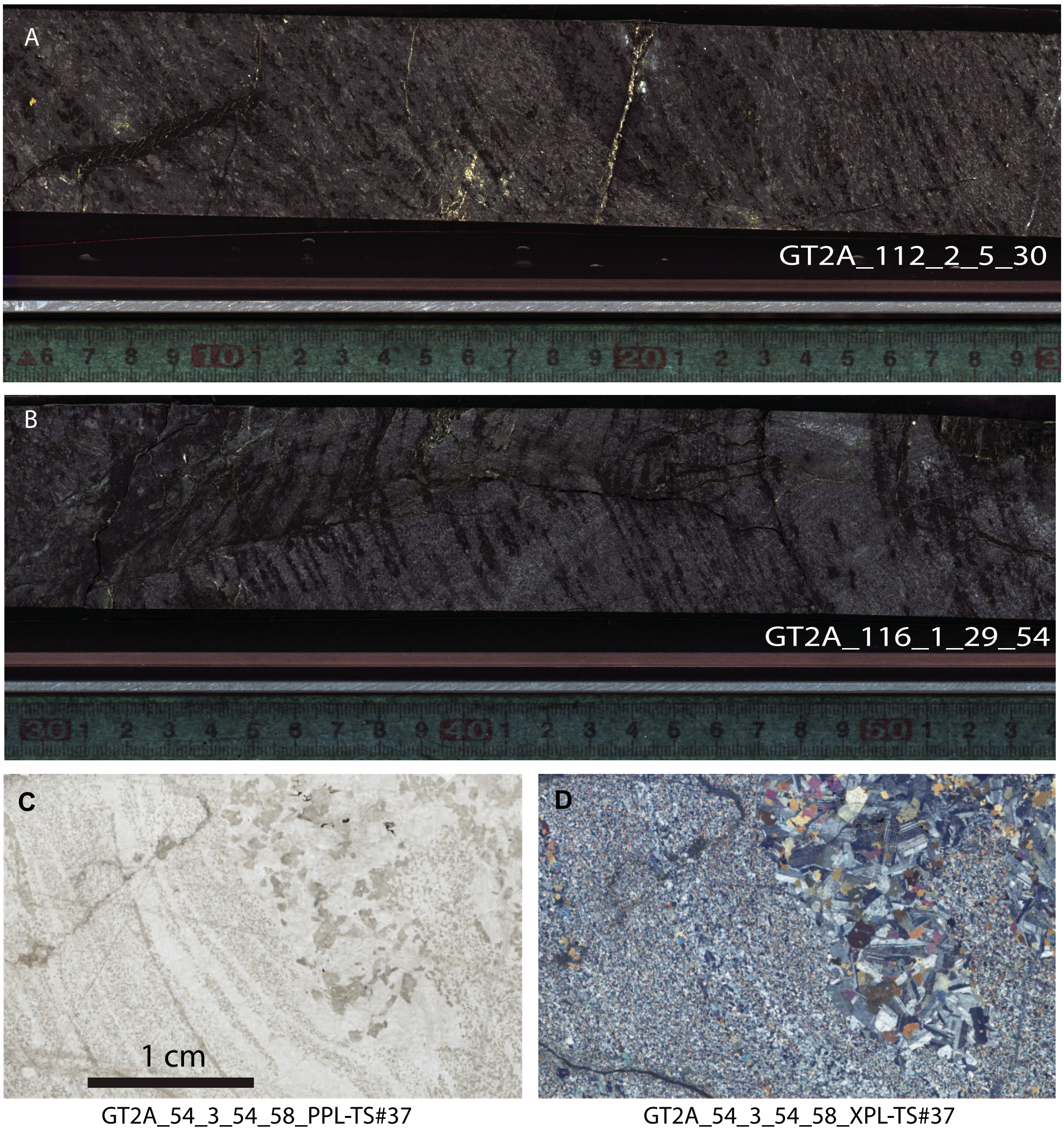

Figure F44. Lithologic column showing igneous units and the measured dip of the magmatic contacts, layering, and foliation downcore (NB, dip angles are in the core reference frame).

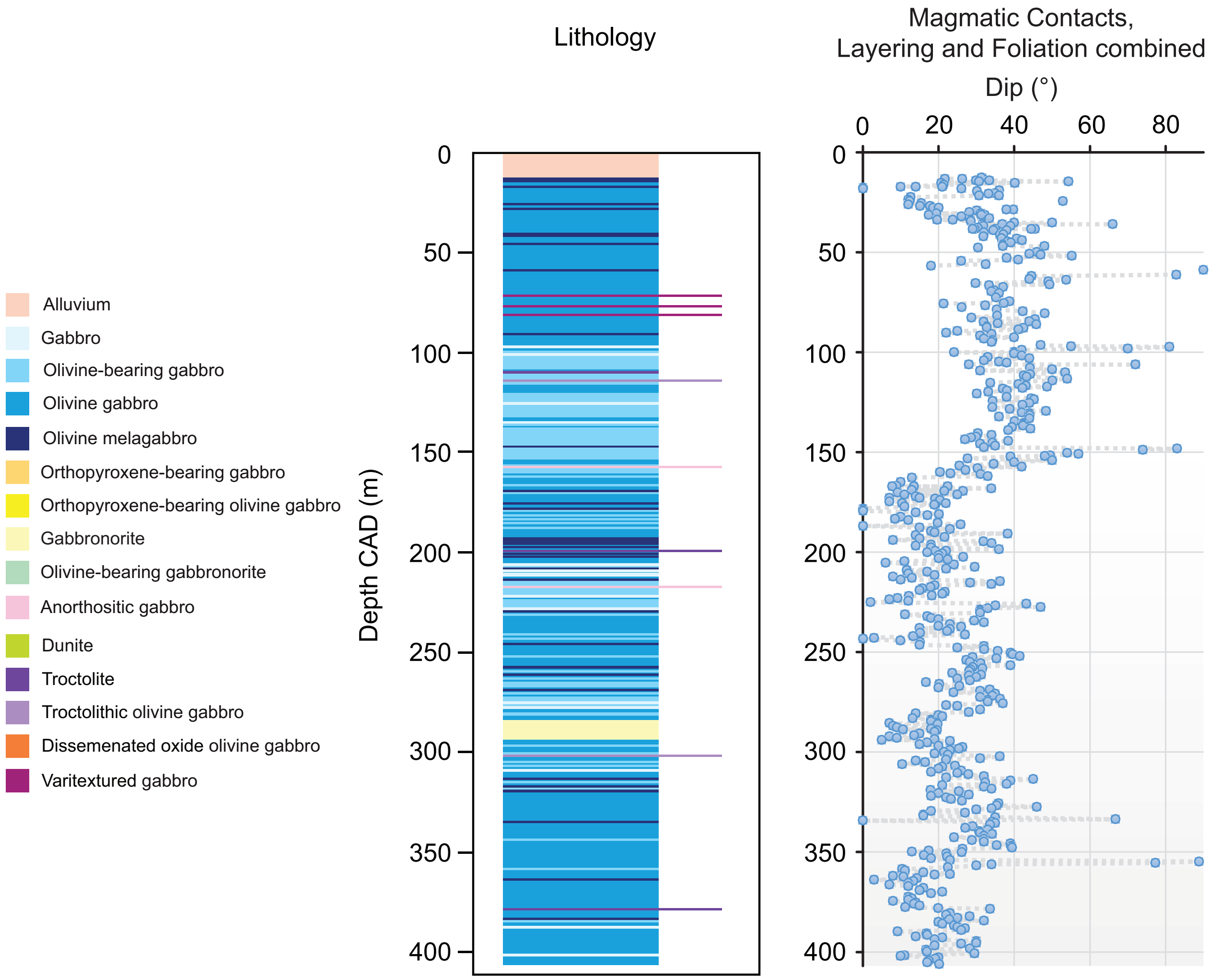

Figure F45. Local rotation of the olivine foliation to steeply dipping (>50°) by brittle faulting (green arrows). Orientation of the foliation is shown by red arrows. **A.** Olivine foliation steepens to 72° as the brittle fault zone at ~106.5 m CAD is approached. **B.** 70° dipping olivine foliation approaching near core perpendicular brittle fault zone at 359 m CAD. The olivine foliation is more gently dipping below the brittle fault zone. **C.** Olivine foliation (red dashed line) exhibiting a kink band due to local shearing (green arrow).

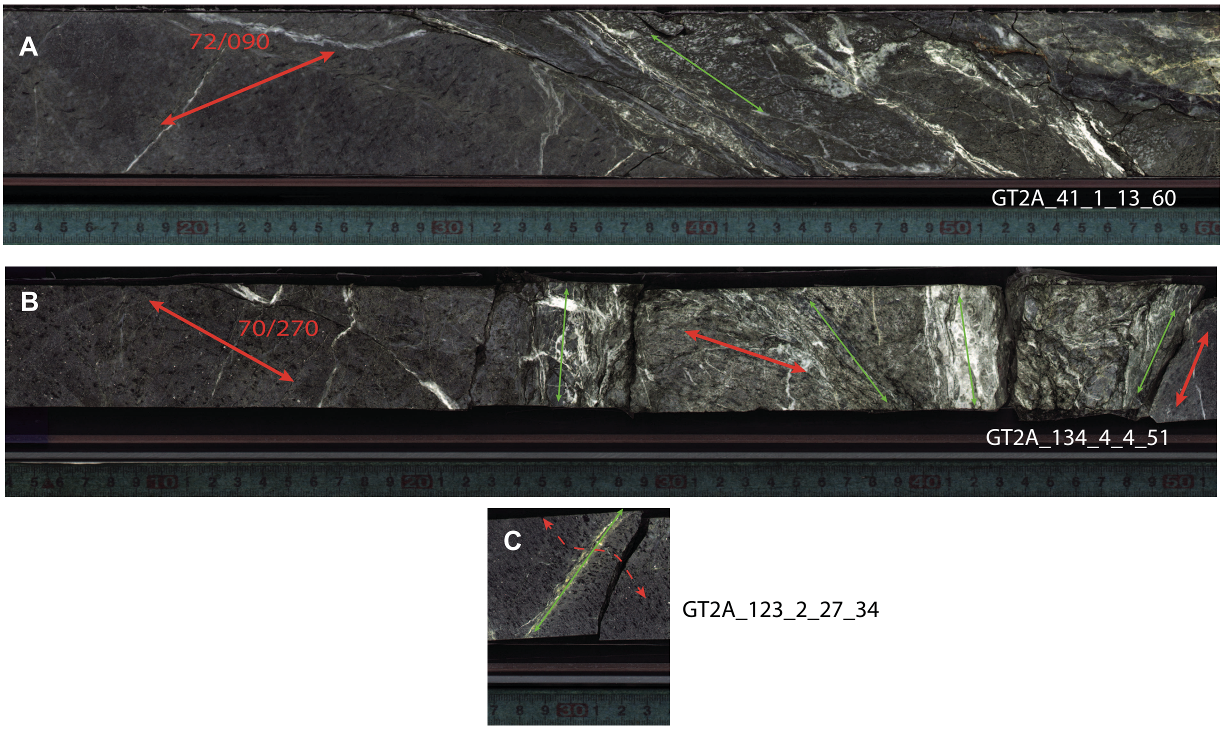

Figure F46. Lithologic column and dip of magmatic contacts, layering, and foliation and the location of major brittle fault zones (indicated by red arrows). Red lines indicate the interpreted mean variation of magmatic fabric dip vs. depth. The boundaries of the foliated gabbro, transition zone, and layered gabbro sequences are projected from the location of these boundaries as mapped at the surface.

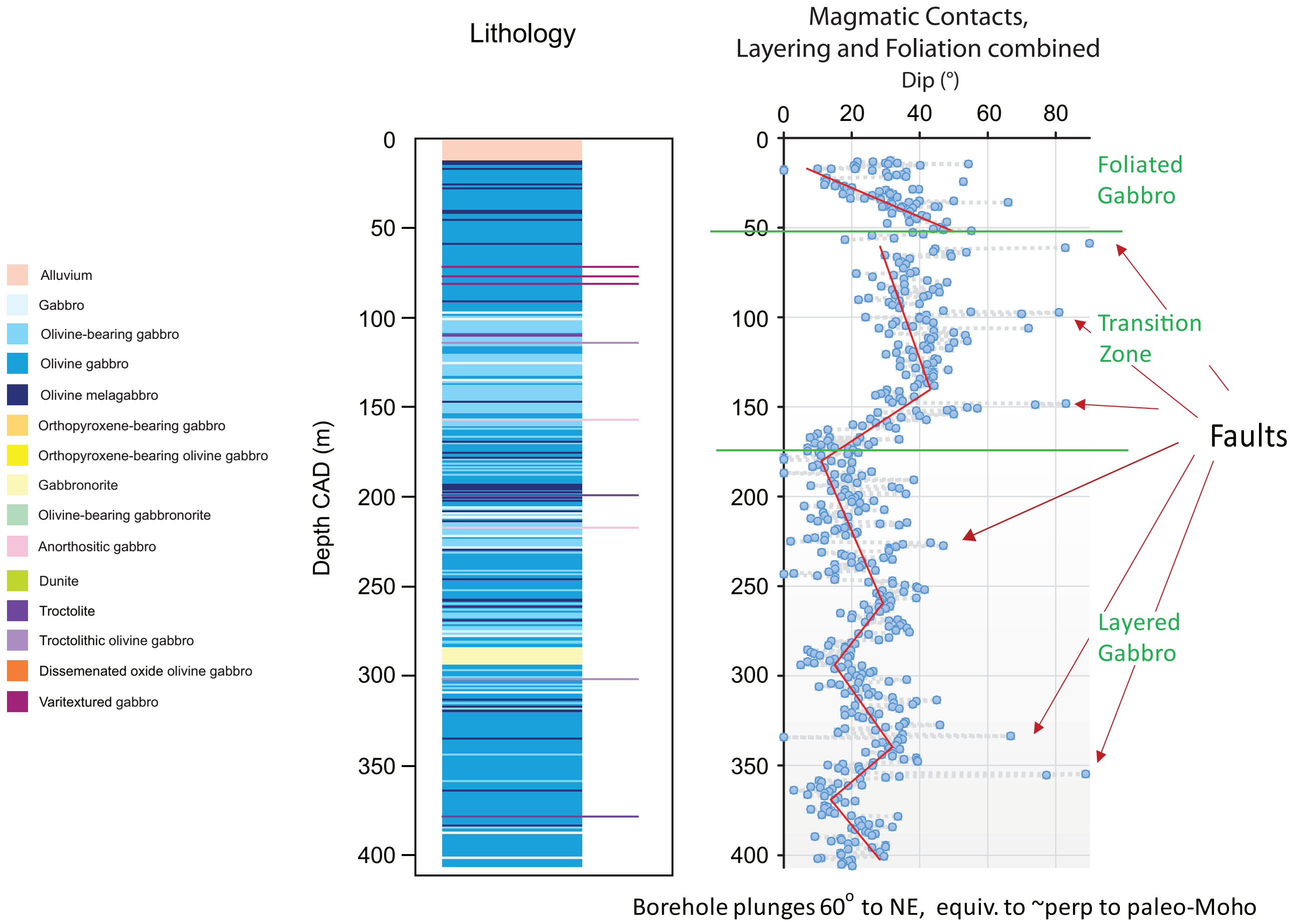

Figure F47. Brittle-plastic fabrics with incipient crystal-plastic fabrics from Hole GT2A. These zones tend to be fine-grained, altered, and overprinted by brittle structures.

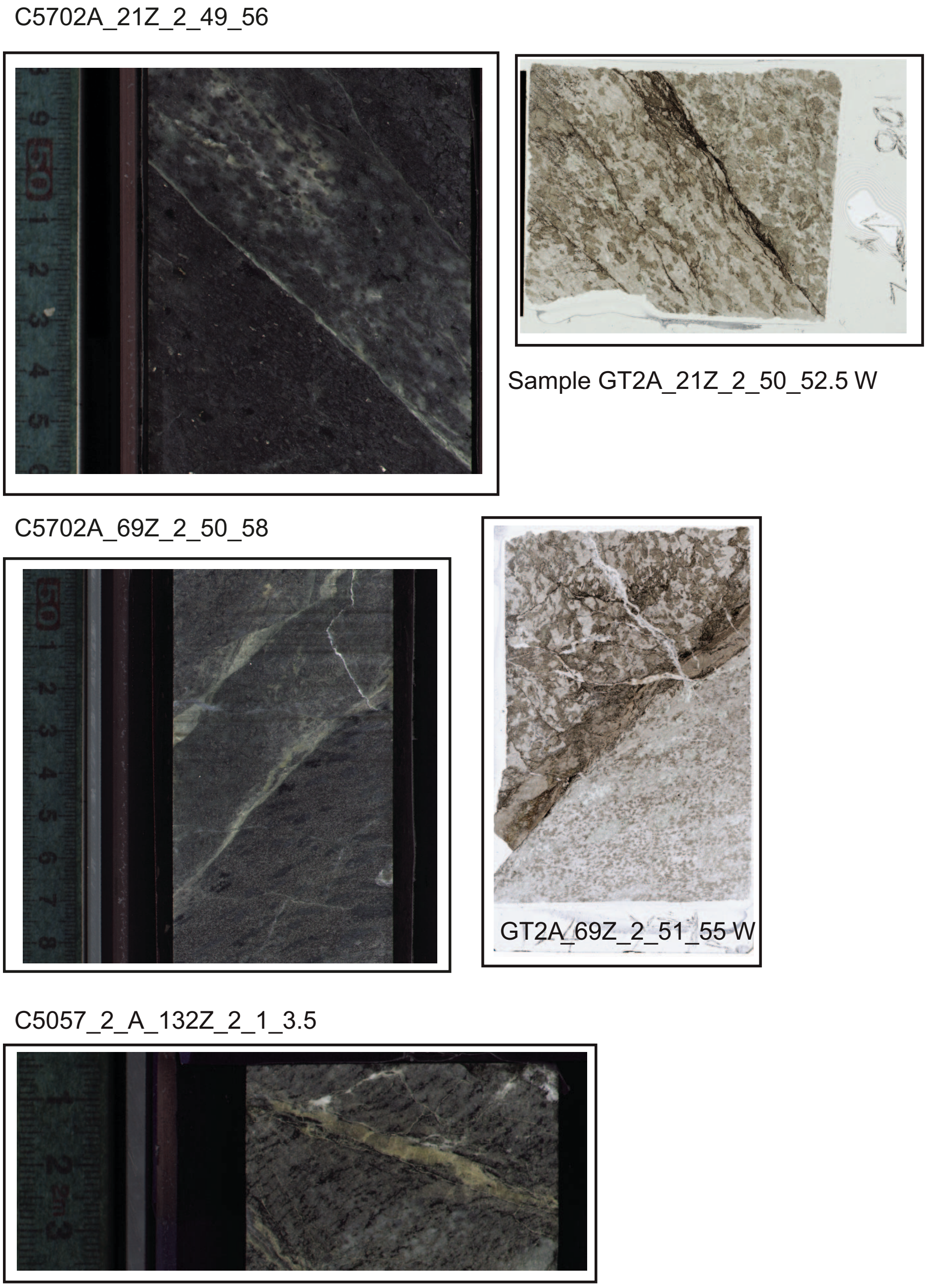

Figure F48. **A.** Downhole variations in fracturing intensity, Hole GT2A. Semiquantitative scale of the general fracturing intensity per each section (i.e., intensity per ~1 m of core): Slight = ~5%–10%, Moderate = 10%–40%, High = 40%–70%, Complete = 70%–100%. L = complete fracturing is localized in the section. **B.** Downhole variation in brittle fabric deformation intensity (780 structures).

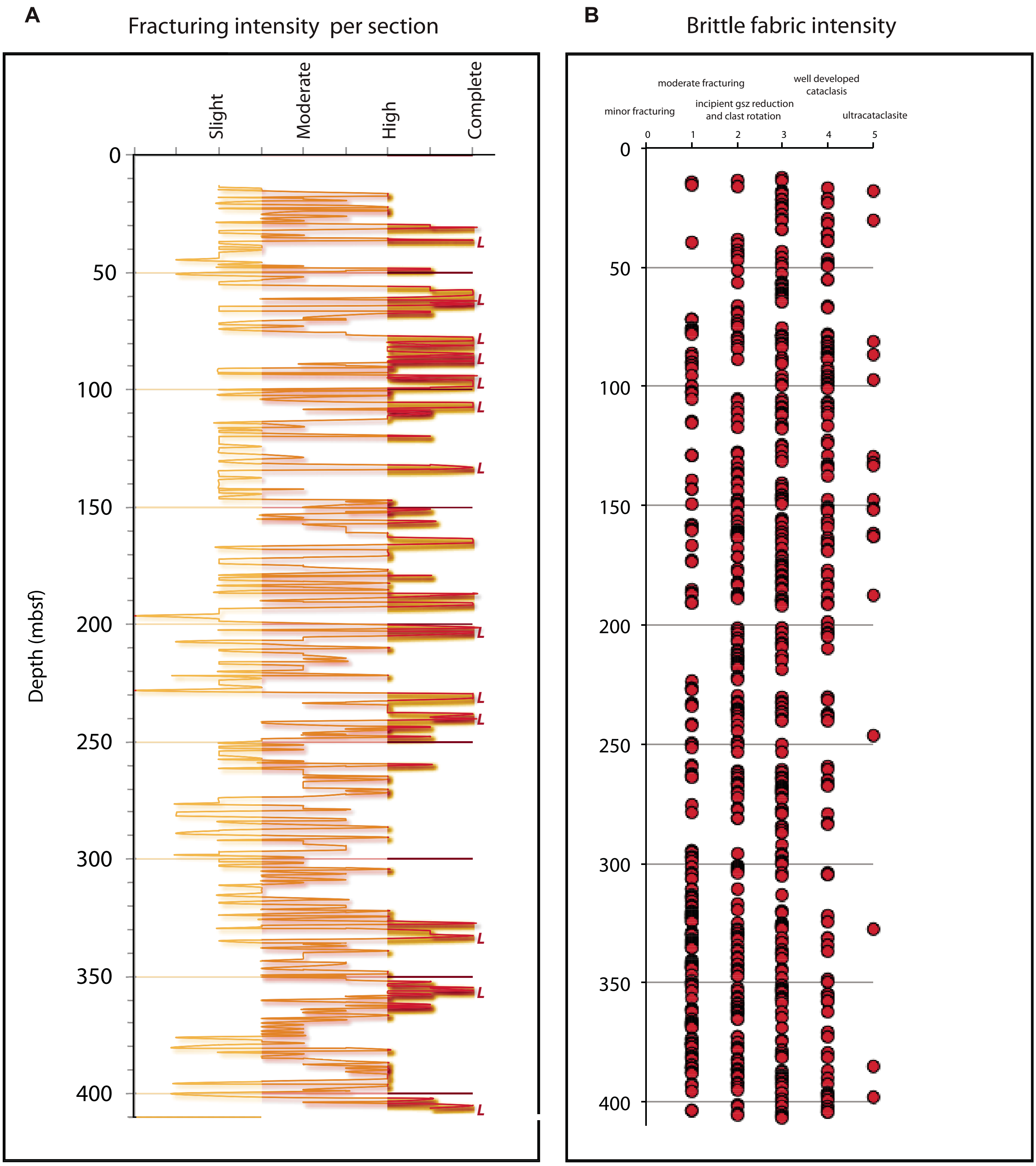

Figure F49. A. Location of logged fault zones and cataclastic zones downhole. **B.** Vertical thickness of the zones (note: thicknesses are not corrected for the features that continue across two sections). **C.** Brittle fabric deformation intensity of faults and cataclastic zones (410 structures). **D.** Preliminary interpretation of the location of main discrete fault zones.

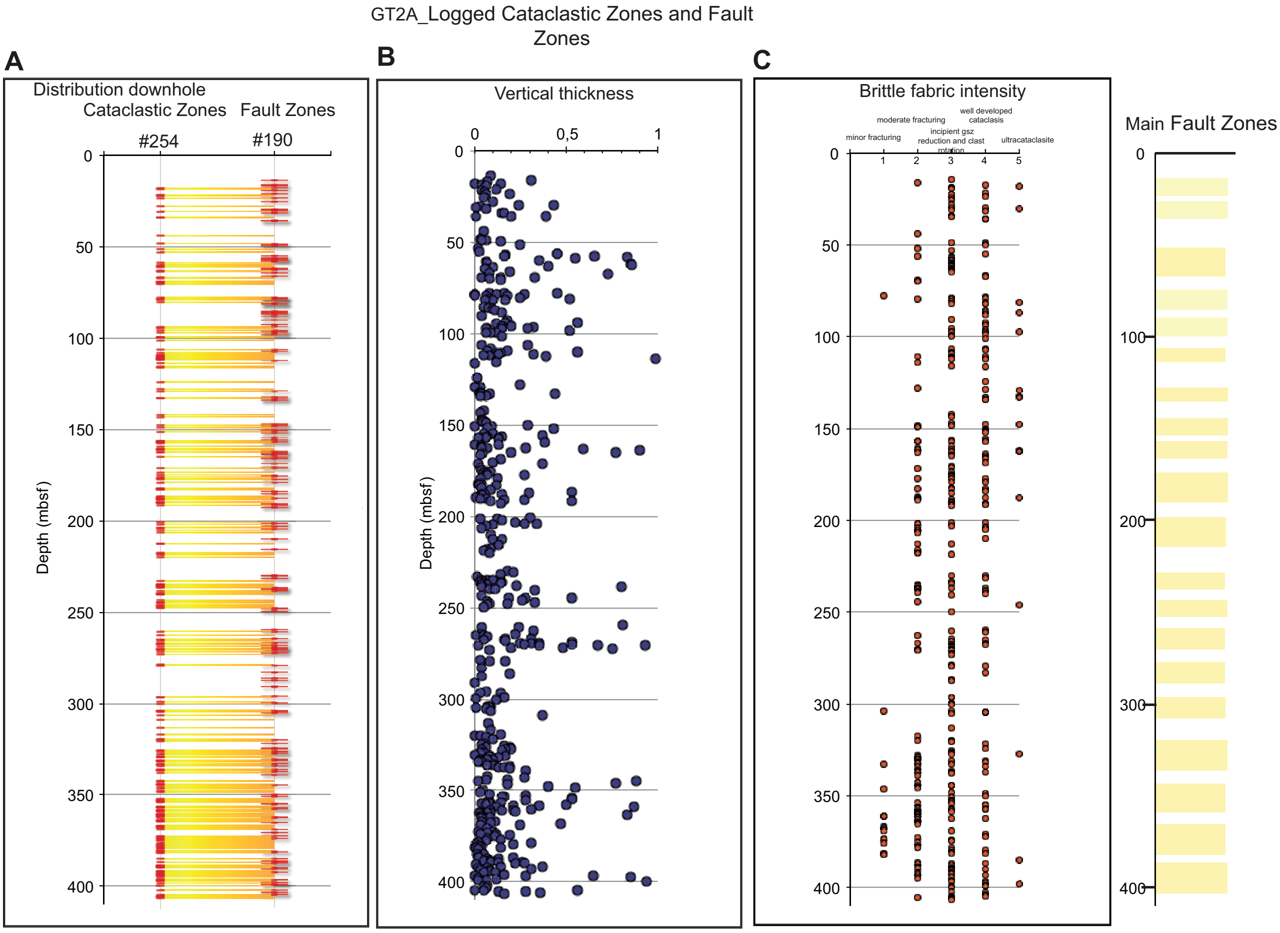

Figure F50. Complex multilayered fault zones and associated brecciated rocks, Hole GT2A.

Figure F51. Fault zones with layers of foliated cataclasite and ultracataclasite (and possibly pseudotachylite), Hole GT2A.

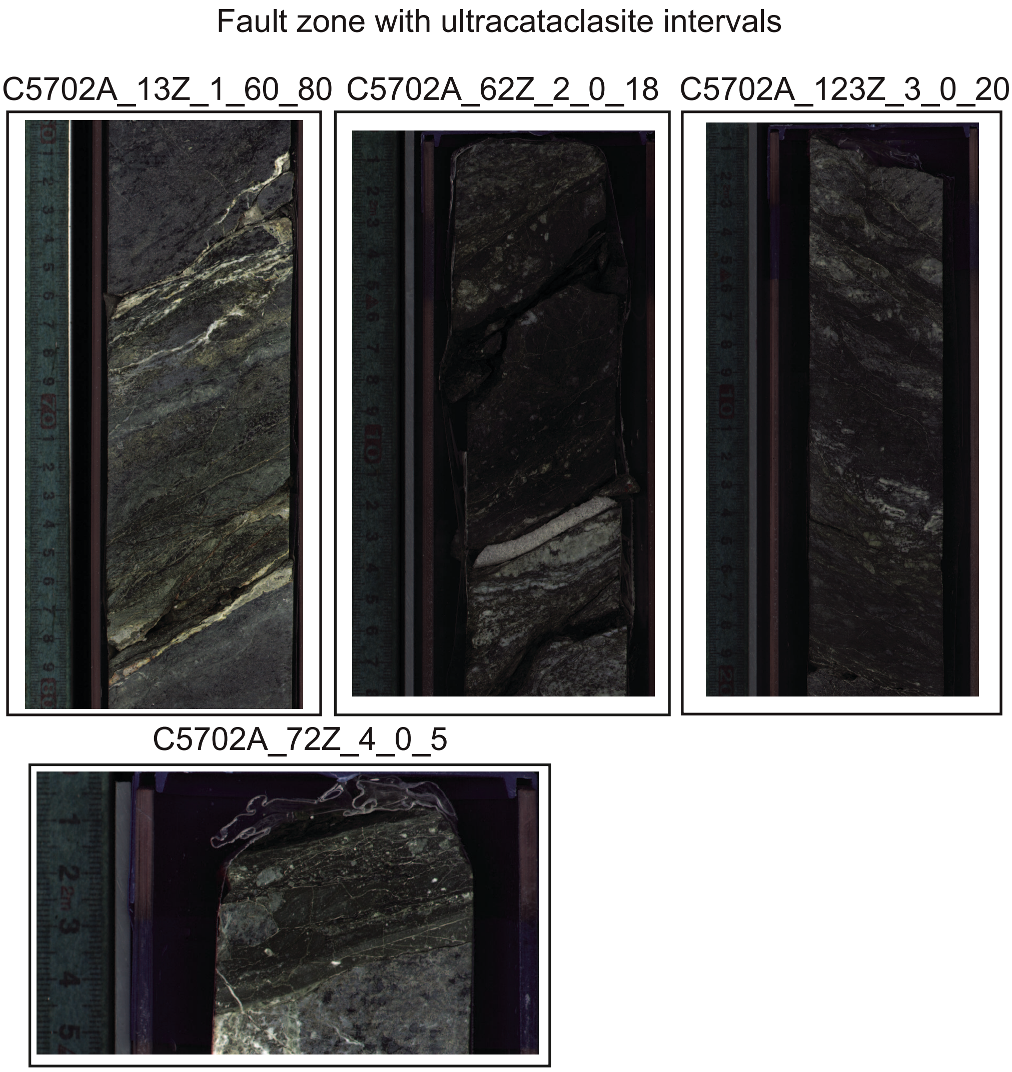

Figure F52. Fault breccias, Hole GT2A.

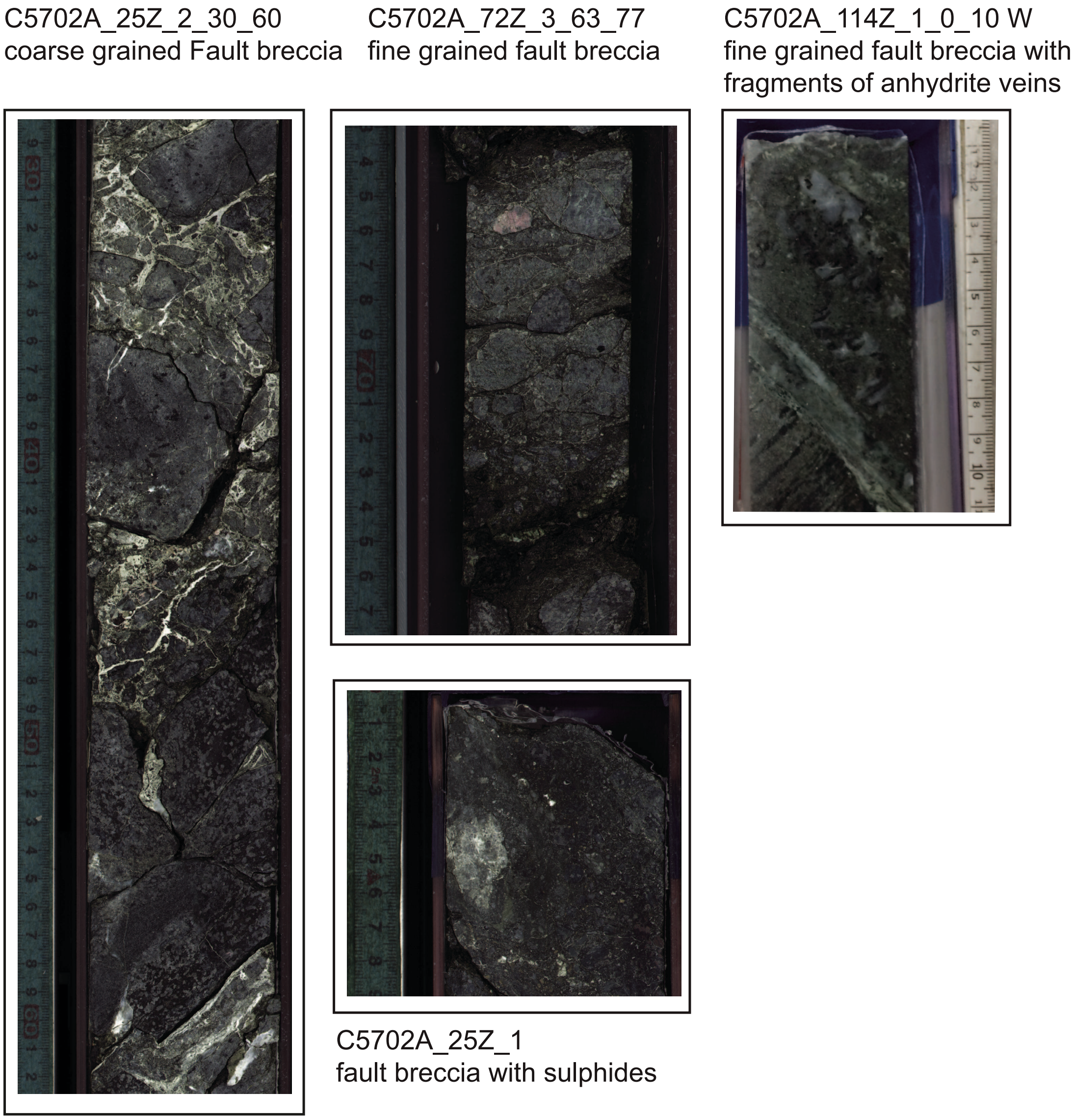

Figure F53. Hydrothermal breccias (epidotized and silicified), Hole GT2A.

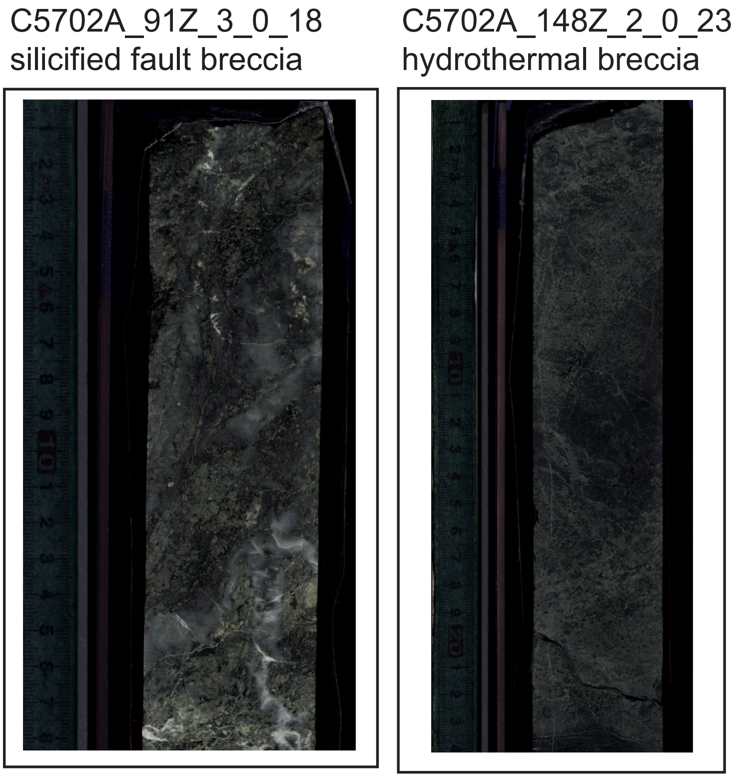

Figure F54. Altered and deformed ultramafic layers rich in secondary chlorite, serpentine, amphibole, and sulfide minerals. These examples display moderate to intense deformation, with a variety of structures that grade from protomylonitic S-C fabrics to a semicohesive scaly fabric.

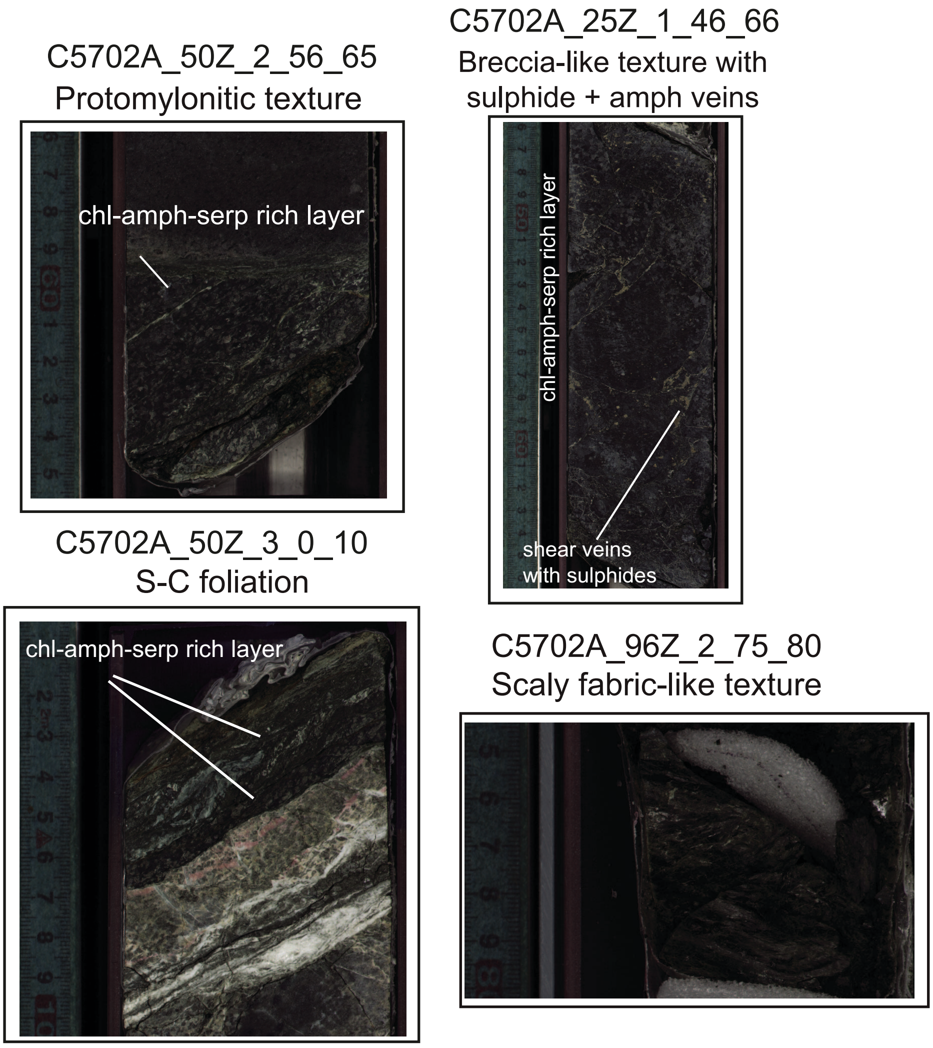

Figure F55. A. Shear sense indicators from 171 shear fractures in fault zones showing both normal and reverse senses of shear. **B.** Mean value of dip angle of fault zones in the CRF is ~45° (ranging 30°–60°).

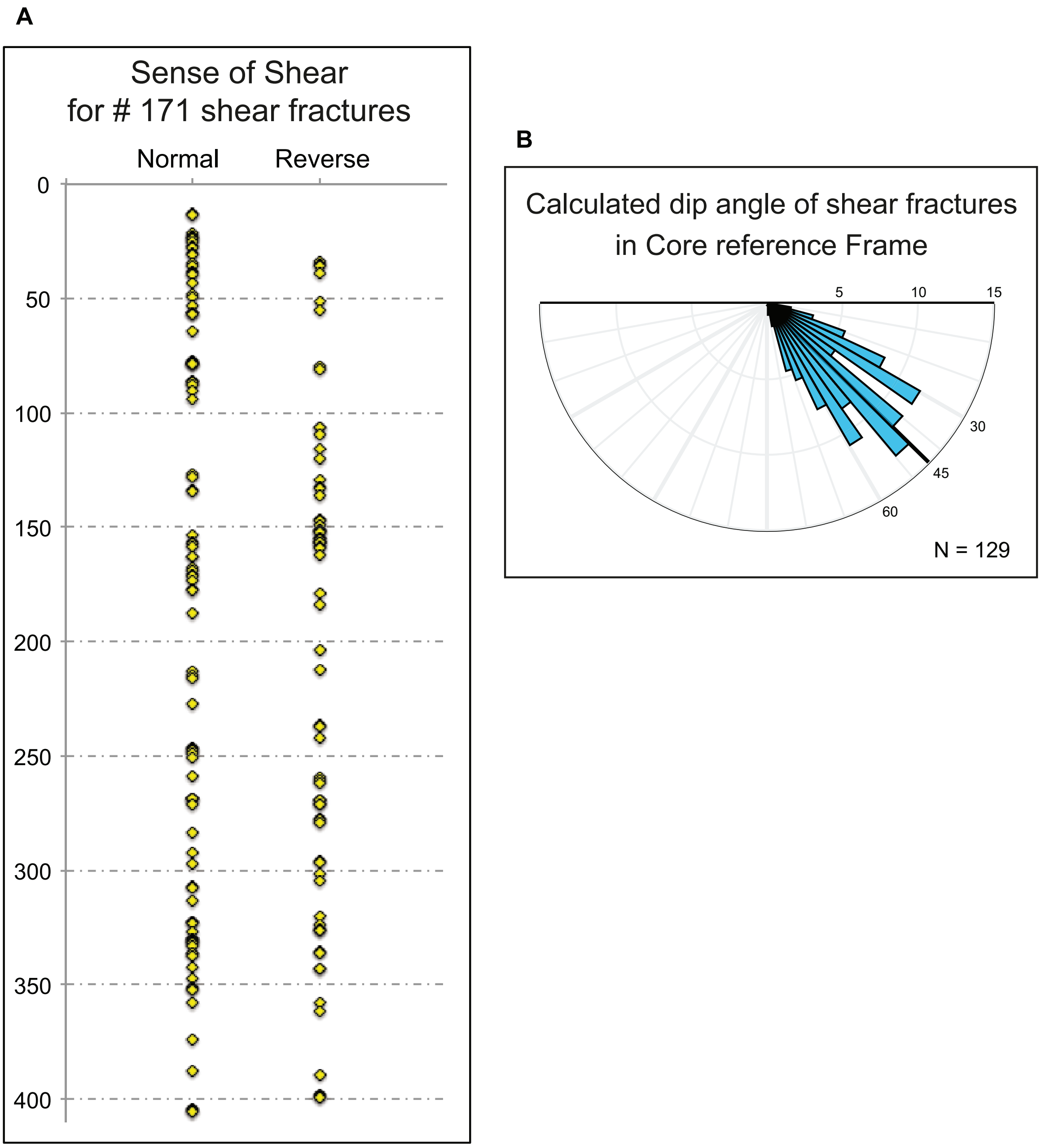

Figure F56. Logged kinematic indicators. **A.** Normal sense of shear. **B.** Structures with superimposed senses of shear.

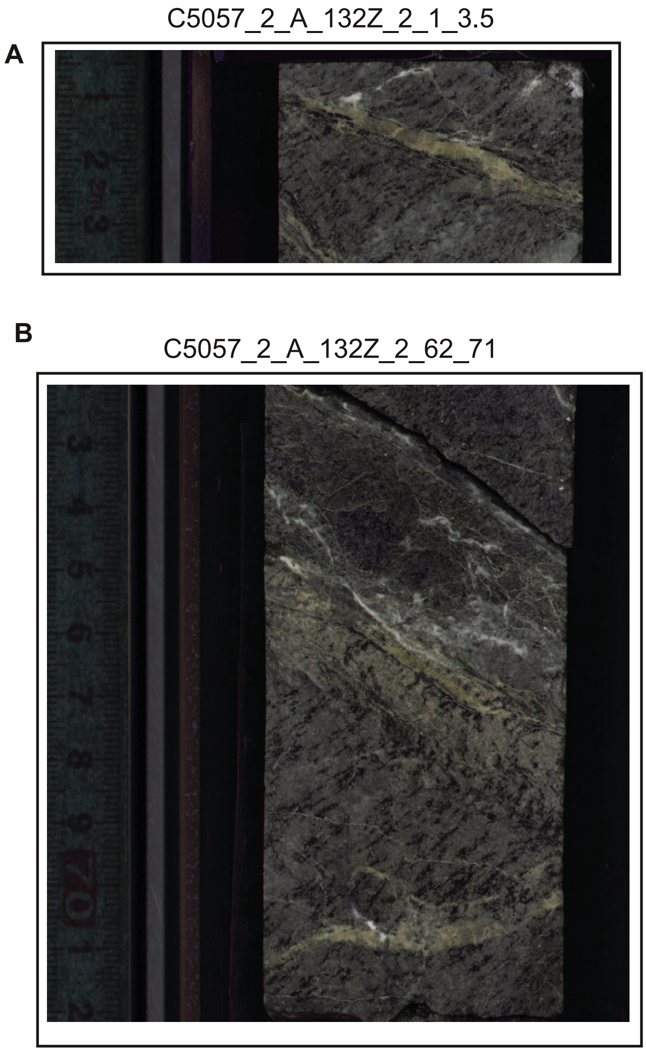

Figure F57. CT (left) and image (right) scans. Magmatic foliation above the fault is subvertical and rotates into the fault zone, indicating a reverse sense of shear. Below the fault zone the magmatic fabric has a moderate to gentle dip, similar to the dip of magmatic fabric farther away from the fault. The fault zone has the lowest CT value (i.e., darker) and therefore is most likely altered and potentially porous. The gabbro above the fault also has a lower CT value, indicating alteration of the hanging wall. The gabbro below the fault has the highest CT value, suggesting it is not as altered and did not deform brittlely during faulting.

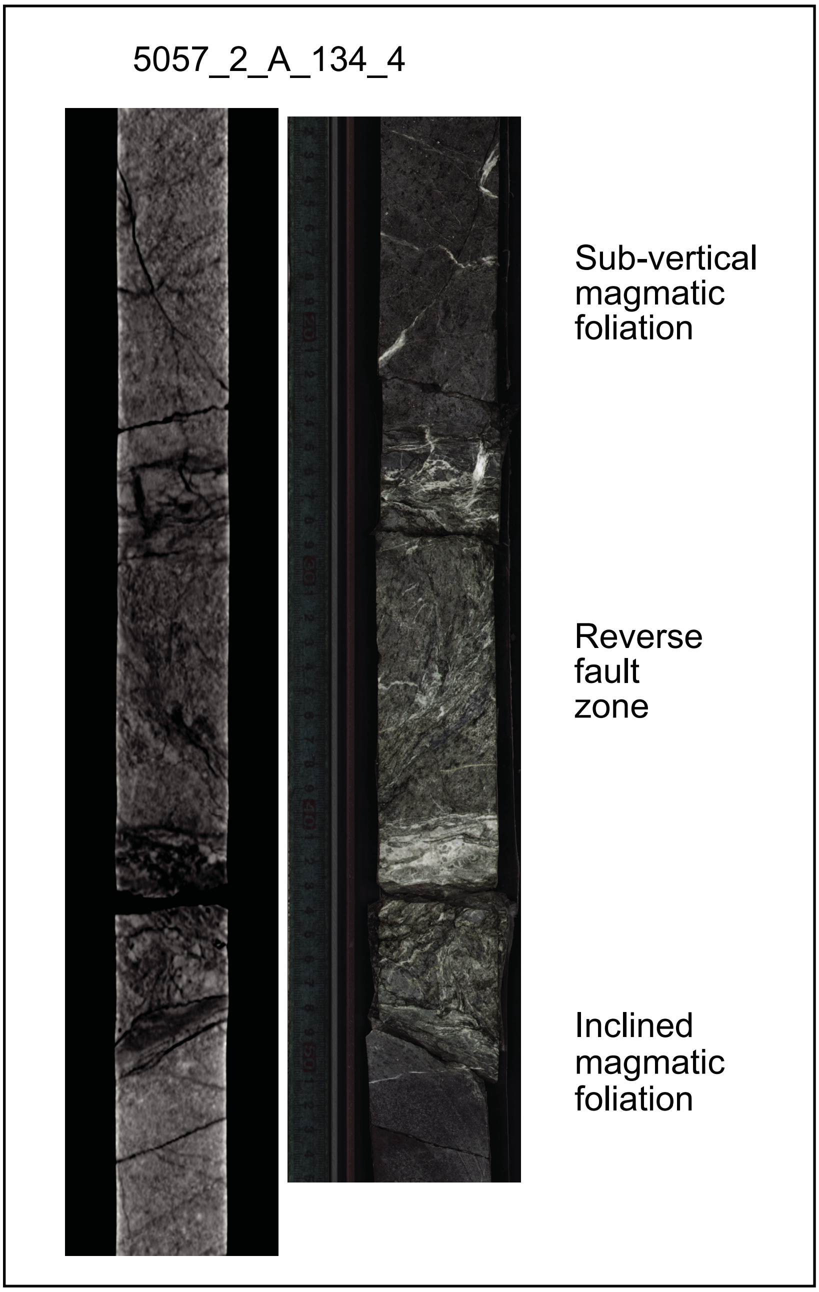

Figure F58. **A.** Dip of veins with depth. **B.** Histogram of dips.

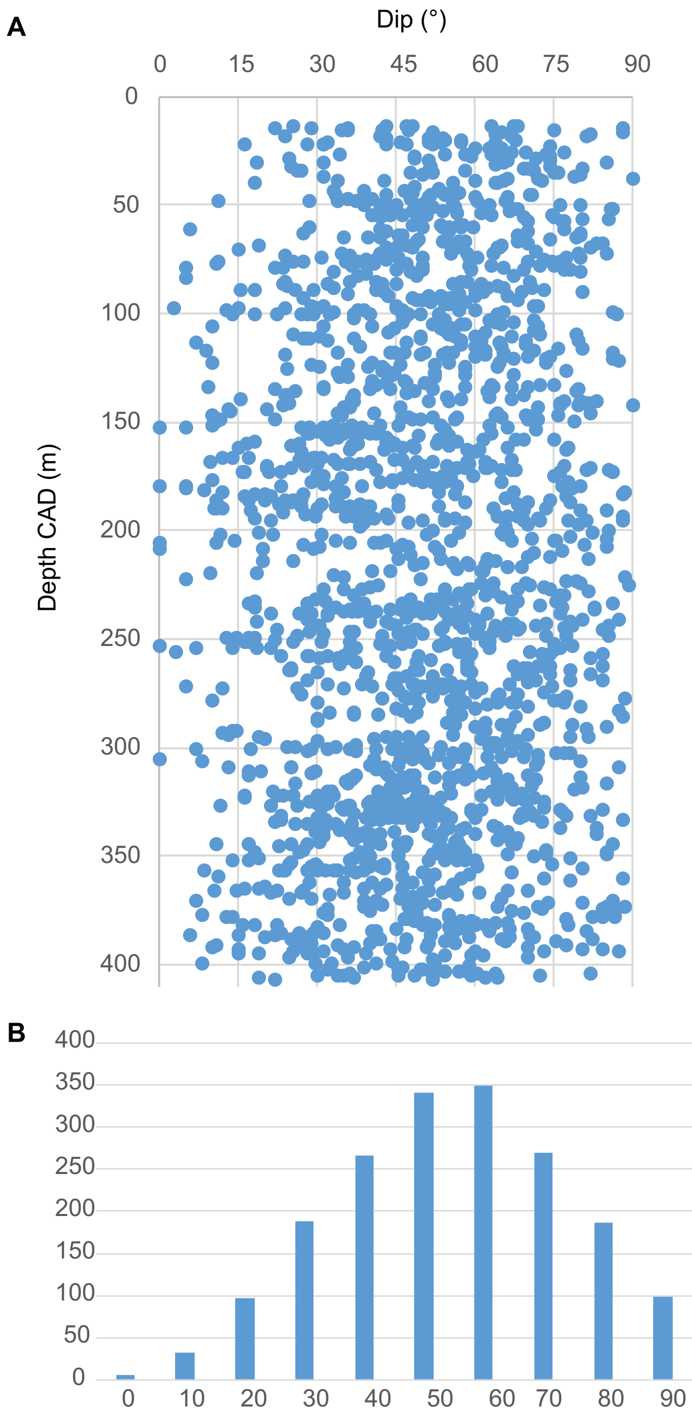

Figure F59. Histograms of true dips (relative to the CRF) organized by the mineralogy of the vein fill, amphibole, epidote, chlorite, prehnite, laumontite, and quartz. The vein fill is considered of that type of vein if it contains 50% or more of that mineral. n = number of veins measured.

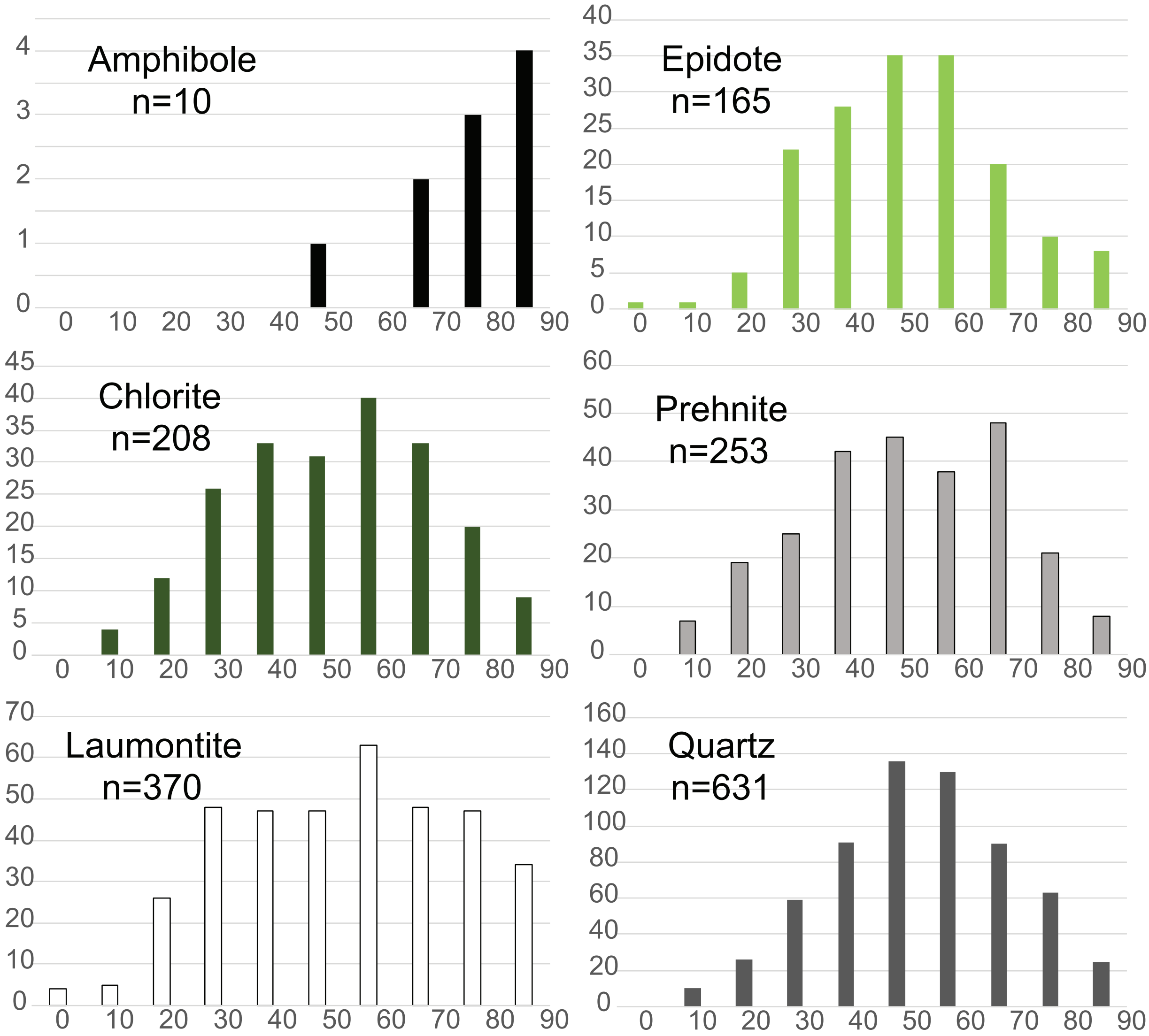

Figure F60. **A.** Plunge of slickenfibers with shear sense indicated if it was identified. **B.** Angular difference between the dip and the plunge. **C.** Plunge plotted against dip. Many slickenfibers have a plunge <15° and indicate oblique-slip.

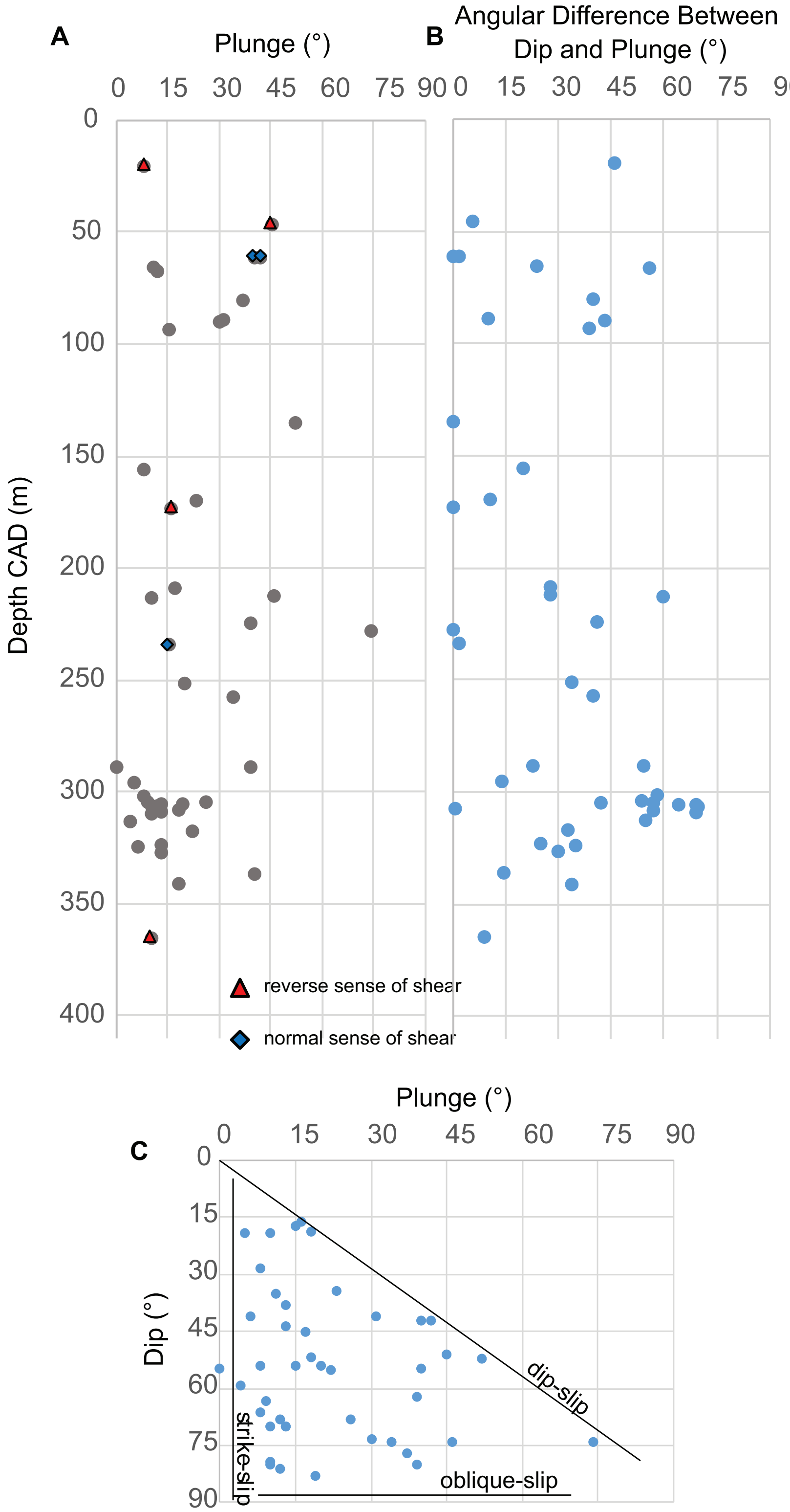

Figure F61. Shear sense indicators in veins including slickenfibers along slickensides and pull-apart veins. Both normal and reverse sense of shear indicators occur throughout the drilled interval. Normal and reverse shear sense indicators tend to occur over similar intervals, although there are a few intervals with only one shear sense (e.g., normal shear at 225–275 m and below 375 m).

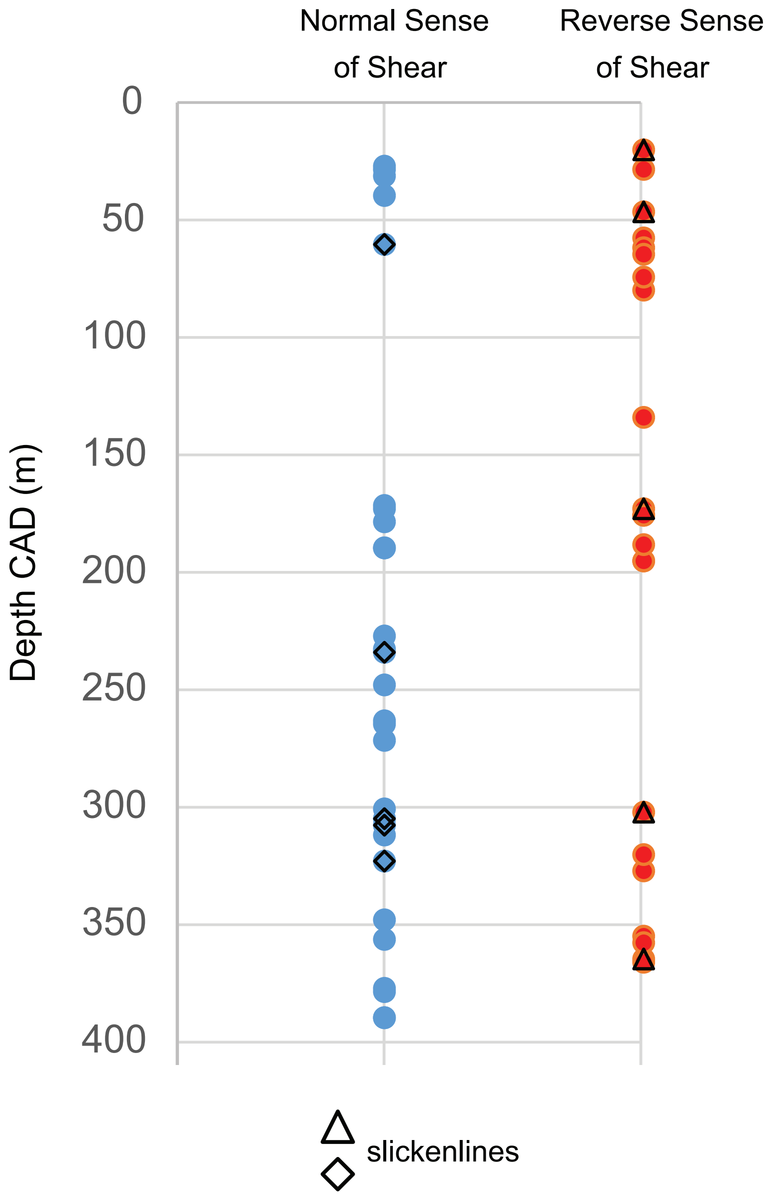

Figure F62. Examples of crosscutting relationships in veins. **A.** Clinozoisite (pink) and epidote (green) vein crosscut by a prehnite/laumontite vein (white). Sense of shear could not be determined. **B.** Quartz vein crosscut by a normal sense shear vein filled with laumontite. **C.** Epidote (yellowish green) crosscut by a reverse sense shear vein filled with quartz. **D.** Clinozoisite vein offset by both normal and reverse sense shear veins filled with laumontite.

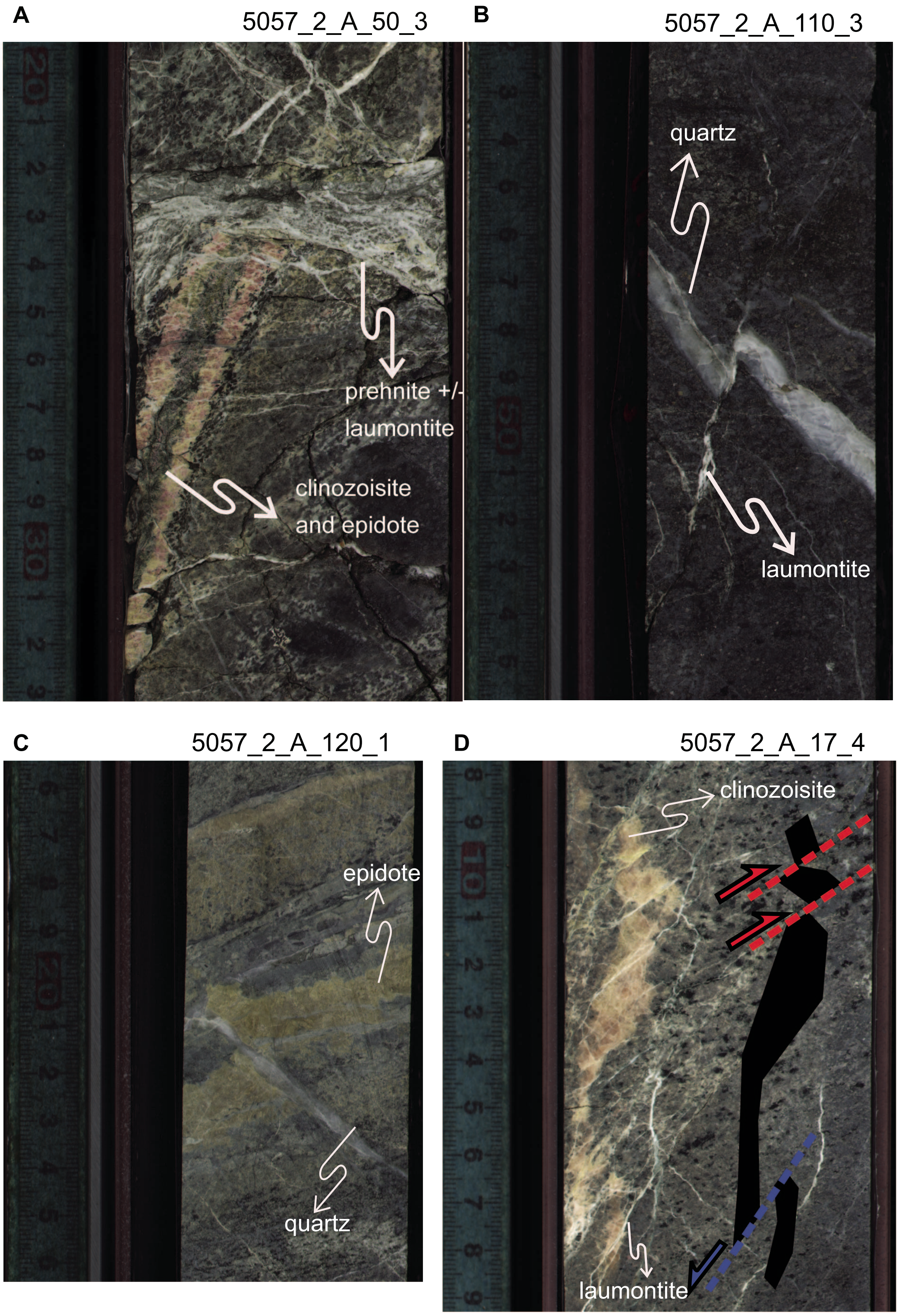

Figure F63. Geochemistry of rocks from Hole GT2A differentiated by rock type as logged and compared to those from Hole GT1A; Mg# vs. Ca#; Mg# vs. Cr; Mg# vs. Y; Mg# vs. Cr. opx = orthopyroxene. Omani lavas are plotted for comparison. Data sources: V1 magmatism (Alabaster et al., 1982; Lippard et al., 1986; Einaudi et al., 2003; Godard et al., 2003, 2006; Kusano et al., 2012, 2017; MacLeod et al., 2013) and sheeted dike complex (Miyashita et al., 2003; Umino et al., 2003; MacLeod et al., 2013).

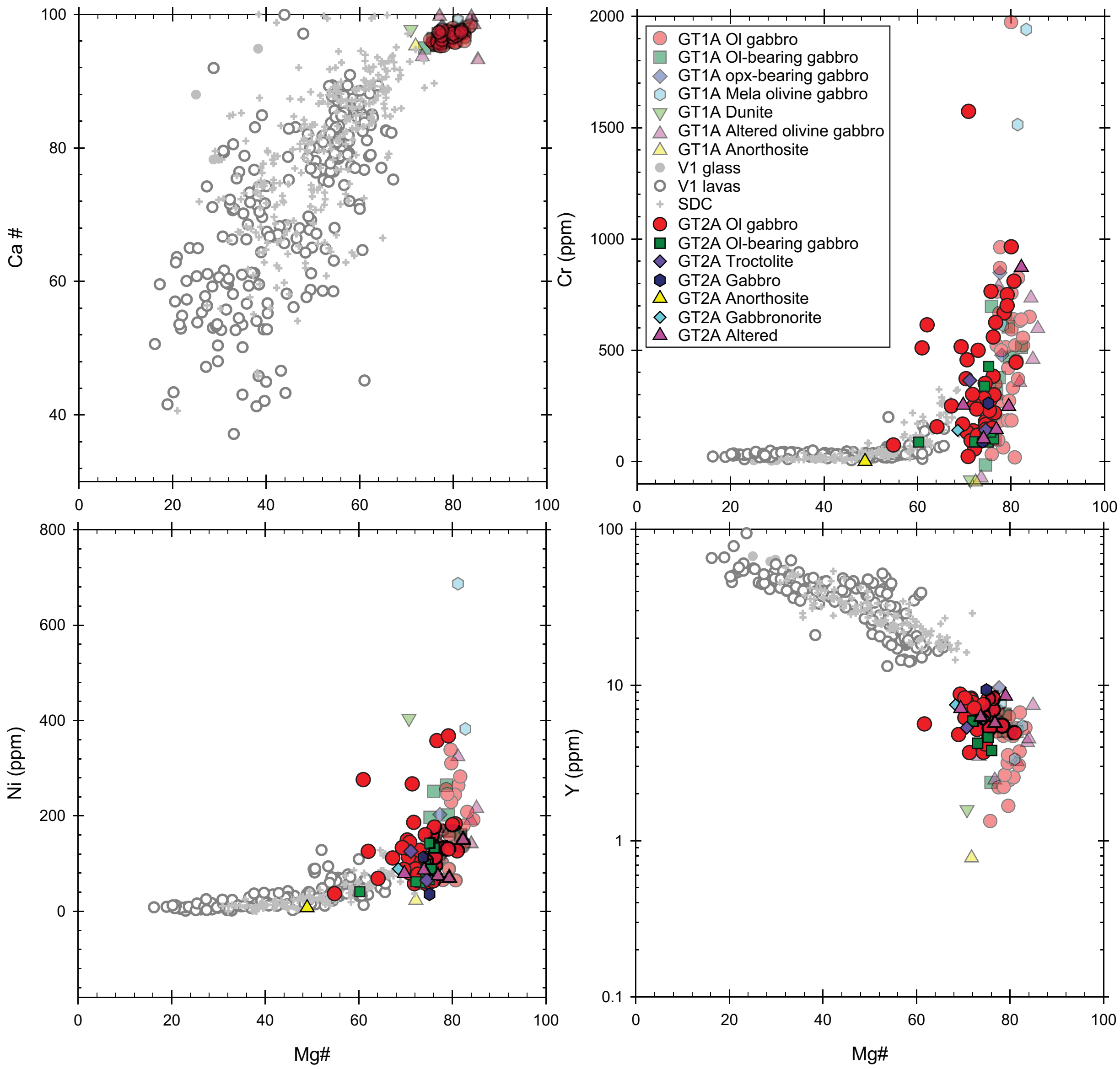

Figure F64. CaO and Al_2O_3 vs. MgO for lithologies recovered in Hole GT2A and Hole GT1A. Bulk crustal estimates and parental magma composition after Pallister (1984). Mineral chemistry data from Pallister and Hopson (1981), plagioclases plotted range from An64.5 to An88.3. Data sources: V1 magmatism (Alabaster et al., 1982; Lippard et al., 1986; Einaudi et al., 2003; Godard et al., 2003, 2006; Kusano et al., 2012, 2017; MacLeod et al., 2013) and sheeted dike complex (Miyashita et al., 2003; Umino et al., 2003; MacLeod et al., 2013). V1 fractionation path at 0.4% H_2O modeled using rhyoliteMELTS with similar parameters used by MacLeod et al., 2013.

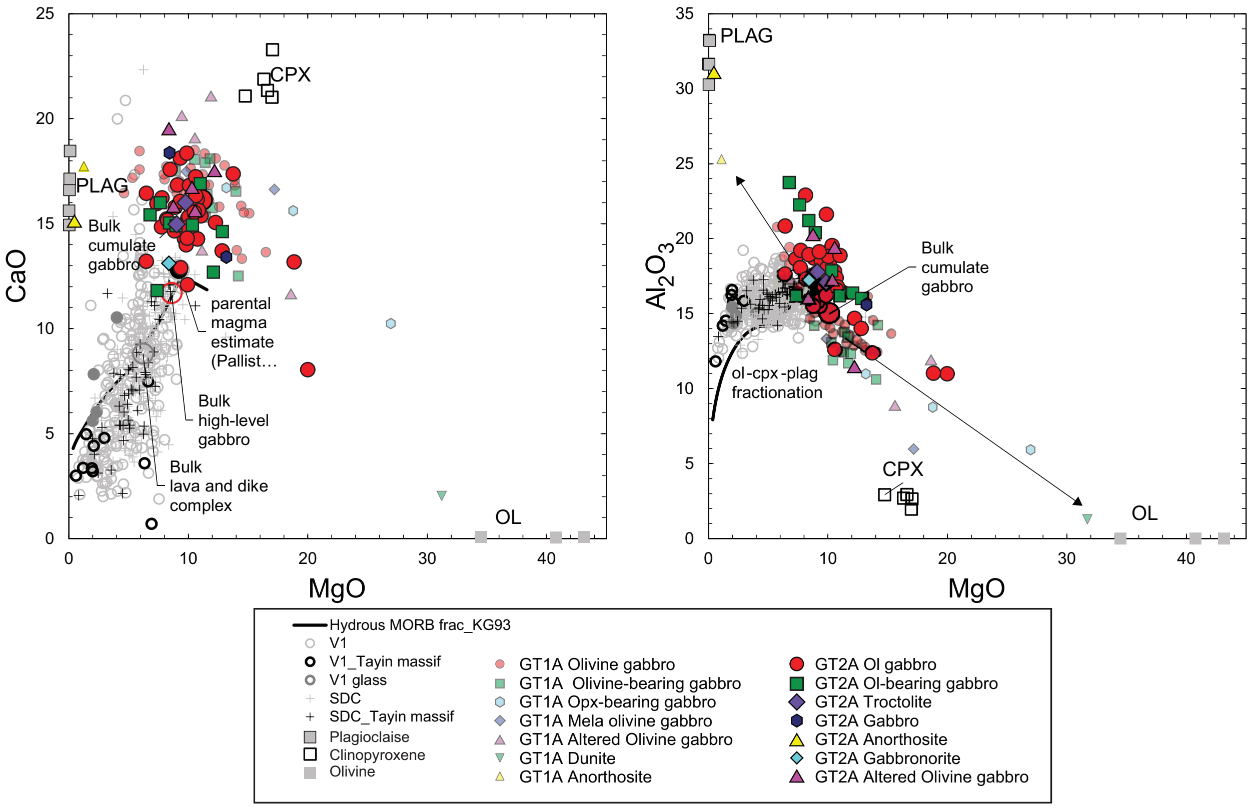

Figure F65. Trace and rare earth elements (REE) plotted normalized to primitive mantle (Hoffmann, 1988). Hole GT1A and GT2A samples have an LREE-depleted profile and are compared to V1 lavas from Oman (Einaudi, et al., 2003; Godard, et al., 2003) that have flat primitive mantle–normalized profiles and higher REE concentrations. All gabbros have higher Sr and display a Sr anomaly that is not present in lavas.

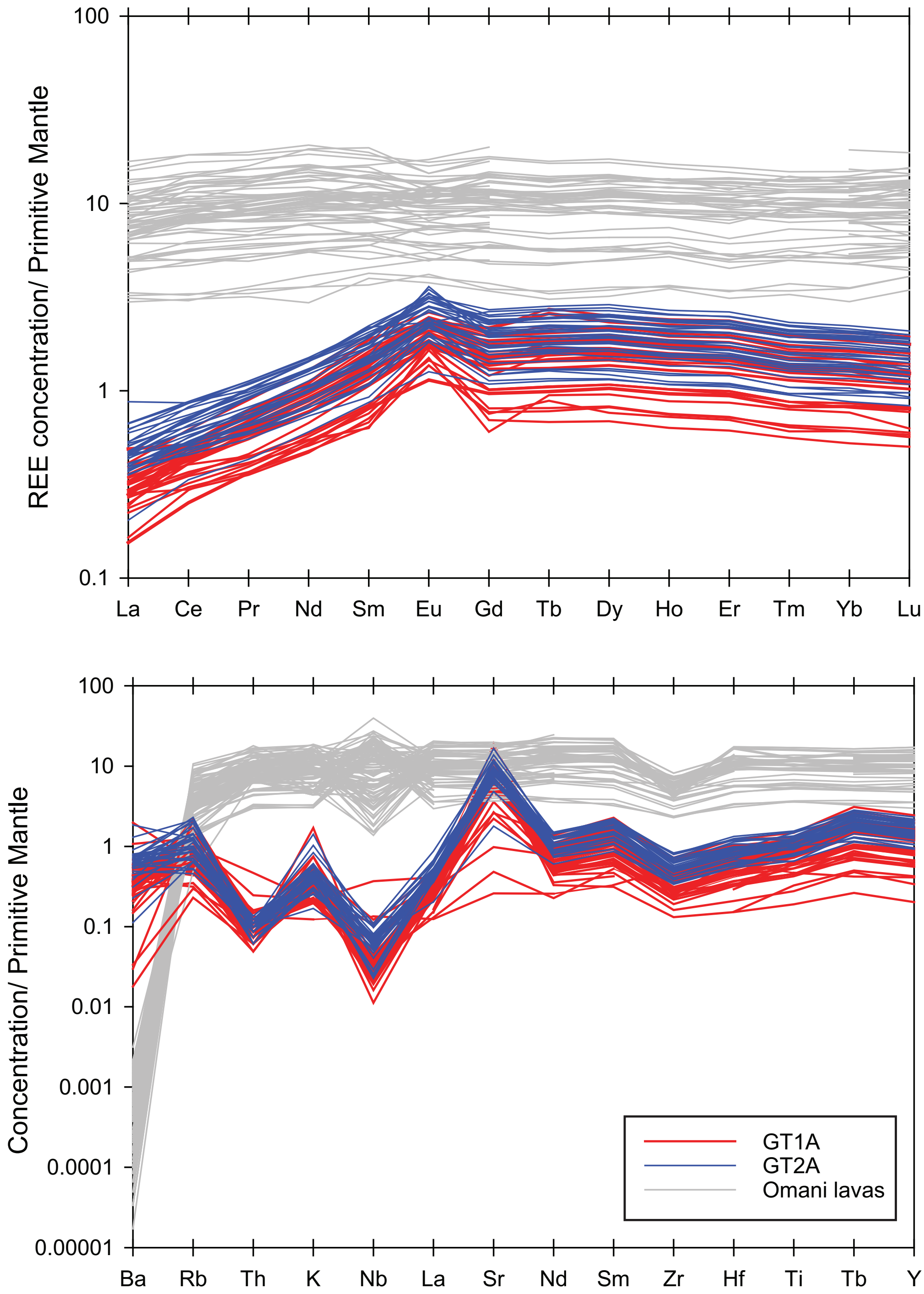

Figure F66. Ce/Sm and Eu anomalies, Holes GT1A and GT2A compared with lavas.

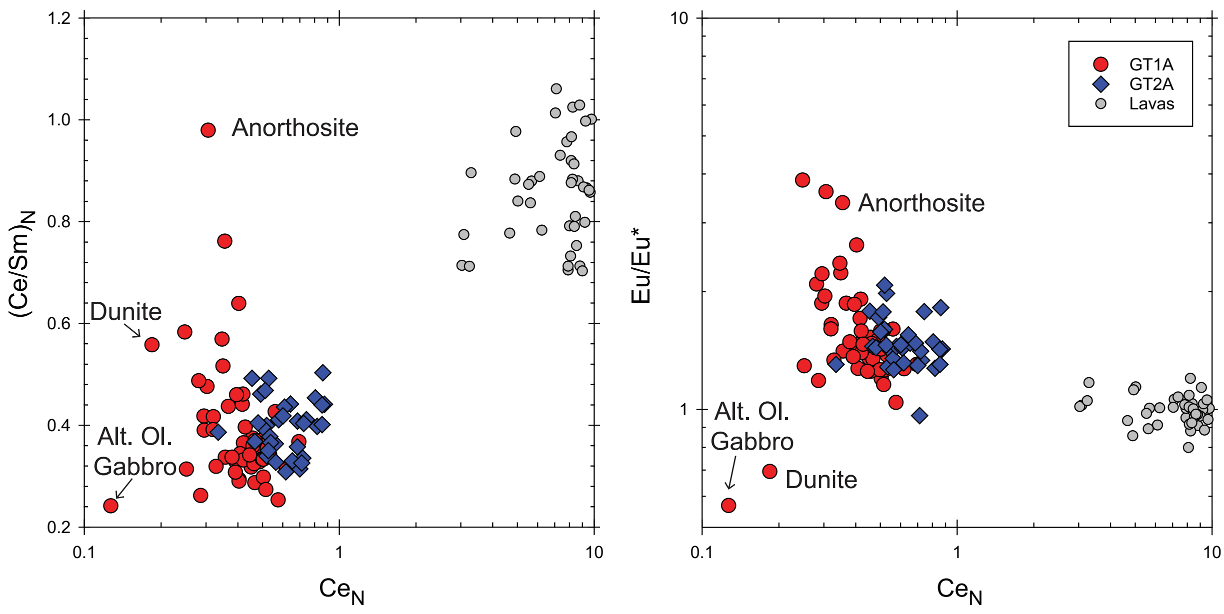

Figure F67. Downhole geochemical variation plotted with modal% olivine, plagioclase, and clinopyroxene as identified in thin section. Lithologic units defined in Igneous petrology in the **Site GT1** chapter are labeled I–VII, and their boundary lines are labeled with the depths of the contacts. Altered samples (pink triangles) are not included in the line plot downhole, as these samples have undergone mass change and do not represent the igneous stratigraphy that the profile is compared to. Circles = olivine gabbro; squares = olivine-bearing gabbro; diamonds = orthopyroxene-bearing gabbro; hexagons = melaolivine gabbro; green triangles = dunite; pink triangles = altered olivine gabbro; yellow triangles = anorthositic gabbro.

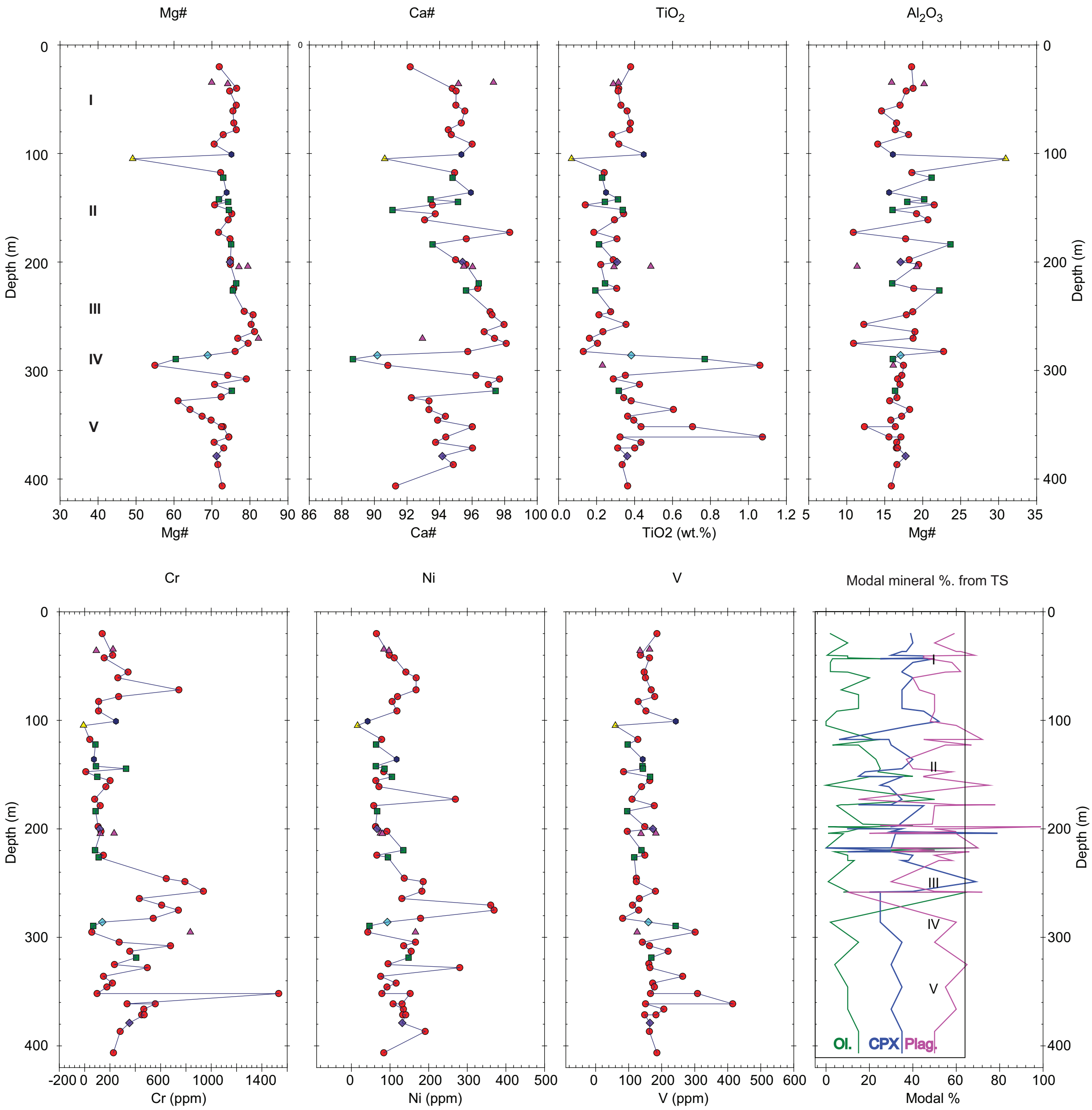

Figure F68. Volatile content of rocks, comparison of LOI data with water and carbon dioxide.

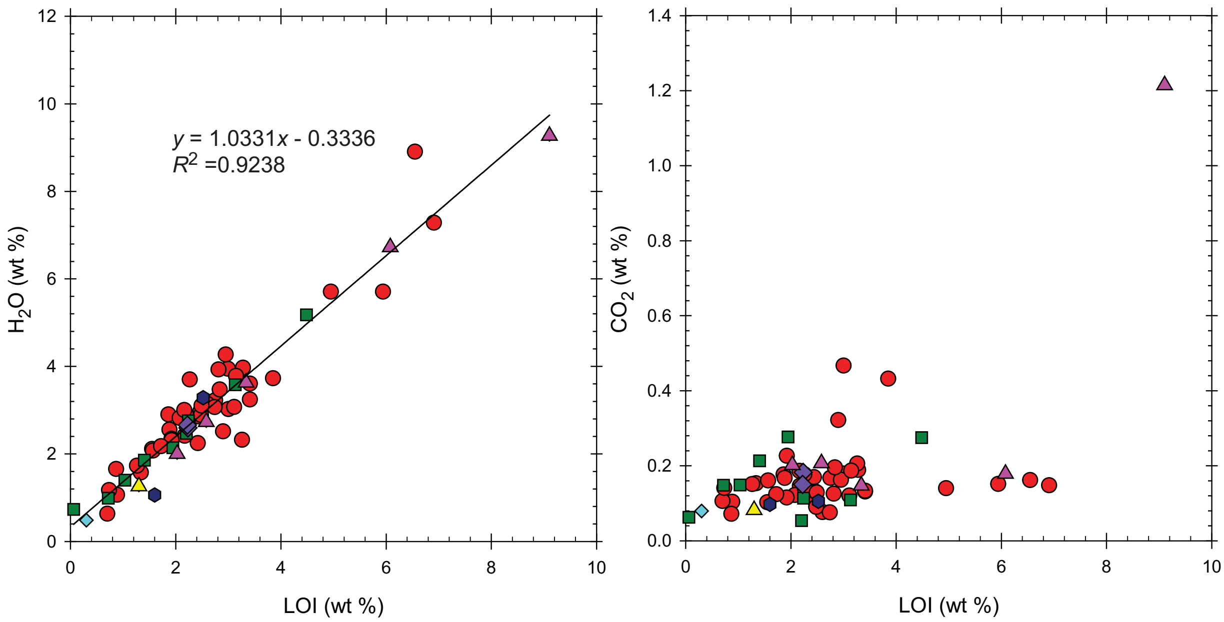

Figure F69. Variation in volatile content (H_2O, CO_2, S, and TIC/TOC) of rocks downhole with main fault zones logged plotted next to these data.

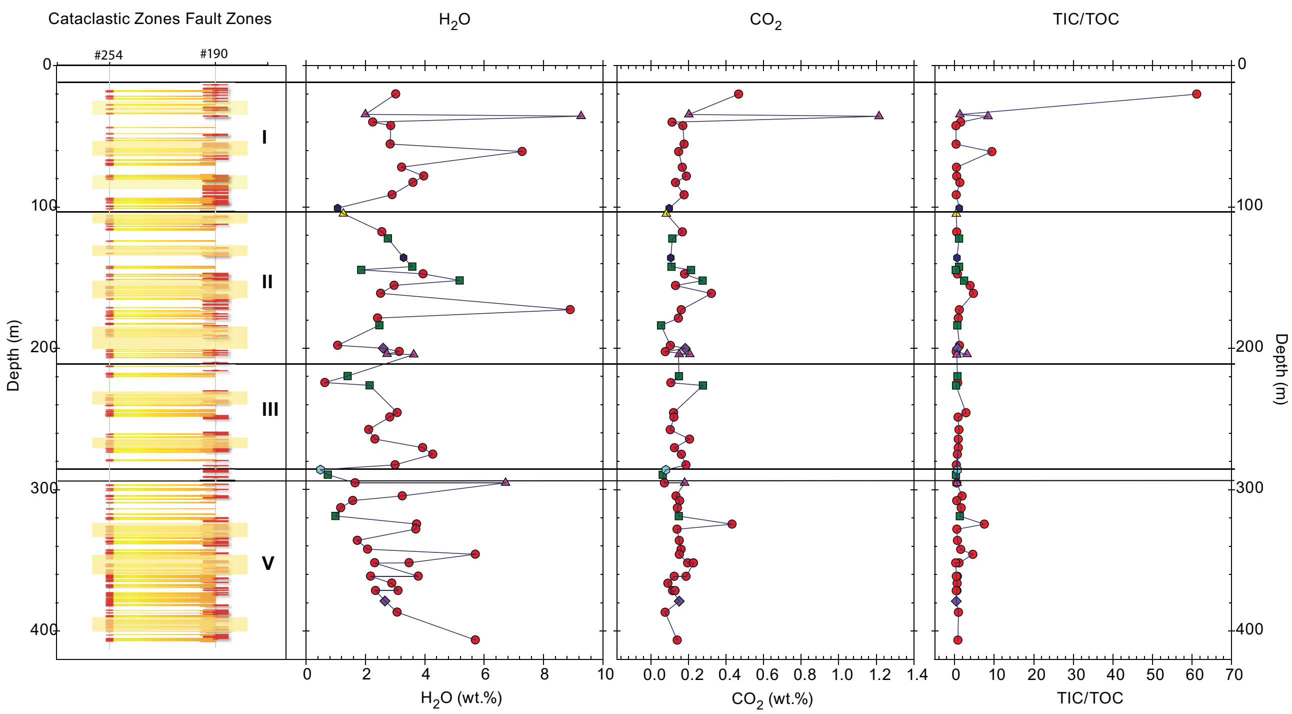

Figure F70. Comparison of bleached gabbro in the outer zone of a fault zone (17Z-3, 15–20 cm) and cataclased highly altered gabbro from within a fault zone (17Z-4, 56–61 cm). Isocon lines of no mass change are plotted using ΣREE as an immobile reference component. CO_2, H_2O, Na_2O, and K_2O have increased in the most altered sample, and CaO and Sr have decreased. REEs are plotted as red circles. In order to plot these data, elements had multipliers applied to them.

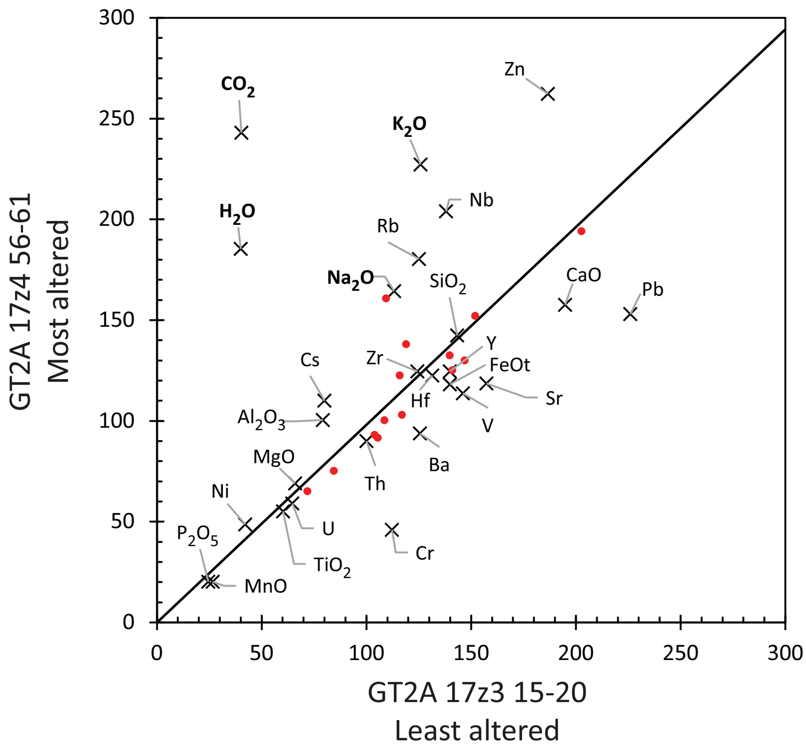

Figure F71. Locations of seven sections measured by CS-XRF.

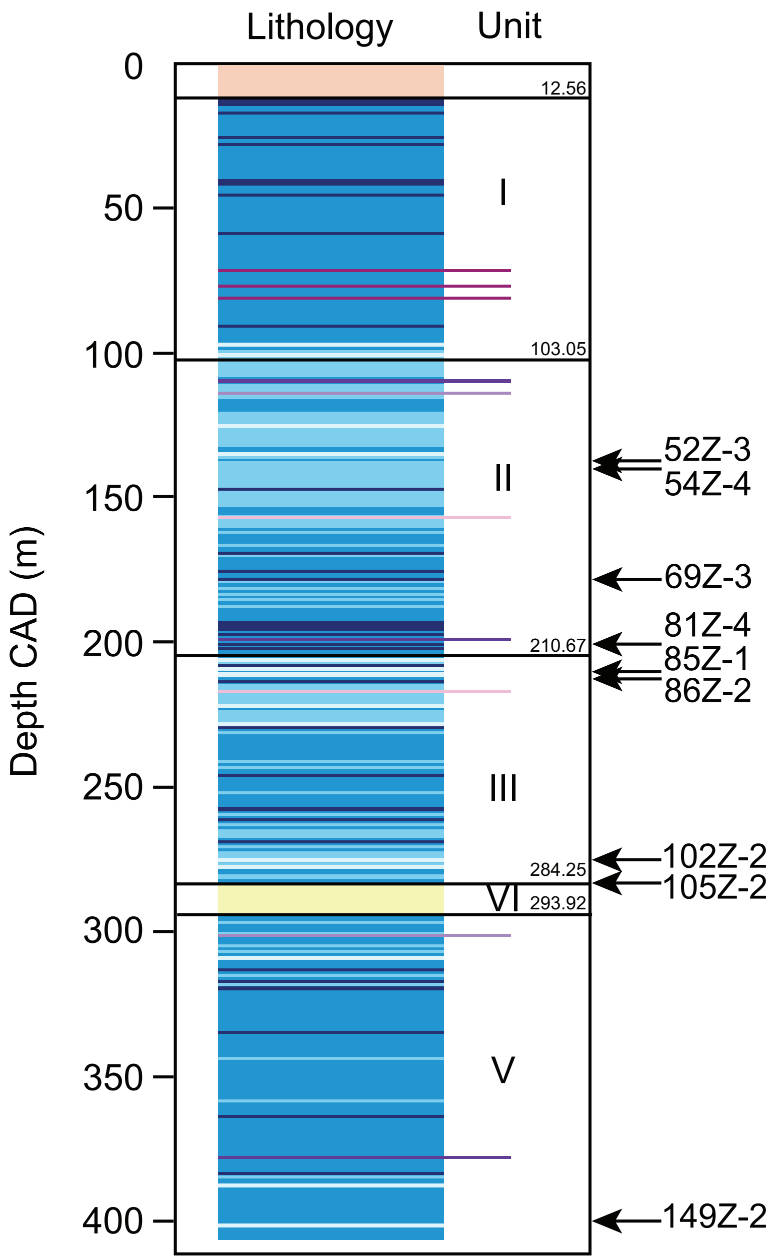

Figure F72. Downhole compositional variations of major elements, Cr, and Ni for GT2A-52Z-3, 1–74 cm. (Continued below.)

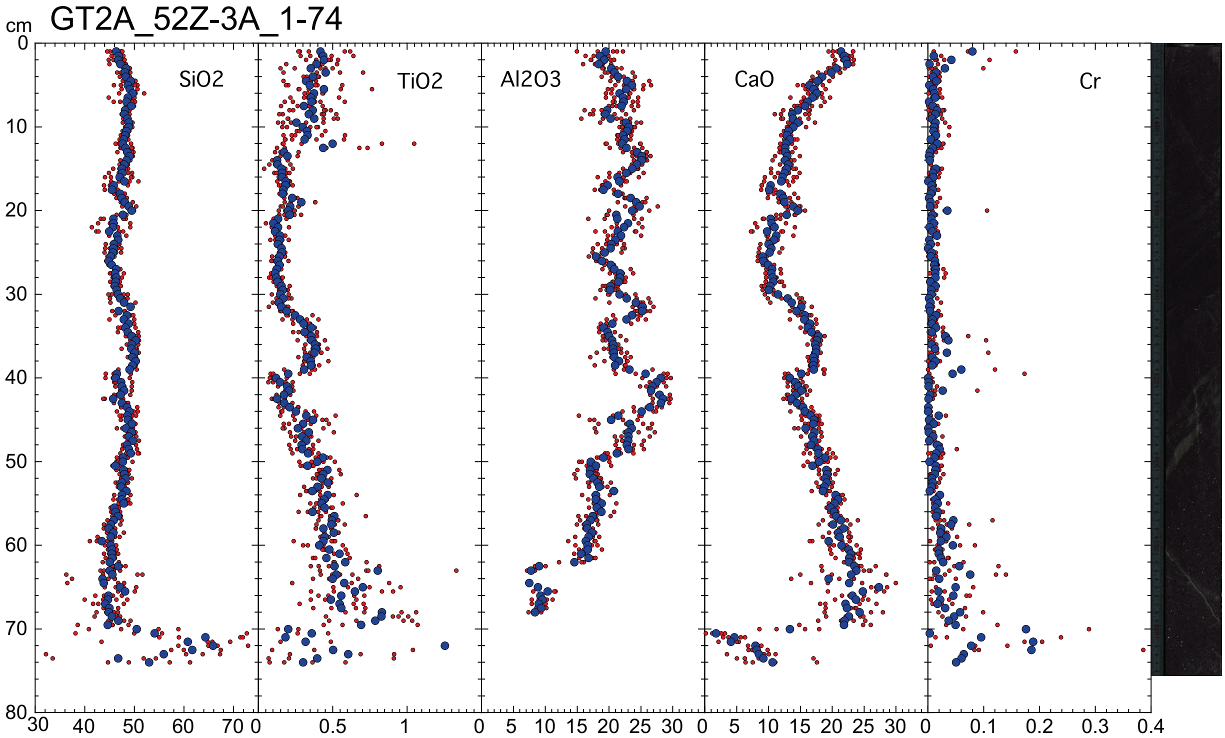

Figure F72 (continued).

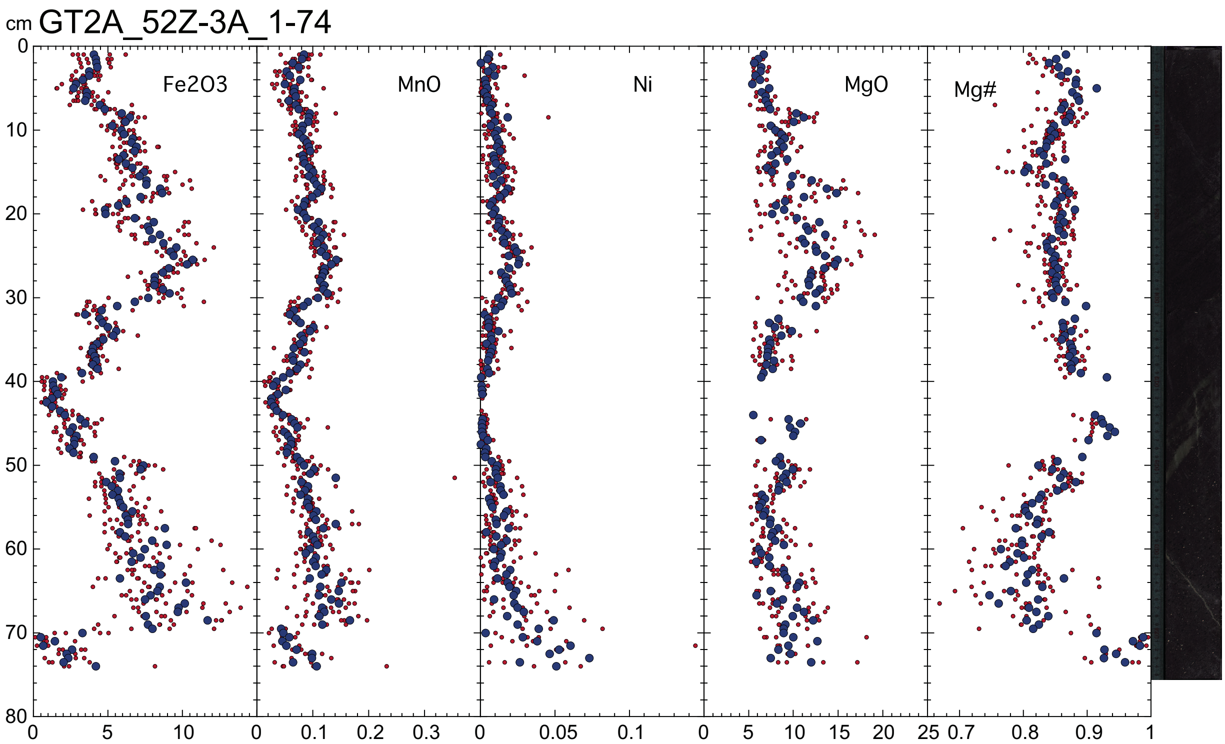

Figure F73. Color-coded images for variations of major elements, Cr, and Ni for GT2A-52Z-3, 1–74 cm.

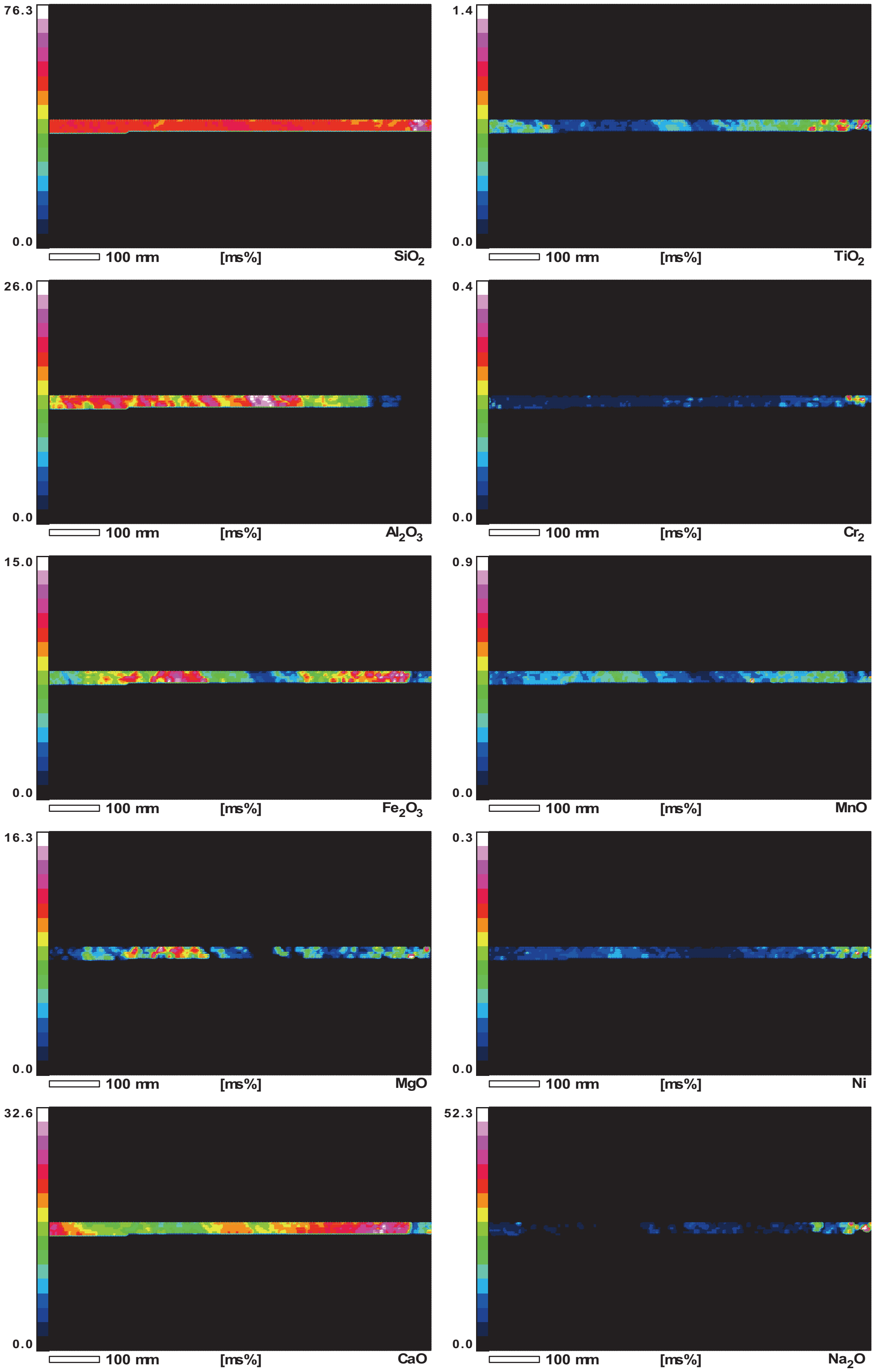

Figure F74. Downhole compositional variations of major elements, Cr, and Ni for GT2A-54Z-4, 4–66 cm. (Continued below.)

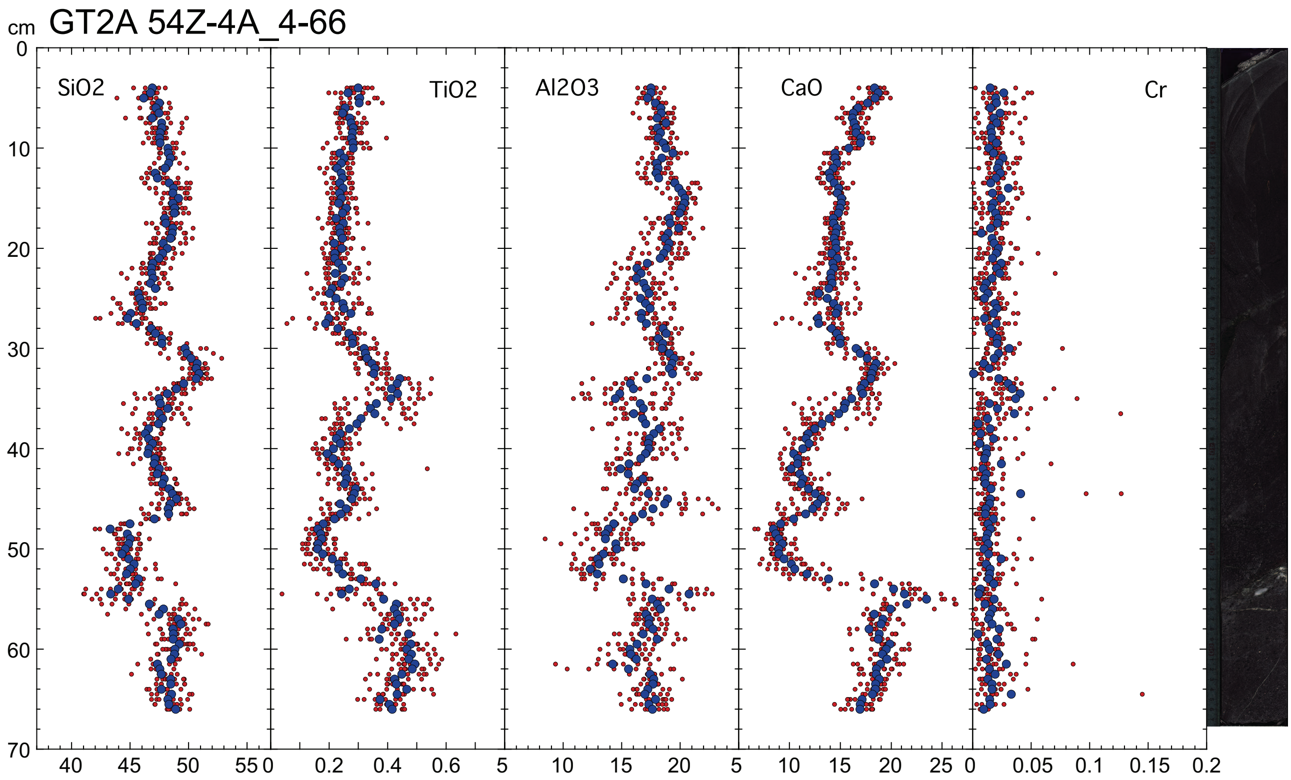

Figure F74 (continued).

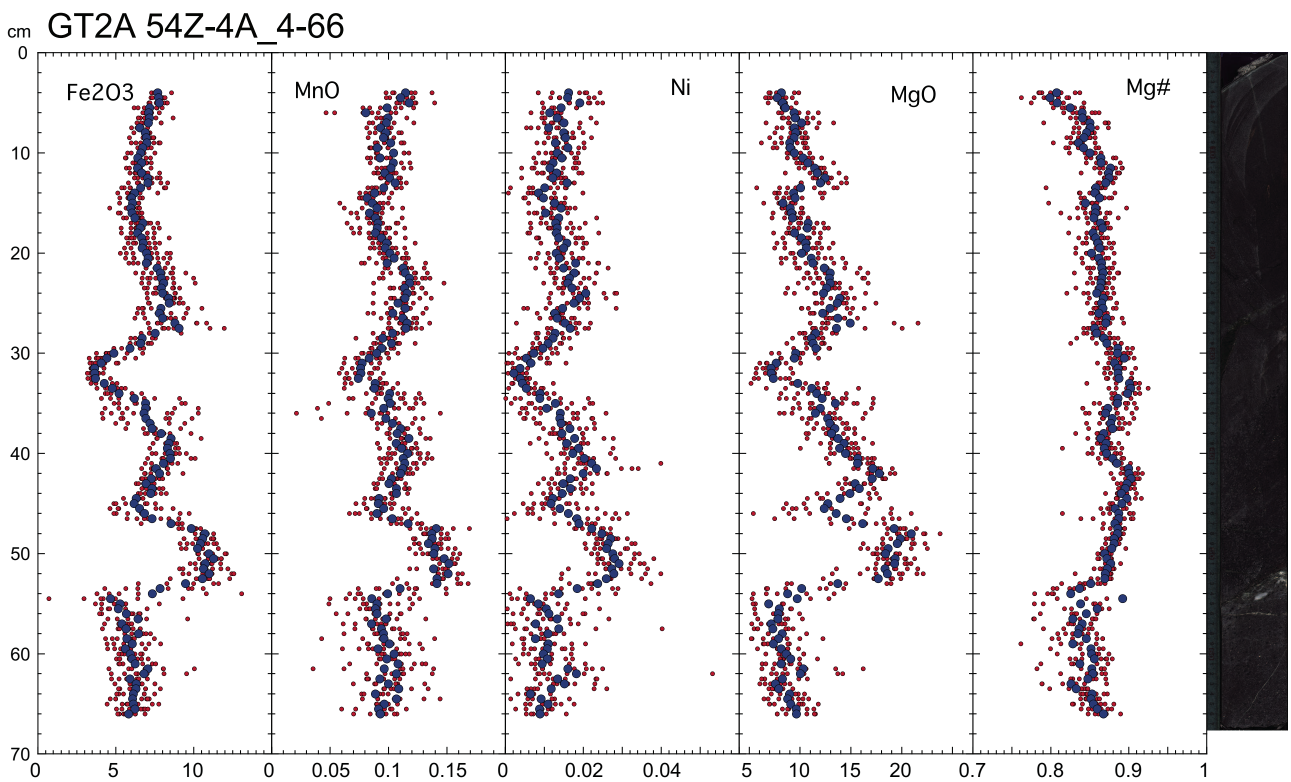

Figure F75. Color-coded images for variations of major elements, Cr, and Ni for GT2A-54Z-4, 4–66 cm.

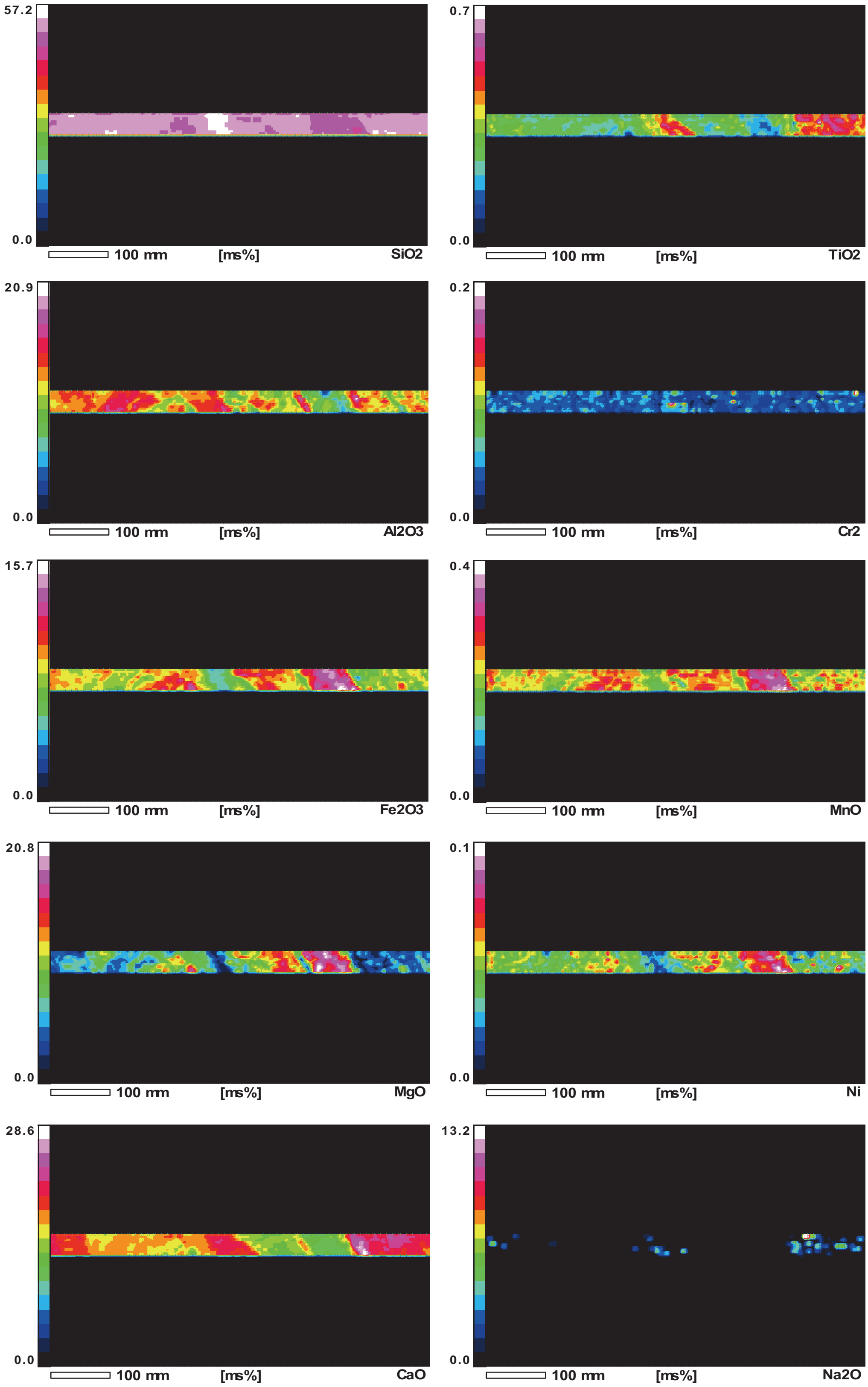

Figure F76. Downhole compositional variations of major elements, Cr, and Ni for GT2A-69Z-3, 2–57 cm. (Continued below.)

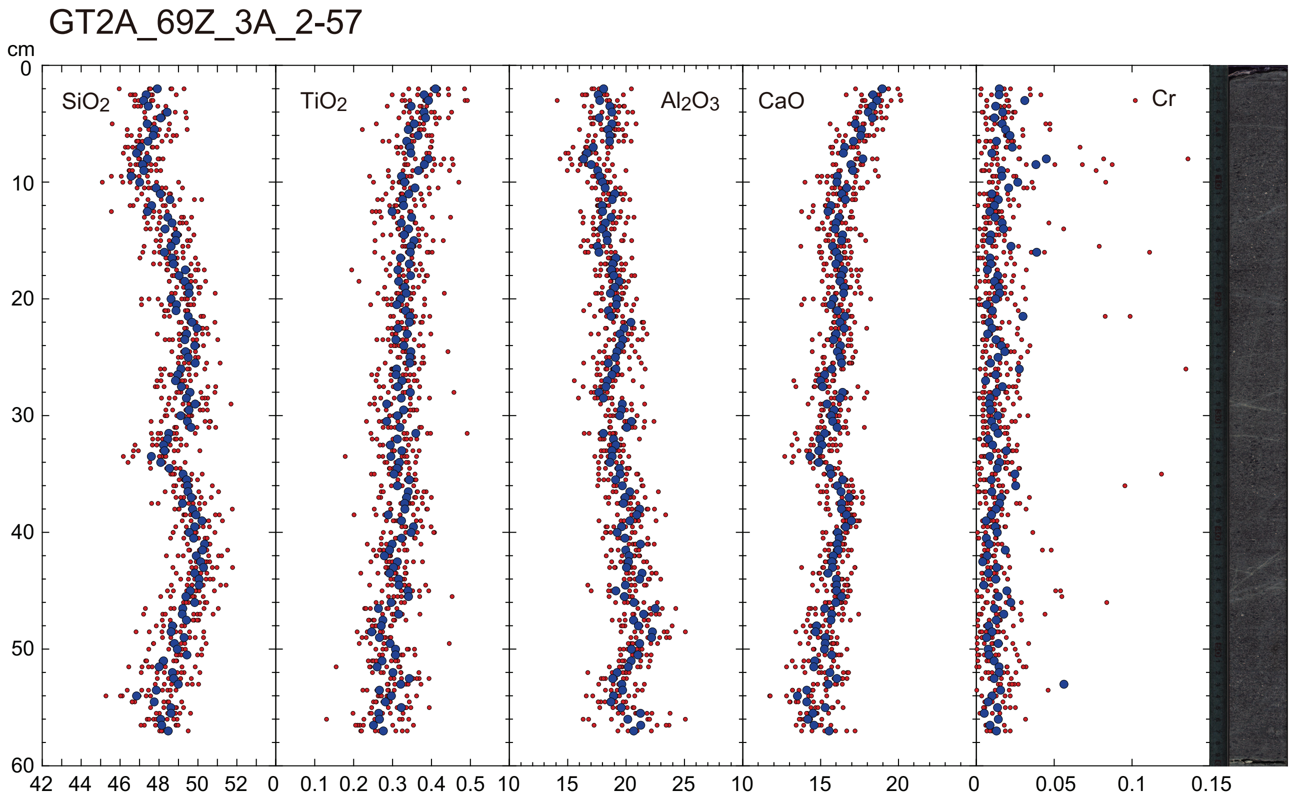

Figure F76 (continued).

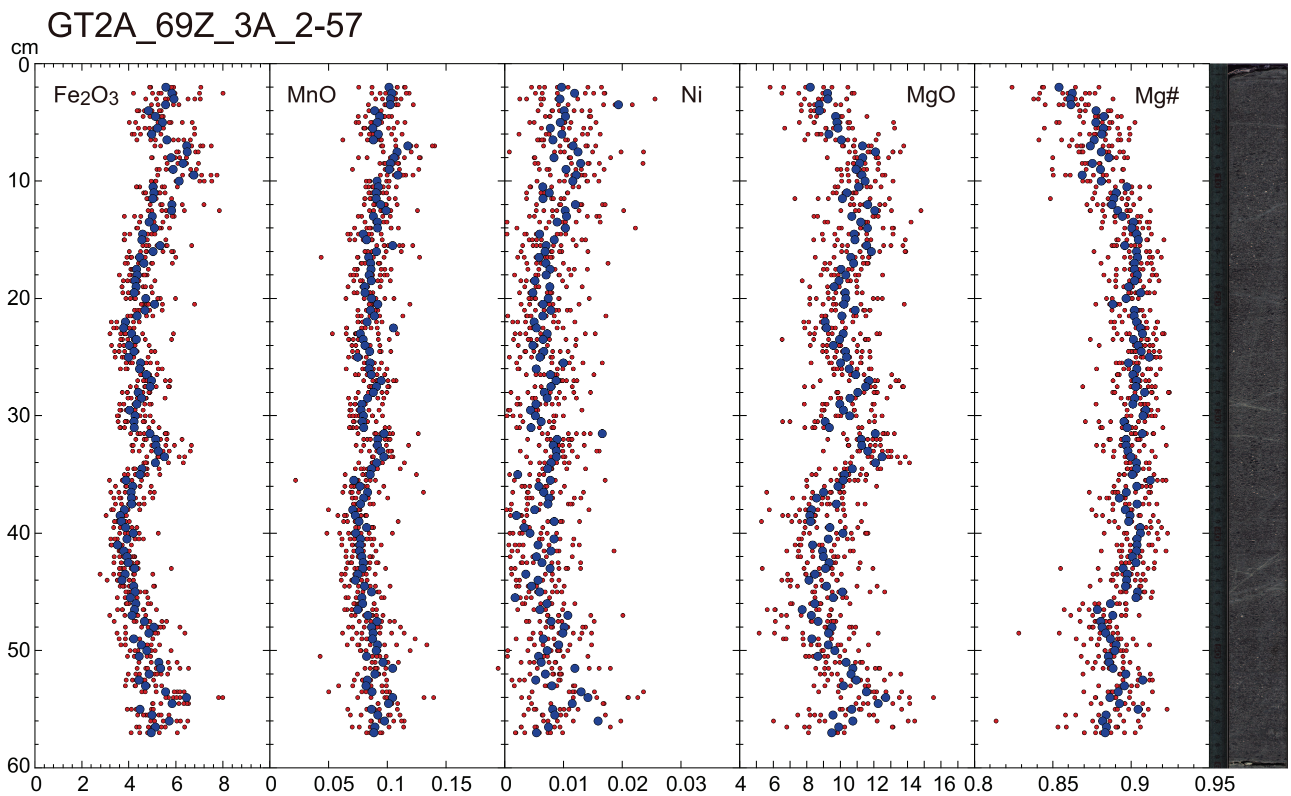

Figure F77. Color-coded images for variations of major elements, Cr, and Ni for GT2A-69Z-3, 2–57 cm.

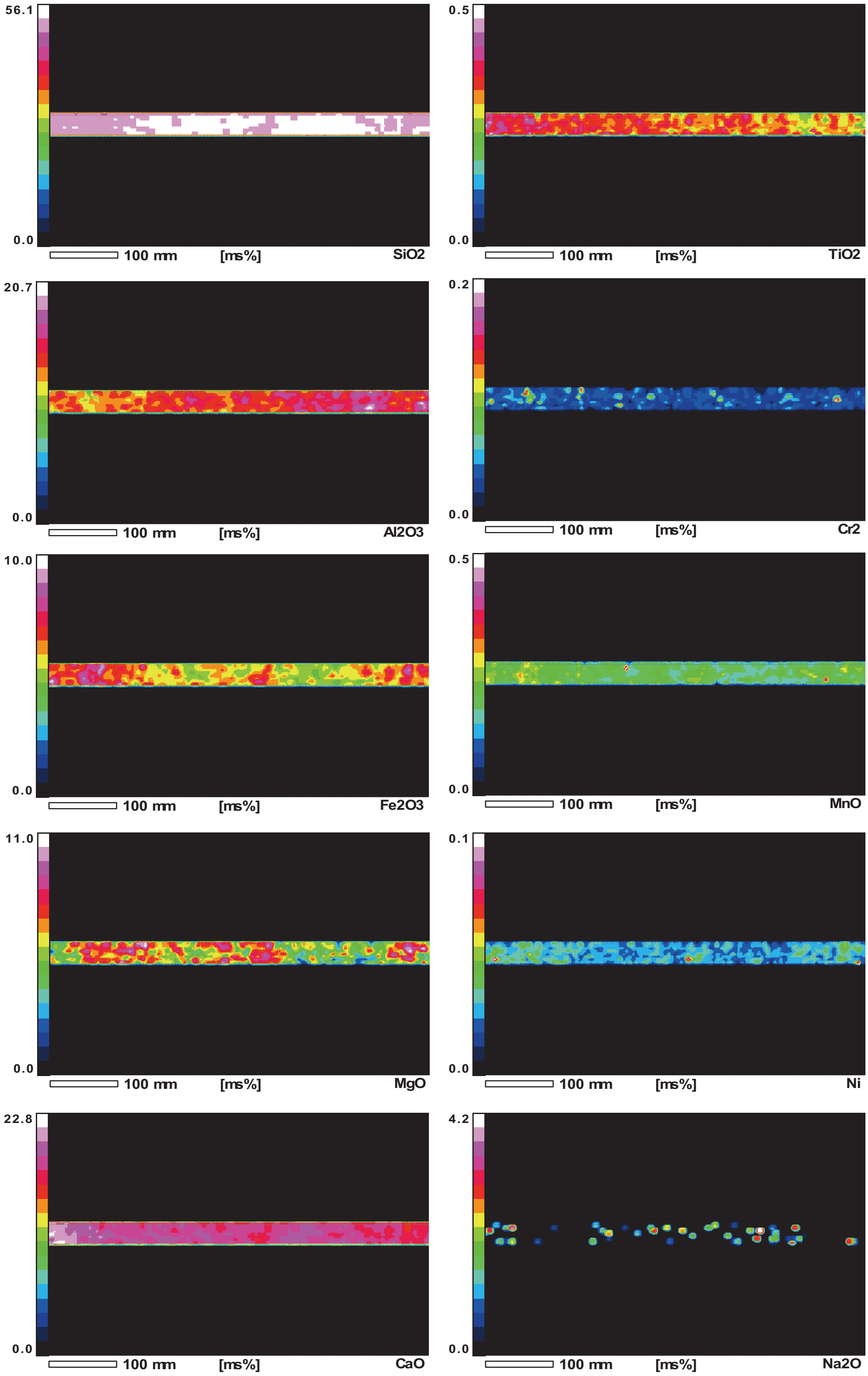

Figure F78. Downhole compositional variations of major elements, Cr, and Ni for GT2A-81Z-4, 1–43 cm. (Continued below.)

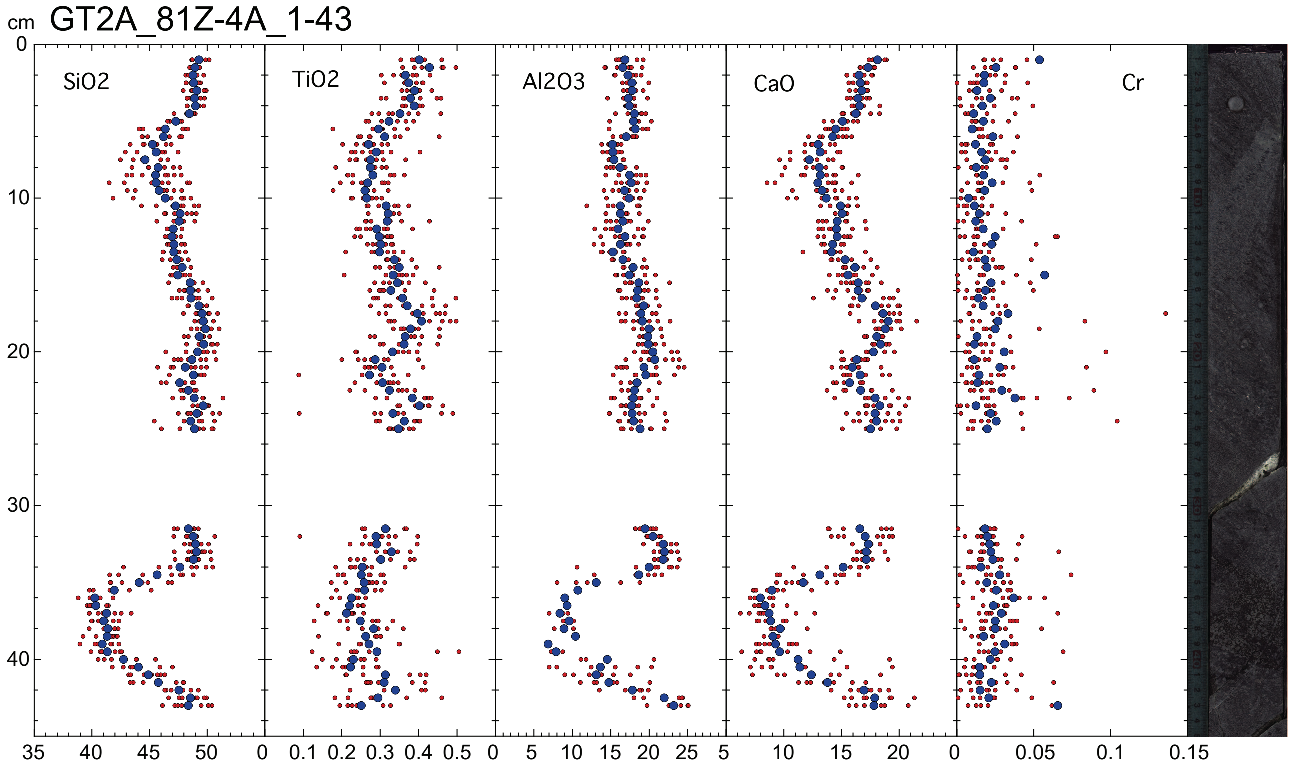

Figure F78 (continued).

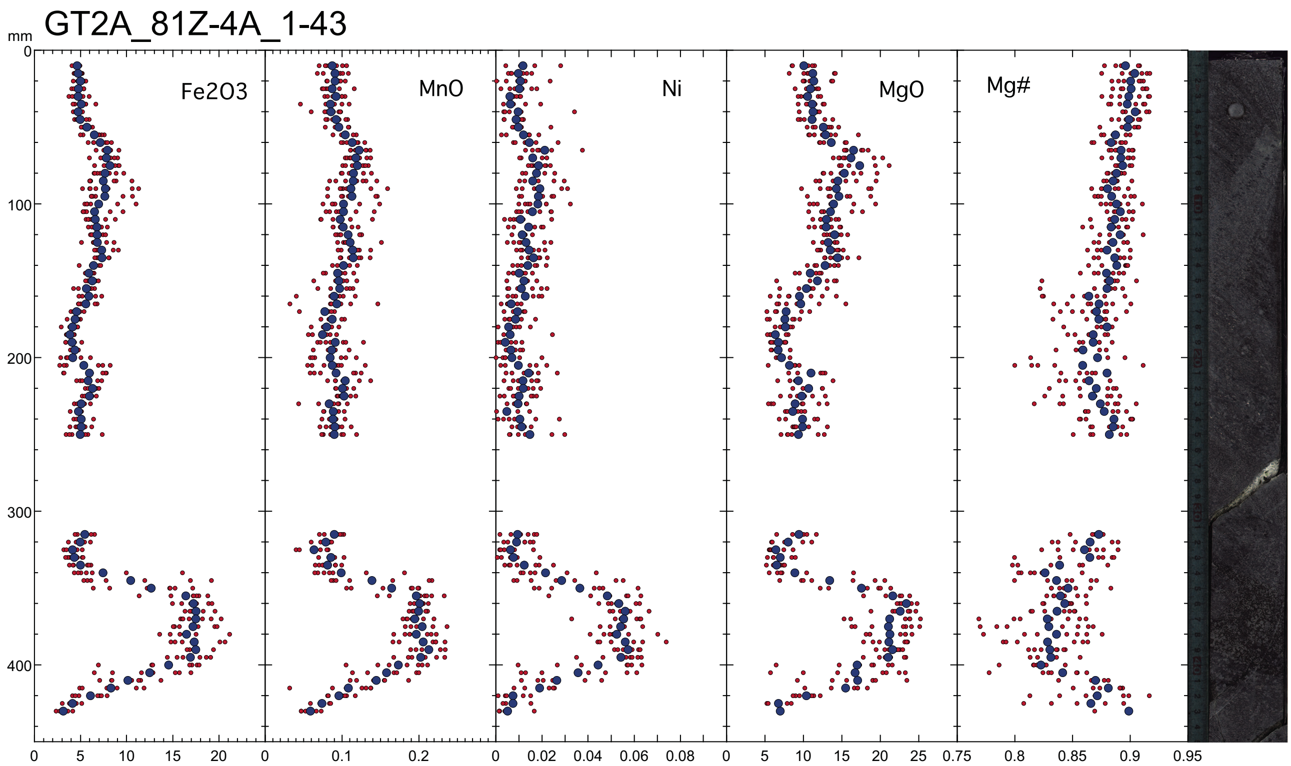

Figure F79. A. Color-coded images for variations of major elements, Cr, and Ni for GT2A-81Z-4, 1–25 cm. **B.** Color-coded images for variations of major elements, Cr, and Ni for GT2A-81Z-4, 31.5–43 cm. (Continued on next page.)

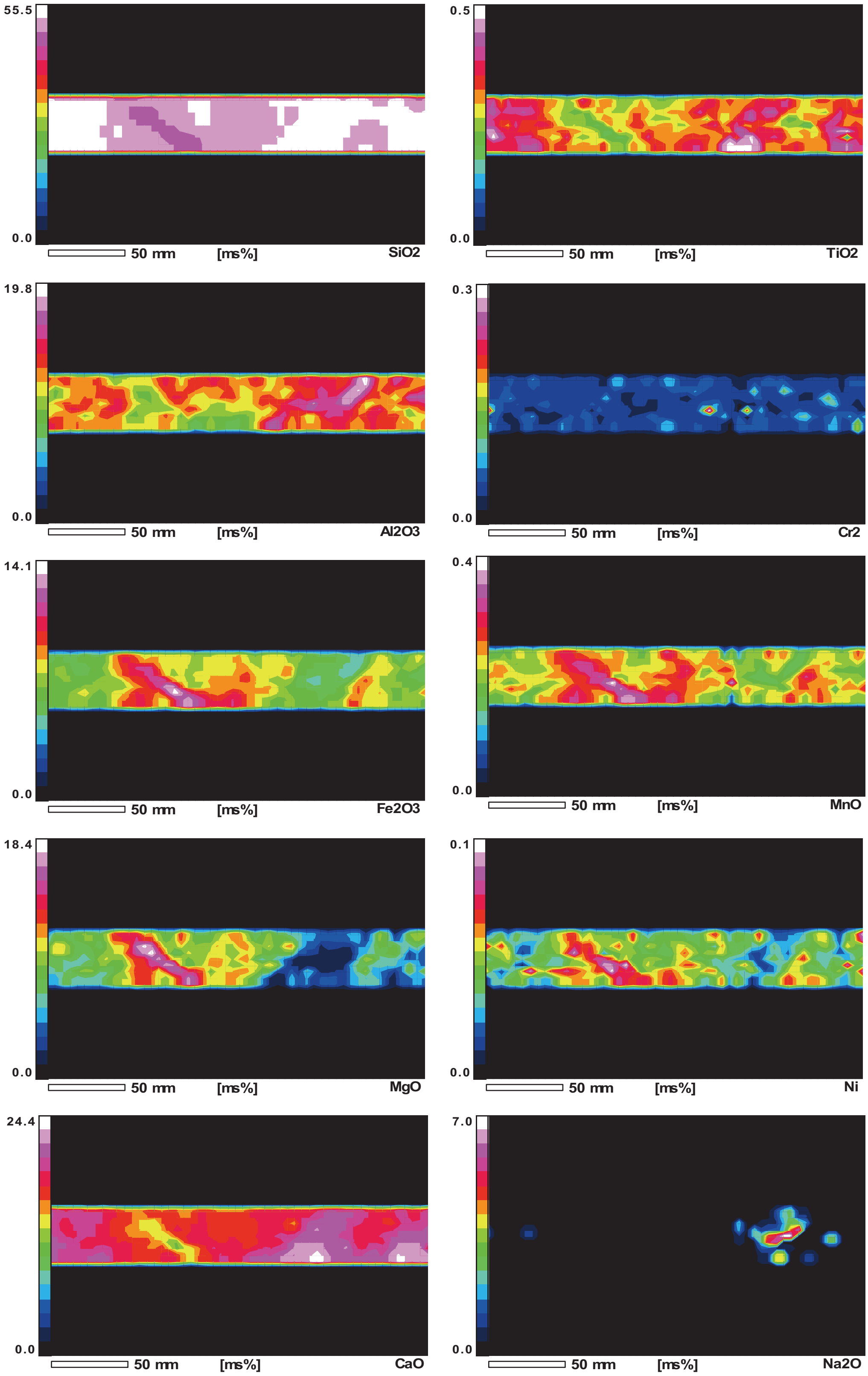

Figure F79 (continued).

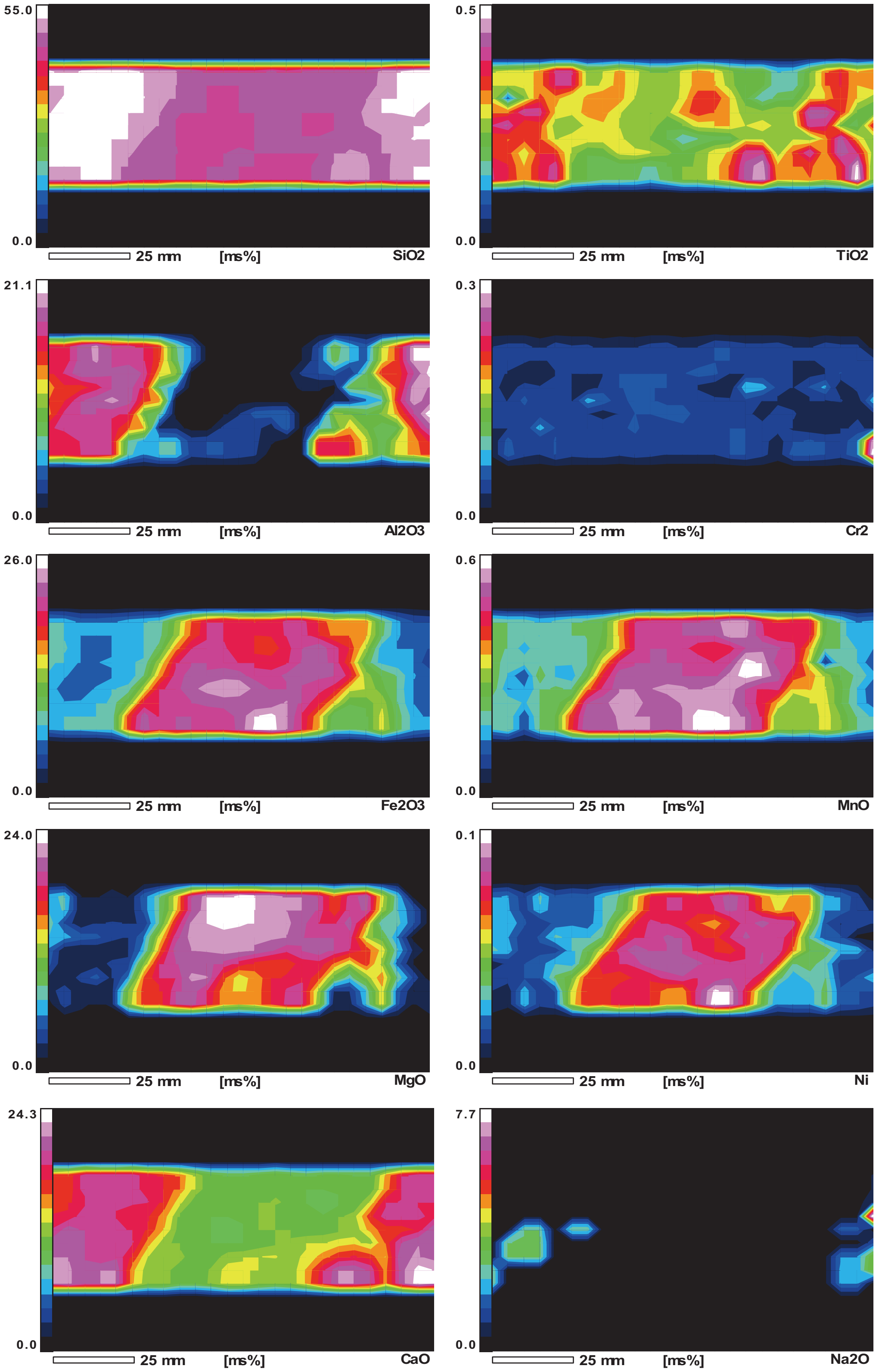

Figure F80. Downhole compositional variations of major elements, Cr, and Ni for GT2A-85Z-1, 1–59 cm. (Continued below.)

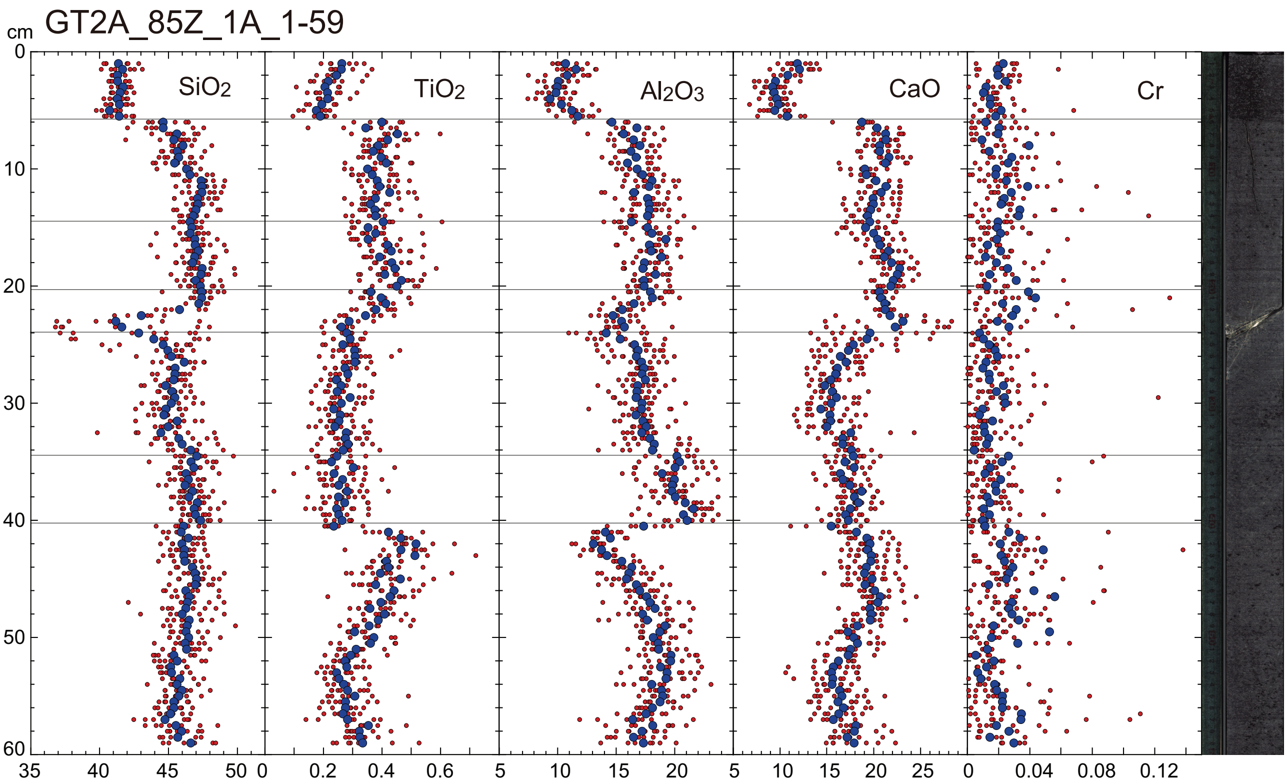

Figure F80 (continued).

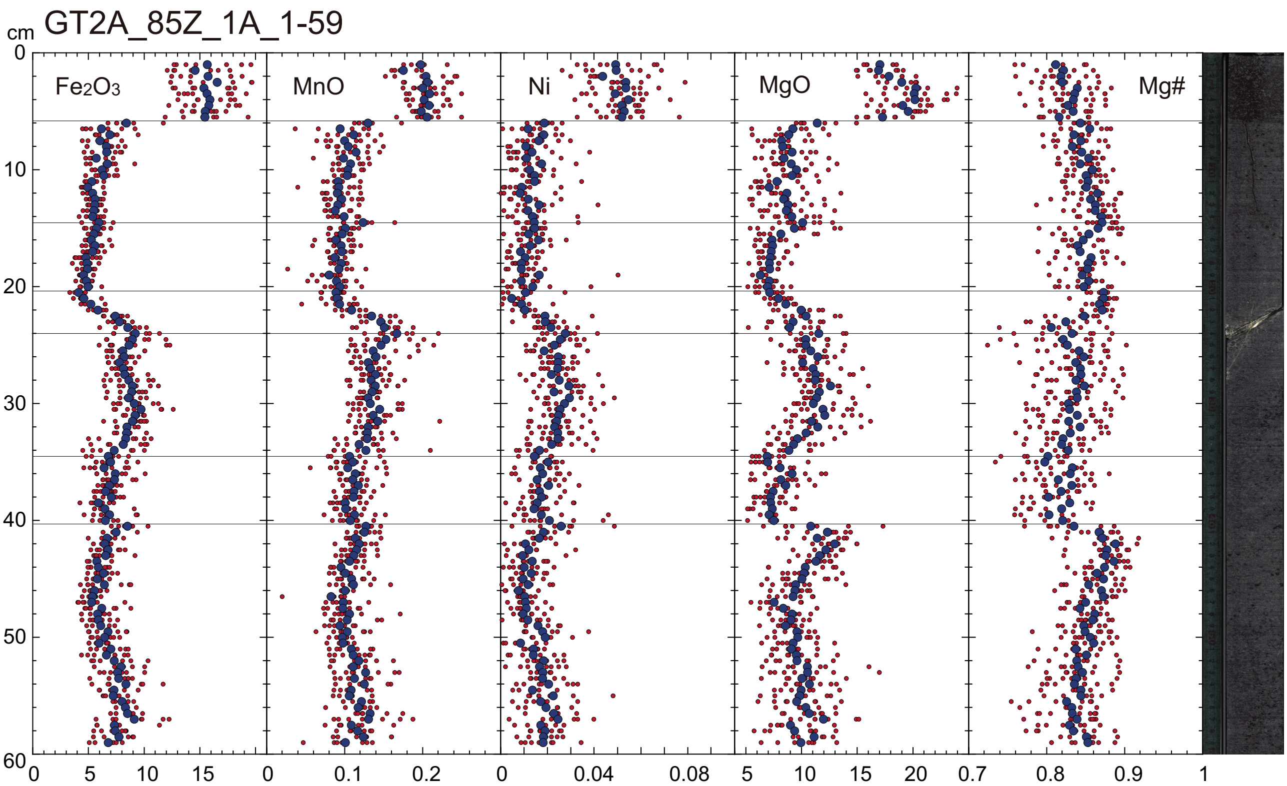

Figure F81. Color-coded images for variations of major elements, Cr, and Ni for GT2A-85Z-1, 1–59 cm.

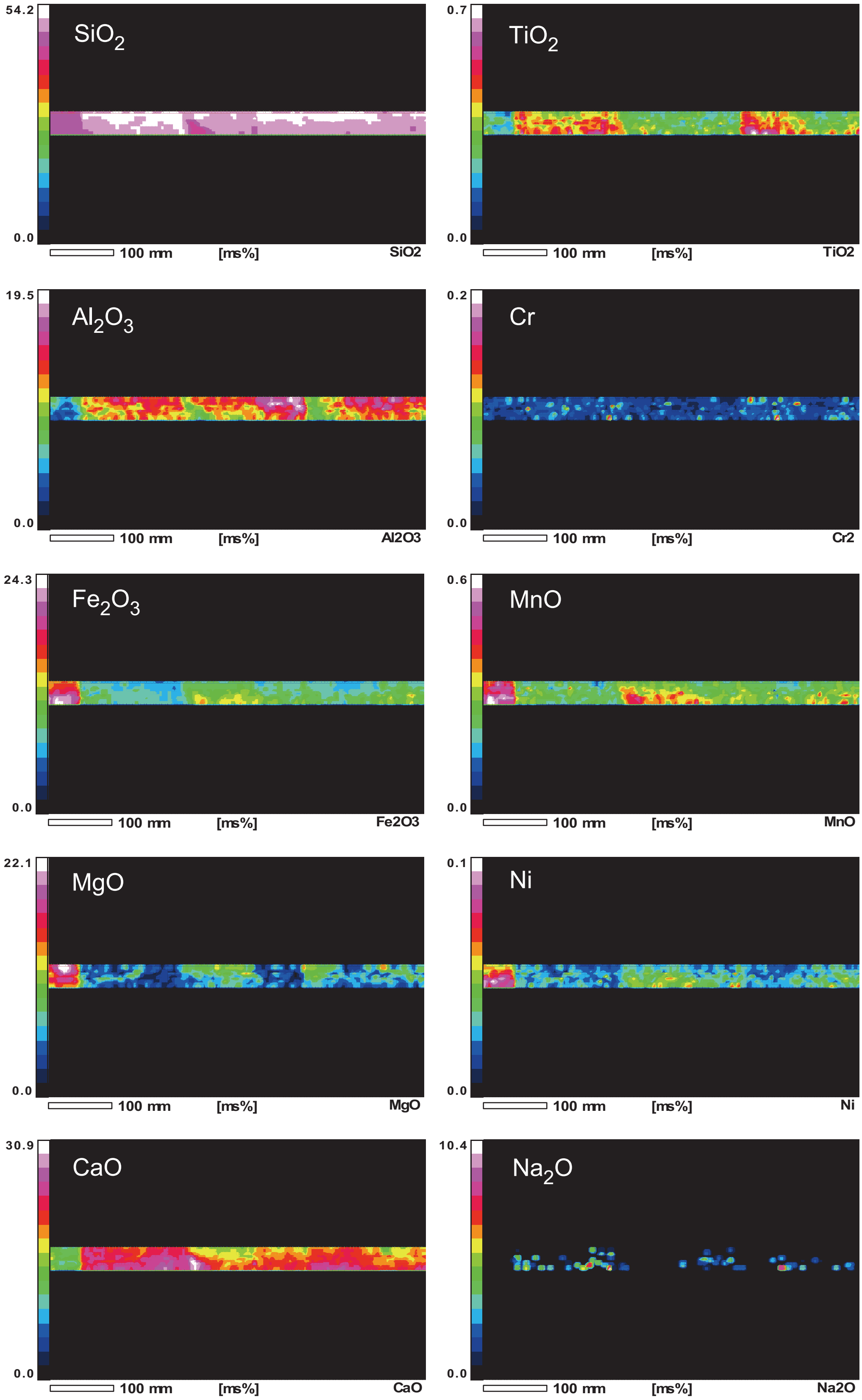

Figure F82. Downhole compositional variations of major elements, Cr, and Ni for GT2A-86Z-2, 1–52 cm. (Continued below.)

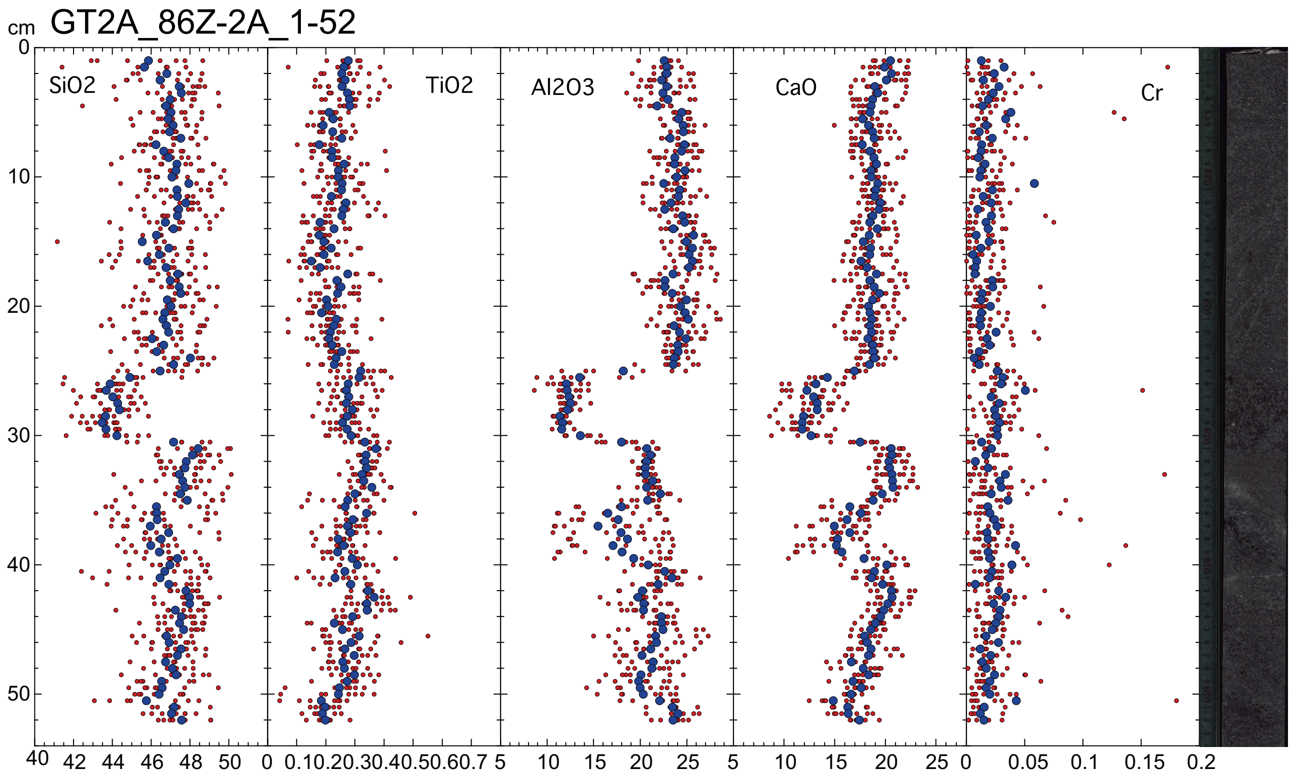

Figure F82 (continued).

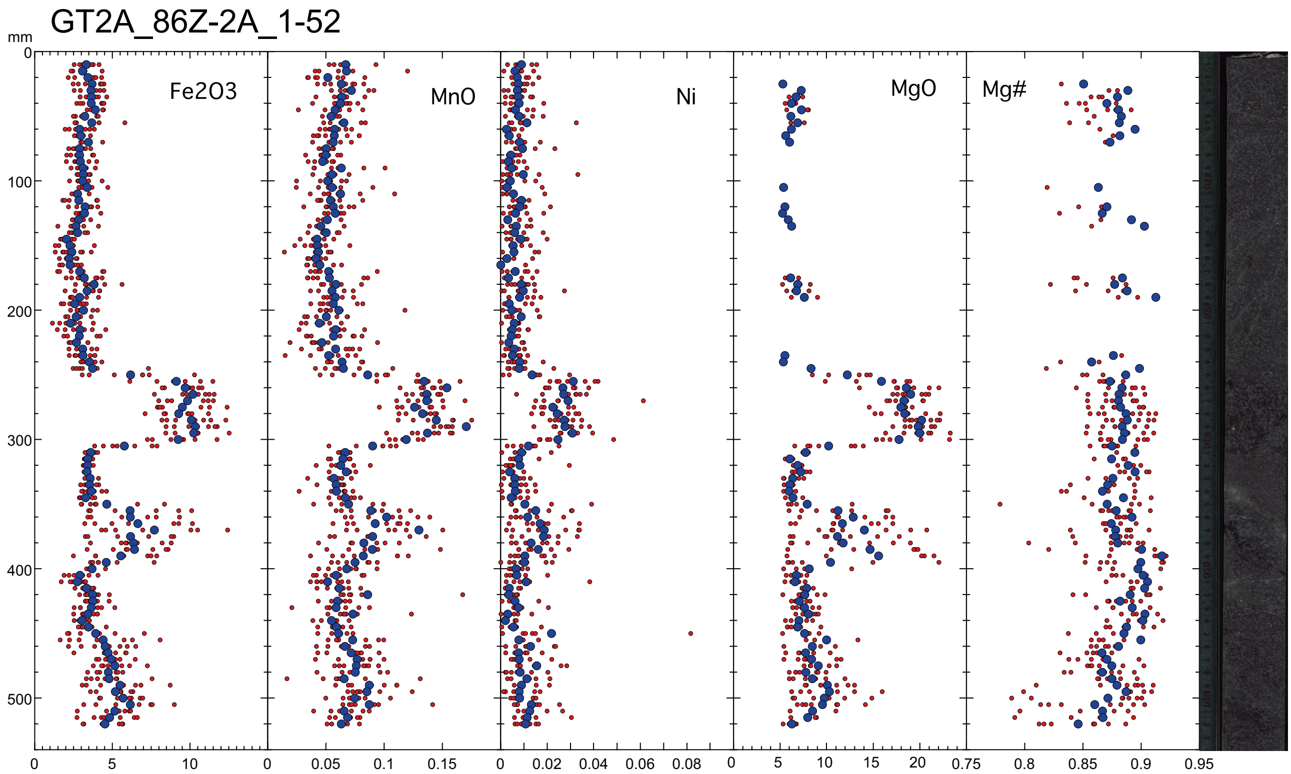

Figure F83. Color-coded images for variations of major elements, Cr, and Ni for GT2A-86Z-2, 1–52 cm.

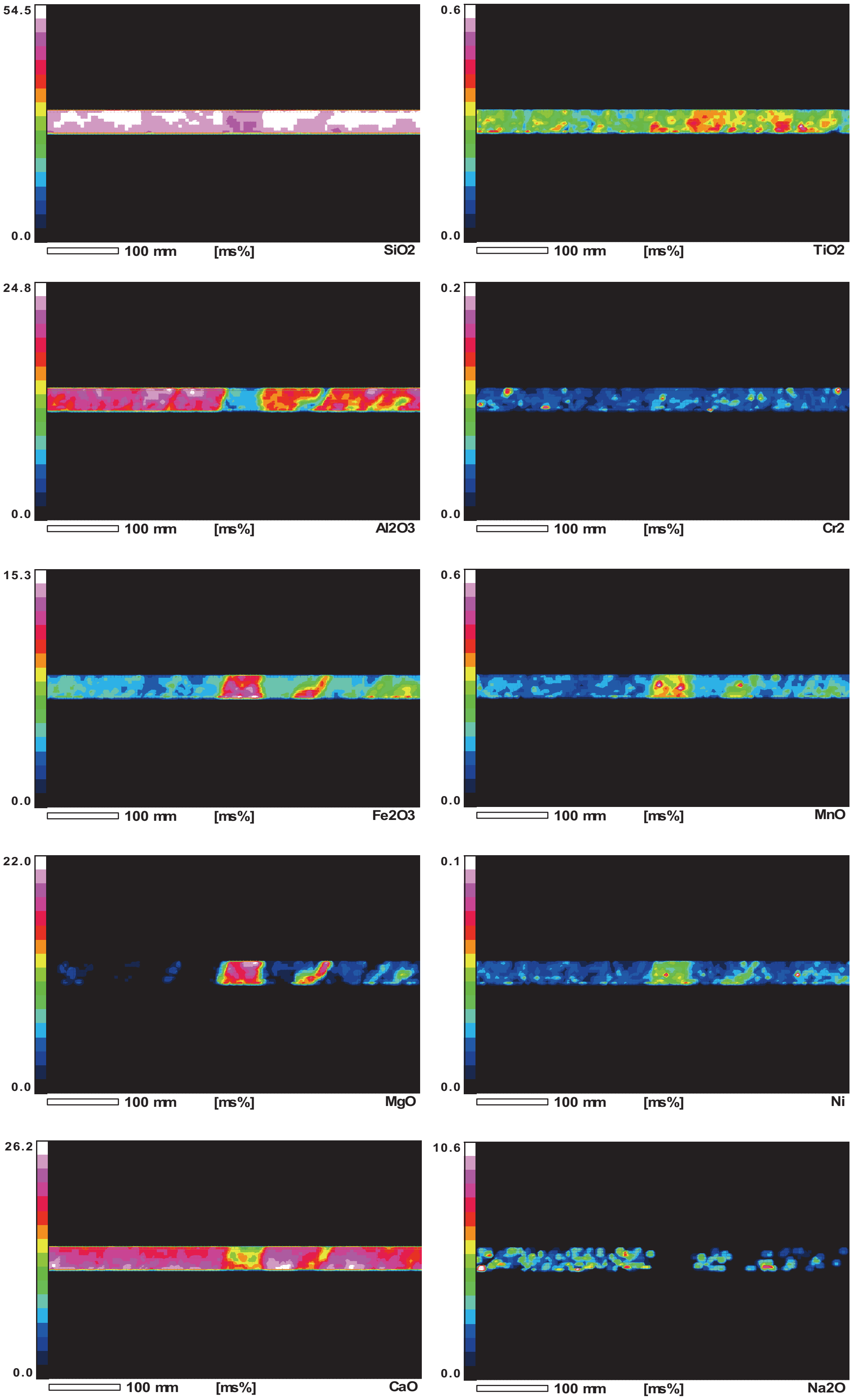

Figure F84. Downhole compositional variations of major elements, Cr, and Ni for GT2A-102Z-2, 4–71 cm. (Continued below.)

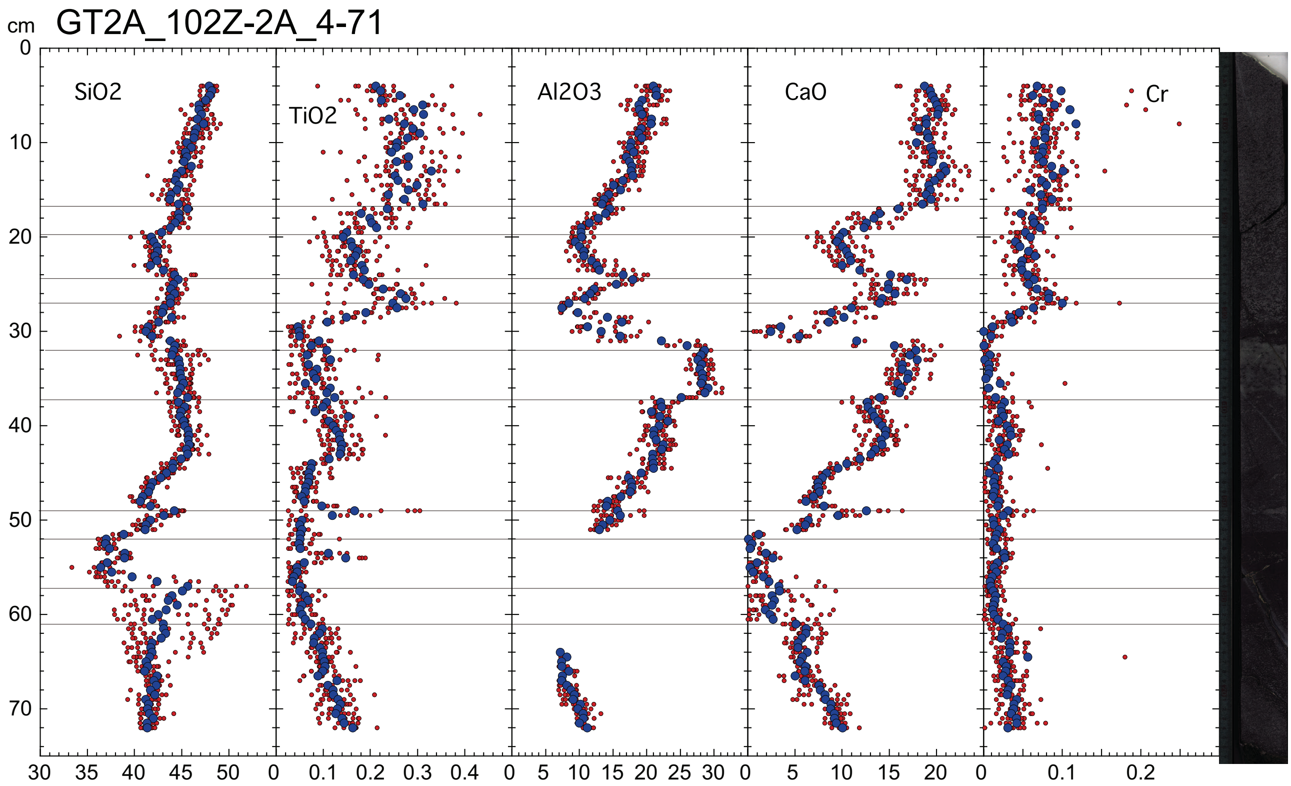

Figure F84 (continued).

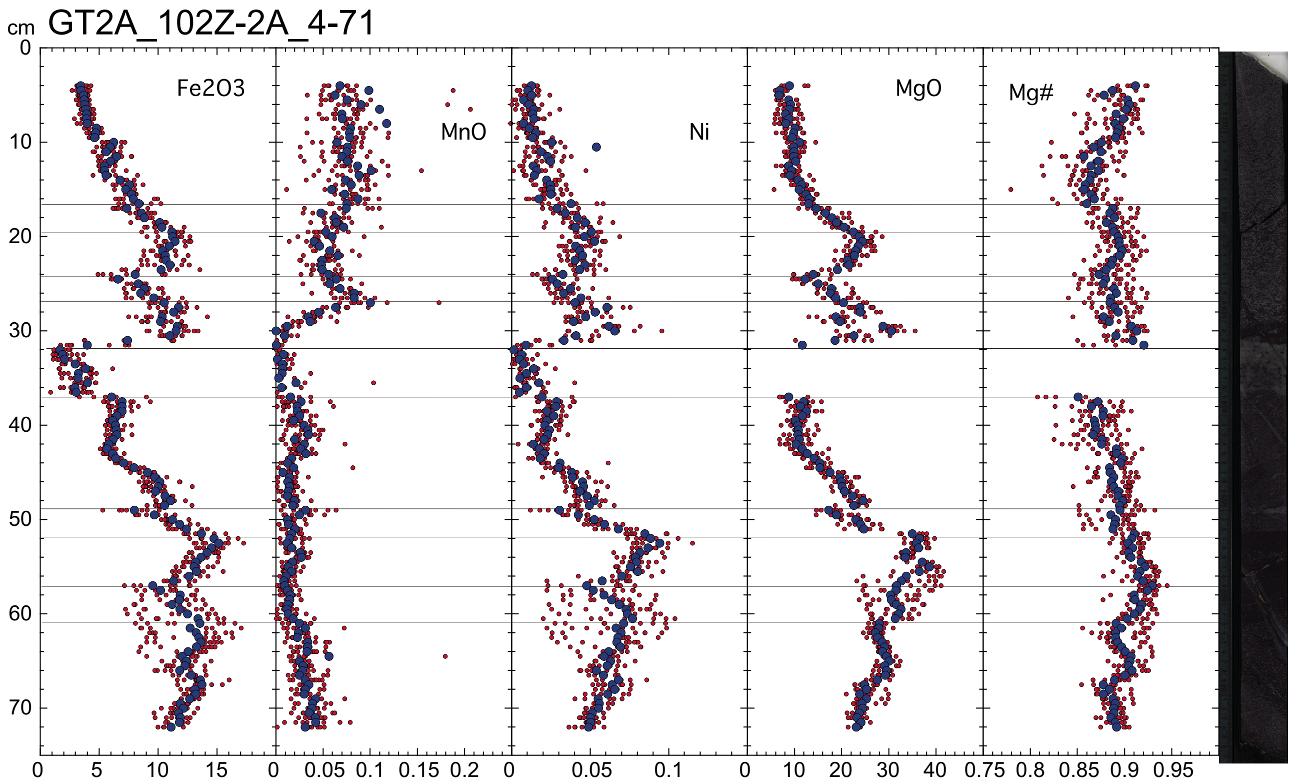

Figure F85. Color-coded images for variations of major elements, Cr, and Ni for GT2A-102Z-2, 4–71 cm.

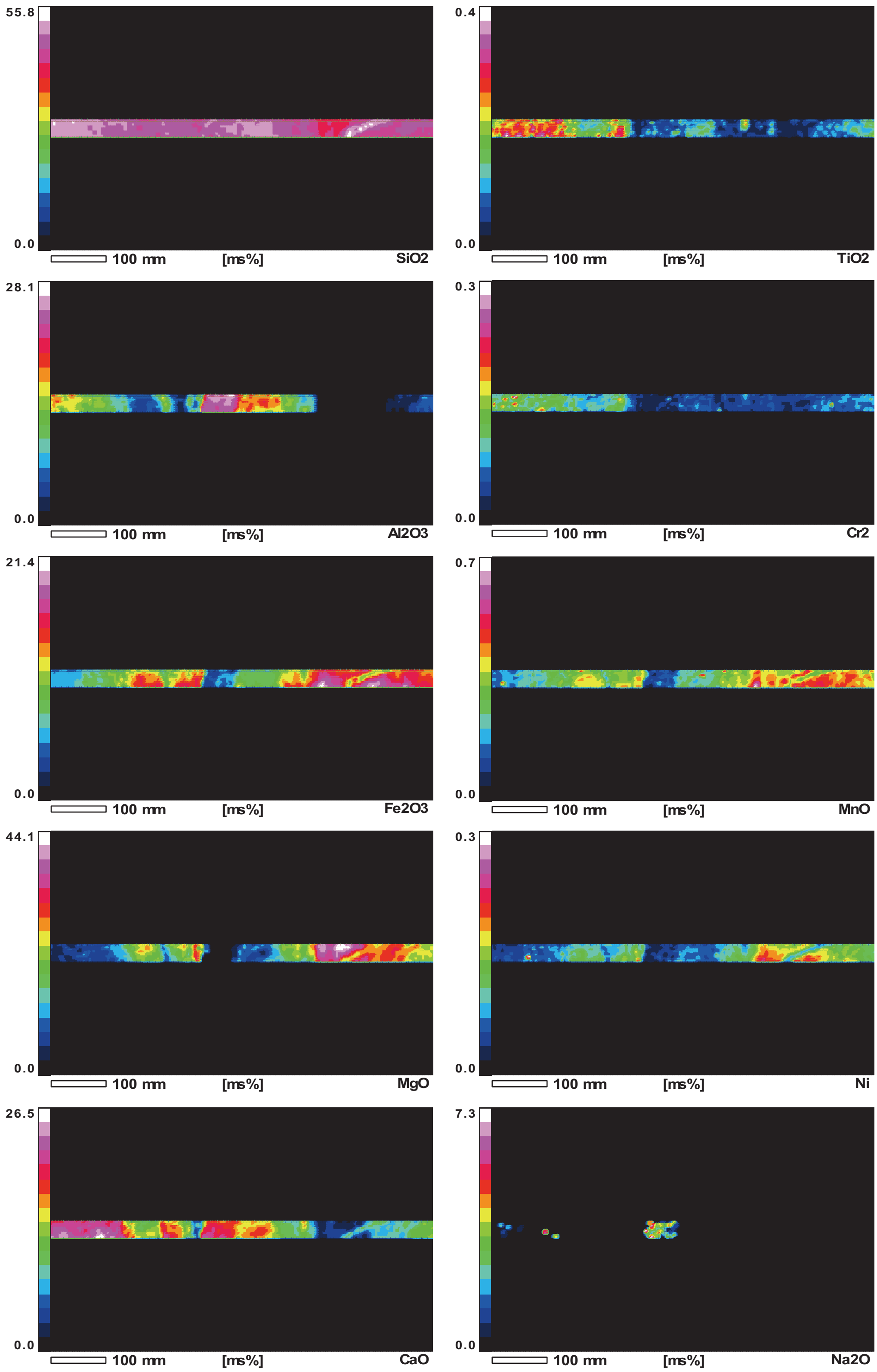

Figure F86. Downhole compositional variations of major elements, Cr, and Ni for GT2A-105Z-2, 39–54 cm. (Continued below.)

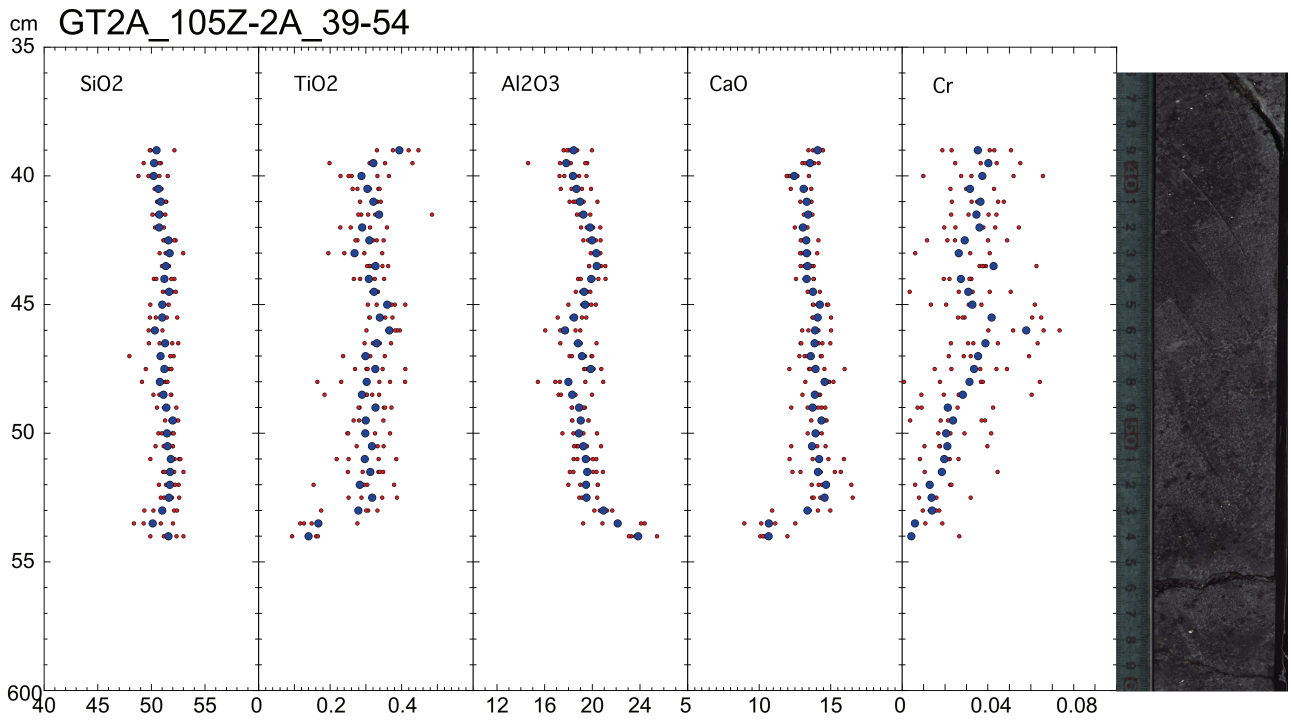

Figure F86 (continued).

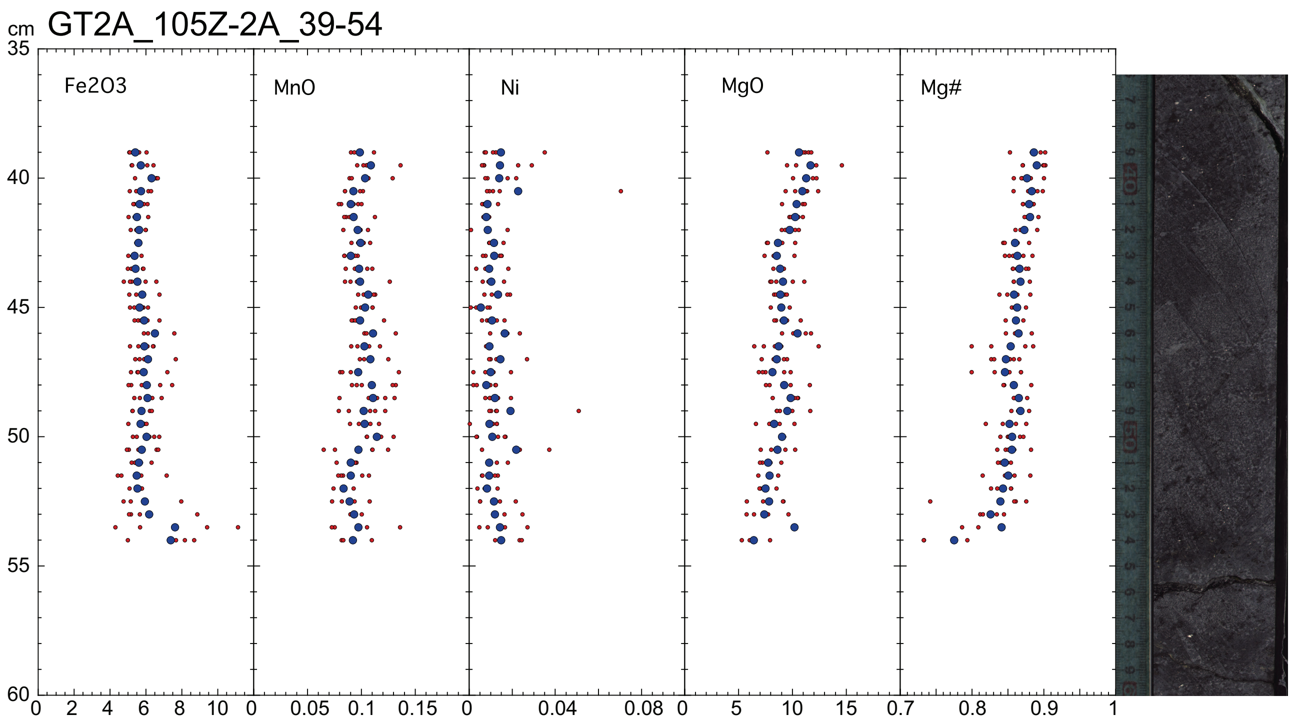

Figure F87. Color-coded images for variations of major elements, Cr and Ni, for GT2A-105Z-2, 39–54 cm.

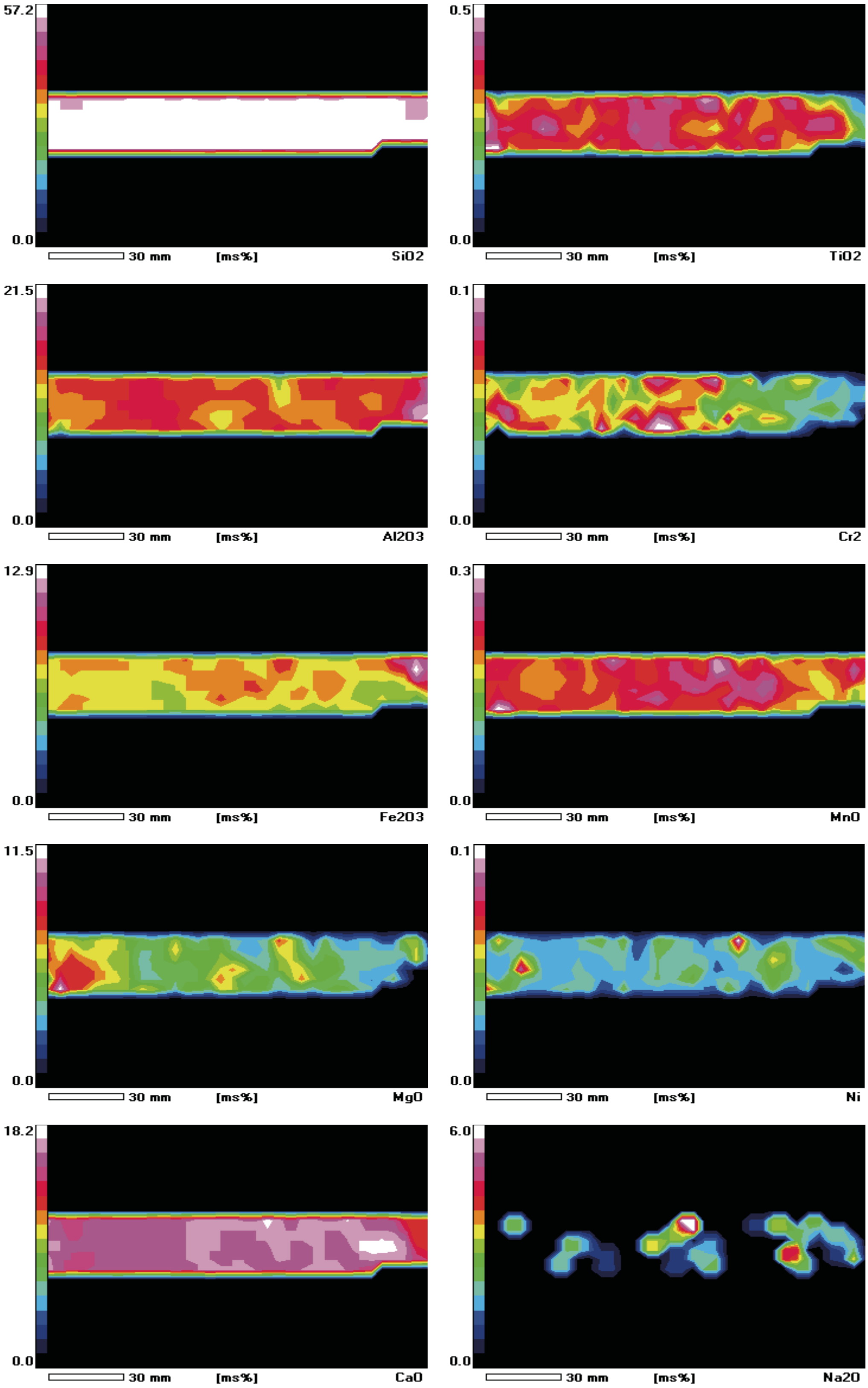

Figure F88. Downhole compositional variations of major elements, Cr, and Ni for GT2A-1049Z-2, 1–92 cm. (Continued below.)

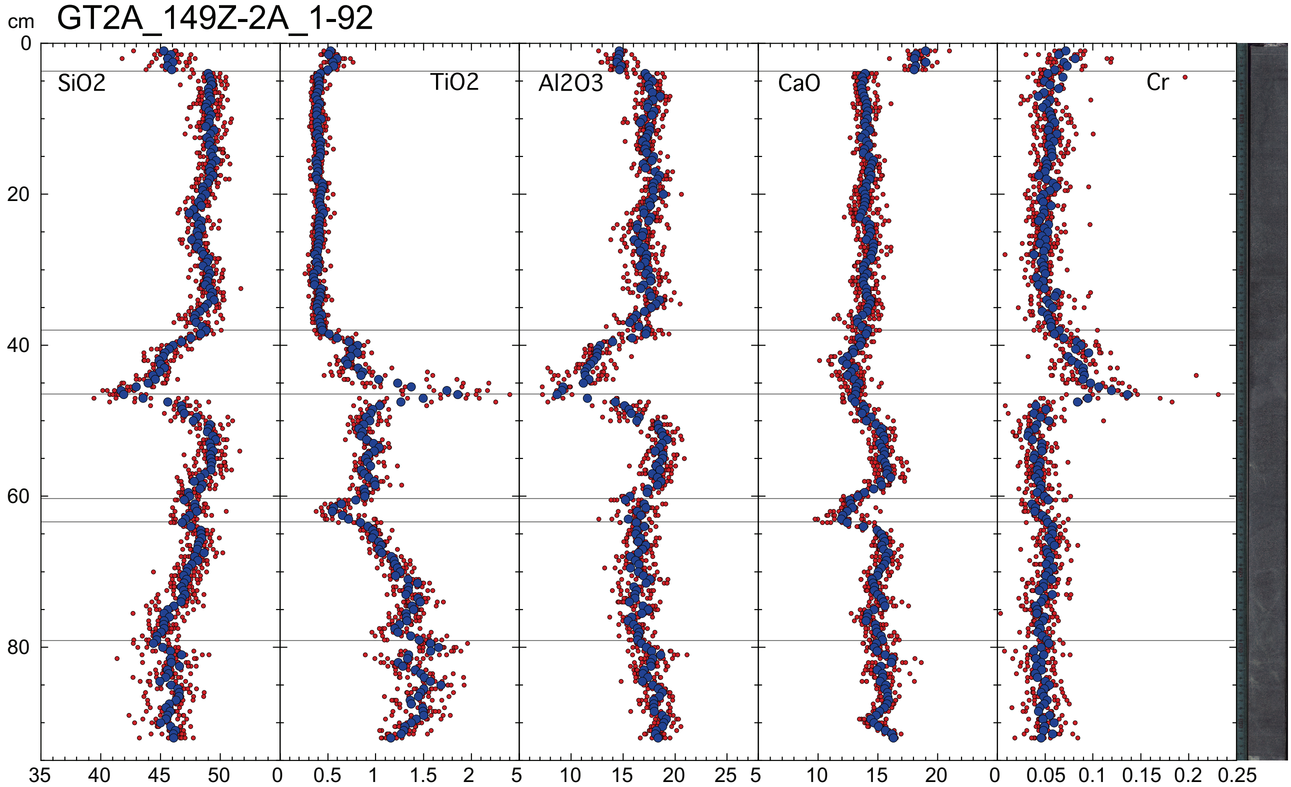

Figure F88 (continued).

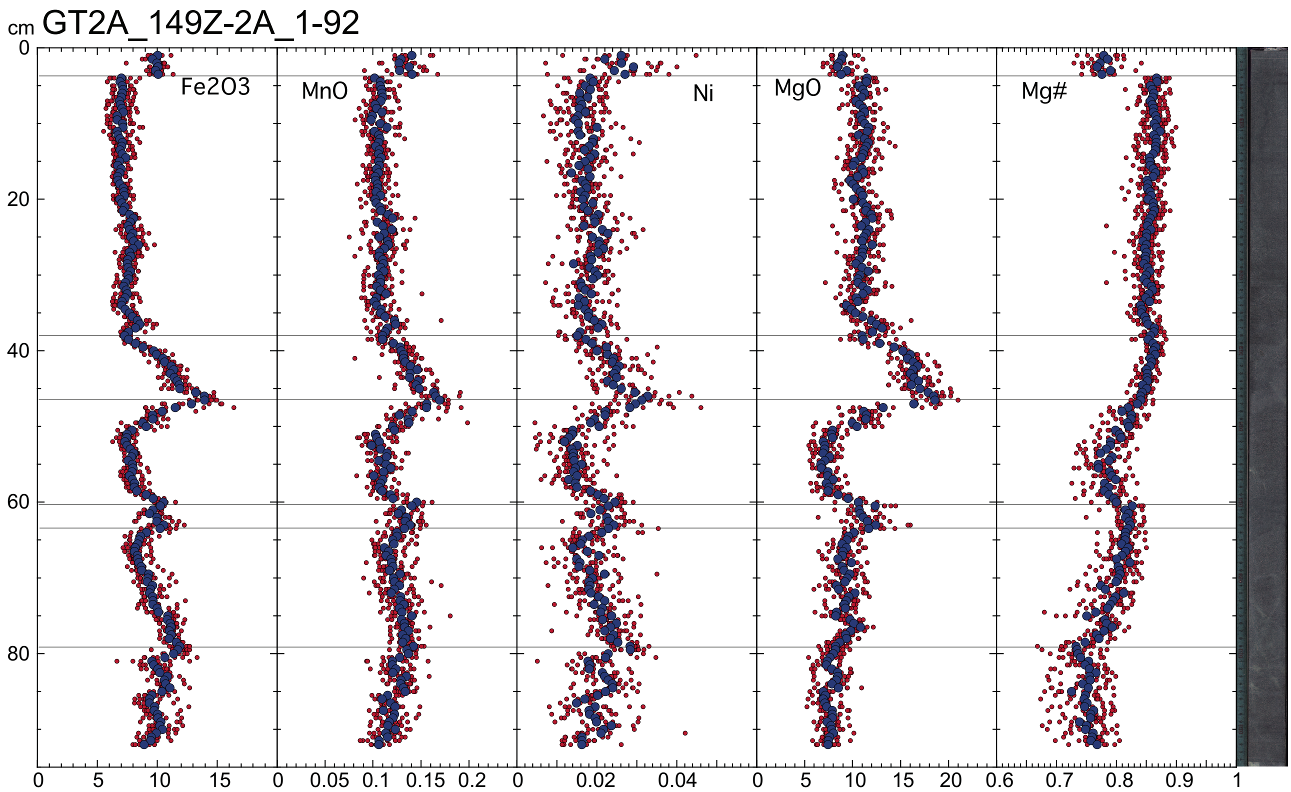

Figure F89. Color-coded images for variations of major elements, Cr, and Ni for GT2A-1049Z-2, 1–92 cm.

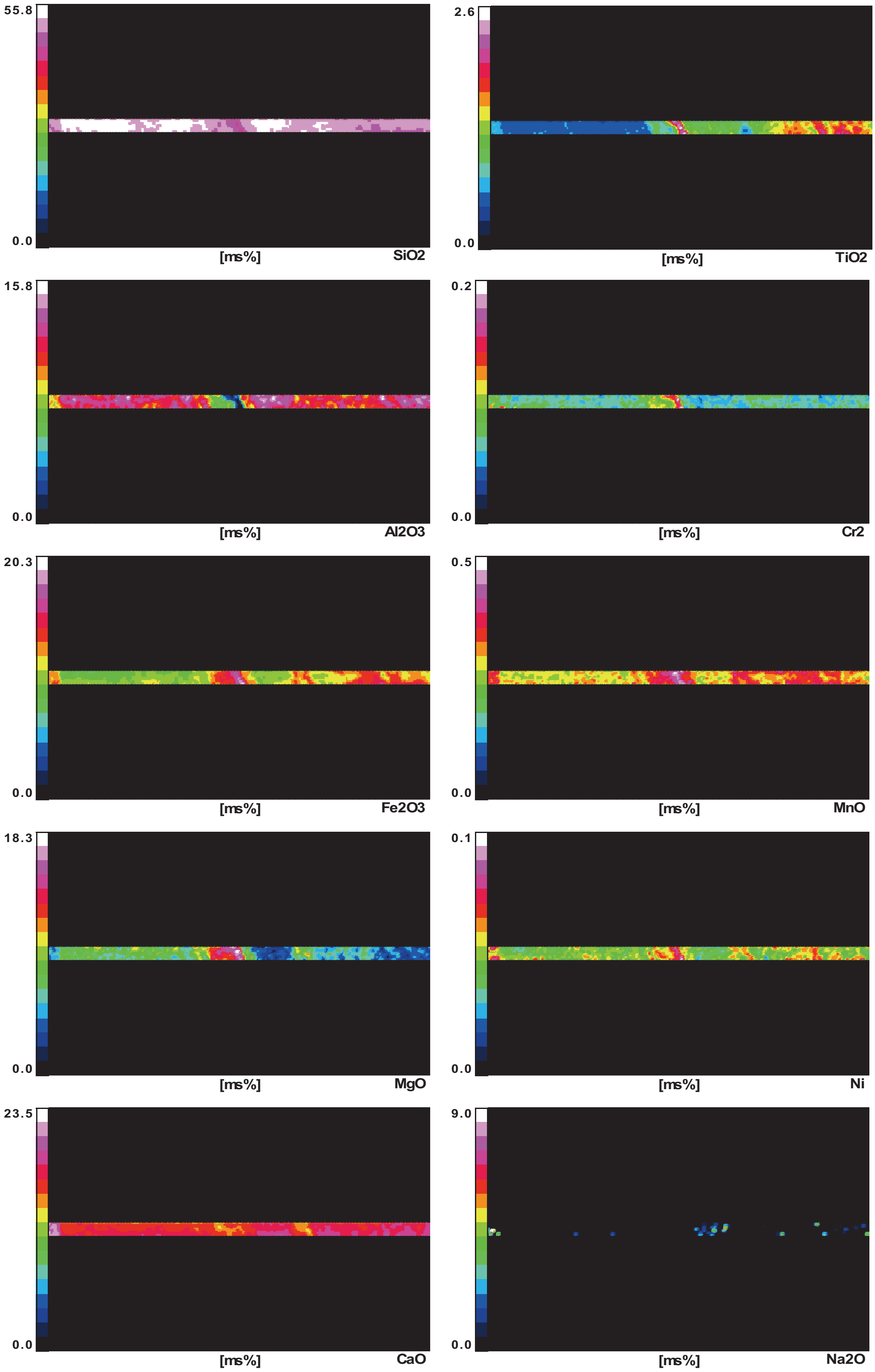

Figure F90. **A.** Downhole plots of bulk magnetic susceptibility, NRM intensity, and Königsberger ratios measured on discrete samples compared with modal abundances of olivine. **B.** Histograms of bulk susceptibility, NRM intensity, and *Q* values.

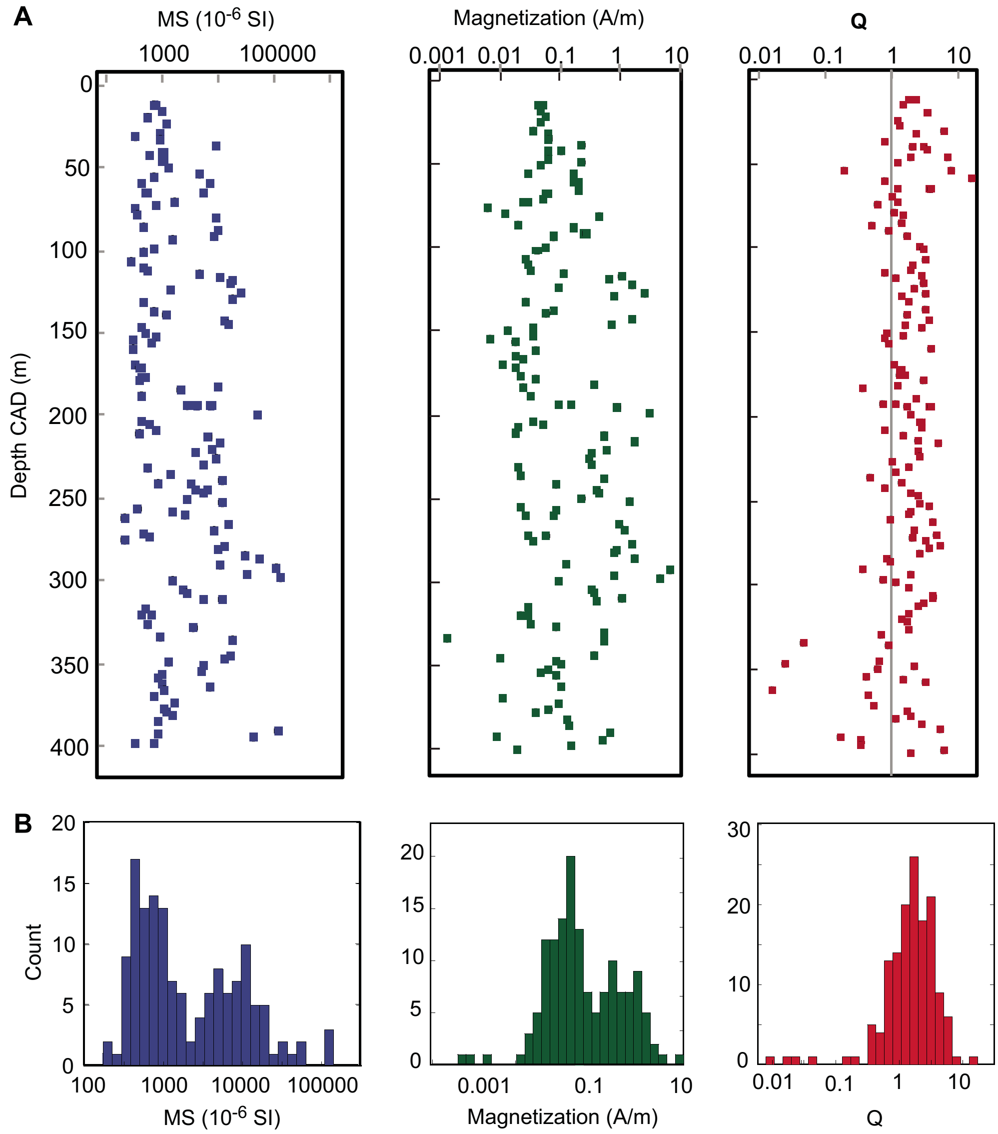

Figure F91. Downhole plot of NRM inclinations and inclinations of the low, intermediate, and stable remanence components determined from principal component analysis.

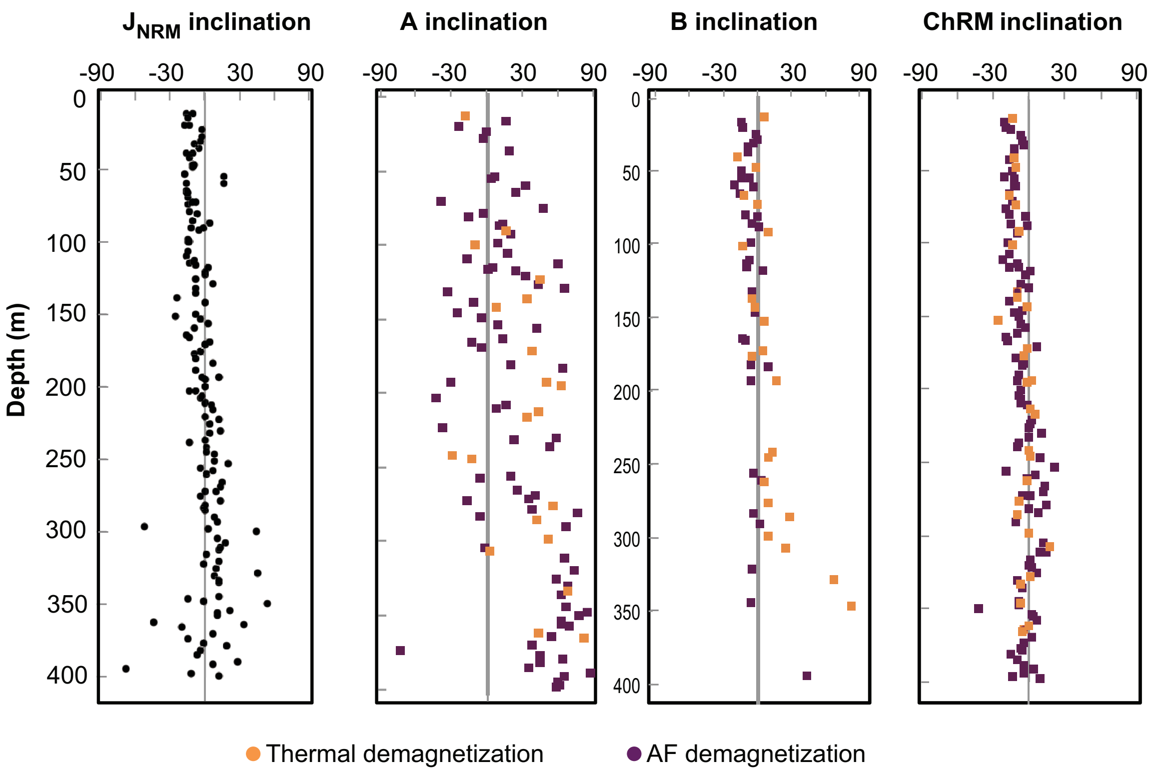

Figure F92. A. Representative orthogonal vector projections displaying behavior of magnetic remanence directions during progressive thermal demagnetization of discrete samples. **B.** Curves of intensity as a function of temperature. **C.** Bulk susceptibility changes during progressive thermal demagnetization.

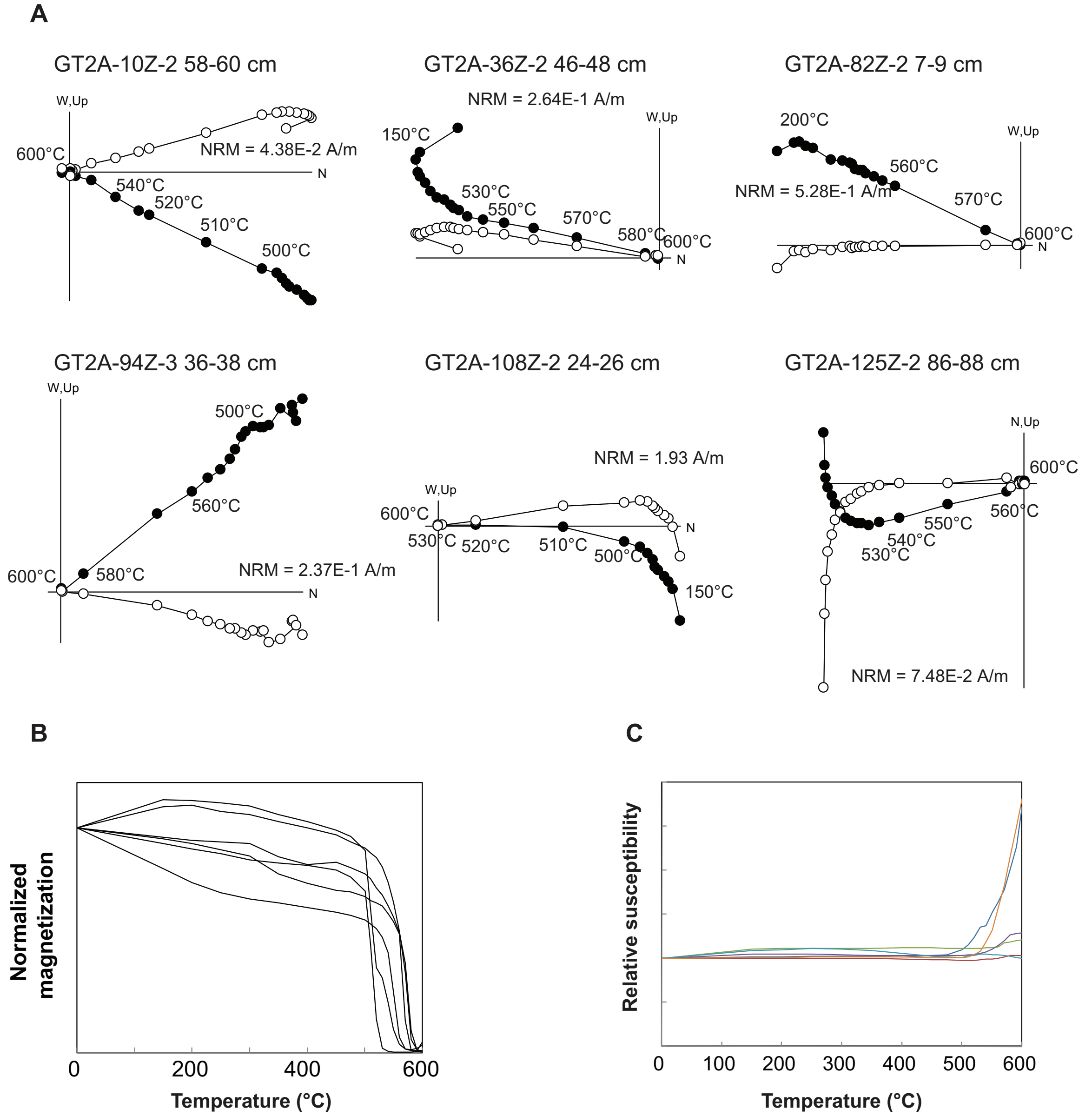

Figure F93. A. Representative orthogonal vector projections displaying behavior of magnetic remanence directions during progressive AF demagnetization of discrete samples. **B.** Curves of intensity as a function of field strength.

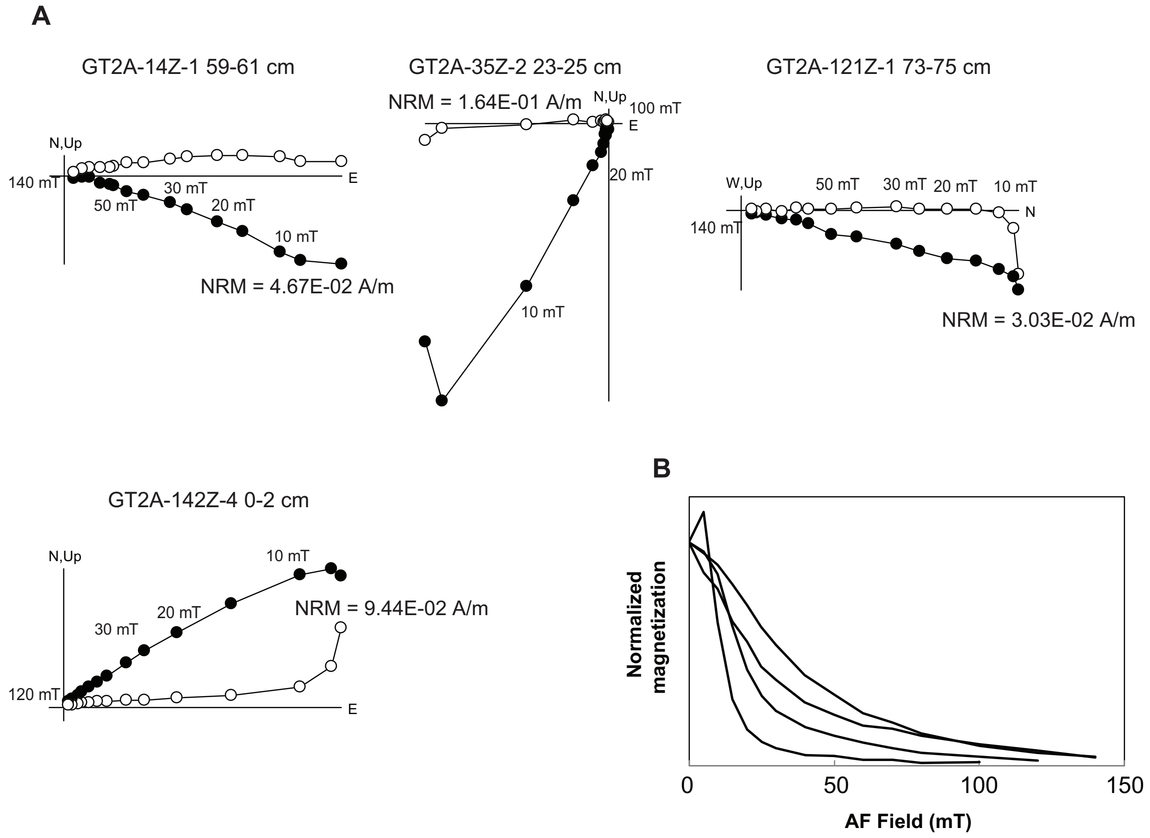

Figure F94. Stereoplots of remanence component orientations identified by principal component analysis. Open (solid) symbols represent upper (lower) hemisphere directions.

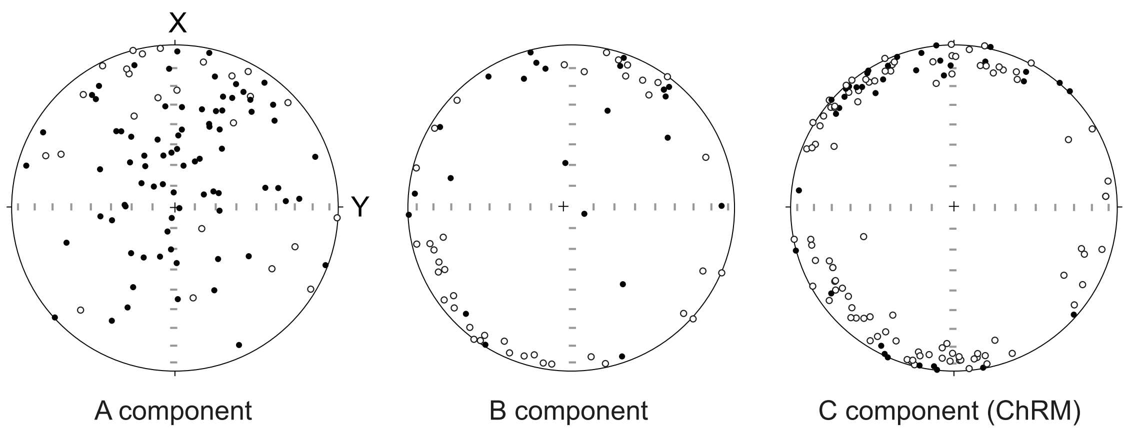

Figure F95. Stereoplots of principal susceptibility axes from anisotropy of magnetic susceptibility measurements plotted on lower hemisphere equal-area projections in the core reference frame.

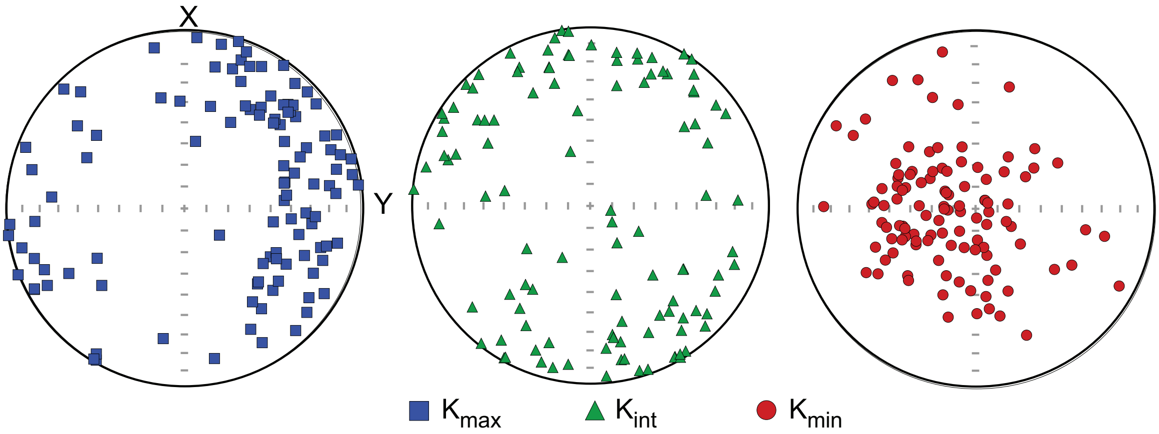

Figure F96. **A.** Downhole plots of magnetic anisotropy intensity, shape, and K_{min} orientation. **B.** Degree of anisotropy as a function of bulk susceptibility. **C.** Shape parameter vs. degree of anisotropy of magnetic susceptibility.

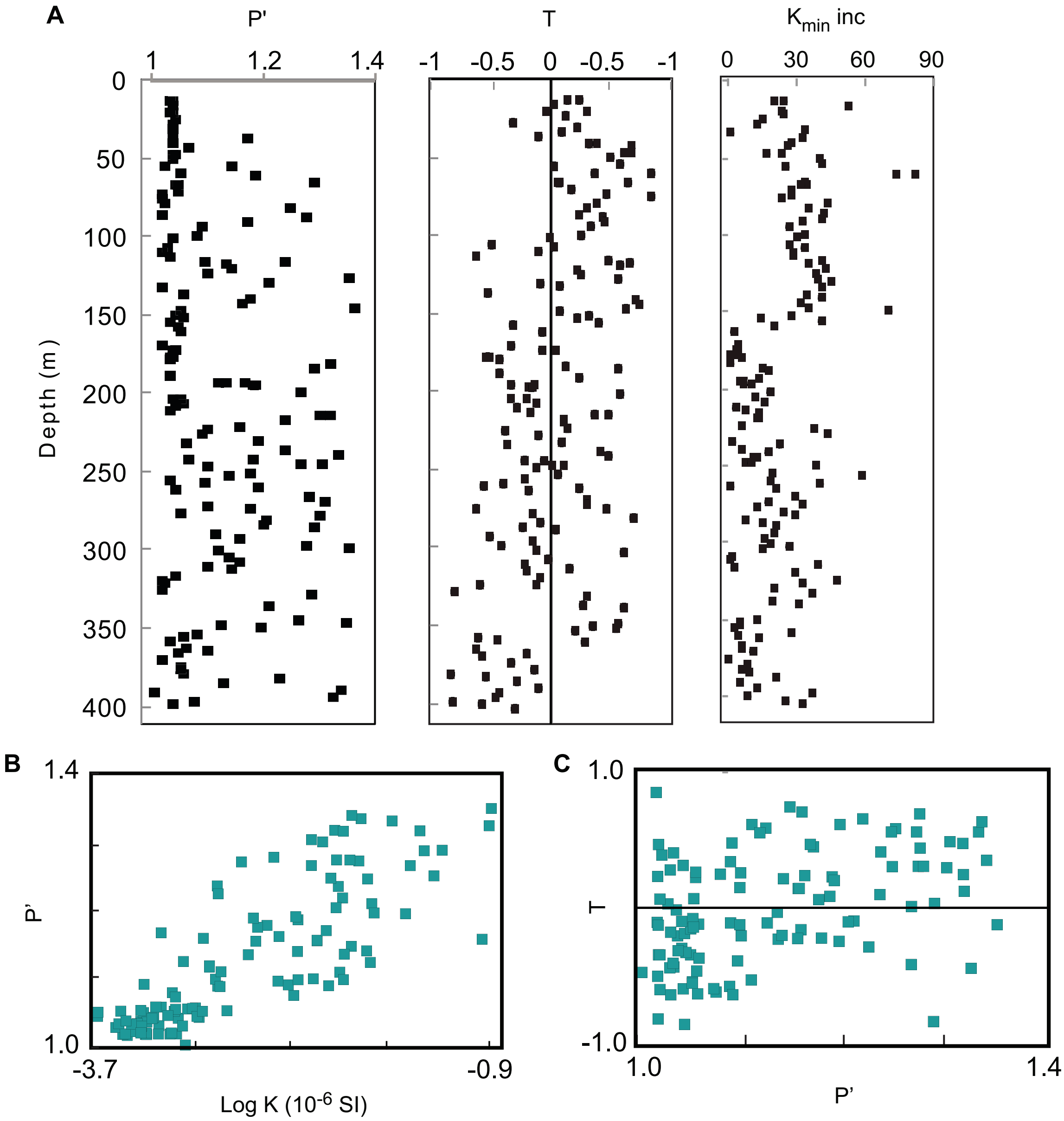

Figure F97. **A.** Stereoplot of magnetic anisotropy orientations after azimuthal rotation of ChRM declinations around the core axis to a reference paleomagnetic declination. **B.** Downhole plot of rotated K_{max} declinations.

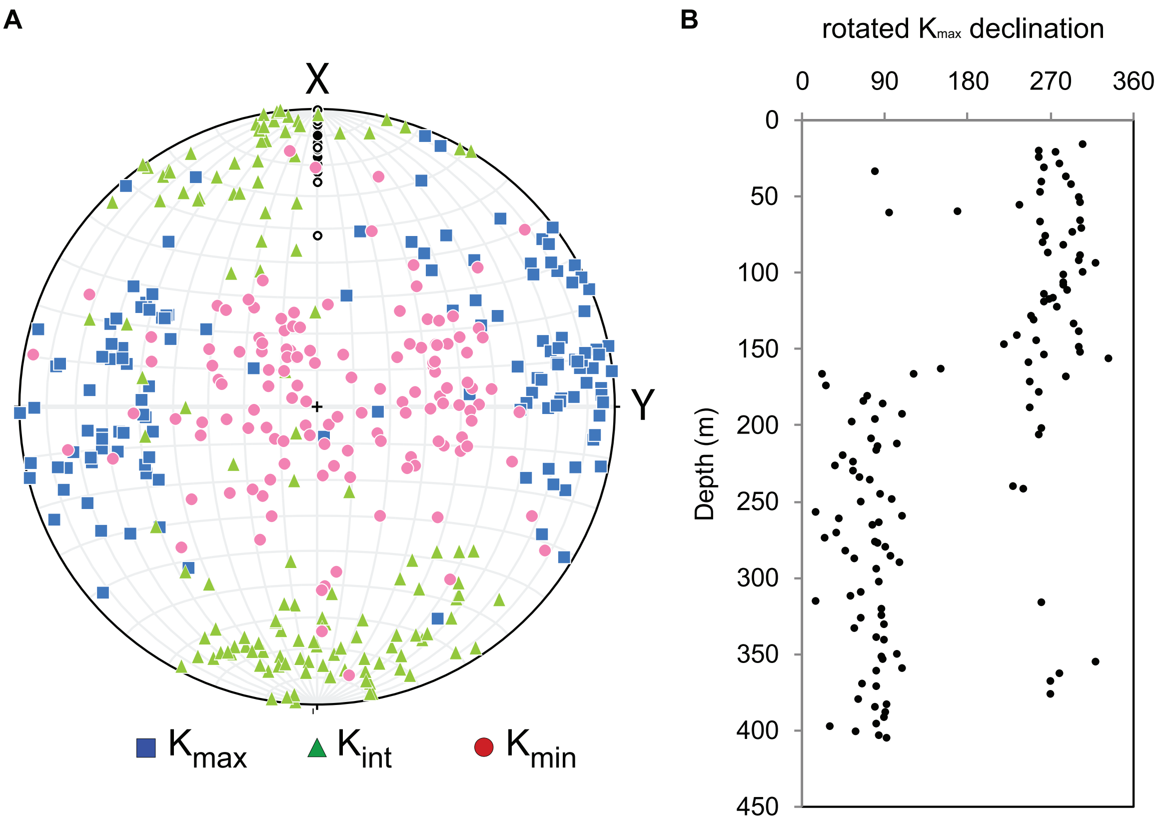

Figure F98. **A.** Photomicrograph of a primary Fe-Ti oxide grain containing a modified oxyexsolution texture (121Z-3, 73–78 cm; reflected light [RL]). **B.** Pale yellow sulfide grains (146Z-1, 78–81 cm; RL). **C.** Opaque mesh texture in an altered olivine grain (115Z-1, 43.5–75 cm; PPL). **D.** Fine-grained oxides in same region shown in C (RL).

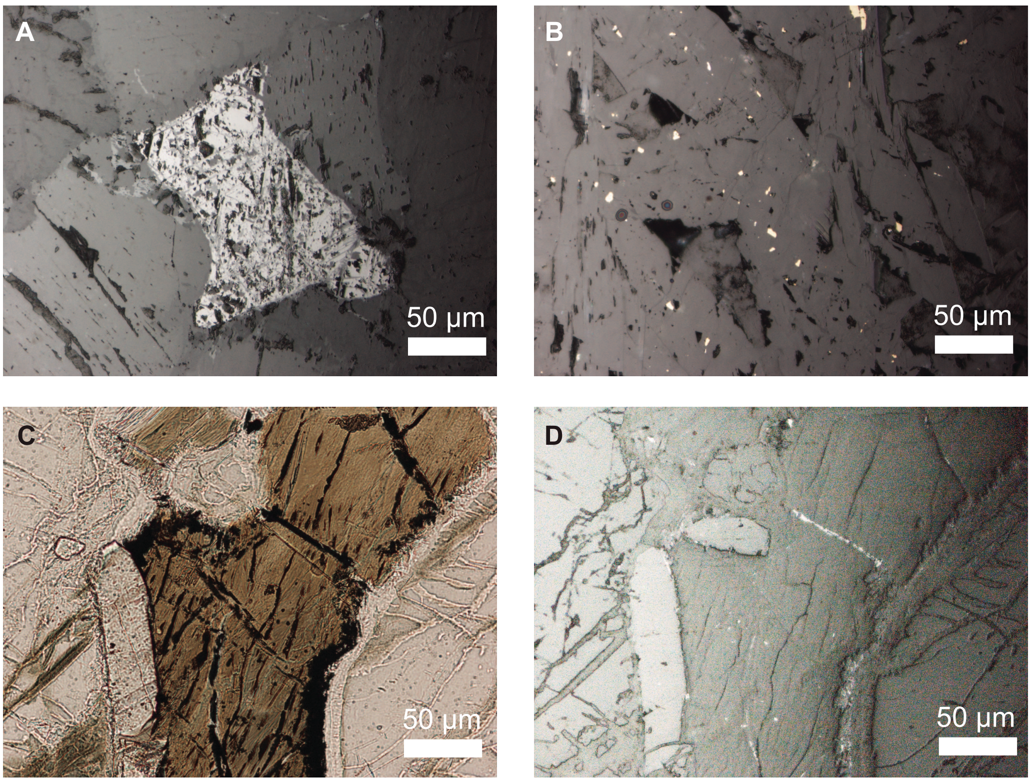

Figure F99. Downhole plots for natural gamma radiation (NGR), (**A**) filtered and (**B**) nonfiltered NGR. Point magnetic susceptibility (MS) on (**C**) linear and (**D**) logarithm scales. Whole-round MS by MSCL-W on (**E**) linear and (**F**) logarithm scales.

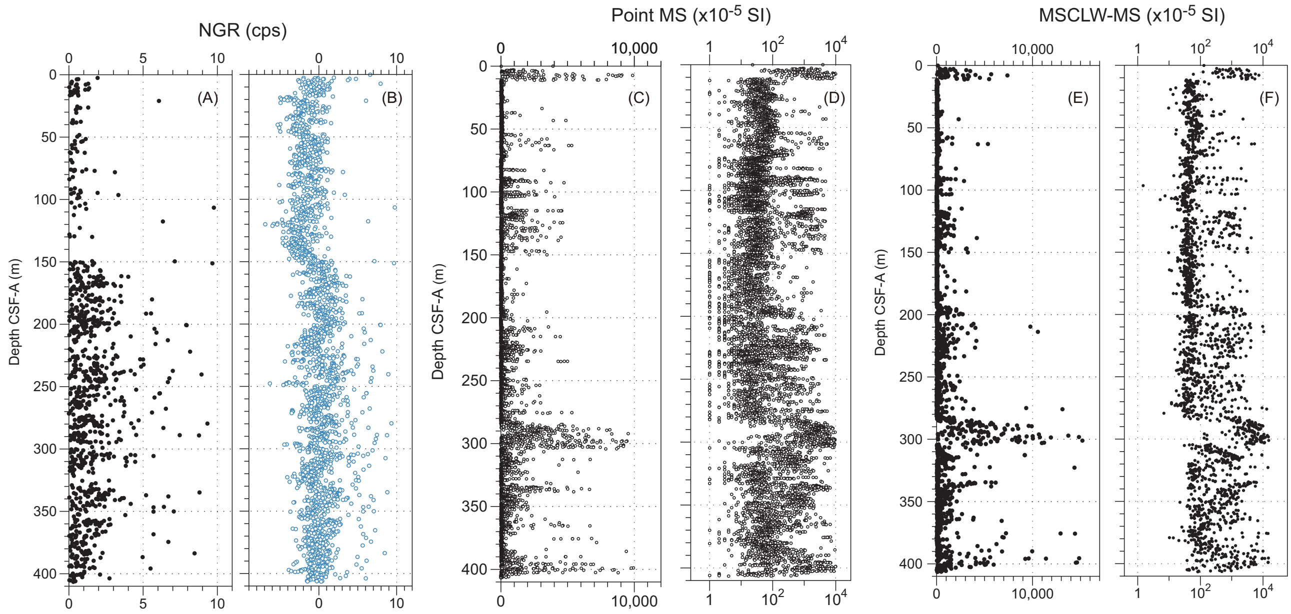

Figure F100. (A) MSCL-I image, (B) X-ray CT image, and (C) average CT values.

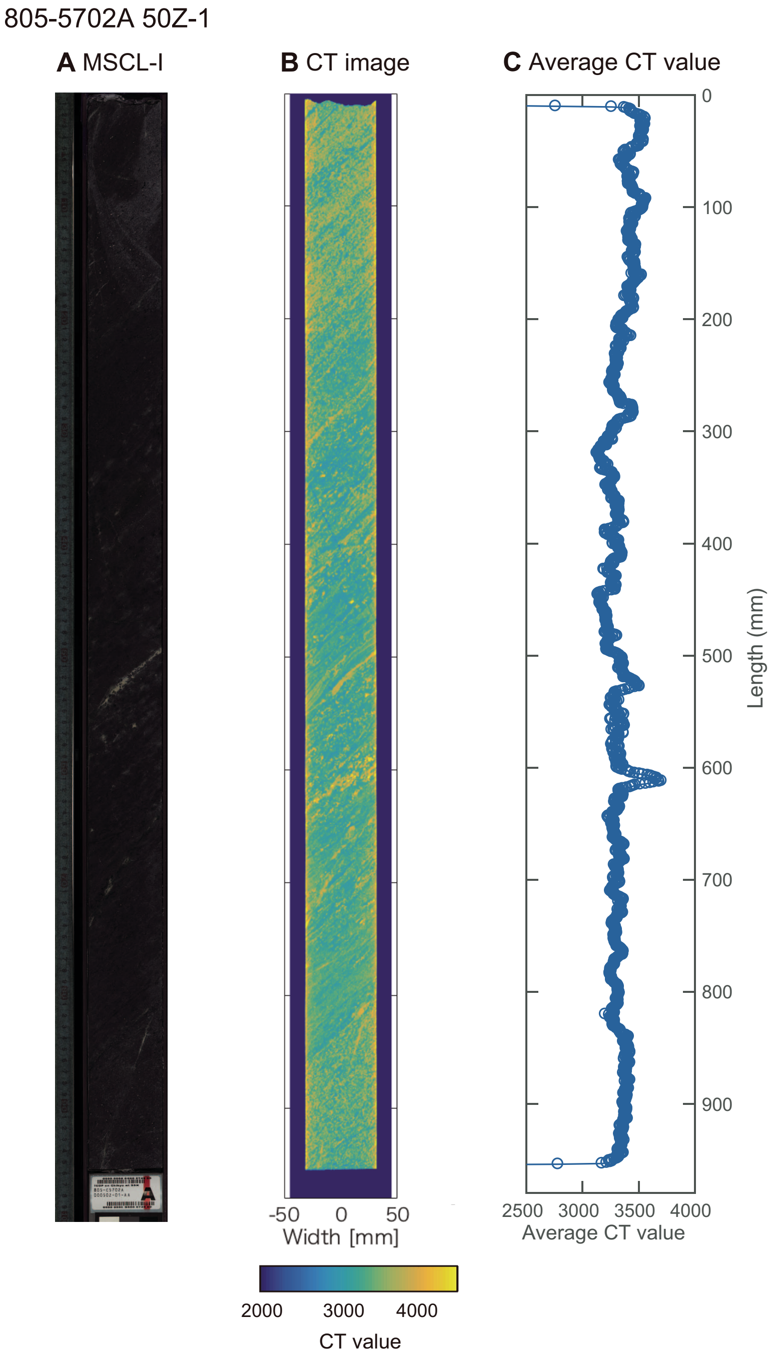

Figure F101. (**A**) Linescan image with (**B**) MSCL-W MS and (**C**) NGR.

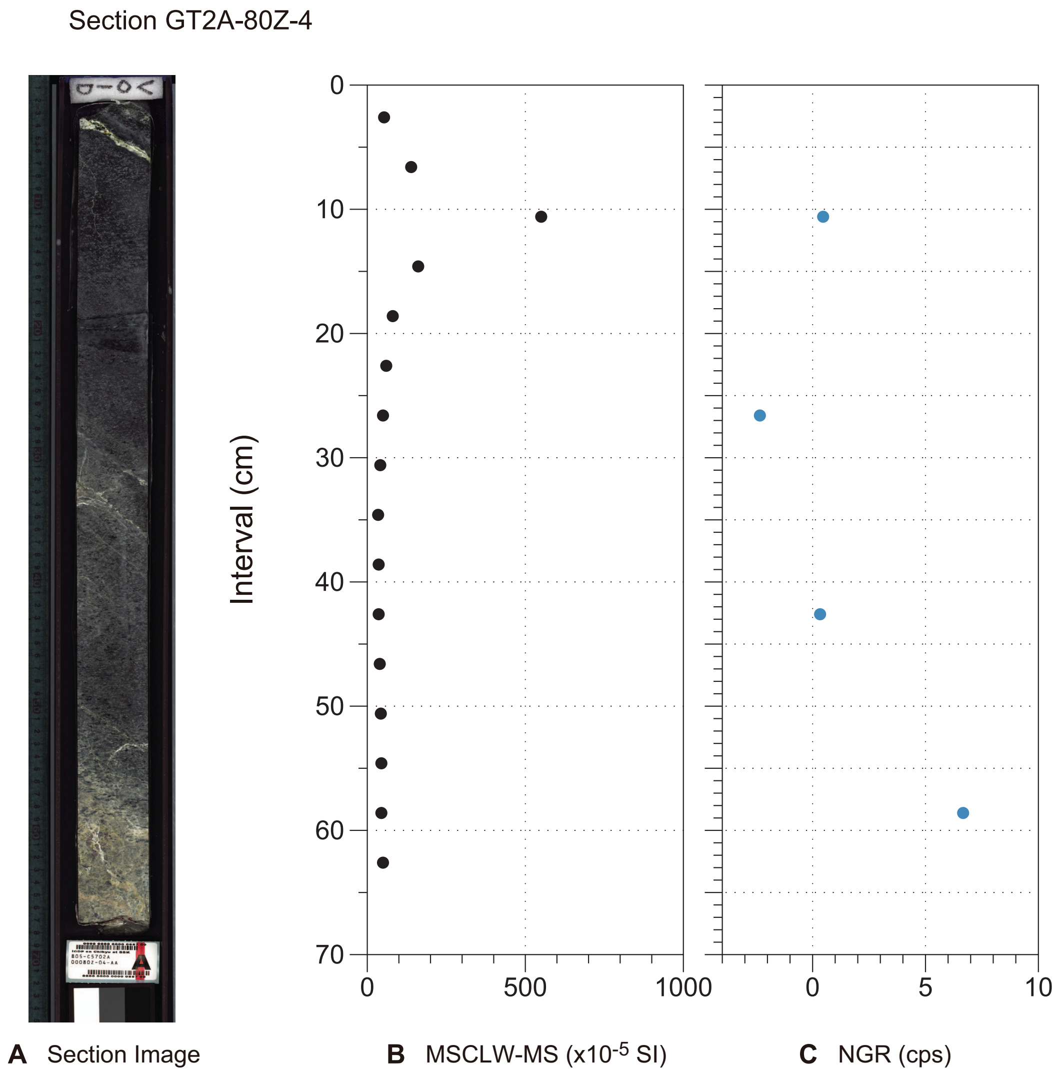

Figure F102. MSCL-C downhole plot.

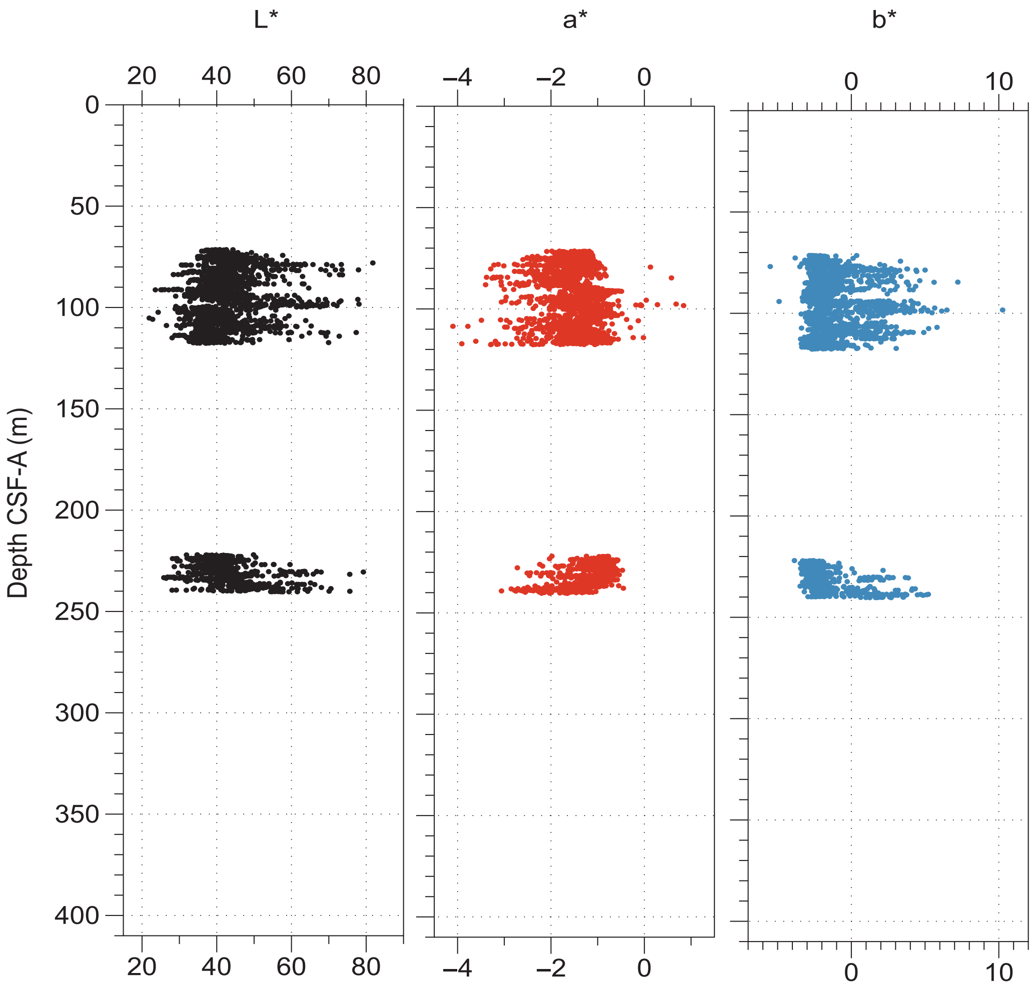

Figure F103. Downhole distribution of *P*-wave velocity, grain density, and porosity measured on discrete samples. Lithology of samples is that of host igneous intervals.

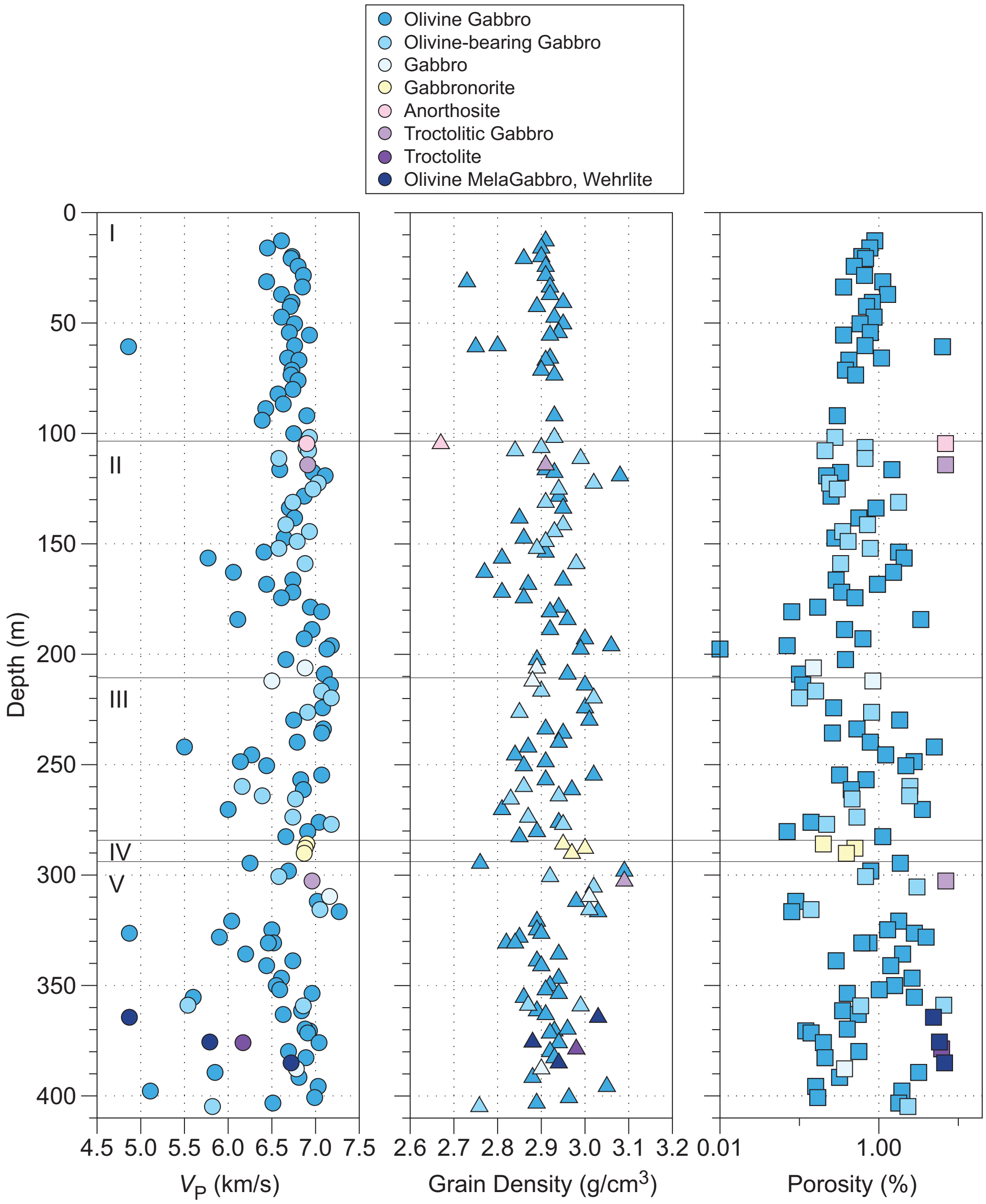

Figure F104. **A.** *P*-wave velocity vs. porosity. **B.** bulk density vs. porosity. **C.** *P*-wave velocity vs. average olivine mode of host interval. **D.** grain density vs. average olivine mode of host interval.

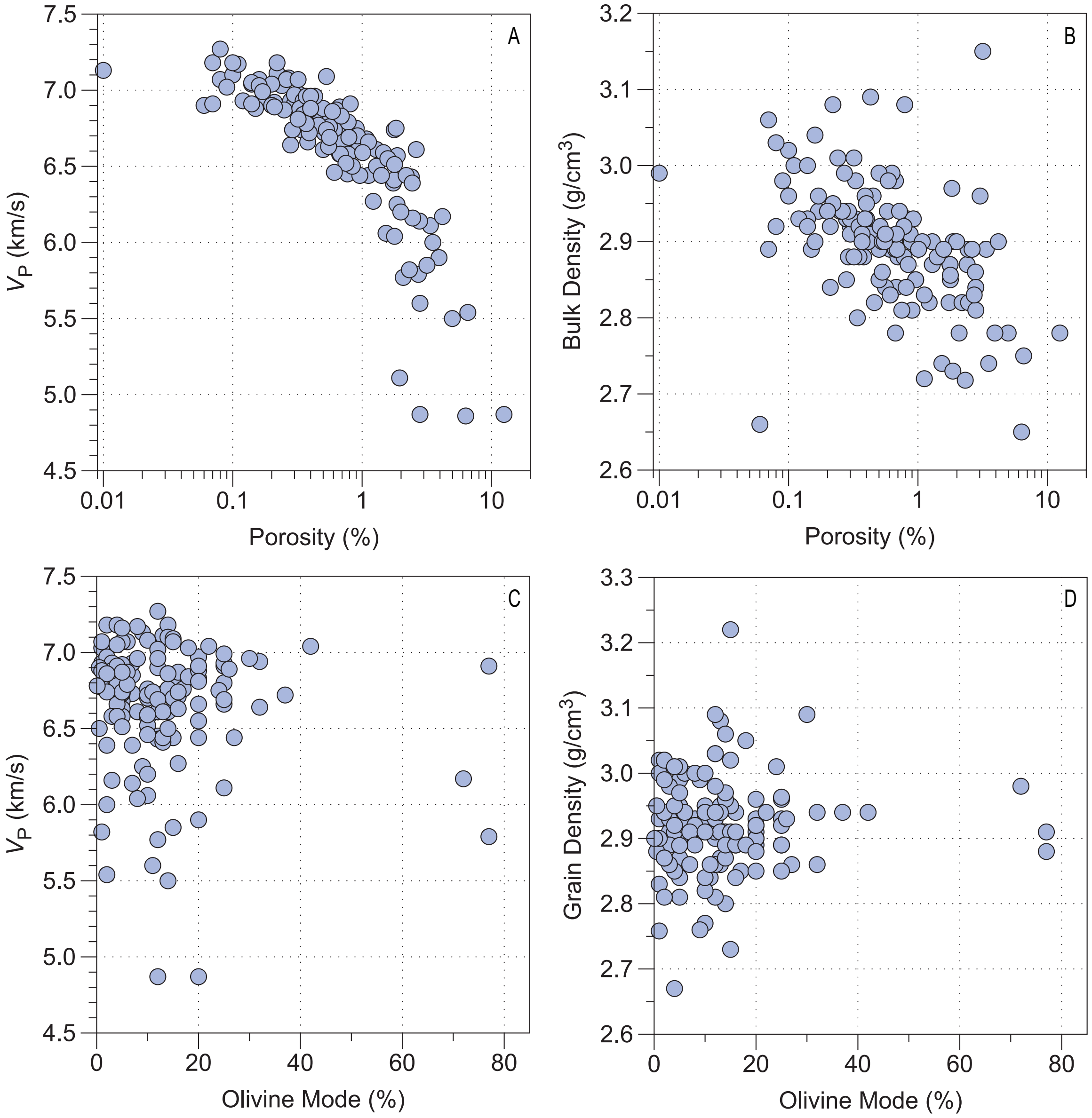

Figure F105. *P*-wave velocity vs. (**A**) bulk density and (**B**) grain density. Background data are from Blackman et al., 2006 (Atlantis Massif), Gillis et al., 2014 (Hess Deep), and MacLeod et al., 2017 (Atlantis Bank). The average Oman gabbro data in B is from Abers and Hacker (2016).

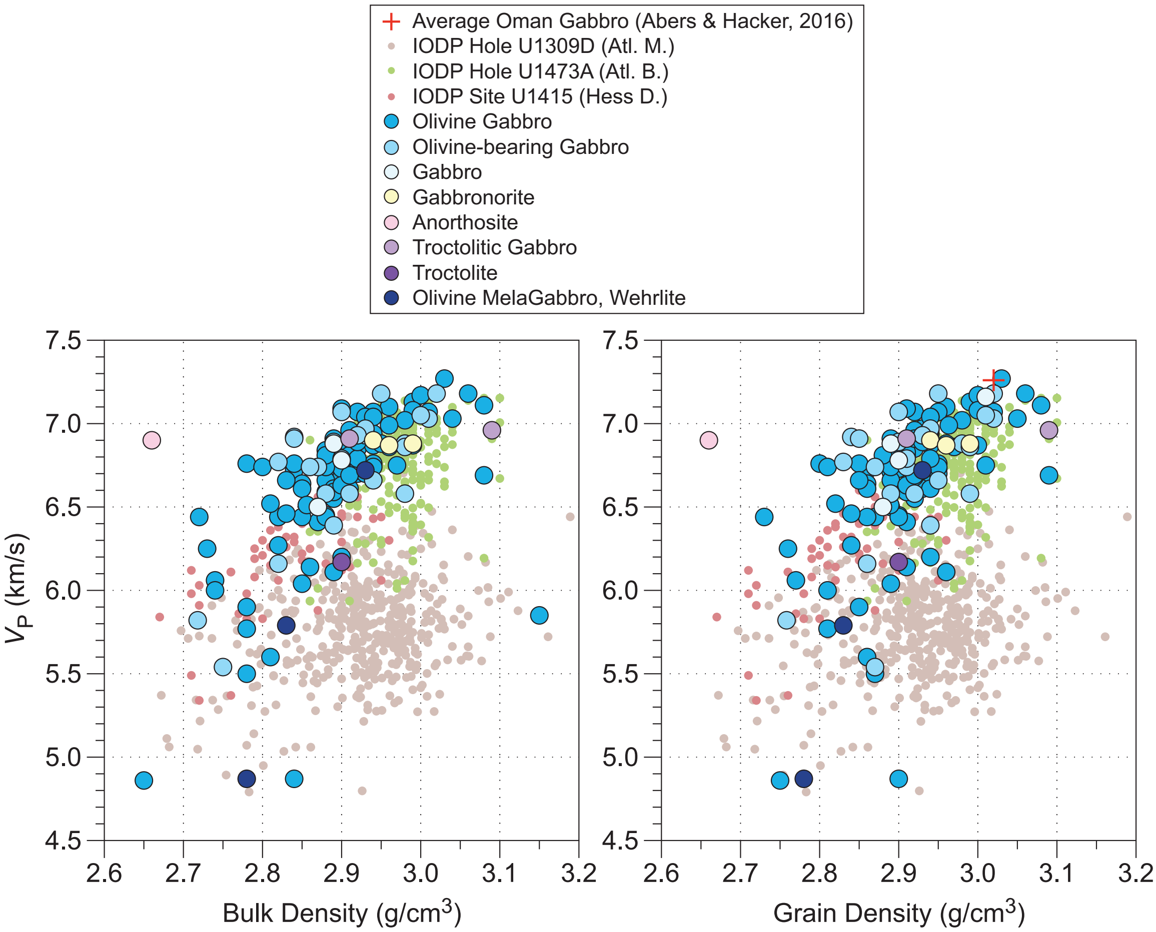

Figure F106. Downhole distribution of thermal conductivity. Lithology of samples is that of host igneous intervals.

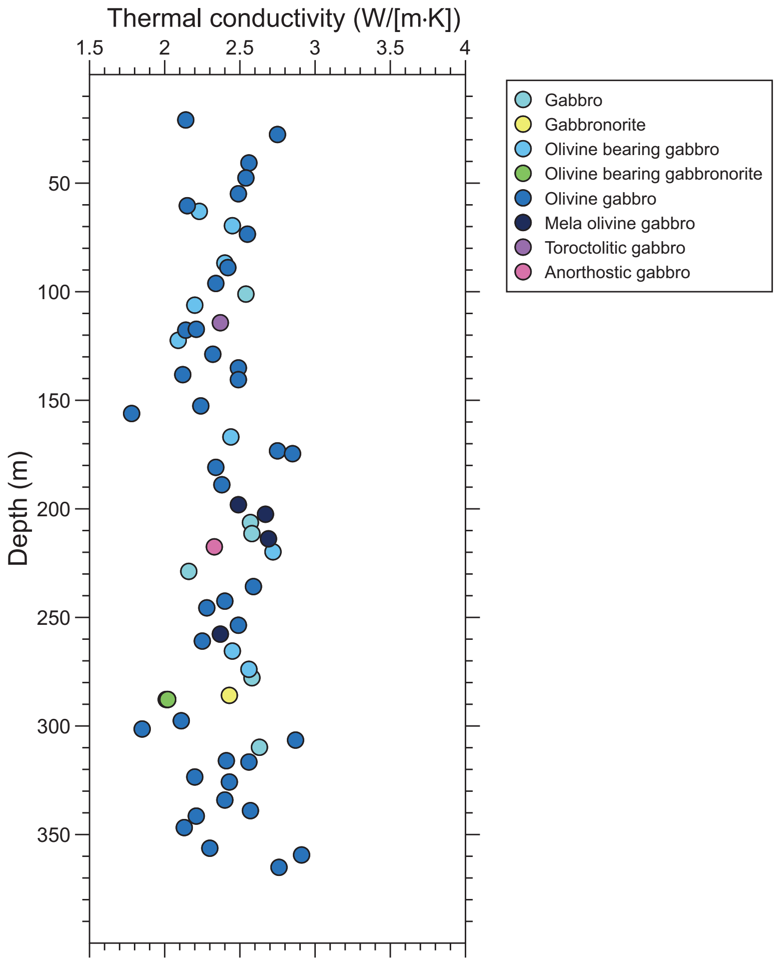

Figure F107. Thermal conductivity of different rock types from Hole GT2A vs. olivine modal abundance.

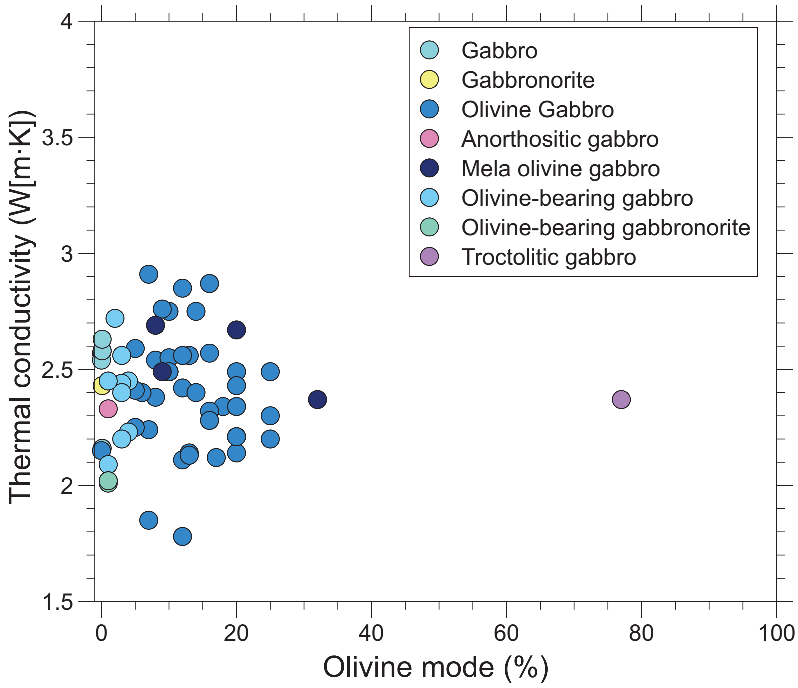

Figure F108. **A.** MSCL-I scan of the upper portion of a core section. **B.** Preliminary map of minerals of interest derived from imaging spectroscopy data.

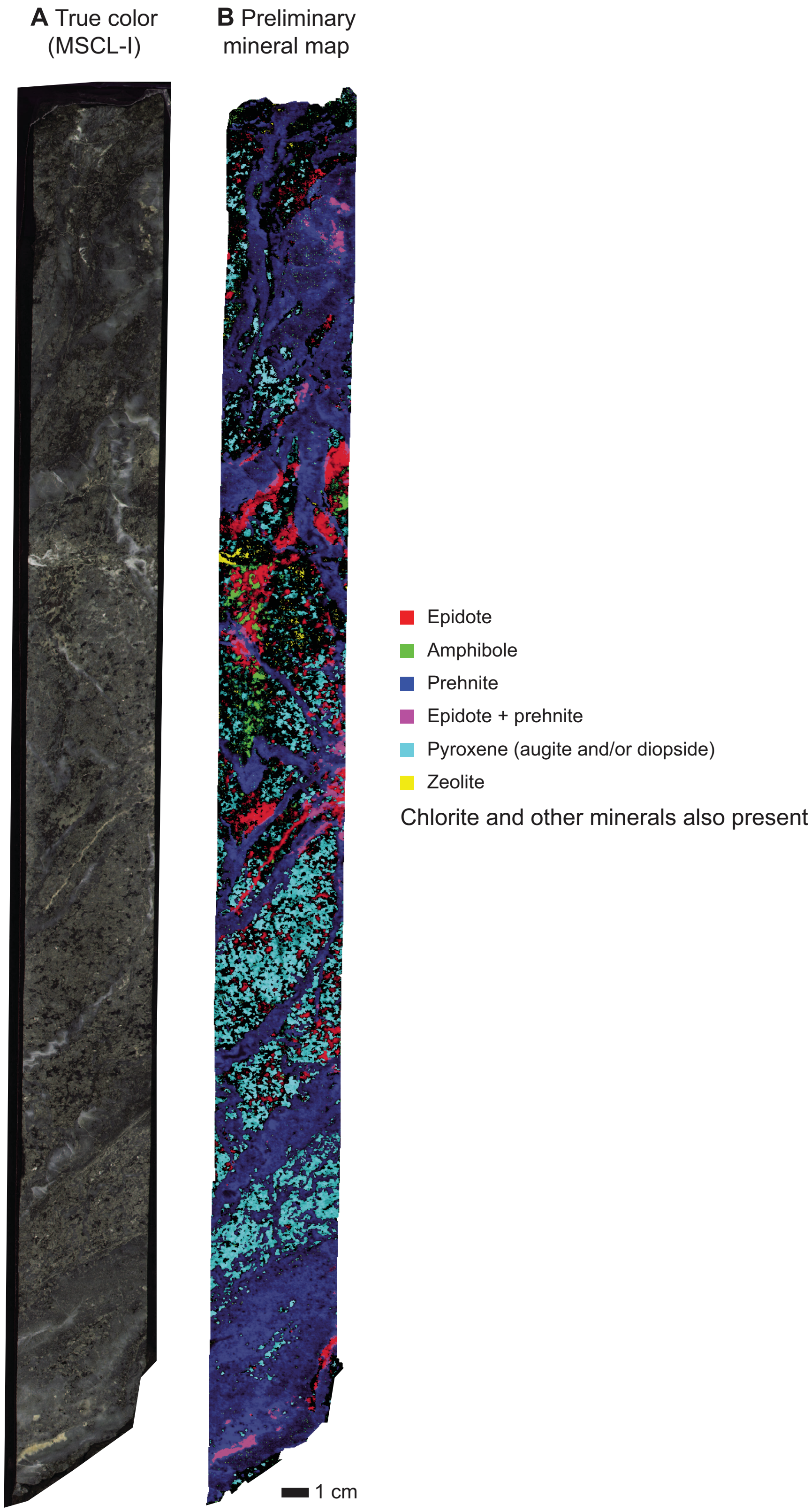

Tables

Table T1. Operations, Site GT2. **This table is available in Microsoft Excel format.**

Table T2. Lithologic units, igneous intervals, and contacts, Hole GT2A. **This table is available in Microsoft Excel format.**

Table T3. Summary of thin section descriptions, Hole GT2A. **This table is available in Microsoft Excel format.**

Table T4. Shipboard XRD mineral identifications, Hole GT2A. **This table is available in Microsoft Excel format.**

Table T5. Average dips of magmatic foliation and layering in the gabbro sequences of Hole GT2A relative to the core reference frame, local outcrops, and the crust/mantle boundary in Wadi Gideah. **This table is available in Microsoft Excel format.**

Table T6. Summary of major, trace, and rare earth element concentrations, total H_2O, C, N, and S, and inorganic carbon in rock powders, Hole GT2A. **This table is available in Microsoft Excel format.**

Table T7. List of analyzed cores measured by CS-XRF. **This table is available in Microsoft Excel format.**

Table T8. Raw analytical data for GT2A-52Z-3, 1–74 cm, without correction. **This table is available in Microsoft Excel format.**

Table T9. Raw analytical data for GT2A-54Z-4, 4–66 cm, without correction. **This table is available in Microsoft Excel format.**

Table T10. Raw analytical data for GT2A-69Z-3, 2–57 cm, without correction. **This table is available in Microsoft Excel format.**

Table T11. Raw analytical data for GT2A-81Z-4, 1–43 cm, without correction. **This table is available in Microsoft Excel format.**

Table T12. Raw analytical data for GT2A-85Z-1, 1–59 cm, without correction. **This table is available in Microsoft Excel format.**

Table T13. Raw analytical data for GT2A-86Z-2, 1–52 cm, without correction. **This table is available in Microsoft Excel format.**

Table T14. Raw analytical data for GT2A-102Z-2, 4–71 cm, without correction. **This table is available in Microsoft Excel format.**

Table T15. Raw analytical data for GT2A-105Z-2, 39–54 cm, without correction. **This table is available in Microsoft Excel format.**

Table T16. Raw analytical data for GT2A-149Z-2, 1–92 cm, without correction. **This table is available in Microsoft Excel format.**

Table T17. Average compositions with standard deviation of the studied cores, Hole GT2A. **This table is available in Microsoft Excel format.**

Table T18. Natural remanent magnetization values and principal component analysis results, Hole GT2A. **This table is available in Microsoft Excel format.**

Table T19. Inclination-only statistics after Arason and Levi (2010). **This table is available in Microsoft Excel format.**

Table T20. Magnetic susceptibility values and anisotropy parameters, Hole GT2A. **This table is available in Microsoft Excel format.**

Table T21. Summary of discrete physical properties measurements, Hole GT2A. **This table is available in Microsoft Excel format.**

Table T22. Velocity, density, and porosity measurements, Hole GT2A. **This table is available in Microsoft Excel format.**

Table T23. Thermal conductivity measurements, Hole GT2A. **This table is available in Microsoft Excel format.**

Table T24. SWIR/NVIR samples, Hole GT2A. **This table is available in Microsoft Excel format.**

Supplemental tables

Table ST1. Hole GT2A plutonic rocks. **This table is available in Microsoft Excel format.**

Table ST2. Hole GT2A igneous intervals. **This table is available in Microsoft Excel format.**

Table ST3. Geochemistry results, Hole GT2A. **This table is available in Microsoft Excel format.**

Table ST4. MSCL-W (MS and NGR), Hole GT2A. **This table is available in Microsoft Excel format.**

Table ST5. MSCL-C (color spectrum and MS), Hole GT2A. **This table is available in Microsoft Excel format.**